DEVELOPMENT OF LOW FREQUENCY FERRITE CORE MATERIALS USING MAGNETITE, A BEACH SAND MINERAL

Ph.D Thesis

By

Shireen Akhter

DEPARTMENT OF APPLIED PHYSICS, ELECTRONICS AND COMMUNICATION ENGINEERING, UNIVERSITY OF DHAKA, DHAKA, BANGLADESH

NOVEMBER-2014

DEVELOPMENT OF LOW FREQUENCY FERRITE CORE MATERIALS USING MAGNETITE, A BEACH SAND MINERAL

By

Shireen Akhter

Ph.D Registration No. 162

Session: 2010-2011

A THESIS SUBMITTED TO THE DEPARTMENT OF APPLIED PHYSICS, ELECTRONICS AND COMMUNICATION ENGINEERING, UNIVERSITY OF DHAKA, DHAKA, IN PARTIAL FULFILLMENT OF THE REQUIREMENT FOR THE DEGREE OF DOCTOR OF PHILOSOPHY

DEPARTMENT OF APPLIED PHYSICS, ELECTRONICS AND COMMUNICATION ENGINEERING, UNIVERSITY OF DHAKA, DHAKA, BANGLADESH

NOVEMBER-2014

DECLARATION

The material embodied in this thesis is original and has not been submitted in part or full for any other diploma or degree of any university.

Prof. Dr. Jalalur Rahman
Supervisor
Dept. of Applied Physics, Electronics &
Communication Engineering, University of Dhaka

Shireen Akhter
Ph.D research student

Prof. Dr. Zahid Hasan Mahmood
Co-Supervisor
Dept. of Applied Physics, Electronics &
Communication Engineering, University of Dhaka

To

My Late parents

Acknowledgement

It gives me immense pleasure and satisfaction to acknowledge the blessings of the Almighty Allah, the creator of the universe who is the most gracious, compassionate and beneficent to His creature, who blessed me with knowledge and potential to implement my research work.

I express with due respect, my deep sense of sincere gratitude and indebtedness to my supervisor Professor Dr. Jalalur Rahman, Department of Applied Physics, Electronics and Communication Engineering, University of Dhaka, for his constant guidance, helpful suggestion, fruitful discussion throughout the research work.

I also express my deepest gratitude and indebtedness to my co-supervisor Professor Dr. Zahid Hasan Mahmood, Department of Applied Physics, Electronics and Communication Engineering, University of Dhaka for his supervision, inspiring guidance and valuable suggestion throughout this research work.

I express, with due respect my sincere gratitude to Professor Dr. Md. Amanullah Choudhury, Head, Department of Electrical and Electronic Engineering, World University of Bangladesh, Dhaka for introducing the present research topic, for his inspiring guidance and valuable suggestions throughout this research work. It would have not been possible for me to bring out this thesis without his help and constant encouragement.

I am grateful to the Chairman of Bangladesh Atomic Energy Commission for giving me permission for the Ph. D. research work.

I express my grateful thanks to Professor Subrata K. Aditya, Ex-Chairman and Professor Dr. Adnan Kiber, present Chairman, Department of Applied Physics, Electronics and Communication Engineering, University of Dhaka for their interest and confidence in my work.

I am also grateful to Dr. D. K. Saha, CSO, Materials Science Division, Atomic Energy Centre, Dhaka for his help in XRD measurements.

I am also thankful to Dr. S. M. Hoque, PSO, Dr. M. Huq, Dr. M. N. I Khan, H. N. Das, SSO, and Mr. Al Mamun, Engineer, Materials Science Division, AECD, for their help and co-operation in experimental works.

I am thankful to Ms. Alhamra Parveen, EO and Ms. Anjuman Ara Begum, JEO of Materials Science Division, AECD, for their help in preparing the samples and measurements.

I would like to give thanks to Ms. N. Begum, Mr. K. Hasan, Mr. A. Hossain, Mr. N. Islam and Ms. Z. Begum of Materials Science Division, AECD for their help during my experimental works.

Abstract

Low frequency ferrite core materials of iron deficient Ni-Zn ferrites and iron excess Mn-Zn ferrites have been developed using cheap beach sand mineral magnetite (Fe_3O_4) as the basic ingredient as well as with the addition of low melting CuO, V_2O_5, Eu_2O_3 and In_2O_3 from the following compositions:

(i) $Ni_{0.65}Zn_{0.35}Fe_{1.96}O_4$+x[CuO, V_2O_5, Eu_2O_3, In_2O_3]

(ii) $Mn_{0.451}Zn_{0.484}Fe_{2.065}O_4$+x[CuO, V_2O_5, Eu_2O_3, In_2O_3]

A series of polycrystalline samples of mixed ferrites were prepared by standard ceramic method for systematic investigation of their physical, magnetic and electrical properties. Single phase cubic spinel structure of the prepared core materials has been confirmed by X-ray diffraction analysis. Physical properties such as; sintered density, lattice constant and microstructural properties of the materials have been measured. The magnetic and electrical properties of the core materials have been investigated by studying saturation magnetization, Curie temperature, initial magnetic permeability, normalized loss factor, dc resistivity and eddy current loss.

The addition of divalent V_2O_5 (melting point 700°C) and CuO (melting point (1026°C-1235°C) in the composition of iron deficient Ni-Zn ferrite enhances the chemical reactivity of the resulting mixture, facilitates the attainment of high degree of uniformity in the sintered body, increases the anion vacancy concentration and prohibit discontinuous grain growth which in turn enhances the density of the core materials. The lattice constant values of the ferrite system remain almost unaffected with the addition of V_2O_5 and CuO. The saturation magnetization, Curie temperature and initial magnetic permeability are enhanced appreciably with the addition of these two oxides. The minimum value of normalized loss factor, maximum value of dc resistivity and minimum value of eddy current loss are achieved for core samples containing 0.4 mol% and 1 mol% of V_2O_5 content respectively. For CuO addition, the minimum value of normalized loss factor, maximum value of dc resistivity and minimum value of eddy current loss are achieved for core samples containing 2 mol% of CuO content.

The addition of trivalent In_2O_3 (melting point 680°C) and Eu_2O_3 (melting point 623°C) in the composition of iron deficient Ni-Zn ferrite enhances the chemical reactivity of

the resulting mixture, forms liquid phase on the grain surface of the ferrite and facilitates the attainment of high degree of uniformity in the sintered body which eventually promotes densification. The lattice constant values of the ferrite system increase almost linearly with the addition of these two oxides. The saturation magnetization, Curie temperature and initial magnetic permeability of the ferrite system decrease with the addition of In_2O_3. Whereas, all these parameters of the ferrite system increase markably with the addition of Eu_2O_3. However, the minimum value of normalized loss factor, the maximum value of dc resistivity and minimum value of eddy current loss of the ferrite system are achieved for core samples containing 3.5 mol% of In_2O_3 and 2 mol% of Eu_2O_3 respectively.

The addition of CuO and V_2O_5 in the composition of iron excess Mn-Zn ferrite enhances the density, however the lattice constant values of the ferrite system remain almost unaffected. The saturation magnetization of the ferrite system increases appreciably, whereas the Curie temperature decreases a little with the addition of CuO. The saturation magnetization and Curie temperature of the ferrite system increases markably with the addition of V_2O_5. However, the initial magnetic permeability of the ferrite system increases appreciably with the addition of CuO and V_2O_5. The minimum value of normalized loss factor, maximum value of dc resistivity and minimum value of eddy current loss are achieved for core samples containing 4 mol% of CuO. For V_2O_5 addition, the minimum value of normalized loss factor, maximum value of dc resistivity and minimum value of eddy current loss can be attained for core samples containing 0.6 mol% and 1 mol% of V_2O_5 content respectively.

The addition of Eu_2O_3 and In_2O_3 in the composition of iron excess Mn-Zn ferrite enhances the density as well as the lattice constant values of the ferrite system. The saturation magnetization and initial magnetic permeability of the ferrite system increases markably with the addition of these two oxides. There is no noticeable influence of Eu_2O_3 on the Curie temperature of the ferrite system. Whereas, the Curie temperature values of the ferrite system decrease with the increasing addition of In_2O_3.The minimum value of normalized loss factor, maximum value of dc resistivity and minimum value of eddy current loss can be achieved for core samples containing 2 mol% and 4 mol% of Eu_2O_3 content respectively. However the minimum value of normalized loss factor, maximum value of dc resistivitiy and minimum value of eddy current loss can be achieved for core sample containing 3.5 mol% of In_2O_3 addition. The possible applications of developed ferrite core materials are also discussed.

Contents

		Page No.
Chapter One: General Introduction and Overview		1
1.1	Introduction	1
1.2	Soft ferrite core materials	2
1.3	Review works	5
1.4	Magnetite (Fe_3O_4), a beach sand mineral	9
1.4.1	Chemical composition of Fe_3O_4	10
1.4.2	Quality of mineral magnetite (Fe_3O_4) used as a basic raw material for the preparation of soft ferrites	10
1.5	Objective of the work	11
References:		13
Chapter Two: Theoretical Background		15
2.1	**General aspects of magnetism**	15
2.1.1	Origin of magnetism	15
2.1.2	Magnetic moment of atoms	16
2.1.3.	Magnetic moment of electrons	17
2.1.4.	Magnetic behaviour	18
2.1.5.	Hysteresis	23
2.1.6	Magnetic domains	25
2.1.7	Structure of domain wall	27
2.2	**Ferrites**	30
2..2.1.	Soft ferrites	30
2.2.2	Hard ferrites	31
2.2.3.	Spinel ferrites	31
2.3	**Cation distribution in ferrites**	31
2.3.1	Normal spinel ferrites	31
2.3.2	Inverse spinel ferrites	32
2.3.3	Mixed or random spinel ferrites	32

2.4 Magnetic exchange interaction 33
2.4.1 Superexchange interaction 33
2.4.2 Two sublattice in spinel ferrites 35
2.5 Magnetic Structure of Substituted ferrites 37
2.5.1. Neel's collinear model of ferrites 37
2.5.2 Non-collinear model 37
References: 39
Chapter Three: The Properties of Soft Ferrites 40
3.1 Crystalline and magnetic structure 40
3.2 Chemistry of soft ferrites 46
3.3 Magnetic properties 51
3.3.1 Saturation magnetization and Curie temperature 52
3.3.2 Initial permeability 55
3.4 Electrical properties 57
References: 60
Chapter Four : Preparation of low frequency ferrite core materials 61
4.1 Mixing 62
4.2 Presintering 63
4.3 Processing the raw ferrite and forming 63
4.4 Sintering 65
4.5 Preparation of samples 66
4.5.1 Composition of ferrites 66
4.5.2 Sample preparation technique 67
4.5.3 Method of preparation 67
References: 69
Chapter Five: Experimentals 70
5.1 X-ray diffraction 71
5.1.1 Different Parts of the PHILIPS X' Pert PRO XRD System 73
5.1.2 Interpretation of the XRD data 74

5.2 Microstructure study 75

5.2.1 Scanning Electron Microscope (SEM) 76

5.2.2 S50 FEI Quanta Inspect SEM 77

5.2.3 Scanning Process 78

5.3. Magnetization measurement 79

5.3.1 Vibrating Sample Magnetometer (VSM) 79

5.4 Curie temperature measurement 81

5.5 Initial permeability and loss factor measurement 83

5.6 Resistivity measurement 87

References: 88

Chapter Six: Results and Discussion

Study of the influence of V_2O_5, CuO, In_2O_3 and Eu_2O_3 addition on the magnetic and electrical properties of iron-deficient Ni-Zn ferrites. 89

6.1 Introduction 89

6.2 The X-ray Diffraction Analysis of the $Ni_{0.65}Zn_{0.35}Fe_{1.96}O_4$ Ferrite System: 91

6.3 The ferrite system $Ni_{0.65}Zn_{0.35}Fe_{1.96}O_4$+x$V_2O_5$, where, x (in mol unit) = 0, 0.002, 0.004,0.006, 0.008, 0.01 92

6.3.1 Physical Properties: 92

6.3.2 Magnetic and Electrical Properties: 93

6.4 The ferrite system $Ni_{0.65}Zn_{0.35}Fe_{1.96}O_4$ + x CuO, where, x (in mol unit) = 0,0.005,0.01,0.015,0.20. 98

6.4.1 Physical Properties: 98

6.4.2 Magnetic and Electrical Properties: 99

6.5. The ferrite system $Ni_{0.65}Zn_{0.35}Fe_{1.96}O_4$+ x$In_2O_3$, where, x (in mol unit) = 0, 0.005, 0.01,0.015, 0.02, 0.025, 0.03 and 0.035. 105

6.5.1 Physical Properties: 105

6.5.2 Magnetic and Electrical Properties: 106

6.6. The ferrite system $Ni_{0.65}Zn_{0.35}Fe_{1.96}O_4$+ x$Eu_2O_3$, where, x (in mol unit) = 0, 0.005, 0.01,0.015, 0.02, 0.025, 0.030,0.035. 112

6.6.1 Physical Properties: 112

6.6.2 Magnetic and Electrical Properties: 113

Study of the influence of CuO, V_2O_5, Eu_2O_3 and In_2O_3 addition on the magnetic and electrical properties of iron-excess Mn-Zn ferrites. 119

6.7 Introduction 119

6.8 X-ray Diffraction Analysis of $Mn_{0.451}Zn_{0.484}Fe_{2.065}O_4$ Ferrite 120

6.9 Ferrite system $Mn_{0.451}Zn_{0.484}Fe_{2.065}O_4$ +x CuO; where x(in mol unit) = 0, 0.01,0.02,0.03,0.04, 0.05, 0.06 121

6.9.1. Physical Properties: 121

6.9.2. Magnetic and Electrical Properties: 122

6.10 Ferrite system $Mn_{0.451}Zn_{0.484}Fe_{2.065}O_4$+x V_2O_5; where, x (in mol unit) = 0, 0.002, 0.004,0.006,0.008,0.01 128

6.10.1 Physical Properties: 128

6.10.2 Magnetic and Electrical Properties**:** 129

6.11 Ferrite system $Mn_{0.451}Zn_{0.484}Fe_{2.065}O_4$+x Eu_2O_3; where, x (in mol unit) = 0, 0.005,0.01,0.015,0.02,0.025,0.03,0.035,0.04 135

6.11.1 Physical properties: 135

6.11.2 Magnetic and Electrical properties: 136

6.12 Ferrite system $Mn_{0.451}Zn_{0.484}Fe_{2.065}O_4$+x In_2O_3;where, x(in mol unit) = 0, 0.005,0.01,0.015,0.02,0.025,0.03,0.035: 142

6.12.1 Physical properties: 142

6.12.2 Magnetic and Electrical Properties: 143

References: 149

Chapter Seven: Conclusion 153

References: 160

List of Publications:

List of Tables

		Page No.
Table 3.1	Arrangements of Metal Irons in the Unit Cell of a Ferrite MeO. Fe_2O_3	42
Table 3.2	Electronic configuration of the transition elements with unfilled 3d electrons.	43
Table 3.3	Lattice parameter of single ferrite spinels with cation distribution ($Me^{2+}Fe_2O_4$).	44
Table 3.4	Saturation magnetization values σ, M_s, and $4\pi M_s$, and Curie points T_c of some simple spinel ferrites.	55
Table 6.1	Comparison of eddy current loss of $Ni_{0.65}Zn_{0.35}Fe_{1.96}O_4$ ferrite samples with V_2O_5 addition.	97
Table 6.2	Comparison of eddy current loss of $Ni_{0.65}Zn_{0.35}Fe_{1.96}O_4$ ferrite samples with CuO addition.	104
Table 6.3	Comparison of eddy current loss of $Ni_{0.65}Zn_{0.35}Fe_{1.96}O_4$ ferrite samples with In_2O_3 addition.	111
Table 6.4	Comparison of eddy current loss of $Ni_{0.65}Zn_{0.35}Fe_{1.96}O_4$ ferrite samples with Eu_2O_3 addition.	118
Table 6.5	Comparison of eddy current loss of $Mn_{0.451}Zn_{0.484}Fe_{2.065}O_4$ ferrite samples with CuO addition.	127
Table 6.6	Comparison of eddy current loss of $Mn_{0.451}Zn_{0.484}Fe_{2.065}O_4$ ferrite samples with V_2O_5 addition.	134
Table 6.7	Comparison of eddy current loss of $Mn_{0.451}Zn_{0.484}Fe_{2.065}O_4$ ferrite samples with Eu_2O_3 addition.	141
Table 6.8	Comparison of eddy current loss of $Mn_{0.451}Zn_{0.484}Fe_{2.065}O_4$ ferrite samples with In_2O_3 addition.	148

List of Figures

Chapter One Page No.

Fig. 1.1 The four basic operations in ferrite preparation. Some components of the ceramic method are on the left; on the right, some of the new methods are indicated. 2

Chapter Two

Fig. 2.1 The orbit of a spinning electron around the nucleus of an atom. 15

Fig. 2.2 Varieties of magnetic orderings (a) paramagnetic, (b) ferromagnetic, (c) ferrimagnetic,(d) antiferromagnetic and (e) superparamagnetic. 20

Fig. 2.3 The inverse susceptibility varies with temperature T for (a) paramagnetic, (b) ferromagnetic, (c) ferrimagnetic, (d) antiferromagnetic materials. T_N and T_c are Neel temperature and Curie temperature, respectively. 22

Fig. 2.4 Magnetic hysteresis loop. 23

Fig. 2.5 Illustration of domains in ferromagnetic materials. 26

Fig. 2.6 Schematic illustration of the break up of magnetization into domains (a) single domain, (b) two domains, (c) four domains and (d) closure domains. 27

Fig. 2.7 Schematic representation of a 180°C domain wall. 28

Fig. 2.8 Three major types of superexchange interactions in spinel ferrites are as follows: J_{AB}, J_{BB} and J_{AA} the small empty circle is A site, the small solid circle is B site, and the large empty circle is oxygen anion. 34

Fig. 2.9 Schematic representation of ions M and M′ and the O^{2-} ion through which the superexchange is made. r and q are the centre to centre distances from M and M′ respectively to O^{2-} and φ is the angle between them. 36

Chapter Three

Fig.3.1 Crystal structure of a cubic ferrite. 41

Fig.3.2 Diagram showing the orientation of the 2p orbit of the oxygen ion with respect to the metal ions, which is responsible for the indirect exchange. 45

Fig. 3.3	Diagram showing the angle of interaction of the cations via oxygen anions.	45
Fig. 3.4	Oxygen equilibrium pressures of different iron oxides as a function of temperature	47
Fig. 3.5	Temperature of complete dissociation of excessive Fe_2O_3 in air.	47
Fig. 3.6	Formation by counterdiffusion (a) formation of $MgAl_2O_4$: counterdiffusion of Mg^{2+} and Al^{3+} cations, no anion diffusion (Wagner mechanism); no marker displacement. (b) Formation of $MgFe_2O_4$: counterdiffusion of Mg^{2+} and Fe^{2+} cations, no O^{2-} anion diffusion but reduction and oxidation of Fe ions at respective phase boundaries, which is equivalent to an oxygen transport through the gas phase; marker displacement.	49
Fig. 3.7	Saturation magnetization as a function of temperature for some ferrites $Mn_{1-\delta}\ Zn_\delta Fe_2O_4$.	54
Fig. 3.8	Saturation magnetization as a function of temperature for some ferrites $Ni_{1-\delta}\ Zn_\delta Fe_2O_4$.	54
Fig. 3.9	Eddy currents. The variations in current i produced a varying field, H; an emf is generated, resulting in eddy currents, i_e. The intensity of the emf depends on the specimen magnetic permeability.	58
Fig.3.10	Effect of Fe content, δ , on the electrical conductivity of Ni-Zn ferrites.	59

Chapter Four

Fig. 4.1	Flow chart of ferrite sample preparation.	62
Fig. 4.2	Neck formation during sintering of spherical particles (a) when there is no overall shrinkage and (b) when shrinkage occurs	65

Chapter Five

Fig. 5.1	Block diagram of the PHILIPS PW 3040 X'Pert PRO XRD system.	71
Fig. 5.2	Bragg's diffraction pattern.	72
Fig. 5.3	Reflecting planes in a simple cubic lattice. A set of only two parallel planes is shown in each case.	73

Fig. 5.4	X-ray Powder Diffractometer (Model : PW 3040-X'Pert PRO Philips).	74
Fig. 5.5	S50 FEI Quanta Inspect SEM.	77
Fig. 5.6	Block diagram of a SEM.	78
Fig. 5.7	Block diagram of Vibrating Sample Magnetometer.	80
Fig. 5.8	Vibrating Sample Magnetometer (Model EV7 system).	81
Fig. 5.9	Impedance Analyzer Model-Hewlett-Packard 4192A.	82
Fig. 5.10	Schematic diagram of the Impedance Analyzer.	84
Fig. 5.11	Vector Voltage Ratio Detector basic diagram.	86
Fig. 5.12	Phase detection Vector diagram.	86
Fig. 5.13	Electrometer Model No. 6514, Keithley.	87

Chapter Six

Fig. 6.1	XRD pattern of sintered $Ni_{0.65}Zn_{0.35}Fe_{1.96}O_4$ ferrite.	91
Fig. 6.2	Variation of sintered density (d_s) and lattice constant (**a**) of $Ni_{0.65}Zn_{0.35}Fe_{1.96}O_4$ ferrite with V_2O_5 addition.	92
Fig. 6.3	Variation of Saturation magnetization (M_s) and Curie temperature (T_c) of $Ni_{0.65}Zn_{0.35}Fe_{1.96}O_4$ ferrite with V_2O_5 addition.	93
Fig. 6.4	Permeability spectra of the $Ni_{0.65}Zn_{0.35}Fe_{1.96}O_4$ ferrite system with V_2O_5 addition.	94
Fig. 6.5	Variation of initial magnetic permeability (μ') of $Ni_{0.65}Zn_{0.35}Fe_{1.96}O_4$ ferrite at 100 kHz with V_2O_5 addition.	94
Fig. 6.6	SEM Microphotographs of $Ni_{0.65}Zn_{0.35}Fe_{1.96}O_4$ ferrite samples with V_2O_5 addition.	95
Fig. 6.7	Variation of normalized loss factor ($1/\mu Q$) and dc resistivity (ρ) of $Ni_{0.65}Zn_{0.35}Fe_{1.96}O_4$ ferrite with V_2O_5 addition.	96

Fig. 6.8	Variation of sintered density (d_s) and lattice constant (**a**) of $Ni_{0.65}Zn_{0.35}Fe_{1.96}O_4$ ferrite with CuO addition.	98
Fig. 6.9	Variation of Saturation magnetization (M_s) and Curie temperature (T_c) of $Ni_{0.65}Zn_{0.35}Fe_{1.96}O_4$ ferrite with CuO addition.	99
Fig. 6.10	Permeability spectra of the $Ni_{0.65}Zn_{0.35}Fe_{1.96}O_4$ ferrite system with CuO addition	100
Fig. 6.11	Variation of initial magnetic permeability (μ') of $Ni_{0.65}Zn_{0.35}Fe_{1.96}O_4$ ferrite at 100 kHz with CuO addition.	101
Fig. 6.12	SEM Microphotographs of $Ni_{0.65}Zn_{0.35}Fe_{1.96}O_4$ ferrite samples with CuO addition	102
Fig. 6.13	Variation of normalized loss factor ($1/\mu Q$) and dc resistivity (ρ) of $Ni_{0.65}Zn_{0.35}Fe_{1.96}O_4$ ferrite with CuO addition.	103
Fig. 6.14	Variation of sintered density (d_s) and lattice constant (**a**) of $Ni_{0.65}Zn_{0.35}Fe_{1.96}O_4$ ferrite with In_2O_3 addition.	105
Fig. 6.15	Variation of Saturation magnetization (M_s) and Curie temperature (T_c) of $Ni_{0.65}Zn_{0.35}Fe_{1.96}O_4$ ferrite with In_2O_3 addition.	106
Fig. 6.16	Frequency dependent initial magnetic permeability spectra of the $Ni_{0.65}Zn_{0.35}Fe_{1.96}O_4$ ferrite system with In_2O_3 addition.	107
Fig. 6.17	Variation of initial magnetic permeability (μ') of $Ni_{0.65}Zn_{0.35}Fe_{1.96}O_4$ ferrite at 100 kHz with In_2O_3 addition.	108
Fig.6.18	SEM Microphotographs of $Ni_{0.65}Zn_{0.35}Fe_{1.96}O_4$ ferrite sample with In_2O_3 addition	109
Fig. 6.19	Variation of normalized loss factor ($1/\mu Q$) and dc resistivity (ρ) of $Ni_{0.65}Zn_{0.35}Fe_{1.96}O_4$ ferrite with In_2O_3 addition.	110
Fig. 6.20	Variation of sintered density (d_s) and lattice constant (**a**) of $Ni_{0.65}Zn_{0.35}Fe_{1.96}O_4$ ferrite with Eu_2O_3 addition	112
Fig. 6.21	Variation of Saturation magnetization (M_s) and Curie temperature (T_c) of $Ni_{0.65}Zn_{0.35}Fe_{1.96}O_4$ ferrite with Eu_2O_3 addition.	113

Fig. 6.22	Frequency dependent initial magnetic permeability (μ′) of $Ni_{0.65}Zn_{0.35}Fe_{1.96}O_4$ ferrite with Eu_2O_3 addition	114
Fig. 6.23	Variation of initial magnetic permeability (μ′) of $Ni_{0.65}Zn_{0.35}Fe_{1.96}O_4$ ferrite at 100 kHz with Eu_2O_3 addition.	115
Fig. 6.24	SEM Microphotographs of $Ni_{0.65}Zn_{0.35}Fe_{1.96}O_4$ ferrite sample with Eu_2O_3 addition	116
Fig. 6.25	Variation of normalized loss factor (1/μQ) and dc resistivity (ρ) of $Ni_{0.65}Zn_{0.35}Fe_{1.96}O_4$ ferrite with Eu_2O_3 addition	117
Fig. 6.26	XRD pattern of sintered $Mn_{0.451}Zn_{0.484}Fe_{2.065}O_4$ ferrite.	120
Fig. 6.27	Variation of sintered density (d_s) and lattice constant (**a)** of $Mn_{0.451}Zn_{0.484}Fe_{2.065}O_4$ ferrite with CuO addition.	121
Fig. 6.28	Variation of saturation magnetization (M_s) and Curie temperature (T_c) of $Mn_{0.451}Zn_{0.484}Fe_{2.065}O_4$ ferrite with CuO addition.	122
Fig. 6.29	Frequency dependent initial magnetic permeability of $Mn_{0.451}Zn_{0.484}Fe_{2.065}O_4$ ferrite with CuO addition.	123
Fig. 6.30	Dependence of initial magnetic permeability (μ′) of $Mn_{0.451}Zn_{0.484}Fe_{2.065}O_4$ ferrite at 100 kHz with CuO addition.	124
Fig. 6.31	SEM Microphotographs of $Mn_{0.451}Zn_{0.484}Fe_{2.065}O_4$ ferrite samples with CuO addition	125
Fig. 6.32	Dependence of normalized loss factor (1/μQ) and dc resistivity (ρ) of $Mn_{0.451}Zn_{0.484}Fe_{2.065}O_4$ ferrite with CuO addition.	126
Fig. 6.33	Variation of sintered density (d_s) and lattice constant (**a)** of $Mn_{0.451}Zn_{0.484}Fe_{2.065}O_4$ ferrite with V_2O_5 addition.	127
Fig. 6.34	Variation of saturation magnetization (M_s) and Curie temperature (T_c) of $Mn_{0.451}Zn_{0.484}Fe_{2.065}O_4$ ferrite with V_2O_5 addition.	129
Fig.6.35	Frequency dependent initial magnetic permeability, μ' of $Mn_{0.451}Zn_{0.484}Fe_{2.065}O_4$ ferrite with V_2O_5 addition.	130
Fig. 6.36	Variation of initial magnetic permeability (μ′) of $Mn_{0.451}Zn_{0.484}Fe_{2.065}O_4$ ferrite at 100 kHz with V_2O_5 addition	131
Fig. 6.37	SEM microphotographs of $Mn_{0.451}Zn_{0.484}Fe_{2.065}O_4$ ferrite samples with	132

V_2O_5 addition

Fig. 6.38 Variation of normalized loss factor (1/μQ) and dc resistivity (ρ) of the ferrite system $Mn_{0.451}Zn_{0.484}Fe_{2.065}O_4$ with V_2O_5 addition. 133

Fig. 6.39 Variation of sintered density (d_s) and lattice constant (**a)** of the ferrite system $Mn_{0.451}Zn_{0.484}Fe_{2.065}O_4$ with Eu_2O_3 addition 135

Fig. 6.40 Variation of saturation magnetization (M_s) and Curie temperature (T_c) of the ferrite system $Mn_{0.451}Zn_{0.484}Fe_{2.065}O_4$ with Eu_2O_3 addition. 136

Fig. 6.41. Frequency dependent initial magnetic permeability, μ' of the ferrite system $Mn_{0.451}Zn_{0.484}Fe_{2.065}O_4$ with Eu_2O_3 addition. 137

Fig. 6.42 Variation of initial magnetic permeability (μ′) of the ferrite system $Mn_{0.451}Zn_{0.484}Fe_{2.065}O_4$ at 100 kHz with Eu_2O_3 addition. 138

Fig. 6.43 SEM microphotographs of $Mn_{0.451}Zn_{0.484}Fe_{2.065}O_4$ ferrite samples with Eu_2O_3 addition. 139

Fig. 6.44 Variation of normalized loss factor (1/μQ) and dc resistivity (ρ) of the ferrite system $Mn_{0.451}Zn_{0.484}Fe_{2.065}O_4$ on Eu_2O_3 addition. 140

Fig. 6.45 Variation of sintered density (d_s) and lattice constant (**a)** of $Mn_{0.451}Zn_{0.484}Fe_{2.065}O_4$ ferrite with In_2O_3 addition. 142

Fig. 6.46 Variation of saturation magnetization (M_s) and Curie temperature (T_c) of $Mn_{0.451}Zn_{0.484}Fe_{2.065}O_4$ ferrite with In_2O_3 addition. 143

Fig. 6.47 Frequency dependent initial magnetic permeability of $Mn_{0.451}Zn_{0.484}Fe_{2.065}O_4$ ferrite with In_2O_3 addition. 144

Fig. 6.48 Variation of initial magnetic permeability (μ') of the ferrite system $Mn_{0.451}Zn_{0.484}Fe_{2.065}O_4$ at 100 kHz with In_2O_3 addition 145

Fig. 6.49 SEM microphotographs of $Mn_{0.451}Zn_{0.484}Fe_{2.065}O_4$ ferrite samples with In_2O_3 content. 146

Fig. 6.50 Variation of normalized loss factor (1/μQ) and dc resistivity (ρ) of $Mn_{0.451}Zn_{0.484}Fe_{2.065}O_4$ ferrite with In_2O_3 addition. 147

List of Symbols

Anisotropy constant	K_1
Anti ferromagnetic	AFM
Bohr magneton	μ_B
Bragg's angle	θ
Charge of electron	e
Coercive force	H_c
Curie constant	C
Curie temperature	T_c
Exchange integral	J_{ij}
Face centered cubic	FCC
Ferromagnetic	FM
Frequency	f
Imaginry part of initial permeability	μ''
Impedance	Z
Initial magnetic permeability	μ'
Inductance	L
Lattice constant	**a**
Loss tangent	$\tan\delta$
Magnetic induction	B
Magnetic field intensity	H
Multi-domain	MD
Neel temperature	T_N
Nelson-Reley Function	$F(\theta)$
Normalized loss factor	$1/\mu Q$
Permeability in free space	μ_0
Resistivity	ρ
Retentivity	B_r
Reactance	X
Saturation magnetization	M_s
Scanning Electron Microscope	SEM
Sintered density	d_s
Single Domain	SD
Spin quantum Number	m_s
Susceptibility	χ
Vibrating Sample Magnetometer	VSM
Wave length	λ
X-ray Diffraction	XRD
Yafet-Kittle	Y-K

Chapter One

General Introduction and Overview

1.1 Introduction

Ferrimagnetic oxides, or ferrites as they are usually known, have become available as practical magnetic materials over the course of the last sixty years. During this time their use has become established in many branches of communication and electronic engineering and they now include a very wide varieties of compositions, properties and applications [1.1]. Ferrites which are magnetically soft (soft ferrites) and which are of technical importance; and to the applications of such ferrites in devices may be described in the broadest sense as inductors or transformers. Ferrites are ceramic materials, dark grey or black in appearance, very hard and brittle. The magnetic properties of soft ferrites arise from interactions between metallic ions occupying particular positions relative to the oxygen ions in the crystal structure of the oxide. In magnetite, in the first synthetic ferrites and indeed in the majority of soft ferrites the crystal structure is cubic; it has the form of the mineral spinel (Mg Al_2O_4). The general formula of the spinel ferrite is Me Fe_2O_4, where Me usually represents one or, in mixed ferrites, more than one of the divalent transition metals Mn, Fe, Co, Ni, Cu, Zn, Mg and Cd. It is possible to replace some or all of the trivalent iron (Fe^{3+}) ions with other trivalent metal ions.

In the early practical ferrites Me represented Cu+Zn, Mn+Zn or Ni+Zn. The first of these compounds was soon abandoned and the other two, referred to as manganese zinc ferrite and nickel zinc ferrite (often abbreviated as Mn-Zn ferrite and Ni-Zn ferrite) were developed for a wide range of applications where high permeability and low loss were the main requirements [1.2]. These two compounds are still by far the most important ferrites for high permeability, low-loss applications and constitute the vast majority of present day ferrite production. By varying the ratio of Zn to Mn or Ni or by other means, both types of ferrite may be made in variety of grades, each grade having properties that suit it to a particular class of application.

The applications of soft ferrites started in the field of carrier telephony where the combination of good magnetic properties and high resistivity made these materials very suitable as cores for inductors and transformers. Since the resistivities were at least a million times greater than the values for metallic magnetic materials, laminated or

powdered cores could be replaced with solid ferrite cores and these could often be made in a more convenient shape than their laminated counterparts. The applications was extended to domestic television receivers where they became, and still remain, the undisputed core materials for the line scanning transformer and picture tube deflection yokes. In domestic radio receivers, rods or pellets of ferrite are used as cores for magnetic antennas. Many other high permeability, low-loss applications have been found [1.3-1.4].

1.2 Soft ferrite core materials

Soft ferrite core materials are prepared by almost all the existing techniques of solid state chemistry, leading to a very wide variety of forms : polycrystalline materials, thin and thick films and single crystals. Some of these methods have been developed to prepare ferrite materials with specific microstructures. The oldest one, the ceramic method involves the same operations as the classical techniques for fabrication of conventional ceramics. Many of the techniques recently developed consist of improvements in one or several of the basic operations of ceramic method are shown schematically in Fig. 1.1.

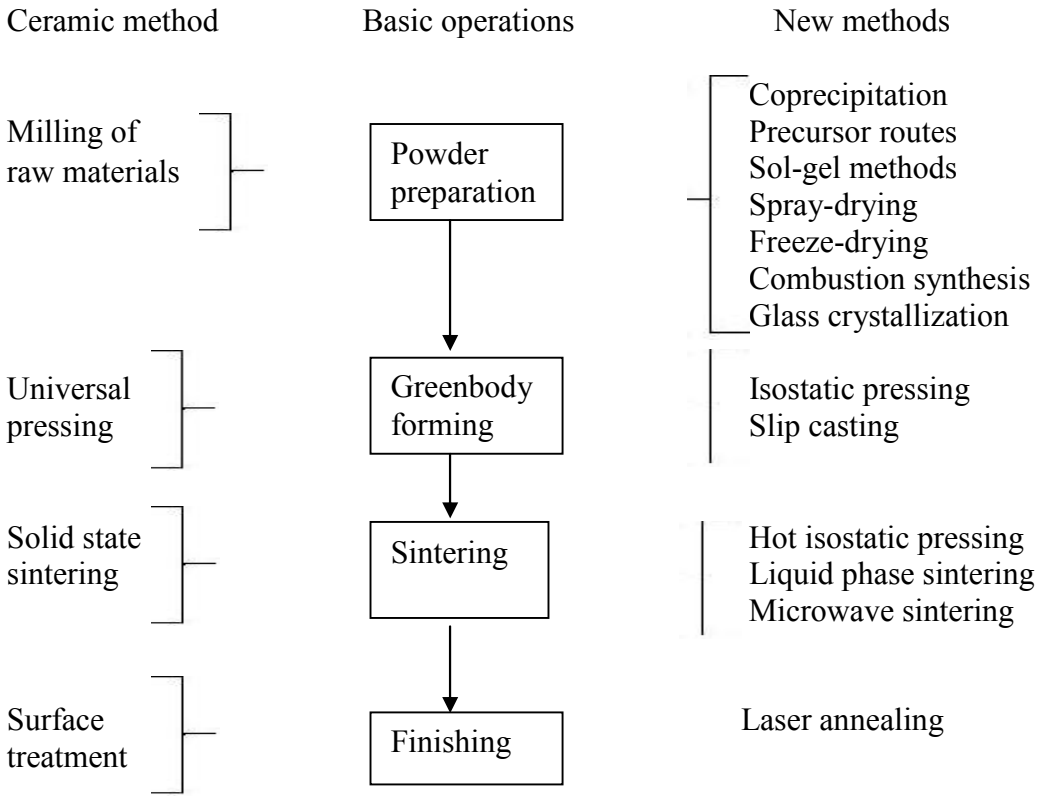

Fig. 1.1. The four basic operations in ferrite preparation. Some components of the ceramic method are on the left; on the right, some of the new methods are indicated.

The raw materials are usually iron oxide (Fe_2O_3) and the oxide or the carbonate of the other cations in the desired ferrite. Chemical analysis, particle size and price are important characteristics of these starting materials. Since minor constituents or impurities may have a great influence on the properties of the ferrite core materials, it is normal to analyze incoming materials in an attempt to ensure that the composition does not deviate significantly from batch to batch. Particle size of the starting material has a profound effect on the behavior of the product during preparation [1.5]. The ease of mixing, the compressibility, the shrinkage and the chemical reactivity all depend on the particle size so it is normal to keep a check on this parameter to ensure uniformity between batches. Starting materials of adequate purity and uniformity are usually **prohibitively expensive**, and successful large scale ferrite core preparation depends on the skill with which **reasonably-priced materials** may be used to produce consistently ferrites having the required magnetic and electrical properties.

The constituent raw materials are weighed into batches to give the proportions required for the composition ignoring the influence of the minor constituents, the relative proportions of the principal metal ions (cations) and the oxygen ions have a basic effect on the properties of ferrite. In mixed ferrites there are three or more different metal ions and this gives a wide range of possible relations. In case of Mn-Zn ferrite and Ni-Zn ferrite, ratio of zinc to non-ferrous metal effects the magnetic properties of ferrite. Zinc ferrite is paramagnetic at room temperatures; it is seen that an increasing proportion of zinc has the effect of reducing the Curie temperature and except at the higher temperatures, it gives rise to a maximum saturation flux density. If more iron is used than the amount required for the exact composition, $MeFe_2O_4$, then the excess iron appears in the form of divalent ions. Then Me, representing the divalent ions, includes some ferrous ions, e.g. manganese-zinc-ferrous ferrite. The effects of excess iron are complicated [1.6-1.7]. Trace elements such as cobalt, calcium, silicon are often added to modify the properties of the ferrite [1.8-1.9]. Since these elements, and others, are usually present in small quantities as impurities in the main raw materials the amount to be added depends on the amount present when the materials are received.

The Fe_2O_3 (hematite) and the other carbonates or oxides are generally mixed and milled in ball mills; this operation is carried out in liquid suspension (water, alcohol) to promote a better mixing of the raw materials. After drying, the powder is compacted by dry-pressing in steel dies to obtain the green body in the desired, final form, but with

slightly greater dimensions, because during the next operation, sintering, shrinkage takes place. To facilitate compaction and to increase the strength of the green body, a binder is usually added before pressing. Sintering is carried out in the solid state, at temperatures between 1000°C and 1400°C for times typically 2-24 hours, and in atmospheres ranging from air (O_2) to pure N_2, depending on the ferrite composition and sintering temperature. Chemical reactions depending on the particular composition, takes place during sintering as well as the process of elimination of voids, or porosity, between the particles in the green body, leading to an increased density. The initial particle size is critical since the driving force for sintering is the reduction in surface free energy of the powder. A finishing process is usually needed to obtain a final piece with the exact required dimensions, and is carried out by mechanical machining with diamond tools.

Since ferrites possess a very high melting temperature, both reaction and densification usually take place in the solid state. Initial formation of the product occurs at the contact surface between particles of the two reactants. As reaction proceeds, the product layer becomes thicker, increasing the length of the diffusion paths of the reactants and thus decreasing the reaction rate. The main diffusion mechanism at this stage is volume (or bulk) diffusion, which depends on the point-defect structure of the solid. A simple method of increasing reaction rates is to crush, mill and repress the product of a first thermal treatment (the prefiring stage), and perform a second sintering. By these means, fresh contact surface between the reactants are created; this technique also leads to more homogeneous products.

The principal low frequency applications for Mn-Zn and Ni-Zn ferrite core materials are classified as follows [1.10-1.12] :

Manganese Zinc ferrites

(i) Inductors for frequencies up to about 200 kHz.

(ii) Loading coils for the frequency range 100 kHz to 2 MHz.

(iii) Antenna rods for medium and long wave broadcast bands for the frequency range 100 kHz to 2 MHz.

(iv) Television line scanning transformers, deflection yokes and power transformers for the frequency range 700 Hz to 100 kHz.

(v) Coils in filter circuits at frequencies below 1 MHz.

(vi) Wide band transformers and pulse transformers for frequency range up to about 5 MHz.

Nickel Zinc ferrites

(vii) Antenna rods for medium and long wave broadcast bands for the frequency range 100 kHz to 1 MHz.

(viii) Power transformers for the frequency range 100 kHz to 1 MHz.

(ix) Fly back transformers up to 100 kHz frequencies.

(x) IF (intermediate frequency) transformers for the frequency range 150 kHz to 160 kHz.

(xi) EMI (electromagnetic interference) suppression devices for the frequency range 150 kHz to 5 MHz.

(xii) Inductors and antenna rods for short wave broadcast bands for the frequency range 2 to 20 MHz.

1.3 Review works :

Ferrites have been investigated since 1935, when Snoek started research on ferrites in 1935. Since then these materials are under investigations over the decades. In 1947, it was reported that Mn-Zn and Ni-Zn have excellent magnetic properties [1.13]. Verway and Heilmann [1.14] in Netherland studied the distribution of metal ions over the tetrahedral and octahedral sites, Neel [1.15] presented the theory about the magnetic properties of ferrites. It was reported that the magnetic properties depend upon cation distribution among tetrahedral sites (A sites) and octahedral sites (B-sites) which aligned their magnetic moments in opposite directions. Negative exchange interaction exists among A-A, B-B and A-B sites. The unpaired spins at A and B sites will be magnetized antiparallel below a transition temperature when A-B exchange interaction is dominant then Neel reported that the material remain paramagnetic down to the lowest temperature.

The properties of ferrites have been improved through extensive research. In 1950, ferrites attract world-wide attention because new applications such as microwave devices, electronic media, computer and telephone industry were rapidly expanding. Quality ferrites continued to be prepared having new properties. Among the noteworthy are barium and strontium ferrite [1.16] and Mn-Mg ferrites [1.17] with a square type hysteresis loop for magnetic memories, acicular γ-Fe_2O_3 particles, Yttrium Iron Garnet (YIG) [1.18]. In 1952, Hogan [1.19] studied microwave ferrite devices. Yafet et.al [1.20] studied antiferromagnetic arrangements in ferrites. They extended the Neel theory and showed that tetrahedral (A site) and octahedral (B site) sublattices could be further

subdivided into sub-lattices in such a way that the resultant magnetic moments of the sub-lattices are again aligned in opposite directions to each other, leading to ferrimagnetism.

Albergs-Schoenberg [1.17] prepared Mn-Mg ferrites suitable for magnetic memories in 1954. Uitert reported [1.21] dc resistivity in the Ni and Ni-Zn ferrite system prepared by solid-state reaction method. It was found that in Ni-Zn ferrites having deficiency in Fe^{2+} ions have high resistivity. Beyond 1300°C, all Ni and Ni-Zn samples exhibit low resistivities due to formation of Fe^{2+} ions. The loss of zinc in Ni-Zn materials at high temperature is expected to introduce Fe^{2+} ions. Addition of small amount of excess iron in NiZn ferrite was reported to have low resistivity and high conductivity.

The influence of minor addition of Mn and Co in high resistivity nickel ferrite prepared by solid-state reaction method was reported by Uitert [1.22]. Koops [1.23] reported that both dielectric constant and resistivity of $Ni_{0.4}Zn_{0.6}Fe_2O_4$ fall with rising frequency. The dc resistivity of $Ni_{0.62}Zn_{0.40}Fe_{1.98}O_4$+x V_2O_5 (x= 0.002-0.01; step 0.002) prepared by solid – state reaction method were reported by Jain et.al [1.24]. It was found that the smallest value of electrical conductivity was observed at 0.4 mol% (0.004) of V_2O_5 content. The results were explained on the basis of solubility limit of V_2O_5 in the spinel lattice. Joshi et.al [1.25] reported magnetization, Curie temperature and Y-K angles of Cu substituted Ni-Zn mixed ferrites.

The effects of rare-earth oxides on physical properties of $Ni_{0.7}Zn_{0.3}Fe_{1.98}R_{0.02}O_4$; where R= Yb, Er, Dy, Tb, Gd, Sm or Ce ferrtie synthesized by ceramic method was reported by Rezlescu et.al.[1.26]. It was concluded that the permeability increase with the size of ionic radius. It was reported that the formation of thin insulating layer boundaries of ortho ferrite enhances electrical resistivity and thereby reducing the eddy current losses at higher frequencies. Rare-earth ions having large size and stable valence 3^+ were found to be the best substituent in order to improve electrical and magnetic properties. Gadolinium was found to be the best substituent.

Pigram et.al. [1.27] investigated the effect of binder additions on the green and sintered properties of Mn-Zn ferrite. An overall comparison of the binders indicated that PVA, PEG and PAM all show excellent binding properties. Influence of processing parameters on the magnetic properties of Mn-Zn ferrites were investigated by S.A. El-Badry [1.28]. Ping Hu et.al. [1.29] investigated the effect of heat treatment temperature on crystalline phase formation, microstructure and magnetic properties of Mn-Zn ferrite. The

electrical conductivity of Mn-Zn ferrites was investigated by D. Ravinder et al.[1.30]. They observed that the electrical conductivity in room temperature in varying from $5.23\times10^{-9}\Omega^{-1}cm^{-1}$ for $MnFe_2O_4$ to $1.79\times10^{-5}\Omega^{-1}cm^{-1}$ for $Mn_{0.2}Zn_{0.8}Fe_2O_4$.

J. Hu et.al. [1.31] investigated about the ways of reducing sintering temperature of high permeability Ni-Zn ferrites. It was found that optimum additions of CuO and V_2O_5 contributed to the grain growth and the densification matrix in the sintering process, leading to decrease in sintering temperature of Ni-Zn ferrites. Nan et.al [1.32] reported the in-situ reaction between CaO and MnZn ferrite in TEM. The Ca was observed to stay at grain boundaries in form of amorphous intermediate phase at low sintering temperatures.

E. Calderon-oritz et. al. [1.33] studied the $Mn_xZn_{1-x}Fe_{2-y}R_yO_4$ (R=Gd, Eu) ferrites for magnetocaloric applications. Dielectric constant, ac conductivity and seeback coefficient were investigated for ferrite samples $Mn_{0.5}Zn_{0.5}R_yFe_2O_4$ (R= Dy, Gd, Sm, Ce and La) prepared by standard ceramic technique and sintered at 1200°C with a heating rate 4°C/m by E. Ateia et. al [1.34].

Nam et. al. [1.35] reported the effect of Cu substitution on the physical properties of Ni-Zn ferrite prepared by solid state reaction method. It was found that the dc resistivity increased up to $x \leq 0.2$ and then decreased with the substitution level x (Cu). The bulk density of the samples sintered at 1000°C increased with Cu contents that might be attributed to atomic mobility of copper atoms at low temperature and above 1000°C, the sintering density was found to be decreased due to intergranular porosity and exaggerated grain growth. Copper substitution improved its electrical and magnetic properties and is the best material than NiZn ferrite at radio frequency region.

The dc resistivity on two series of $Ni_{0.65}Zn_{0.35}Fe_{2-x}Sc_xO_4$ and $Ni_{0.65-x}Zn_{0.35+x}Fe_{2-x}Sc_xO_4$ were reported by Rao et. al. [1.36]. The resistivity has been found to increase with the increase of Sc/Zn content in both series. The influence of rare-earth ions on the electrical and mechanical properties of Ni-Zn ferrites were reported by Rezlescu et. al.[1.37]. It was concluded that the incorporation of small amount of rare-earth ions formed second phase and inhomogeneous solid solution and thereby increasing the resistivity.

High insulating thin grain boundaries in doped Mn-Zn ferrites for high frequency power supplies were reported by Drofenik et. al.[1.38]. The eddy current loss at higher frequencies depends upon grain size and boundary permittivity to thickness ratio. The

influence of R_2O_3 (R= La, Gd) on dielectric properties of Ni-Zn ferrite in the frequency range 1-40 MHz were reported by Sun et. al.[1.39]. It was concluded that the values of dielectric constant increases with the increasing concentration of R_2O_3 whereas tanδ decreases with increasing R_2O_3. The R_2O_3 substitution decreases bulk density and increases lattice parameter.

Low loss high initial permeability Mn-Zn ferrites with the addition of CaO and GeO_2 was reported by E. Hirota [1.40]. The combined addtion of CaO and GeO_2 increases effectively the resistivity of the ferrite. The precipitation of Ca^{2+} ions at the grain boundary may accompany Ge^{4+} ions and forms a compound in high resistivity on the surface of each constituent grain. The CaO and GeO_2 added Mn-Zn ferrites provide much higher μ-Q values such as 8×10^4 at 1MHz.

Effects of various substitutions on the dc resistivity of ferrites was reported by Long Wu et. al. [1.41]. The effects of additions come from three different aspects: by the valence controlled action, such as in the case of TiO_2, Cu_2O, ZrO_2 and SnO_2 doping; by the formation of a highly resistive grain boundary, such as in the case SiO_2, Nb_2O_5 and Sb_2O_5, which may be regarded as acidic oxides; and by the structure distortion, which occurs in doping with large sized ions.

Effect of Cr addition on the dc resistivity of Mn-Zn ferrites was reported by K. H. Rao et. al [1.42]. The increase of resistivity was explained on the basis of resistivity due to grains and resistivity due to the grain boundary. The strength of Mn-Zn ferrites of composition ranged from Fe deficient to Fe excess was studied as a function of atmosphere and temperature by R. C. Neyts et. al.[1.43]. Fe excess and Fe deficient ferrite exhibit large differences in strength when process in air. The strength of Fe excess materials increases with firing temperature, whereas the strength of Fe deficient ferrites is inherently low. Strength appears to be determined by reoxidation of (Mn^{2+} relative to Fe^{2+}) at all grain boundaries.

Ataa et. al. [1.44] reported initial magnetic permeability and ac electrical conductivity of $Li_{0.5-0.5x}Co_xFe_{2.4-0.5x}R_{0.1}O_4$ (where x= 0.0, 0.5 and R=Y, Yb., Eu, Ho and Gd) prepared by standard ceramic techniques. The ac electrical conductivity measurements exhibit dispersion with frequency at low temperatures. The hoping mechanism is the predominant one in these samples. The behavior of the initial magnetic

permeability with temperature shows multidomain structure for the samples with x= 0 and single domain structure for all other compositions.

1.4 Magnetite (Fe_3O_4), a beach sand mineral

There is a considerable reserve of mineral magnetite in the Cox's Bazar beach sand as reported and explored by Beach Sand Mineral Exploitation Centre, Cox's Bazar of Bangladesh Atomic Energy Commission. The chemical purity of available mineral magnetite is 95.5% and the impurities present are SiO_2, Al_2O_3, CaO, P, S etc. Mineral magnetite ($Fe_3O_4 \equiv Fe^{2+}OFe_2^{3+}O_3$) contains one ferrous ion (Fe^{2+}) and two ferrite ions (Fe^{3+}) in each formula unit. It is a typical ferrite called iron ferrite: $Fe^{2+}O\ Fe_2^{3+}O_3 \cong Me^{2+}OFe_2^{3+}O_3$, where Me is the divalent metal ions like Fe, Ni, Mn, Cu, Co etc. Divalent oxides (FeO, NiO, CoO etc) has only octahedral sites (each cation is surrounded by 6 neighboring oxygen ions). Fe_3O_4 is a mixed valency oxides form spinel lattice (same as mineral spinel Mg Al_2O_4). Mg Al_2O_4 (normal spinel) is cubic which contains both octahedral (B-site) and tetrahedral (A-site) sites. As for example zinc ferrite ($Zn^{2+}\ Fe_2^{3+}O_4$) is a normal spinel:

$$\underline{Zn^{2+}}\ \underline{[Fe^{3+}\uparrow Fe^{3+}\downarrow]}O_4$$

A-site B-site

has no net magnetic moment. Normal spinels are non-magnetic; whereas inverted spinels are magnetic. Magnetite, Fe_3O_4 is an inverted spinel:

$$\underline{Fe^{3+}\uparrow}\ \underline{[Fe^{2+}\downarrow Fe^{3+}\downarrow]}O_4$$

A-site B-site

Spins of Fe^{3+} of A and B-site cancel each other, so only spins of Fe^{2+} at B-site is effective. Hence, the magnetic moment of Fe_3O_4, $M=M_B-M_A= (5\ \mu_B+4\mu_B)-(5\mu_B) = 4\mu_B$ (Fe^{3+} ions have spin-only moment of $5\mu_B$ and Fe^{2+} ions have $4\mu_B$).

Resistivity of magnetite is low due to the presence of both $Fe^{2+}$and Fe^{3+} ions at the equivalent lattice site i.e. at octahedral site (B-site) and easy transfer of electrons from Fe^{2+} to Fe^{3+} ions occurs. Resistivity is of the order of 10^{-2} ohm-cm at room temperature. Molecular weight of magnetite is 231.54, lattice constant, **a** (cubic) is 8.39 Å with x-ray density of 5.24 g/cc.

1.4.1 Chemical composition of Fe_3O_4:

The chemical composition of the beach sand mineral magnetite as collected by magnetic separation in the pilot plant of Beach Sand Mineral Exploitation Centre (BSMEC) of Cox's Bazar is as follows:

Component	Concentration
Fe_3O_4	95.5%
SiO_2	2-3.3%
Al_2O_3	1.8%
CaO	0.15%
P	0.04%
S	0.01%

The impurity level of mineral magnetite (Fe_3O_4) is higher than that of hematite (Fe_2O_3) normally used as the basic raw material for ferrites. Silica content (SiO_2) in Fe_2O_3 is generally less than 1% whereas it is well above 1% in the mineral magnetite. However, the impurities like SiO_2, Al_2O_3 and CaO somewhat helps to improve the characteristic properties of soft ferrites [1.45-1.47]. It has been reported that the electrical resistivity is known to be increased by adding a small quantity of impurities such as CaO, CuO and SiO_2 together in soft ferrites such as Mn-Zn and Ni-Zn ferrites [1.48-1.49]. The presence of CaO and Al_2O_3 together has also the effect on the resistivity and grain size and other features of the microstructure of ferrites [1.50-1.51].

1.4.2 Quality of mineral magnetite (Fe_3O_4) used as a basic raw material for the preparation of soft ferrites.

Quantity of Fe in Fe_2O_3 (hematite) for 100% purity is (At. wt. of Fe: 55.847 and O: 15.999):

$$\frac{Fe_2}{Fe_2O_3} = \frac{55.847 \times 2}{(55.847 \times 2 + 15.999 \times 3)} = 0.6994$$

That is the percentage wise quantity of the Fe in Fe_2O_3 is 69.94%

Quantity of Fe in Fe_3O_4 (mineral magnetite) considering 100% purity is:

$$\frac{Fe_3}{Fe_3O_4} = \frac{55.847 \times 3}{(55.847 \times 3 + 15.999 \times 4)} = 0.7236$$

That is the percentage wise quantity of Fe in Fe_3O_4 is 72.36%. But, it is mentioned earlier that the purity of beach sand mineral magnetite is 95.5%. So, percentage wise exact (true) quantity of Fe in Fe_3O_4 will be:

$$72.36 \times \frac{95.5}{100}\% = 69.1038\%$$

Hence, the available quantity of Fe in 100% pure Fe_2O_3 and quantity of Fe in Cox's Bazar's beach sand mineral magnetite (Fe_3O_4) are more or less equal. Therefore, it is possible to use mineral magnetite as a basic raw material for the preparation of soft ferrites instead of using Fe_2O_3 (hematite).

1.5 Objective of the work

Ferrites are complex magnetic oxides which contain (70-90)% Fe_2O_3 (hematite) as the basic ingredient. Soft ferrites have high resistivity and attractive magnetic properties, as a result they have been widely used in low and high frequency applications. Soft ferrites such as Ni-Zn and Mn-Zn ferrites are mostly used as core materials for transformers, inductors, antennas, television line scanning transformers, picture tube deflection yokes, loading coils and coils in filter circuits, power supplies and for other devices in radio, television and communication equipment. Research activities in the field of soft ferrites has generated an increasing demand for quality ferrite materials for power supplies, transformer cores, deflection yokes, recording and interface suppression. Many researchers achieved remarkable results both in the basic research as well as in the applied study of soft ferrites. On the other hand, investigators have not been succeeded in making an ideal ferrite product which fulfills all the requirements of electronic industry particularly in the field of telecommunication. Each ferrite product has its own advantages and disadvantages. Scientists still have not been able to make hard and fast rules about a single property. It is not easy to make novel ferrite materials. However, the search for quality material is going on to prepare cheap (low cost) ferrite core materials which have optimum properties like high saturation magnetization, high resistivity, high permeability, low eddy current losses and good homogeneous structure. **The objective of this research work is to develop Ni-Zn ferrite and Mn-Zn ferrite core materials for low frequency application using cheap beach sand mineral magnetite (Fe_3O_4) as a basic ingredient instead of using Fe_2O_3 (hematite).** In terms of magnetic point of view (magnetic property) there is no constraint of using magnetite (Fe_3O_4) as a basic ingredient for the

preparation of ferrites (as discussed earlier). However, the particle size of the magnetite is large for the preparation of ferrite core materials but it can be solved by vigorous milling of the magnetite before using for ferrite preparation. Nevertheless, the main constraint is the resistivity (electrical property) of magnetite (Fe_3O_4), it is very low due to the presence of both Fe^{2+} and Fe^{3+} ions at the equivalent lattice site (octahedral site). But it is very encouraging to be mentioned that the presence of SiO_2, CaO and Al_2O_3 as impurities might be helpful to get higher resistivity of the ferrite product. Usually, at the grain of such polycrystalline ferrites (Mn-Zn and Ni-Zn ferrites) there are possibly formed layers having a higher resistivity than that of its constituent grains during cooling process [1.52]. The formation of layers having a higher resistivity is attributed to the oxidation of Fe^{2+} ions located near the grain boundary. In addition the CaO or CaO and SiO_2 together has a tendency to precipitate at the grain boundary. The precipitation and the oxidation of Fe^{2+} ions increase the resistivity of ferrites appreciably by forming an insulating layer at the grain boundary [1.53]. The presence of Al_2O_3 increases the temperature stability as well as resistivity of the ferrite product [1.54].

Ni-Zn ferrites and Mn-Zn ferrites for applications up to 1 MHz frequency range as core materials for transformers, inductors, antennas, television line scanning transformers, deflection yokes, loading coils and coils in filter circuits and power supplies should have high permeability, high resistivity, and high value of saturation magnetization. Other factors such as, magnetic losses and eddy current losses and temperature stability are also important for applications in all the above mentioned electronic and electrical devices.

In this research work a modest attempt has been taken to develop high permeability, high resistivity, low losses Ni-Zn ferrite and Mn-Zn ferrite core materials using low cost indigenous magnetite (a beach sand mineral), cheap commercial grade $MnCO_3$ and NiO by finding suitable composition and preparation process. Moreover, goal of this investigation is to enhance the characteristic properties of the developed core materials by putting several additives such as CuO, V_2O_5 (divalent oxides) and Eu_2O_3, In_2O_3 (trivalent oxides) in some compositions of iron-excess Mn-Zn and iron-deficient Ni-Zn ferrites. Efforts have been made to meet these objectives in the present investigation.

References:

[1.1] J. L. Snoek, New Developments in Ferromagnetism, Elsevier, **139** (1949).

[1.2] D. Polder, Proc. Instn. Elect. Engrs; **97**, part II, 246, (1950).

[1.3] C.D. Owens, Proc. Inst. Radio Engrs. **44**, 1234, (1956).

[1.4] E.C. Snelling Proc. Br. Ceram. Soc., **2**, 151, (1964).

[1.5] P. Ergberger, Proc. Brit. Ceram. Soc. **2**, 19, (1964).

[1.6] E. W. Gorter, Proc. Inst. Radio Engrs, **43**, (1945).

[1.7] A. L. Stuijts, Trans. Br. Ceram. Soc., **55,** 57, (1956).

[1.8] C. M. Vander Burgt, Philips Res. Rep., **12**, 97, (1957).

[1.9] T. Akashi, Trans. J. Inst. Metals, **2**, 171 (1961).

[1.10] A. Goldman, Hand book of Modern Ferromagnetic Materials, Kluwer Academic publishers, Boston/Dordrecht/London (2002).

[1.11] A User's Guide, Magnetic Materials producers Association, Chicago, IL 60603 (1998).

[1.12] Wm. Colonel, T. McLyman, Magnetic core selection for Transformers and Inductors, Marcel Dekkar Inc., New York, (1997).

[1.13] J. L. Snoek, New Development in Ferromagnetic Materials, Elsevier, N. Y. (1947).

[1.14] E. J. W. verway, E. L. Heilmann, J. Chem. phys. **15**, 174 (1947).

[1.15] L. Neel, Ann.phys; **3**, 137 (1948).

[1.16] J.L. Went, G. W.Ratenau, E. W. Gorter, G. W. Van Oosterhout, Philips Tech. Rev., **13**, 194 [1951].

[1.17] E. Allbers-Schoenberg, J. Appl. phys. , **25**, 152 (1954).

[1.18] F. Bertaut, F. Forrat, Comt.Rend., **242**, 382 (1956).

[1.19] C. L. Hogan, Bell Syst. Tech. J., **31**, 1 (1952).

[1.20] Y. Yafet, C. Kittel, Phys. Rev., **87**, 290 (1952).

[1.21] L. G. Uitert, J. of Chemical Physics, **23**, 1883 (1955).

[1.22] L. G. Uitert, J. of Chemical Physics, **24**, 306(1956).

[1.23] C. G. Koops, Phys. Rev., **83(2),** 121 (1951).

[1.24] G. C. Jain, K. Bijoy Das, B. Ramesh Tripathi, R. Narayan, IEEE transcations on Magnetics, **MAG- 18 (2),** 776 (1982).

[1.25] G. K. Joshi, A. Y. Khot, S. R. Sawant, Solid State communication, **65**, 1593 (1988).

[1.26] N. Rezlescu, E. Rezlescu, C. Pasnicu, M. L. craus, J. Phys. Condes. Matter, **6**, 5707 (1994).

[1.27] A. J. Pigram, R. Freer, Ceramics International, **21**, 33(1995).

[1.28] S. A. El- Badry, J. Mine. Mater.char. Eng., **10**, 397 (2011).

[1.29] P. Hu, H-b Yang, D-a Pan, H. Wang, J-j Tian, S-g Zhang, x-f. Wang, A. A. Volinsky, J. Magn. Magn. Mater., **322**, 173 (2010).

[1.30] D. Ravinder, K. Latha, J. Appl. Phys., **75**, 6118 (1994).

[1.31] J. Hu, M. Yan and W. Luo, Physica B, **368**, 251 (2005).

[1.32] I-Nan, Raja K. Mishra and G. Thomas, IEEE Trans. on Mag., **18 (6),** 544(1992).

[1.33] E. Calderon-ortiz, O. Perales-perez, P. Voyles, G. Gutierrez, M. S. Tomar, Microcelectronics J. **40**, 677 (2009).

[1.34] E. Ateia, M. A. Ahmed, A. K. El-Aziz, J. Magn. Magn. Mater., **192**, 271 (1992).

[1.35] J. H. Nam, H. H. Jung, J. Y. Shin, J. H. oh., IEEE Trans. on Magnetics, **31(6),** 3985 (1995).

[1.36] B. P. Rao, K. H. Rao, J. Appl. Phys., **80 (12),** 6804(1996).

[1.37] E. Rezlescu, N. Rezlescu, P. D. Popa, L. Rezlescu and C. Pasnicu, Phys. Stat. sol. (a), **162 (673),** 673 (1997).

[1.38] M. Drofenik, A. Znidarsic, I. Zajc, J. Appl. Phys. **82 (1),** 333 (1997).

[1.39] J. Sun, J. Li, G. Sun, J. of Magn and Magn. Mater., **250**, 20 (2002).

[1.40] E. Hirota, Japanese J. of Appl. Phys., **vol. 5**, 1125 (1966).

[1.41] Long Wu, T-S Wu, C-C Wei, J. Phys. D: Appl. Phys., **13**, 259 (1980).

[1.42] K. H. Rao, S. B. Raju, K. Aggarwal and R. G. Mendiratta, J. Appl. Phys., **52 (3),** 1376 (1981).

[1.43] R.C. Neyts, W. M. Dawson, Proceedings ICF-5, India, 293 (1989).

[1.44] A. M. Abo El Ata, M. K. El Nimara, S. M. Attia, D. El. Konya, A. H. Al-Hamand, J. Magn. Magn. Mater., **297**, 33 (2006).

[1.45] C. Guillaud, Proc. Inst. Elect. Engrs. B. Suppl. **104**, 165(1957).

[1.46] M. Paulus, et.al. J. Phys. Soc. Japan, Suppl. B-1, **17,**632 (1962).

[1.47] E. Hirota, Japanese, J. of Appl. Phys. **5**, **No. 12**, 1125, Dec.(1966).

[1.48] M. Akashi, J. Japan Soc. of powder Metallurgy, **8**, 101, 195 (1961).

[1.49] L. G. Van Uitert, Proc. Inst. Radio Engrs, **44**, 1294 (1956).

[1.50] A. Hamelin, M. Paulus, Ferrites, eds. Y. Hoshino, S. Iida, and M. Sugimoto (University of Tokyo Press, Tokyo), 134 (1971).

[1.51] M. Paulus, Mater. Sic. Res., **3**, 31 (1966).

[1.52] M. Paulus, C. Guillaud, J. phys. Soc. Jpn, **17**, Suppl. B1, 632 (1962).

[1.53] M. Robbins, J. phys. chem. Solids **26**, 831 (1965).

[1.54] P. Perriat, R. Lebourgeois, J. L. Rolland, proc ICF6, Jap. Soc. of powder and powder Met., 827 (1992).

Chapter Two

Theoretical Background

2.1 General Aspects of Magnetism

2.1.1 Origin of magnetism

The origin of magnetism lies in the orbital and spin motions of electrons and how the electrons interact with one another. The best way to introduce the different types of magnetism is to describe how materials respond to magnetic fields. This may be surprising to some but all matter is magnetic. It is just that some materials are much more magnetic than others. The main distinction is that in some materials there is no collective interaction of atomic magnetic moments, whereas in other materials there is a very strong interaction between atomic moments.

A simple electromagnet can be produced by wrapping copper wire into the form of a coil and connecting the wire to a battery. A magnetic field is created in the coil but it remains there only while electricity flows through the wire. The field created by the magnet is associated with the motions and interactions of its electrons, the minute charged particles which orbit the nucleus of each atom. Electricity is the movement of electrons, where in a wire or in and atom, so each atom represents a tiny permanent magnet in its own right. The circulating electron produces its own orbital magnetic moment, measured in Bohr magnetons (μ_B), and there is also a spin magnetic moment associated with it due to the electron itself spinning, like the earth, on its own axis (illustrated in figure 2.1). In most materials there is resultant magnetic moment due to the electrons being grouped in pairs causing the magnetic moment to be cancelled by its neighbour.

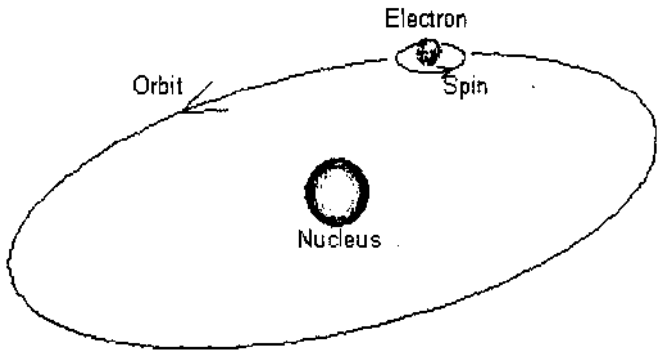

Fig. 2.1 The orbit of a spinning electron around the nucleus of an atom.

In certain magnetic materials the magnetic moments of a large proportion of the electrons align, producing a unified magnetic field. The field produced in the material (or by an electromagnet) has a direction of flow and any magnet will experience a force trying to align it with an externally applied field, just like a compass needle. These forces are used to drive electric motors, produce sounds in a speaker system control the voice coil in a CD player, etc.

2.1.2 Magnetic moment of atoms

The strength of a magnetic dipole, called the magnetic dipole moment, may be thought of as a measure of a dipole's ability to turn itself into alignment with a given external magnetic field. In a uniform magnetic field, then magnitude of the dipole moment is proportional to the maximum amount of torque on the dipole, which occurs when the dipole is at right angles to the magnetic field.

The magnetic moment of magnetic dipole moment is a measure of the strength of a magnetic source. In the simplest case of current loop, the magnetic moment is defined as:

$$\mu_m = I\int da \qquad (2.1)$$

where 'a' is the vector area of the current loop, and the current I, is constant. By convention, the direction of the vector area is given by the right hand rule (moving one`s right hand in the current direction around the loop when the palm of the hand is "touching" the loop`s surface, and the straight thumb indicate the direction).

In the more complicated case of a spinning charged solid, the magnetic moment can be found by the following equation:

$$\vec{\mu}_m = \frac{1}{2}\int \vec{r} \times \vec{J} d\tau \qquad (2.2)$$

where, $d\tau = r^2 \sin\theta \, dr \, d\theta \, d\phi$, $\vec{J}$ is the current density.

Magnetic moment can be explained by a bar magnet which has magnetic poles of equal magnitude but opposite polarity. Each pole is the source of magnetic force which weakens with distance. Since magnetic poles come in pairs, their forces interfere with each other because while one pole pulls, the other repels. This interference is greatest when the poles are close to each other i.e. when the bar magnet is short. The magnetic force produced by a bar magnet, at a given point in space, therefore depends on two factors: on both the strength p of its poles, and on the distance d separating them. The force is proportional to the product, μ=pd, where, μ describes the "magnetic moment" or " dipole

moment" of the magnet along a distance R and its direction as the angle between R and the axis of the bar magnet. Magnetism can be created by electric current in loops and coils so any current circulating in a planar loop produces a magnetic moment whose magnitude is equal to the product of the current and the area of the loop. When any charged particle is rotating, it behaves like a current loop with a magnetic moment.

The equation for magnetic moment in the current-carrying loop, carrying current I and of area vector $\vec{a}$ for which the magnitude is given by:

$$\vec{\mu}_m = I\vec{a} \qquad (2.3)$$

where, $\vec{\mu}_m$ is the magnetic moment, a vector measured in ampere-square meters, or equivalently joules per tesla, I is the current, a scalar measured in amperes, and $\vec{a}$ is the loop area vector, having as x, y, and z coordinates the area in square meters of the projection of the loop into the yz-,zx-, and xy-planes.

2.1.3 Magnetic moment of electrons

The electron is a negatively charged particle with angular momentum. A rotating electrically charged body in classical electrodynamics causes a magnetic dipole effect creating magnetic poles of equal magnitude but opposite polarity like a bar magnet. For magnetic dipoles, the dipole moment points from the magnetic south to the magnetic north pole. The electron exists in a magnetic field which exerts a torque opposing its alignment creation a potential energy that depends on its orientation with respect to the field. The magnetic energy of an electron is approximately twice what it should be in classical mechanics. The factor of two multiplying the electron spin angular momentum comes from the fact that it is twice as effective in producing magnetic moment. This factor is called the electronic spin g-factor. The persistent early spectroscopists, such as Alfred Lande, worked out a way to calculate the effect of the various directions of angular momenta. The resulting geometric factor is called the Lande g-factor.

The intrinsic magnetic moment μ of a particle with charge q, mass m, and spin s, is

$$\vec{\mu}_m = g\,\frac{q}{2m}\vec{s} \qquad (2.4)$$

where, the dimensionless quantity g is called the g-factor.

The g-factor is an essential value related to the magnetic moment of the subatomic particles and corrects for the precession of the angular momentum. One of the triumphs of the theory of quantum electrodynamics is its accurate prediction of the electron g-factor,

which has been experimentally determined to have the value 2.002319. The value of 2 arises from the Dirac equation, a fundamental equation connecting the electron`s spin with its electromagnetic properties, and the correction of 0.002319, called the anomalous magnetic dipole moment of the electron, arises from the electron`s interaction with virtual photons in quantum electrodynamics. Reduction of the Dirac equation for an electron in a magnetic field to its non-relativistic limit yields the Schrdinger equation with a correction term which takes account of the interaction of the electron`s intrinsic magnetic moment with the magnetic field giving the current energy. The total spin magnetic moment of the electron is

$$\vec{\mu}_s = -g_s \mu_B (\vec{s} / \hbar) \qquad (2.5)$$

where g_s = 2 in Dirac mechanics, but is slightly larger due to Quantum Electrodynamic effects, μ_B is the Bohr magneton and s is the electron spin. The component of the electron magnetic moment is

$$\mu_z = -g_s \mu_B m_s \qquad (2.6)$$

where, m_s is the spin quantum number.

The total magnetic dipole moment due to orbital angular momentum is given by

$$\mu_L = -\frac{e}{2m_e} L = -\mu_B \sqrt{l(l+1)} \qquad (2.7)$$

where, μ_B is the Bohr magneton.

The z-component of the orbital magnetic dipole moment for an electron with a magnetic quantum number m_l is given by

$$\mu_Z = -\mu_B m_l \qquad (2.8)$$

2.1.4 Magnetic behavior

The magnetic properties of a matter are fundamentally the result of the electrons of the atom, which have a magnetic moment by means of the electron motion. There are two types of electronic motion, spin and orbital, and each has a magnetic moment associated with it. Since the response of a material to a magnetic field (H) is characteristic of the magnetic induction or the flux density (B) and the effect that a material has upon the magnetic induction in a magnetic field is represented by the magnetization (M). Thus a universal equation can be established, relating these three magnetic quantities, by

$$B = \mu_0(H+M) \qquad (2.9)$$

$$B=\mu H \qquad (2.10)$$

Where, μ_0 is a universal constant of permeability in a free space and μ is the permeability of a material. In equation (2.9), one can see that $\mu_0 H$ is the magnetic induction generated by the field alone and $\mu_0 M$ is the additional magnetic induction contributed by a material. The magnetic susceptibility (χ) is defined as the ratio of magnetic field

$$\chi = \frac{M}{H} \qquad (2.11)$$

The permeability and susceptibility of a material is correlated with respect to each other by

$$\mu = \mu_0(1+\chi) \qquad (2.12)$$

The magnetic behavior of materials can be classified into the following five major groups:

(1) Diamagnetism

(2) Paramagnetism

(3) Ferromegnetism

(4) Antiferromagnetism

(5) Ferrimagnetism

Materials in the first two groups are those that exhibit no collective magnetic interactions and are not magnetically ordered. Materials in the last three groups exhibit long-range magnetic order below a certain critical temperature. Ferromagnetic and ferrimagnetic materials are usually what we consider as being magnetic (i.e., behaving like iron). The remaining three are so weakly magnetic that they are usually thought of as "nonmagnetic". The varieties of magnetic orderings are schematically presented in Fig 2.2.

A brief description of the above mentioned classes of magnetic materials are as follows:

(1) Diamagnetism

Diamagnetism is a fundamental property of all matter, although it is usually very weak. It is due to the non-cooperative behavior of orbiting electrons when exposed to an applied magnetic field. Diamagnetic substances are composed of atoms which have no net magnetic moments (i.e., all the orbital shells are filled and there are no unpaired electrons). However, when exposed to a field, a negative magnetization is produced and thus the susceptibility is negative. It obeys Lenz1`s law. The other characteristic behavior of diamagnetic materials is that the susceptibility is temperature independent. The typical values of susceptibility on the order of 10^{-5} to 10^{-6}. Most of the materials are diamagnetic, including Cu, B, S, N_2 and most organic compounds.

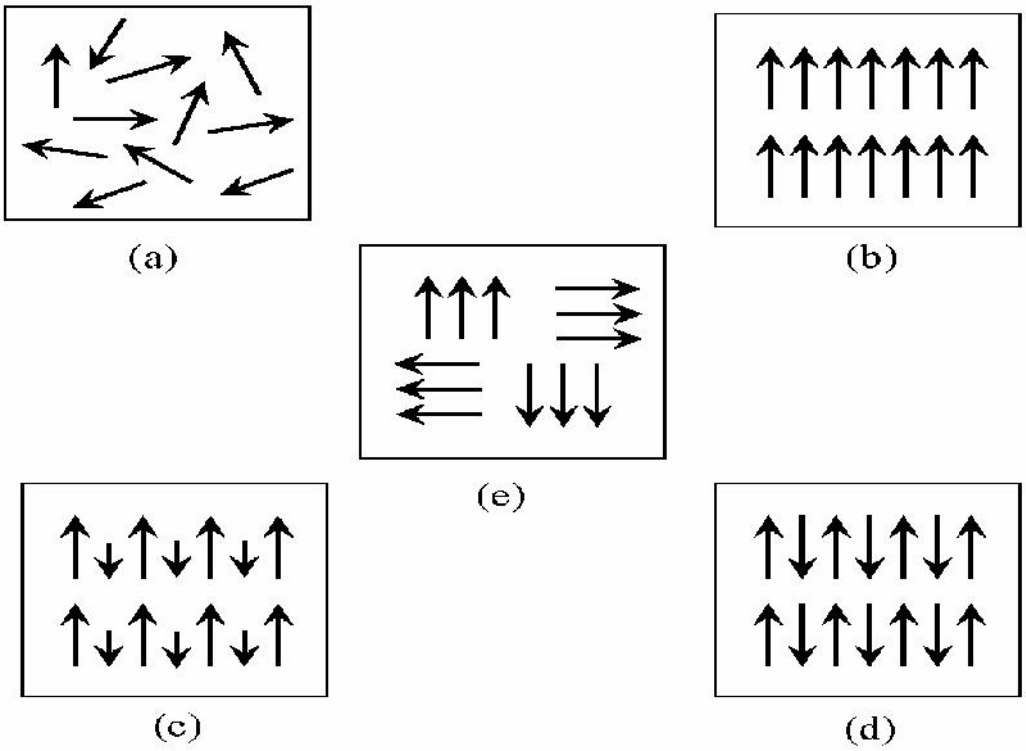

Fig. 2.2. Varieties of magnetic orderings (a) paramagnetic, (b) ferromagnetic, (c) ferrimagnetic,(d) antiferromagnetic and (e) superparamagnetic.

(2) Paramagnetism

Paramagnetic materials possess a permanent dipole moment due to incomplete cancellation of electron spin and/or orbital magnetic moments (unpaired electrons). In the absence of an applied magnetic field the dipole moments are randomly oriented; therefore the material has no net macroscopic magnetization. When a field is applied these moments tend to align by rotation towards the direction of the applied field and the material acquires a net magnetization [2.1]. The magnetic moment can be oriented along an applied field to give rise to a positive susceptibility, and the values of susceptibility are very small with the order of 10^{-5} to 10^{-3}. O_2, NO, Mn and Cr are just a few examples of the paramagnetic materials. The susceptibility of a paramagnetic material is inversely dependent on temperature, which is known as Curie law (Fig. 2.3 a)

$$\chi = C/T \qquad (2.13)$$

where C is the Curie constant.

(3) Ferromagnetism

Ferromagnetic material differs from diamagnetic and paramagnetic materials in many different ways. In a ferromagnetic material, the exchange coupling between neighboring moments leads the moments to align parallel with each other. In ferromagnetic materials, this permanent magnetic moment is the result of the cooperative interaction of large numbers of atomic spins in what are called domains, regions where all spins are aligned in the same direction. The exchange force is a quantum mechanical phenomenon due to the relative orientation of the spins of two electrons.

Therefore, the ferromagnetic materials generally can acquire a large magnetization even in the absence of a magnetic field, since all magnetic moments are easily aligned together. The susceptibility of a ferromagnetic materials does not follow the Curie law, but displayed a modified behavior defined by Curie-Weiss law (Fig. 2.3 b).

$$\chi = \frac{C}{T - \theta} \qquad (2.14)$$

where, C is a constant and θ is called Weiss constant. For ferromagnetic materials, the Weiss constant is almost identical to the Curie temperature (T_c). At temperature below T_c, the magnetic moments are ordered whereas above T_c material losses magnetic ordering and show paramagnetic character. The elements Fe, Ni, and Co and many of their alloys are typical ferromagnetic materials.

Two distinct characteristics of ferromagnetic materials are:

- spontaneous magnetization and
- the existence of magnetic ordering temperature (Curie temperature)

The spontaneous magnetization is the net magnetization that exists inside a uniformly magnetized microscopic volume in the absence of a field. The magnitude of this magnetization, at 0°K, is dependent on the spin magnetic moments of electrons. The saturation magnetization is the maximum induced magnetic moment that can be obtained in a magnetic field (H_{sat}); beyond this field no further increase in magnetization occurs. Saturation magnetization is an intrinsic property, independent of particle size but dependent on temperature.

Even though electronic exchange forces in ferromagnets are very large, thermal energy eventually overcomes the exchange and produces a randomizing effect. This occurs at a particular temperature called the Curie temperature (T_c). Below the Curie temperature, the

ferromagnet is ordered and above it, disordered. The saturation magnetization goes to zero at the Curie temperature. The Curie temperature is also an intrinsic property.

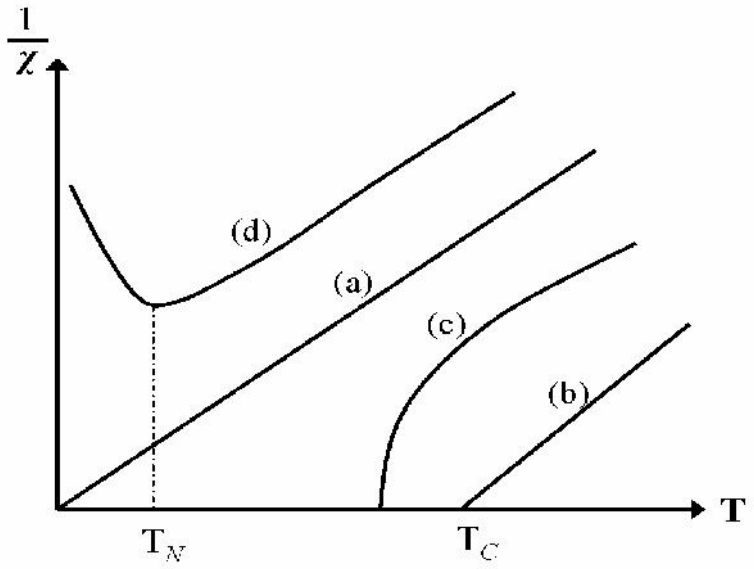

Fig. 2.3. The inverse susceptibility varies with temperature T for (a) paramagnetic, (b) ferromagnetic, (c) ferrimagnetic, (d) antiferromagnetic materials. T_N and T_c are Neel temperature and Curie temperature, respectively.

(4) Antiferromagnetism

Antiferromagnetic material aligns the magnetic moments in a way that all moments are antiparallel to each other, the net moment is zero. The anti-ferromagnetic susceptibility is followed by the Curie-Weiss law with a negative θ as the equation (2.14). The inverse susceptibility as a function of temperature is shown in Fig. 2.3(d). Common examples of materials with antiferromagnetic ordering include MnO, FeO, CoO and NiO.

(5) Ferrimagnetism

Ferrimagnetic material has the same anti-parallel alignment of magnetic moments as an antiferromagnetic material does. However, the magnitude of magnetic moment in one direction differs from that of the opposite direction. As a result, a net magnetic moment remains in the absence of external magnetic field. The behavior of susceptibility of a ferrimagnetic material also obeys Curie-Weiss law and has a negative θ as well in Fig.2.3 (c). In ionic compounds, such as oxides, more complex forms of magnetic ordering can occur as a result of the crystal structure. The magnetic structure is composed of two magnetic sublattices (called A and B) separated by oxygens. The exchange interactions are mediated by the oxygen anions. When this happens, the interactions are called indirect or superexchange interactions. The strongest superexchange interactions result in an

antiparallel alignment of spins between the A and B sublattice. In ferrimagnets, the magnetic moments of A and B sublattices are not equal and result in a net magnetic moment. Ferrimagnetism is therefore similar to ferromagnetism. It exhibits all the hallmarks of ferromagnetic behavior like spontaneous magnetization, Curie temperature, hysteresis, and remanence. However, ferro-and ferrimagnets have very different magnetic ordering.

2.1.5 Hysteresis

Magnetic hysteresis is an important phenomenon and refers to the irreversibility of the magnetization and demagnetization process, when a material shows a degree of irreversibility it is known as hysteretic. When a demagnetized ferromagnetic material is placed in as applied magnetic field grows at the expanse of the other domain wall. Such growth occurs by motion of the domain walls .Initially domain wall motion is reversible, and if the applied field is removes the magnetization will return to the initial demagnetized state. In this region the magnetization curve is reversible and therefore does not show hysteresis. The crystal will contain imperfections which the domain boundaries encounter during their movement. These imperfections have an associated magneto static energy when a domain wall intersects the crystal imperfection this magneto static energy can be eliminated as closure domains from this pins the domain wall to the imperfection as it if a local energy minima.

A great deal of information can be learned about the magnetic properties of a material by studying its hysteresis loop. A hysteresis loop shows the relationship between the induced magnetic flux density (**B)** and the magnetizing force **(H).** It is often referred to as the B-H loop. An example of hysteresis loop is shown below.

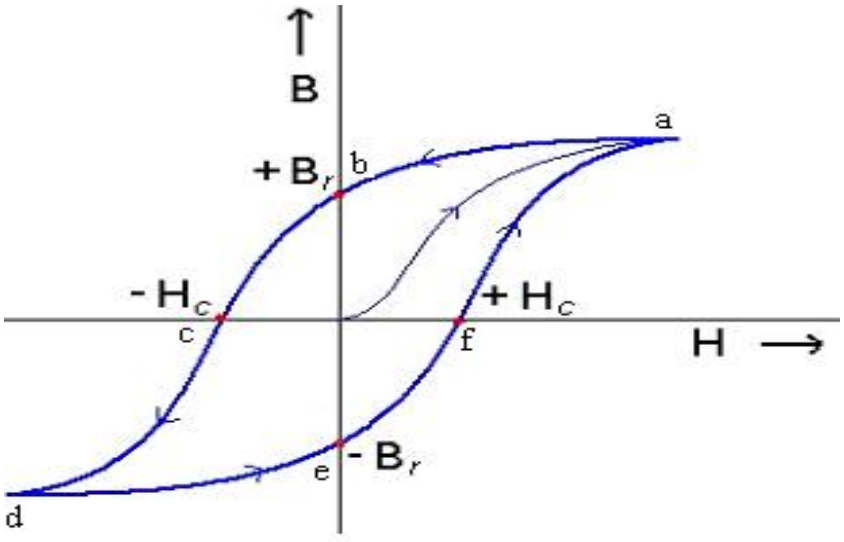

Fig. 2.4 Magnetic hysteresis loop.

The loop is generated by measuring the magnetic flux of a ferromagnetic material while the magnetizing force is changed. A ferromagnetic material that has never been previously magnetized or has been thoroughly demagnetized will follow the dashed line as **H** is increased. As the line demonstrates, the greater the amount of current applied **(+H)**, the stronger the magnetic field in the component **(+B)**. At point "a" almost all of the magnetic domains are aligned and an additional increase in the magnetizing force will produce very little increase in magnetic flux. The material has reached the point of magnetic saturation. When **H** is reduced to zero, the curve will move from point "a" to point "b". At this point, it can be seen that some magnetic flux remains in the material even though the magnetizing force is zero. This is referred to as the point of retentivity on the graph and indicates the remanence (B_r) or level of residual magnetism in the material. (Some of the magnetic domains remain aligned but some have lost their alignment). As the magnetizing force is reversed, the curve moves to point "c", where the flux has been reduced to zero. This is called the point of coercivity on the curve. (The reversed magnetizing force has flipped enough of the domains so that the net flux within the material is zero). The force required to remove the residual magnetism from the material is called the coercive force (H_c) or coercivity of the material. As the magnetizing force is increased in the negative direction, the material will become magnetically saturated but in the opposite direction (point "d"). Reducing **H** to zero brings the curve to point "e". It will have a level of residual magnetism equal to that achieved in the other direction. Increasing **H** back in the positive direction will return **B** to zero. Notice that the curve did not return to the origin of the graph because some force is required to remove the residual magnetism. The curve will take a different path from point "f" back to the saturation point where it with complete the loop.

From the hysteresis loop, a number of primary magnetic properties of a material can be determined:

(i) **Retentivity**, a measure of the residual flux density corresponding to the saturation induction of a magnetic material. In other words, it is a material's ability to retain a certain amount of residual magnetic field when the magnetizing force is removed after achieving saturation. The value of **B** is at point "b" on the hysteresis curve.

(ii) **Residual Magnetization** or **Residual Flux**, the magnetic flux density that remains in a material when the magnetizing force is zero. Residual magnetization and retentivity are the same when the material has been magnetized to the saturation

point. However, the level of residual magnetization may be lower than the retentivity value when the magnetizing force did not reach the saturation level.

(iii) **Coercive Force**, the amount of reverse magnetic field which must be applied to a magnetic material to make the magnetic flux return to zero. The value of **H** is at point "c" on the hysteresis curve.

2.1.6 Magnetic Domains

In 1907 Weiss proposed that a magnetic material consists of physically distinct regions called domains and each of which was magnetically saturated in different directions (the magnetic moments are oriented in a fixed direction) as shown schematically in Fig. 2.5. Even each domain is fully magnetized but the material as a whole may have zero magnetization. The external applied field aligns the domains, so there is net moment. At low fields this alignment occurs through the growth of some domains at the cost of less favorably oriented ones and the intensity of the magnetization increases rapidly. Growth of domains stops as the saturation region is approached and rotation of unfavorably aligned domain occurs. Domain rotation requires more energy than domain growth. In a ferromagnetic domain, there is parallel alignment of the atomic moments. In a ferrite domain, the net moments of the antiferromagnetic interactions are spontaneously oriented parallel to each other.

Domains typically contain from 10^{12} to 10^{15} atoms and are separated by domain boundaries or walls called Bloch walls. The formation of domains allows a ferro or ferri-material to minimize its total magnetic energy. The magnetic energy is composed of several types of energy [2.2, 2.3]:

i) Magnetostatic or demagnetization energy: The magnetized material behaves like a magnet, with a surrounding magnetic field. This field acts to magnetize the material in the direction opposite from its own magnetization, causing a magnetostatic energy which depends on the shape of the material. This magnetostatic energy can be reduced by reducing the net external field through the formation of domains inside the material.

ii) Magnetocrystalline anisotropy energy: In some materials the domain magnetization tends to align in a particular crystal direction (the so-called easy axis).The material is easiest to spontaneous magnetization could exist in the demagnetized state Weiss proposed the concept of magnetic domains. The magnetization within the domain is saturated and will always lie in the easy direction of magnetization when there is no externally applied

field. The direction of the domain alignment across a large volume of material is more or less random and hence the magnetization of a specimen can be zero.

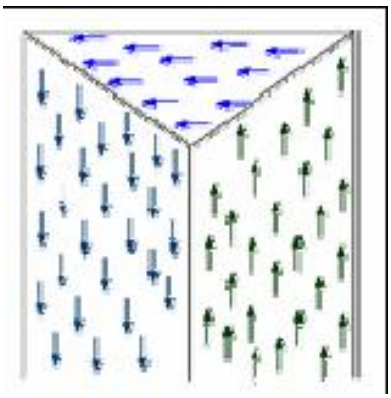

Fig. 2.5 Illustration of domains in ferromagnetic materials.

Magnetic domain exit in order to reduce the energy of the system. A uniformly magnetized specimen as shown in Fig. 2.6(a) has a large magnetostatic energy associated with it. This is the result of the presence of magnetic free poles at the surface of the specimen generating a demagnetizing field, H_d. From the convention adopted for the definition of the magnetic moment for a magnetic dipole the magnetization within the specimen points from the south pole to the north pole, while the direction of the magnetic field points from north to south. Therefore, the demagnetizing field is in opposition to the magnetization of the specimen. The magnitude of H_d is dependent on the geometry and magnetization of the specimen. In general if the sample has a high length to diameter ratio and is magnetized in the long axis then the demagnetizing field and the magnetostatic energy will be low.

The break up of the magnetization into two domains as illustrated in Fig 2.6 (b) reduces the magnetostatic energy by half. In fact if the magnet breaks down into N domains then the magnetostatic energy is reduced by a factor of 1/N, hence Fig 2.6 (c) has a quarter of the magnetostatic energy of Fig. 2.6 (a). Figure 2.6 (d) shows a closure domain structure where the magnetostatic energy is zero, however, this is only possible for materials that do not have a strong uniaxial anisotropy, and the neighbouring domains do not have to be at 180° to each other.

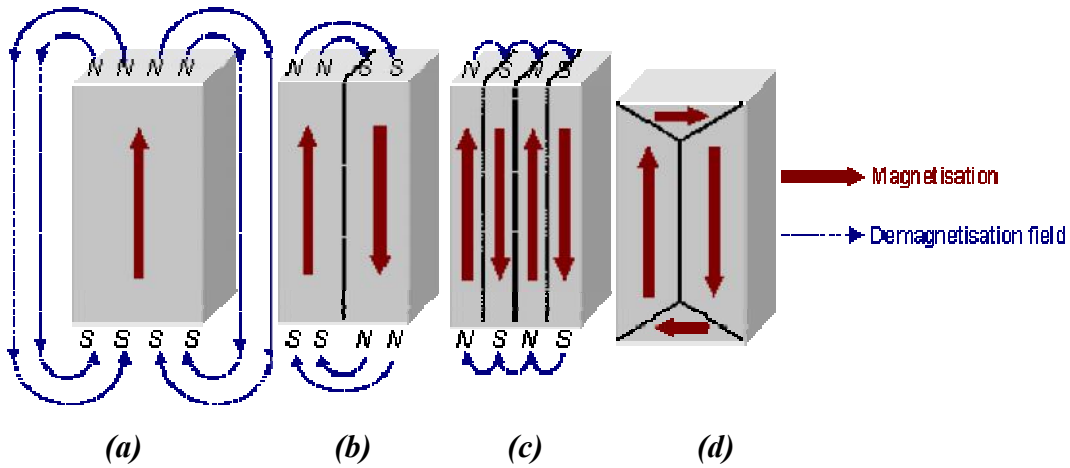

Fig. 2.6. Schematic illustration of the break up of magnetization into domains (a) single domain, (b) two domains, (c) four domains and (d) closure domains.

2.1.7 Structure of domain wall

The introduction of a domain raises the overall energy of the systems, therefore the divisions into domains only continues while the reduction in magnetostatic energy is greater than the energy required to form the domain wall. The energy associated with a domain wall is proportional to its area. The schematic representation of the domain wall, shown in Fig. 2.7 illustrates that the dipole moments of the atoms within the wall are not pointing in the easy direction of magnetization and hence are in a higher energy state. In addition, the atomic dipoles within the wall are not a 180° to each other and so the exchange energy is also raised within the wall. Therefore, the domain wall energy is an intrinsic property of a material depending on the degree of magnetocrystalline anisotropy and the strength of the exchange interaction between neighbouring atoms. The thickness of the wall will also vary in relation to these parameters, as strong magnetocrystalline anisotropy will favor a narrow wall, whereas a strong exchange interaction will favor a wider wall.

A minimum energy can therefore be achieved with a specific number of domains within a specimen. This number of domains will depend on the size and shape of the sample (which will affect the magnetostatic energy) and the intrinsic magnetic properties of the materials which will magnetize to saturation or demagnetize from saturation if the field is applied along an easy axis. The energy difference between aligning the domain in the easy and another direction (hard direction) is called magnetocrystalline anisotropy energy. Anisotropy energy is the energy needed to rotate the moment from the easy

direction to a hard direction. For materials with cubic crystalline structure (such as ferrites), the energy is expressed in terms of anisotropy constants and the direction to which the magnetization rotates

$$E = K_1 \sin^2\theta + K_2 \sin^4\theta \ldots\ldots \quad \text{(hexagonal structure)}$$

$$E = K_1(\alpha_1^2\alpha_2^2 + \alpha_2^2\alpha_3^2 + \alpha_3^2\alpha_1^2) + K_2(\alpha_1^2\alpha_2^2\alpha_3^2 + \ldots\ldots \quad \text{(cubic structure)}$$

where K is the anisotropy constant, θ is the angle between the easy axis and the direction of magnetization, and α's are the direction cosines, which are the ratios of the individual components of the magnetization projected on each axis divided by the magnitude of the magnetization. A crystal is higher in anisotropy energy when the magnetization points in the hard direction rather than along the easy direction. The formation of domains permits the magnetization to point along the easy axis, resulting in a decrease in the net anisotropy energy.

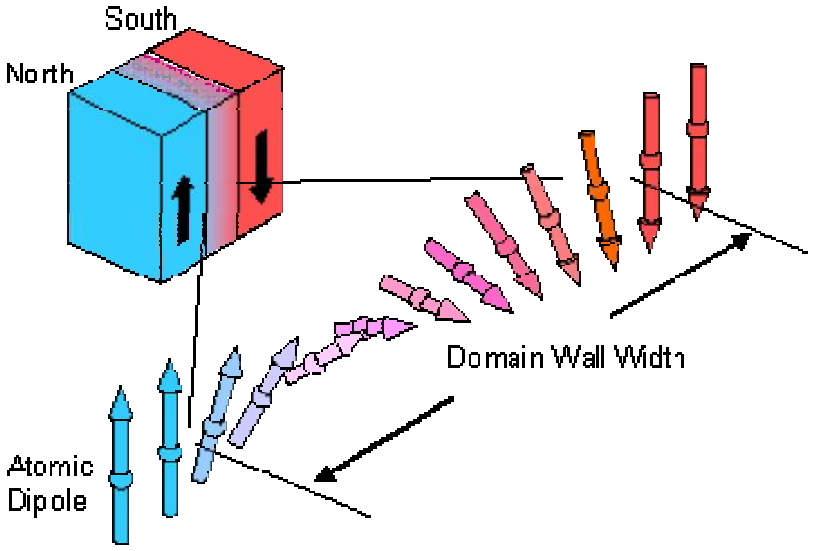

Fig. 2.7. Schematic representation of a 180°C domain wall.

c) Magnetostrictive energy: In a magnetic field, the material may change its dimensions on the order of several parts per million. This change in dimension results in what is called magnetostrictive energy, which is lowered by a reduction in the size of the domains, requiring the formation of more domains.

d) Domain wall energy: This is energy resulting from the increase or decrease in the width of the walls due to the growth /shrinkage of domains.

The magnetization in a domain changes by two mechanisms: rotation of the magnetic dipoles toward the direction of the applied field and change in the domain volume. In the

first case, a certain amount of anisotropy energy is needed to rotate the magnetization in a crystal from the easy to another axis. In the second mechanism, the volume of the domain changes, changing its contribution to the bulk magnetization, while the magnetization direction is unchanged. The change in the magnetization intensity of a domain depends on how close its direction is to the direction of the applied field. If the magnetization direction is close, the intensity in the domain increases, whereas if it is far, the intensity decreases.

The domain volume changes due to motion of the domain wall. This movement is originated by a torque that rotates the moments of the domain in line with the field, moving the center of the wall toward the domain opposed to the field. Consequently, the volume of the domains whose direction is favourable is increased whereas the domains with unfavorable direction decrease in volume [2.2]. In order to explain the fact that ferromagnetic materials with affect the magnetostatic energy and the domain wall energy. Ferromagnetic materials get their magnetic properties not only because their atoms carry a magnetic moment but also because the materials is made up of small regions known as magnetic domains. In each domain, all of the atomic dipoles are coupled together in a preferential direction. During solidification, a trillion or more atom moments are aligned parallel so that the magnetic force within the domain is strong in one direction. Ferromagnetic materials are said to be characterized by "spontaneous magnetization" since they obtain saturation magnetization in each of the domains without an external magnetic field being applied. Even though the domains are magnetically saturated, the bulk material may not show any signs of magnetism because the domains develop themselves and are randomly oriented relative to each other.

Ferromagnetic materials become magnetized when the magnetic domains within the material are aligned. This can be done by placing the material in a strong external magnetic field or by passing electrical current through the material. Some or all of the domains can become aligned. The more domains that are aligned, the stronger the magnetic field in the material. When all of the domains are aligned, the material is said to be magnetically saturated. When a material is magnetically saturated, no additional amount of external magnetization force will cause an increase in its internal level of magnetization. In an unmagnetized sample of material, the domains point in random directions, or form closed loops, so that there is no overall magnetization of the sample. In

a magnetized sample, the domains are aligned so that their magnetic effects combine to produce a strong overall magnetism.

2.2 Ferrites

There are two basic types of magnetic materials; one is metallic and another is metallic oxides or ceramics. These metallic oxides are called ferrites. Ferrites are chemical compounds with the formula AB_2O_4 where A and B represent various metal cations; usually including iron [2.4]. Ferrites are a class of spinels i.e. materials that adopt a crystal motif consisting of cubic closed pack oxides with A cations occupying 1/8th of the octahedral voids. For inverse spinel structure, half the B cations occupy tetrahedral sites and both the A and B cations occupy the octahedral sites. Divalent, trivalent and quadrivalent cations can occupy the A and B sites and they include Mg, Zn, Fe, Mn, Al, Cr, Ti and Si. At high frequencies ferrites are considered superior to other magnetic materials because they have low eddy current losses and high dc electrical resistivity. The dc electrical resistivity of ferrites at room temperature can very depending upon chemical composition between about 10^{-2} ohm-cm and higher than 10^{11} ohm-cm [2.5].

Ferrites are classified into two categories based on their coercive field strength. They are

(1) Soft ferrites

(2) Hard ferrites

2.2.1 Soft ferrites

Soft ferrites are those that can be easily magnetized or demagnetized. This shows that soft magnetic materials have low coercive field and high magnetization that is required in many applications. The hysteresis loop for a soft ferrite should be thin and long, therefore the energy loss is very low in soft magnetic material. Examples are nickel, iron, cobalt, manganese etc. The magnetically soft ferrites first came into commercial production in 1948. Additionally, part of the family of soft ferrite are the microwave ferrites e.g. Ytrium iron garnet. These ferrite are used in the frequency range from 100 MHz to 500 GHz. For waveguides for electromagnetic radiation and in microwave device such as phase shifters. They are used in transformer cores, inductors, recording heads and microwave devices [2.6].

Soft ferrites have certain advantages over other electromagnetic materials including high resistivity and low eddy current losses over wide frequency ranges. They have high

permeability and are stable over a wide temperature range. These advantages make soft ferrites paramount over all other magnetic materials.

2.2.2 Hard ferrites

Hard ferrite referred to as permanent magnets retain their magnetism after being magnetized. Hard ferrite likes Ba-ferrite, Sr-ferrite are used in communication device operating with high frequency currents because of their high resistivity, negligible eddy currents and lower loss of energy due to joule heating and hysteresis.

According to crystallographic structures ferrite can be classified into three different types [2.7].

(1) Spinel ferrites (Cubic ferrites)
(2) Hexagonal Ferrites
(3) Garnets

2.2.3 Spinel ferrites

Cubic ferrite with spinel structure is the most widely used family of ferrites. High values of electrical resistivity and low eddy current losses make them ideal for their use at microwave frequencies. The spinel structure of ferrites as possessed by mineral spinel $MgAl_2O_4$ was first determined by Bragg [2.8]. The chemical composition of a spinel ferrite can be written in general as $MOFe_2O_3$ where Me is the divalent cation such as Mn^{2+}, Ni^{2+}, Mg^{2+}, Zn^{2+}, Cd^{2+}, Cu^{2+}, Co^{2+} etc. A combination of these ions is also possible and it can be named as solid solution of two ferrites or mixed spinel ferrites. Generally, Me represents a combination of ions which has an average valence of two. The trivalent iron ion in $MOFe_2O_3$ can partially be replaced by another trivalent ion such Al^{3+} or Cr^{3+}, giving rise to mixed crystals.

2.3 Cation distribution in ferrites

The cation distribution in the spinel ferrite $Me^{2}+Fe^{3+}O_4$ can be as follows [2.2]:

2.3.1 Normal spinel ferrites

The divalent cation (Me^{2+}) are in tetrahedral A-sites and two trivalent (Fe^{3+}) cations are in octahedral B-sites which is represented as $(Me^{2+})_A[Fe^{3+}]_BO_4$. A typical example of normal spinel ferrite is bulk $ZnFe_2O_4$.

2.3.2 Inverse spinel ferrites

In this case divalent (Me^{2+}) cations are in octahedral B- sites and the trivalent (Fe^{3+}) cations are equally divided between A and B sites (the divalent and trivalent ions normally occupy the B sites in a random fashion i.e. they are disordered) arrangement is as $(Fe^{3+})_A[Me^{2+}Fe^{3+}]_BO_4$. Iron, cobalt and Nickel ferrites have the inverse structure, and they are all ferromagnetic.

2.3.3 Mixed or random spinel ferrites:

X-ray and neutron diffraction experiments and magnetization measurements show that there is a whole range of cation distribution between the normal and inverse structures. The arrangement of the form $\left(Fe^{3+}_{1-x}Me^{2+}_{x}\right)_A[Fe^{3+}_{1+x}Me^{2+}{}_{1-x}]_B O_4^{2-}$ is often referred as mixed spinel, where cations in the parentheses are at (A) sites and those in the brackets are at [B] sites and x is called the inversion parameter. The extreme case x=1 corresponds to the normal spinel structure, and x= 0 corresponds to the inverse structure 0< x <1 for intermediate used commercially are mixed ferrite [2.9].

The factors affecting the cation distribution over A and B sites are as follows [2.2, 2.10]

- The size of the cations
- The electronic configurations of the cations
- The electronic energy
- The saturation magnetization of the lattice

Smaller cations (trivalent) prefer to occupy the A-sites. The cations have special preference for A sites and the preference depends on the following factors:

- Ionic radius
- Size of interstrices
- Sintering temperature
- Orbital preference for the specific coordination

The preference of cations is according to Verway-Heilmar scheme [2.11, 2.12].

Ions with strong preference for A-sites Zn^{2+},Cd^{2+}, Ga^{2+}, In^{3+} Ge^{4+}.

Ions with strong preference for B-sites Ni^{2+}, Cr^{3+}, Ti^{4+}, Sn^{4+}

Indifferent ions are Mg^{2+}, Fe^{3+}, Al^{3+}, Mn^{2+}, Cu^{2+}, Co^{2+}, Fe^{2+}

The cations of the smallest positive charge reside on the B-sites having six anions in surrounding i.e. the most favourable electrostatic condition. It has been observed that X-ray powder diffraction, in conjunction with appropriate computational method, has enough

sensitivity to determine the degree of inversion x, and oxygen positional parameter u.a difference of one electron between two different cations can be enough to render them distinguishable.

2.4 Magnetic exchange interaction

The exchange energy between the two atoms having spins S_i and S_j and be expressed universally in terms of Heigenburg Hamiltonian [2.5]

$$H = -\sum j_g S_i S_j \qquad (2.15)$$

where, J_{ij} the exchange integral represents the strength of exchange coupling between the spin angular momentum i and j. It is well known that the favored situation is the one with the lowest energy and there are two ways in which the wave functions can combine for lowering the energy by H. These are:

If J_{ij} is positive, the parallel spin configuration will minimize the system total energy and all spins aligned to each other in the ground state. This is the case leading to ferromagnetic ordering.

If J_{ij} is negative, J_{ij} favors the antiparallel alignment of spins and consequently gives rise to antiferromagnetic ordering.

2.4.1 Superexchange interaction

The magnetic interaction in magnetic oxides (ferrites) can not be explained on the basis of direct exchange interaction because of the following facts:

- The magnetic ions are located too far apart from each other shielded by the nonmagnetic anion (oxygen). This is because these are not band type semiconductor [2.13]. The nonmagnetic anion is situated in the line joining magnetic cations.
- Superexchange interactrions appear, i.e., indirect exchange via anion p-orbitals that may be strong enough to order the magnetic moments.

Ferrimagnetic oxides are one kind of magnetic systems in which there exist at least two inequivalent sublattices for the magnetic ions. The antiparallel alignment between these sublattices (ferrimagnetic ordering) may occur provided the inter-sublattice exchange interactions are antiferromagnetic (AF) and some requirements concerning the signs and strengths of the intra-sublattice interactions are fulfilled. Since usually in ferrimagnetic oxides the magnetic cations are surrounded by bigger oxygen anions (almost

excluding the direct overlap between cation orbitals) magnetic interactions occur via indirect superexchange interactions depends both on the electronic structure of the cations and their geometrical arrangement [2.14]. In most of ferrimagnetic oxides, the crystallographic and electronic structure give rise to antiferromagnetic inter and intra-sublattice competing interactions. The magnitude of negative exchange energies between two magnetic ions M and M′ depends upon the distances from these ions to the oxygen ion O^{2-}, via which the superexchange takes place, and on the angle M-O^2-M′(ϕ). According to the superexchange theory, the angle ϕ=180° gives rise to the greatest exchange energy, and this energy decreases very rapidly as the distance between the ions increases. If A and B are the tetrahedral and octahedral ions respectively in a spinel structure, the A-B interaction is the greatest and A-A exchange interaction is the weakest [2.5].

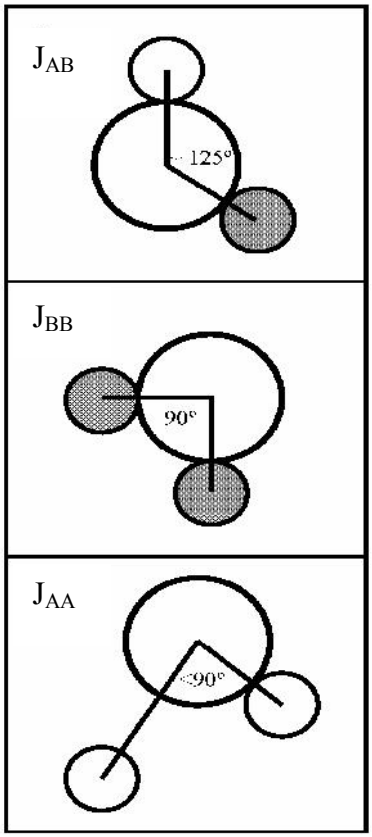

Fig. 2.8. Three major types of superexchange interactions in spinel ferrites are as follows: J_{AB}, J_{BB} and J_{AA}. the small empty circle is A site, the small solid circle is B site, and the large empty circle is oxygen anion.

2.4.2 Two sublattices in spinel ferrites

The term magnetic sublattice is widely used in the study of magnetic structures of the whole spectrum of magnetic materials [2.15]. In the case of ferromagnetic materials, the magnetic sublattice is exactly the same as the crystal structure and no problem arises. In the case of antiferromagnetics, the importance of the direction of the magnetic moments is evident and makes clear the existence of two magnetic sublattices, as for example, in MnO. The difference between the magnetic sublattices is the direction of their magnetic moment. However, ferrimagnetic materials are considerably more complex and the application of the molecular field theory to spinels has pointed to the problem of a clear definition of the concept of magnetic sublattices. In spinel ferrites the metal ions are separated by the oxygen ions and the exchange energy between spins of neighbouring metal ions is found to be negative, that is, antiferromagnetic. This is explained in terms of superexchange interaction of the metal ions via the intermediate oxygen ions [2.16]. There are a few points to line out about the interaction between two ions in tetrahedral (A) sites:

- The distance between two A ions (~3.5Å) is very large compared with their ionic radius (0.64 Å for Fe^{3+}),
- The angle A-O^{2-}-A ($\phi = 79°38'$) is unfavourable for superexchange interaction [2.17], and
- The distance from one A ion to O^{2-} is not the same as the distance from the other A ion to O^{2-} as there is only one A nearest neighbour to an oxygen ion (in figure 2.10, M and M′ are ions, r = 3.3 Å and q = 1.7 Å) [2.5]. As a result, two nearest A ions are connected via two oxygen ions.

These considerations led us to the conclusion that superexchange interaction between A ions is very unlikely. This conclusion together with the observation that direct exchange is also unlikely in this case [2.5] support the assumption that $J_{AA}= 0$ in the spinel ferrites. According to Neel's theory, the total magnetization of a ferrite divided into two sublattices A and B is:

$$M_T(T) = M_B(T)-M_A(T) \qquad (2.16)$$

Where, T is the temperature, $M_B(T)$ and $M_A(T)$ are A and B sublattice magnetizations. Both $M_B(T)$ and $M_A(T)$ are given in terms of the Brillouin function $B_{si}(x_i)$;

$$M_B(T)= M_B(T= 0)\, B_{SB}(x_B) \qquad (2.17)$$

$$M_A(T) = M_A\,(T=O)\,B_{SA}(x_A) \qquad (2.18)$$

With

$$x_A = \frac{\mu_B g_A S_A}{k_B T} M_B N_{AB} \qquad (2.19)$$

$$x_B = \frac{\mu_B g_B S_B}{k_B T}\left(M_B N_{BB} + M_A N_{AB}\right) \qquad (2.20)$$

The molecular field coefficients, N_{ij}, are related to the exchange constants J_{ij} by the following expression:

$$J_{ij} = \frac{n_j g_i g_j \mu^2{}_B}{2 z_{ij}} N_{ij} \qquad (2.21)$$

with n_j the number of magnetic ions per mole in the j^{th} sublattice, g the Lande factor, μ_B is the Bohr magneton and z_{ij} the number of nearest neighbours on the j^{th} sublattice that interact with the i^{th} ion.

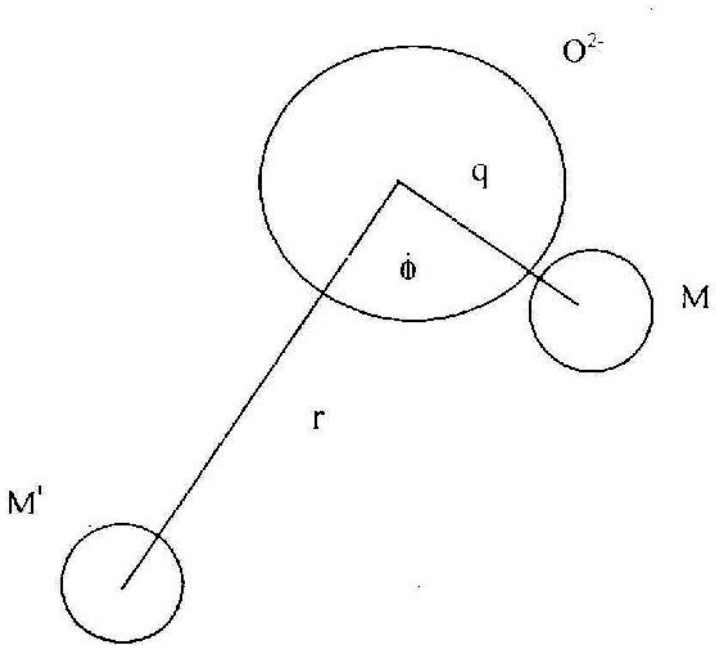

Fig. 2.9. Schematic representation of ions M and M′ and the O^{2-} ion through which the superexchange is made r and q are the centre to centre distances from M and M′ respectively to O^{2-} and ϕ is the angle between them.

According to Neel's theory and using $J_{AA}= 0$, equating the inverse susceptibility $1/\chi=0$ at $T= T_c$ we obtain for the coefficients of the molecular field theory N_{AB} and N_{BB} of the following expression:

$$N_{BB} = \frac{T_c}{C_B} - \frac{C_A N^2{}_{AB}}{T_c} \qquad (2.22)$$

where, C_A and C_B are the Curie constants for each sublattice. Equations (2.16) and (2.21) constitute a set of equations with two unknown, N_{AB} and N_{BB}, provided that M_A and M_B are a known function of T.

2.5 Magnetic structure of substituted ferrites

2.5.1 Neel's collinear model of ferrites

Soft ferrites belong to the cubic spinel structure. According to Neel's theory, the magnetic ions are assumed to be distributed among the tetrahedral A and octahedral B-sites of the spinel structure. The magnetic structure of such crystals essentially depends upon the type of magnetic ions residing on the A and B sites and the relative strengths of the inter-(J_{AB}) and intra sublattice exchange interactions (J_{AA}, J_{BB}). Negative exchange interactions exist between A-A, A-B and B-B ions. When A-B antiferromagnetic interaction is the dominant one, A and B-sublattices will be magnetized in opposite direction below a transition temperature. When the A-A (or B-B) interaction is dominant, Neel found that the above transition will not take place and he concluded that the substance remains paramagnetic down to the lower temperature. But this conclusion was not correct, as in the presence of strong interactions, some kind of ordering may be expected to occur at low temperature as claimed by Yafet and Kittel [2.18].

2.5.2 Non-collinear model

In general, all the interactions are negative (antiferromagnetic) with $|J_{AB}| \gg |J_{BB}|J_{AA}|$. In such situation, collinear or Neel type of ordering is obtained. Yafet and Kittel theoretically considered the stability of the ground state of magnetic ordering, taking all the three exchange interactions into account and concluded that beyond a certain value of J_{BB}/J_{AB}, he stable structure was a non-collinear triangular configuration of moment wherein the B-site moments are oppositely canted relative to the A-site moments. Later on Leyons et.al. [2.19] extending these theoretical considerations showed that for normal spinel the lowest energy correspond to conical spinel structure for the value of $3J_{BB}S_B/2J_{AB}S_A$ greater than unity. Initially one can understand why the collinear Neel structure gets perturbed when J_{BB}/J_{AB} increases. Since all these three exchange interactions are negative (favoring

antiferromagnetic alignment of moments) the inter-and intra-sublattice exchange interaction compete with each other in aligning the moment direction in the sublattice. This is one of the origins of topological frustration in the spinel lattice. By selective magnetic directions of say A-sublatice one can effectively decrease the influence of J_{AB} vis-a-vis J_{BB} and thus perturb the Neel ordering. The first neutron diffraction study of such system i.e, $Zn_xNi_{1-x}Fe_2O_4$ was done at Trombay [2.20] and it was shown to have the Y-K type of magnetic ordering followed by Neel ordering before passing on to the paramagnetic phase [2.14].

It was found that ferrites which have been substituted sufficiently with non-magnetic atoms showed significant departure from Neel collinear model. These theoretical models have been used to explain these departures:

- a paramagnetic centre model in which a number of magnetic nearest neighbours determines whether a magnetic ion remains paramagnetic or contributes to the magnetization.
- a uniform spin canting relative to the average magnetization and
- a localized canting where the canting angle of a magnetic ion spin depends on the local magnetic environment.

The discrepancy in the Neel's theory was resolved by Yafet and Kittle [2.18] and they formulated the non-collinear model of ferrimagnetism. They concluded that the ground state at 0°K might have one of the following configurations:

- have an antiparallel arrangement of the spins on two sites
- consists of triangular arrangements of the spins on the sublattices
- an antiferromagnetic in each of the sites separately.

References:

[2.1] W. Callister, Materials Science and Engineering an introduction, Sixthed. New York: John Wiley & Sons, Inc, (2003).

[2.2] Alex Goldman, "Modern Ferrite Technology" Van nosttrand Reinhold New York, (1990).

[2.3] N. Spaldin Magnetic materials: Fundamentals and device applications Cambridge: Cambridge University press, (2003).

[2.4] Williams F. Smith, Javad Hashemi, Foundations of Materials Science and Engineering, fourth Edit, **888**, Mc Graw –Hill, (2006).

[2.5] J. Smith, H. P. J. Wijn. Ferrites, John Wiley and Sons, New York, (1959).

[2.6] M. S. Vijaya, G. Rangarajan, Materials Science, McGraw-Hill Publishing Company Limited, New Delhi, **447** (1999-2000).

[2.7] K. J. Standley, "Oxide Magnetic Materials" 2nd ed., Oxford University Press, (1972).

[2.8] W.H. Bragg, " The structure of magnetite and the spinels", Nature, **95,** 561 (1915).

[2.9] C. W. Chem, Magnetism and Metallurgy of soft Magnetic Materials, New York (1977).

[2.10] D. S. Craik, 1957, Magnetic oxide, part I, John Wiley and Sons, Ltd, Bristol England.

[2.11] E. J. W. Verway and E. L. Heilmann, J. Chem, Phys. **15 (4),** 174 ,(1947).

[2.12] F. C. Romeign, Philips Rs. Rep. 8, **NR-5**, 304 (1953).

[2.13] B. Viswanathan, VRK Murthy, "Ferrite Materials Science and Technology", Spring Verlag, noarosa Publishing House, New Delhi, (1990).

[2.14] S. Krupicka and P Novak. Oxide spinels. In E. P. Wohlfarth, editor, Ferromagnetic Materials, **vol. 3**, 189-304. North-Holland. The Netherlands, (1982).

[2.15] Virginia Fuentes, S. Abunto and R. Valenzhela, " Magnetic sublattices in nickel ferrites", J. Magn, Magn. Mater. 69, 233 (1987).

[2.16] P. W. Anderson, in Magnetism, vol. 1. Eds, G. T. Rado and H. Suhl , Academic press, New York, (1963).

[2.17] J. D. Livingston, Driving Forces. The Natural Magic of Magnets: Harvard University press : Cambridge, (1996).

[2.18] Y. Yafet and C. Kittle, Antiferromagnetic arrangements in ferrites", Phys. Rev.87 (1952).

[2.19] D. H. Leyons, T. A. Keplan, K. Dwight and N. Menyuk, "Classical theory of the ground spin-state in cubic spinels", Phys. Rev. **126**, 540 (1962).

[2.20] N. S. S. Murthy, M. G. Natera, S. I. Yousuf, R. J. Begum and C. M. Srivatara, "Yafet-Kittle angles in zinc-nickel ferrites", Phys. Rev. **181 (2),** 969 (1964).

Chapter Three

The Properties of Soft Ferrites

3.1 Crystalline and Magnetic Structures

A ferrite can be considered a material containing mostly iron which is derived from magnetite ($Fe^{2+}O.\ Fe_2^{3+}O_3$) by substituting divalent metal ions in place of Fe^{2+}. Trivalent metal ions substitute for Fe^{3+} and other valences (+1, +4, +5 and +6) can be incorporated into the lattice by charge compensation by the appropriate change in the Fe^{2+}/Fe^{3+} ratio. In all cases the ionic radii of the substituting ion should be between about 0.5 to 1.0 Å. The more common divalent metals are from the transition elements: Mn, Fe, Co, and Ni and metals such as Cu, Zn, Mg, Cd and Ge. Trivalent Al, Cr, Ga and Mn can replace Fe^{3+} while monovalent Li and tetravalent Ti and Sn are incorporated into the lattice by the respective decrease or increase in the Fe^{2+}/Fe^{3+} ratio.

Ferrite materials have a crystalline structure similar to the mineral spinel $MgOAl_2O_3$, where the divalent ions replace Mg and the trivalent ions replace Al. Spinel is a close packed cubic structure of oxygen atoms with eight formula units per cell. It means that the structure is complex, in that there are 8 "molecules" or a total of 8×7= 56 ions, per unit cell. The large oxygen ions (radius about 1.3 Å) are packed quite close together in a face-centered cubic arrangement, and the much smaller metal ions (radii from about 0.7 to 0.8 Å) occupy the spaces between them. These spaces are of two kinds. One is called a tetrahedral or A- sites, because it is located at the centre of a tetrahedron whose corners are occupied by oxygen ions as shown in Fig. 3.1 (a). The other is called an octahedral or B-site, because the oxygen ions around it occupy the corners of an octahedron also shown in Fig. 3.1(b). The crystallographic environments of the A and B sites are therefore distinctly different.

The unit cell contains so many ions that a drawing of the complete cell would not be very informative, so one can imagine the unit cell of edge "a" to be divided into eight octants, each of edge a/2, as shown in Fig. 3.1(c). The four shaded octants have identical contents, and so do the four unshaded octants. The contents of the two lower-left octants in Fig 3.1(c) are shown in Fig. 3.1 (d). One tetrahedral site occurs at the centre of the eight octant of Fig. 3.1 (d)., and other tetrahedral sites are at certain octant corners. Four octahedral sites occur in the left octant; one is delineated by dashed lines to six oxygen

ions, two of which, shown dotted, are in adjacent octants behind the below. The oxygen ions are arranged in the same way (tetrahedrally) in all octants.

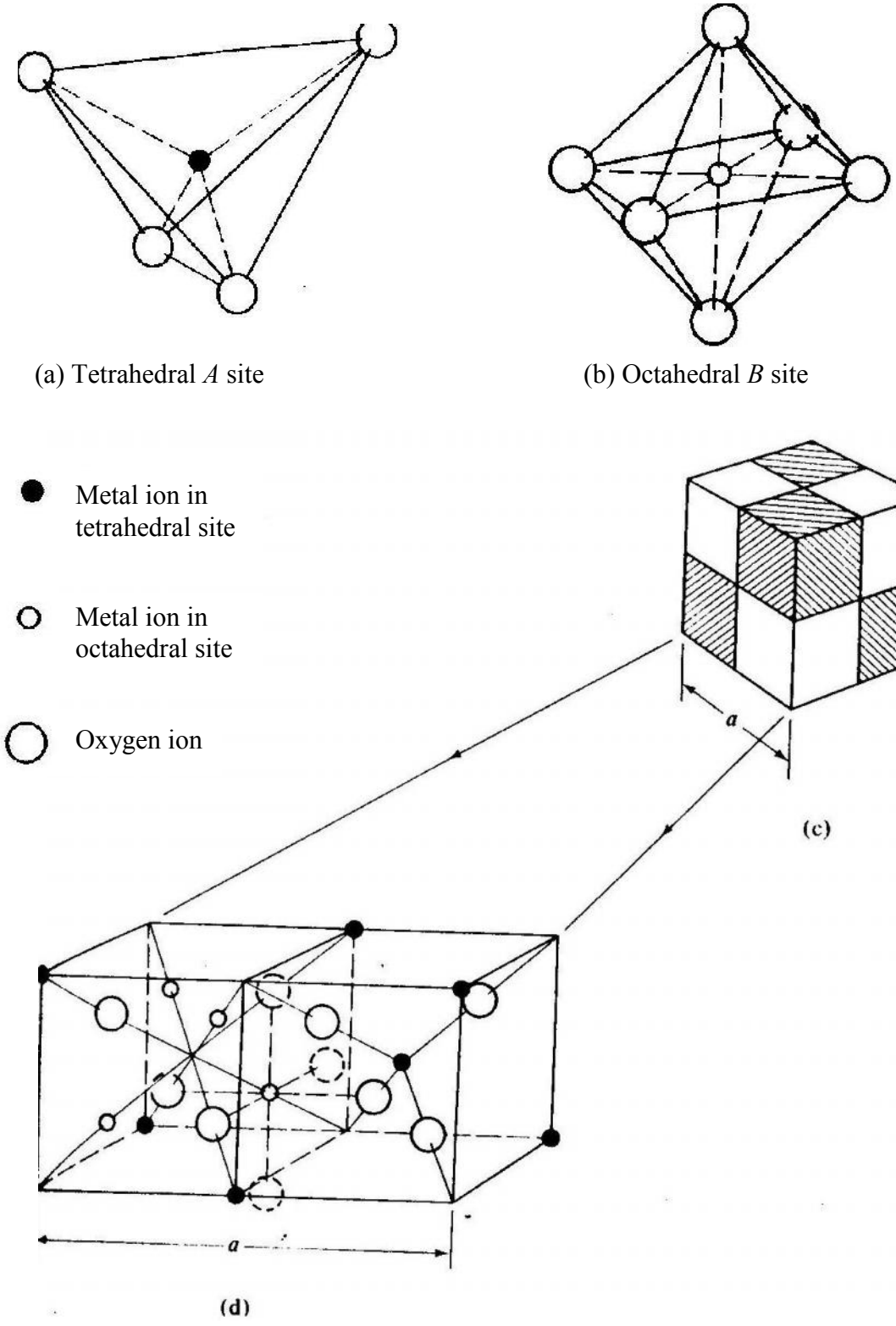

(a) Tetrahedral *A* site (b) Octahedral *B* site

Fig.3.1 Crystal structure of a cubic ferrite.

By no means all of the available sites are actually occupied by metal ions. Only one-eighth is the A-sites and one-half of the B-sites are occupied, as shown in Table 3.1.

Table 3.1 Arrangements of Metal Irons in the Unit Cell of a Ferrite MeO. Fe_2O_3

			Occupants	
Kind of site	Number available	Number occupied	Normal spinel	Inverse spinel
Tetrahedral (A)	64	8	$8Me^{2+}$	$8Fe^{3+}$
Octahedral (B)	32	16	$16Fe^{3+}$	$8Fe^{3+}$ $8M^{2+}$

In the mineral spinel, the Mg^{2+} ions are in A-sites and the Al^{3+} ions are in B-sites. Some ferrites MeO.Fe_2O_3 have exactly this structure, with Me^{2+} in A-sites and Fe^{3+} in B-sites. It is called the normal spinel structure. Both zinc and cadmium ferrite have this structure and they are both nonmagnetic i.e., paramagnetic. Many other ferrites, however have the inverse spinel structure, in which divalent ions are on B-sites and the trivalent ions are equally divided between A and B-sites. Iron, Cobalt and nickel ferrites have the inverse structure, and they are ferrimagnetic. Cobalt ferrite (CoO. Fe_2O_3) is magnetically hard, but all the other cubic ferrites are magnetically soft.

The normal and inverse structures are regarded as extreme cases, intermediate structure also exists. Manganese ferrite is almost but not perfectly, normal; because instead of all the Mn^{2+} ions being on A-sites, a fraction 0.8 is on A- sites and 0.2 on B-Sites. Similarly, magnesium ferrite is not quite inverse, a fraction 0.9 of the Mg^{2+} ions is on B- sites and 0.1 on A-sites. In fact the distribution of the ions between the two types of sites is determined by a delicate balance of contributions, such as the magnitude of ionic radii, their electronic configuration and the electrostatic energy of the lattice. Table 3.2 shows the electronic configuration of the transition elements with 3d unfilled electrons. However, the distribution of the divalent ions on A and B-sites in some ferrites can be altered by heat treatment; it depends, for example, on whether the material is quenched from high temperature or slowly cooled [3.1]. It is to be noted that ferrites can be prepared containing two different kinds of divalent ion, e.g., (NiZn) O. Fe_2O_3. This is called a mixed ferrite, although actually it is a solid solution of NiO. Fe_2O_3 and ZnO. Fe_2O_3. Similarly, (Mn,Zn)O.Fe_2O_3 is the solid solution of MnO.Fe_2O_3 and ZnO.Fe_2O_3. Most of the cubic ferrites used commercially are mixed ferrites.

Table 3.2. Electronic configuration of the transition elements with unfilled 3d electrons.

Atomic Number	Elements and cations	Electronic configuration	Unpaired electrons
25	Mn	$\underline{1S^2\ 2S^2\ 2p^6\ 3S^2\ 3P^6}$ $3d^5\ 4S^2$	5
	Mn^{2+}	Argon core 18 electrons $3d^5\ 4S^0$	5
	Mn^{3+}	----------$3d^4\ 4S^0$	4
	Mn^{4+}	----------$3d^3\ 4S^0$	3
26	Fe	----------$3d^6\ 4S^2$	4
	Fe^{2+}	----------$3d^6\ 4S^0$	4
	Fe^{3+}	----------$3d^5\ 4S^0$	5
27	Co	----------$3d^7\ 4S^2$	3
	Co^{2+}	----------$3d^7\ 4S^0$	3
	Co^{3+}	----------$3d^6\ 4S^0$	4
28	Ni	----------$3d^8\ 4S^2$	2
	Ni^{2+}	----------$3d^8\ 4S^0$	2
	Ni^{3+}	----------$3d^7 4S^0$	3
29	Cu	----------$3d^{10}\ 4S^1$	1
	Cu^{2+}	----------$3d^9 4S^0$	1

Table 3.3 shows the crystallographic lattice constant ‘a’ the oxygen parameter ‘u’ and the distribution of the ions on A and B sites compiled for single ferrite spinels. These single-ferrite spinels are seldom used in actual applications. In most cases mixed compounds of some of these single spinels are prepared, since they exhibit more favourable magnetic properties which can be adapted to the various applications. These mixed compounds are solid solutions, whose lattice constants depend linearly on the lattice constants of the single component ferrite spinels. A further variation of the technical properties can be achieved by substituting different ions for Fe^{3+}. In general a substitution is possible if the ionic radius of the entering ion is of the right size and if the appropriate charge compensation is provided for cations of deviating valency.

Table 3.3 Lattice parameter of single ferrite spinels with cation distribution ($Me^{2+}Fe_2O_4$)

Formula	Cell edge a Å	Oxygen parameter u U_{ideal}=0.375	Cation distribution
$NiFe_2O_4$	8.325	0.382	$\frac{Fe}{A}\ \frac{[NiFe]}{B}$
$MgFe_2O_4$	8.36	0.382	$Mg_{0.1}Fe_{0.9}[Mg_{0.9}Fe_{1.1}]$
$CoFe_2O_4$	8.38		Fe[CoFe]
Fe_3O_4	8.394	0.379	$Fe^{III}[Fe^{II}Fe^{III}]$
$ZnFe_2O_4$	8.44	0.385	$Zn[Fe_2]$
$MnFe_2O_4$	8.507	0.385	$Mn_{0.8}Fe_{0.2}[Mn_{0.2}Fe_{1.8}]$
$CdFe_2O_4$	8.69		$Cd[Fe_2]$
$CuFe_2O_4$*	a= 8.22 c=8.71	0.380	Fe [CuFe]

* Copper ferrite shows a tetragonal deformation below 760°C

The origin of magnetism in ferrites is due to: (i) unpaired 3d electrons, (ii) superexchange (indirect exchange) between adjacent metal ions and (iii) non-equivalence in number of A and B sites. In the free state the total magnetic moment of an atom containing 3d electrons is the sum of the electron spin and orbital moments. In an oxide compound such as ferrite, the orbital magnetic moment is mostly "quenched" by the electronic fields caused by the surrounding oxygen about the metal ion (crystalline field). The atomic moment (m) then becomes the moment of the electron spin and is equivalent to, $m= \mu_B.n$, where μ_B is a Bohr magneton unit, and n the number of unpaired electrons.

Super exchange (indirect exchange) takes place between adjacent metal ions separated by oxygen ions [3.2] as shown in Fig. 3.2. The strength of this interaction depends on the degree of orbital overlap of oxygen p orbital and the transition metal d orbital. The interaction will decrease as the distance between the metals increases and as the angle of Me-O-Me decreases from 180°C to 90°C. The only important interaction in ferrites is the AB interaction since the angle is about 125°C while the BB interaction is negligible because the angle is 90° as shown in Fig. 3.3. This interaction is such that antiparallel

alignment of the moments results between the two metal ions have 5 or more 3d electrons or 4 or fewer 3d electrons. Parallel alignment occurs when one ion has ≤ 4 electrons and the second has ≥ 5 electrons

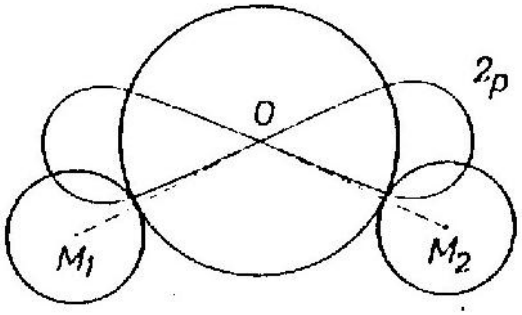

Fig.3.2. Diagram showing the orientation of the 2p orbit of the oxygen ion with respect to the metal ions, which is responsible for the indirect exchange.

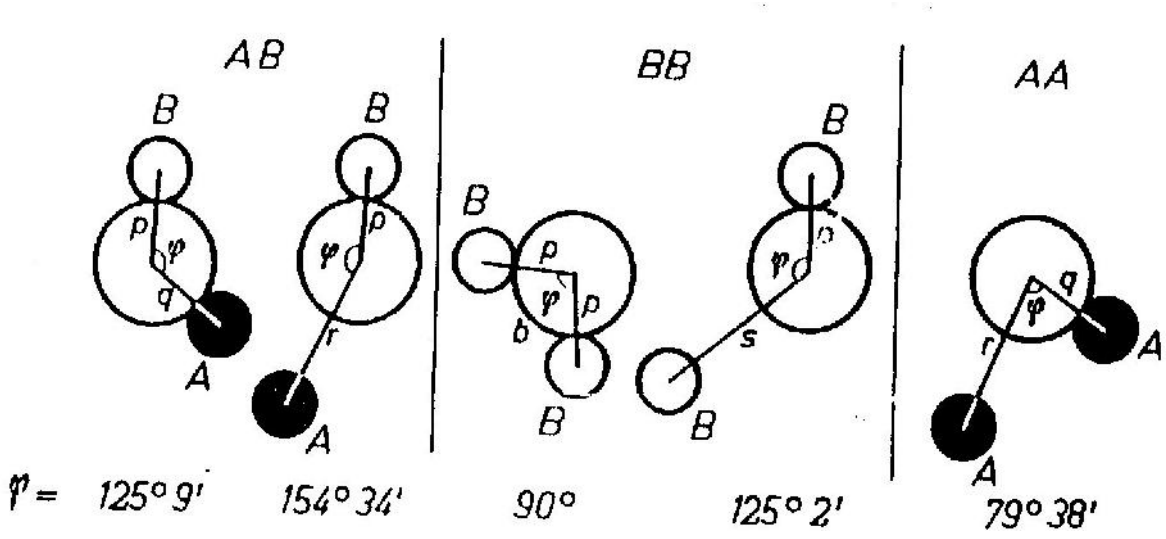

Fig. 3.3. Diagram showing the angle of interaction of the cations via oxygen anions.

Since the common ferrite ions (Mn^{2+}, Fe^{2+}, Ni^{2+}, Co^{2+}) have more than 5d electrons, the magnetic moments are aligned antiparallel between A and B sites. Since there are twice as many B- sites occupied as A-sites, the B-sites will dominate over the A-site resulting in ferrimagnetism [3.3].

Most of the spinel ferrites are inverse $\left(\frac{Fe^{3+}\downarrow}{A}\frac{[Me^{2+}\uparrow Fe^{3+}\uparrow]O_4}{B}\right)$ and the moment of the compound is the moment of Me^{2+}. Magnetic anisotropy refers to the dependence of the internal energy on the direction of magnetization. That is the spins of the magnetic ions are not free to rotate but are bound to a specific crystallographic direction. The source of this magnetic anisotropy is the interaction of magnetic ions with electrostatic fields generated by the first nearest neighbors of oxygens. These anisotropies of common origin are called magnetocrystalline, magnetostriction and induced. The total anisotropy of a material can be determined using the single ion model [3.3], namely the weighted sums of the anisotropies of the individual ions. The ions that play a major role in all magnetic properties of technical ferrites are Co^{2+} and Fe^{2+}. The effects of these ions are great because the orbital angular momentum in octahedral sites is not fully quenched by the crystal field.

Spinel ferrites used in practical applications are mixed ferrites of the type $(M_A+M_B)_{1+x}Fe_{2+x}O_4$; where there are two or more metals besides iron and where x varies between -0.3 to 0.3. It is considered to be stoichimetry from a formula standpoint when x = 0 (or Fe_2O_3= 50 mol%). In contrast to this formula stoichiometry, there exists an atomic stoichiometry where there are exactly 3 metal atoms for every 4 oxygen atoms.

3.2 Chemistry of soft ferrites:

Nearly all ferrites of the spinel type decompose if one tries to melt them under normal conditions (in air or at 1 atm. oxygen pressure). This is because the oxygen splits off at higher temperatures, reducing Fe^{3+} to Fe^{2+}. For example, in the case of stoichiometric spinel,

$$MeFe_2O_4 \text{ (spinel)} \longrightarrow (Me, Fe)O \text{ (wustite)} + O_2\uparrow$$

The oxygen equilibrium pressures of different iron oxides Fe_2O_3 (hematite), Fe_3O_4 (magnetite) and FeO (wustite) as a function of temperature are shown in Fig. 3.4 in terms of the logarithmic ratio $pco_2/\ pco$, which corresponds to the oxygen partial pressure according to $po_2 = K(pco_2/\ pco)^2$.

In the presence of spinels the dissociation temperature of Fe_2O_3 is considerably decreased as the Fe_2O_3 dissolves into $MeFe_2O_4$ under formation of Fe^{2+} ions and cation vacancies. In Fig. 3.5 the change of temperature is represented for the complete

dissociation of excessive Fe_2O_3 in air in the system (Ni, Zn) Fe_2O_4-Fe_2O_3 to a stoichiometric spinel, i.e. a spinel with a cation-anion ratio of 3:4. As can be seen from the figure, the temperature for the complete dissociation of small amounts of Fe_2O_3 in Ni-Zn ferrite is lower by more than 500°C than in pure Fe_2O_3.

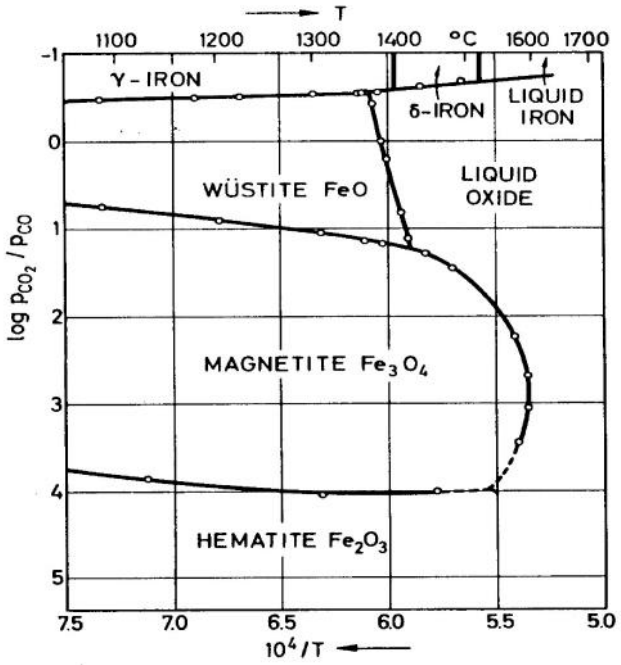

Fig.3.4. Oxygen equilibrium pressures of different iron oxides as a function of temperature.

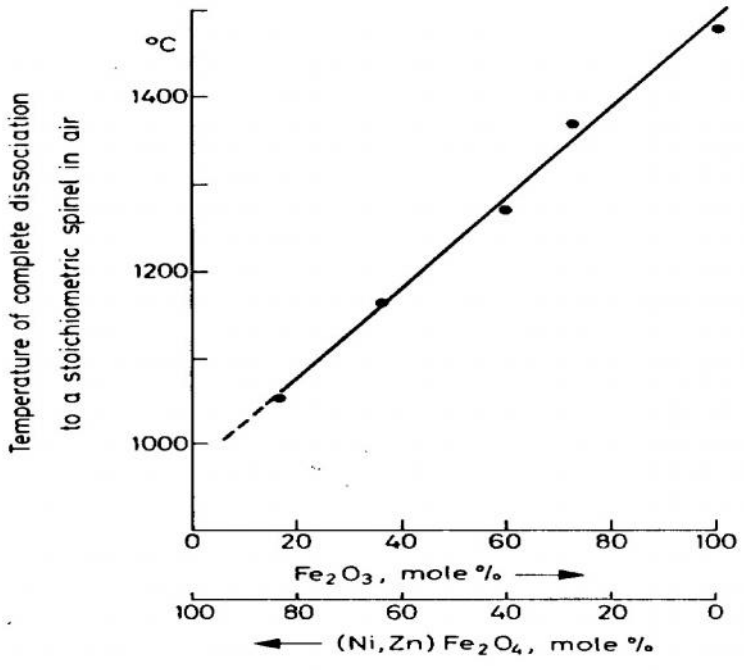

Fig.3.5. Temperature of complete dissociation of excessive Fe_2O_3 in air.

This implies that the ferrites cannot be processed to the desired shapes by melting, as is the case with metals. The normal technology of ferrite materials is thus a ceramic technology. The starting materials, mostly oxides or compounds (such as carbonates, oxalates or sulfates) which are easily convertible into oxides by thermal decomposition, are mixed and converted into the desired products by a solid state reaction at higher temperatures, between 800° and 1400°C. These prefired powders are then pressed into the desired shapes and densified without melting by a sintering process at the elevated temperature. This densification may reach the theoretical x-ray density under proper experimental conditions. When the oxides are taken as starting materials, the reaction must be considered:

Spinel: $Me^{2+}O+Fe_2O_3 \longrightarrow Me^{2+}Fe_2O_4$

The reaction for the formation of spinel has been found to be the simplest. In fact the spinel $MgAl_2O_4$ has been chosen as one of the first models for the precise study of solid-state reactions.

The reactions $MgO+Al_2O_3 \longrightarrow MgAl_2O_4$ and $MgO+Fe_2O_3 \longrightarrow MgFe_2O_4$ are, however, quite dissimilar. In the case of iron the relatively easy valency change of Fe^{3+} to Fe^{2+} and the strong influence of gas atmosphere associated with it complicates the issue, but this does not affect the fundamental consideration.

It is fully confirmed experimentally [3.4] that the spinel phase $Me^{2+}Me_2{}^{3+}O_4$ is formed at the interface of $Me^{2+}O$ and $Me_2{}^{3+}O_3$. The reaction proceeds by counterdiffusion of the cations $Me^{2+}$and Me^{3+} in the ration 3:2 through a practically rigid lattice of oxygen anions as shown in Fig 3.6(a). By providing the interface with markers, the spinel should have formed on either side of the markers in the ratio 1:3. The markers should undergo no shift during the reaction. The ratio 1:3 is found for $MgAl_2O_4$, and the ratio 1:2.7 for $MgFe_2O_4$ [3.5]. In the case of this counterdiffusion process the speed of formation is determined by the slowest- diffusing ion. The separation of volume diffusion, grain boundary, and surface diffusion presents difficulties in the case of polycrystalline samples, at least at lower temperatures. Moreover, the corresponding thermodynamic variables have not always been definitely fixed. In particular, the strong influence of the vacancy concentration on the diffusion coefficient must be considered [3.6]. Diffussion through a solid is possible only by means of ion displacement. Point defects (vacancies and interstitials) play an important part and are formed by dissolution of reactants into the

reaction layer. The vacancy concentration gradient is determined solely by solubility, temperature and oxygen partial pressure.

As mentioned earlier, spinel-ferrite formation may be complicated by the valency change of the iron ions. As in the case of the $MgFe_2O_4$ formation, that Fe_2O_3 at the $MgFe_2O_4$-Fe_2O_3 phase boundary dissolves into the spinel phase without any loss of oxygen; i.e. the iron remain in the trivalent state. However, from data on the phase diagram of the system MgO-FeO-Fe_2O_3 it apparent that this is not the case. The dissolution of Fe_2O_3 into the spinel is accompanied by loss of oxygen. If one assumes a counterdiffusion model with Mg^{2+} and Fe^{2+} diffusing instead of Mg^{2+} and Fe^{3+} and with oxygen transport through the gas phase, the volume ratio of the $MgFe_2O_4$ phase formed on both sides of the markers should be 1:2, and there should be a small displacement of the markers as shown in Fig 3.6(b). This effect has the important consequence that the reaction becomes dependent on the oxygen partial pressure. Reducing conditions will increase the reaction rate, because larger concentration gradients are set up over the reaction layer and more Fe_2O_3 can dissolve into the spinel phase [3.7].

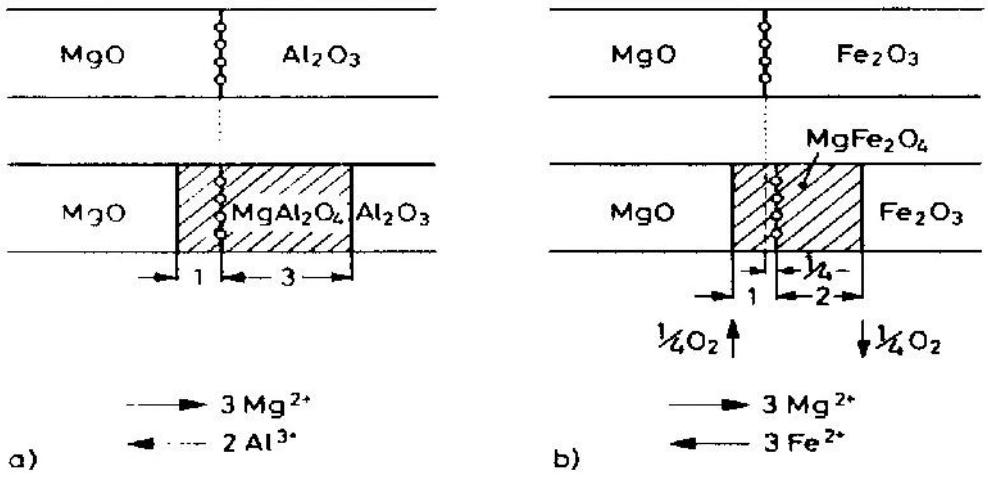

Fig. 3.6. Formation by counterdiffusion . (a) formation of $MgAl_2O_4$: counterdiffusion of Mg^{2+} and Al^{3+} cations, no anion diffusion (Wagner mechanism); no marker displacement.(b) Formation of $MgFe_2O_4$: counterdiffusion of Mg^{2+} and Fe^{2+} cations, no O^{2-} anion diffusion but reduction and oxidation of Fe ions at respective phase boundaries, which is equivalent to an oxygen transport through the gas phase; marker displacement.

From the results of the phase investigation [3.8] it has been concluded that part of the diffusing iron is in the form of ferrous ions, and that the ratio of the spinel phase formed on both sides of the markers must therefore lie between 1:2 and 1.3, depending on the oxygen partial pressure and the temperature. The interpretation [3.9] of these considerations is: a mixture of MgO and Fe_2O_3 powder loses oxygen when the temperature is raised. The oxygen loss reaches a maximum, and thereafter the weight of the sample regains almost its original value. During a second firing period, however the oxygen loss is considerably lower, especially when the reaction product is thoroughly powdered and mixed after the first run. The explanation given [3.7-3.8] is that during the reaction some of the ferric ions are reduced to ferrous ion on the dissolution of α-Fe_2O_3 in the already formed spinel phase. The corresponding evaluation of oxygen is measured as a weight loss of the sample. When the reaction is completed, all iron ions are again in the trivalent state, and the sample will again have its original weight. However, if the ingredient oxides have been poorly mixed, no homogeneous spinel is obtained, and the sample will show some weight loss even after prolonged heating. During cooling this nonhomogeneous sample will regain its original weight, but it will lose oxygen again when it is heated. Only by powdering the mixture between two successive firing periods can the reaction be completed. The same phenomenon occurs during the formation of $NiFe_2O_4$ by heating a mixture of NiO and Fe_2O_3 powders [3.10]. The explanation is undoubtedly the same as for the case of $MgFe_2O_4$.

It is to be expected that the reaction rates of solid-state reactions depend on the morphology of the initial substances. $NiFe_2O_4$ was chosen as an example for an investigation of the formation of the ferrimagnetic spinel phase by different methods [3.11-3.13]. The methods applied on the investigation (thermal, electric, magnetic and x-ray diffraction) show that the beginning of $NiFe_2O_4$ formation occurs at 600 to 780°C. Complete formation of $NiFe_2O_4$ is achieved at 1100° to 1200°C.

For various spinel ferrites a large number of different, often conflicting, mechanisms have been used to describe the kinetics [3.13-3.14]. Moreover, there often is a difference between the behavior at “low” (600° to 1000°C) and “high” temperatures (above 1000°C) and the gas atmosphere will influence the reaction rate.

3.3 Magnetic properties

Although all the magnetic properties of soft magnetic materials are dependent upon composition and temperature, but not all are sensitive to the metallurgical conditions of the materials. Metallurgical conditions mean: (i) the size, shape and orientation of grains; (ii) the concentration and distribution of various crystal imperfections and (iii) the state of the lattice regarding impurities, residual stresses and the atomic arrangement in alloys. Accordingly, the magnetic properties are divided into two groups: intrinsic or structure-insensitive and extrinsic or structure-sensitive.

Saturation magnetization and the Curie temperature are the two prominent structure-insensitive properties. Structure-sensitive properties on the other hand, are numerous and may be classified further as static or dynamic, according to whether or not the property displays a frequency dependence. Induction, permeabilities, hysteresis loop and associated energy loss, coercive force and remanence are structure sensitive, static properties. Eddy-current loss and resonance of spin and domain walls typify structure-sensitive, dynamic properties.

The maximum attainable intensity of magnetization per unit volume is termed the saturation magnetization of a ferromagnetic materials. This quantity is denoted by $M_s(T)$, signifying that it varies as a function of temperature. As $T \rightarrow 0°K$, $M_s(T) \rightarrow M_o$, which is called the absolute saturation magnetization. For each material, M_o is the largest value of M_s, because rising temperature generally exerts a decreasing effect on M_s. When the value of Ms is stated, it is necessary to specify the temperature, otherwise the statement is incomplete. This is particularly true in the temperature range above $0.8\theta c$ ($\theta c \rightarrow$ critical temperature), where the decreasing effect of temperature on M_s becomes severe.

All ferromagnetic material exhibit a characteristic temperature known as the Curie point, θc. This is the critical temperature at which thermal energy is just enough to destroy the spontaneous magnetization. Thus, the Curie temperature marks the transition point at which a ferrromagnet is converted into a paramagnet upon heating. Recent studies reveal that ferromagnetic and ferrimagnetic materials display singularities in their thermodynamic behavior in the vicinity of θc knows as the critical phenomenon.

For paramagnetics and diamagnetics susceptibility, the ratio of M to H is quite useful. However, in ferromagnetic and ferrimagnetics, the total flux density, B is used to define a very important parameter, μ, the magnetic permeability which is the ratio of B to

magnetizing field, H. However this parameter is measured under different sets of condition. If the magnetizing field is very low, approaching zero, the ratio will be called the initial permeability μ_i. Its definition is given by:

$$\mu_i = \lim_{B \to 0} (B/H)$$

This parameter is very important in telecommunication applications where very low drive signal levels are involved.

3.3.1 Saturation magnetization and Curie temperature

The saturation magnetization at absolute zero of a ferrimagnetic oxide is given by the composition and the ion distribution over the various lattice sites. In a spinel ferrite the principal exchange interaction aligns the moments of ions on A-sites antiparallel to those on the B-sites. If the ions on B-sites are denoted by square brackets, an inverse spinel would be:

$$Fe^{3+}\downarrow[Me^{2+}\uparrow Fe^{3+}\uparrow]O_4$$

The net moment per formula unit is then equal to the moment of the Me^{2+} ion.

The simple spinels Fe_3O_4, $CoFe_2O_4$, $NiFe_2O_4$, $CuFe_2O_4$ and $MgFe_2O_4$ are mainly inverse and the spin moments of divalent ions Fe, Co, Ni, Cu, and Mg are respectively, 4, 3, 2, 1 and 0 μ_B. From measurements of the saturation magnetization near 0°K, the number n_B of Bohr magnetons per formula unit can be calculated. The experimental values of n_B in the same sequence are 4.1, 3.7, 2.3, 1.3 and 1.2, values respectively. The higher-than–theoretical values of n_B for $CoFe_2O_4$ and $NiFe_2O_4$ can be ascribed to the orbital moment of the Co and Ni ions, which adds to the spin moment, and to a contribution because these spinels are not completely inverse [3.15-3.16]. This second factor also explains the discrepancies found with $CuFe_2O_4$ and $MgFe_2O_4$. For example, the distribution in $MgFe_2O_4$ can be written as:

$$Fe^{3+}_{1-\delta}\downarrow Mg^{2+}_{\delta}\downarrow\left[Mg^{2+}_{1-\delta}\uparrow Fe^{3+}_{1+\delta}\uparrow\right]O_4$$

It is found $n_B = 5[(1+\delta)-(1-\delta)] = 10\delta$ with the known moment of 5 μ_B for the Fe^{3+} ion. In accordance with this relation, $MgFe_2O_4$ has been found to be 10 to 20% normal ($0.1 < \delta < 0.2$) depending on the preparation conditions. In $Mn^{2+}Fe_2{}^{3+}O_4$ it is expected $n_B = 5$

independently of the ions distribution, because both Mn^{2+} and Fe^{3+} have the moment 5 μ_B. Experimentally, n_B= 4.6 is found.

A normal spinel is Zn $[Fe_2]O_4$. Because Zn^{2+} is diamagnetic, there is no exchange between A and B-sites. In this case only the mutual interaction between the ions on B-sites becomes manifest. This interaction is much weaker than the AB interaction, but also negative. Therefore the spins of Fe^{3+} are oriented antiparallel, so that $ZnFe_2O_4$ is antiferromagnetic.

The substitution of $ZnFe_2O_4$ in other ferrites, however, gives rise to an increase of the low temperature saturation magnetization. For example, in $Ni_{1-\delta}Zn_\delta Fe_2O_4$ the ion distribution is:

$$Zn_\delta^{2+} Fe_{1-\delta}^{3+} \downarrow \left[Ni_{1-\delta}^{2+} \uparrow Fe_{1+\delta}^{3+} \uparrow\right] O_4$$

With δ below about 0.4, the AB interaction dominates the BB interaction, so that for these compositions

$$N_B \approx (1-\delta\ )n_B,\ Ni^{+2\delta}n_B,\ Fe = 2.3+7.7\delta.$$

The Curie temperature, however, decreases with δ because the strength of the interaction per molecule decreases owing to the increase of the diamagnetic Zn^{2+} content. The increase of the magnetization with δ at room temperature is therefore less than at absolute zero. This is illustrated in Fig. 3.7 and 3.8, where the saturation magnetization σ(Gauss-cm^3/g) is shown as a function of temperature T, with δ as parameter, for a number of ferrites $Mn_{1-\delta}\ Zn_\delta Fe_2O_4$ and $Ni_{1-\delta}\ Zn_\delta Fe_2O_4$ respectively.

The relation between σ and n_B is

$$\sigma = \frac{\mu_B N_A}{M_{mol}} n_B = \frac{5585}{M_{mol}} n_B$$

where N_A is the Avogadro's number and M_{mol} is the molecular weight of the ferrite, which ranges in spinel ferrites from about 200 to 240. The magnetization 4 πM_s of a material with a given porosity p is related σ by

$$4\ \pi M_s = 4\ \pi(1-p)d_x\ \sigma$$

where d_x is the x-ray density of the material. In spinel ferrites d_x ranges from 4.6 to 5.4, depending on the composition.

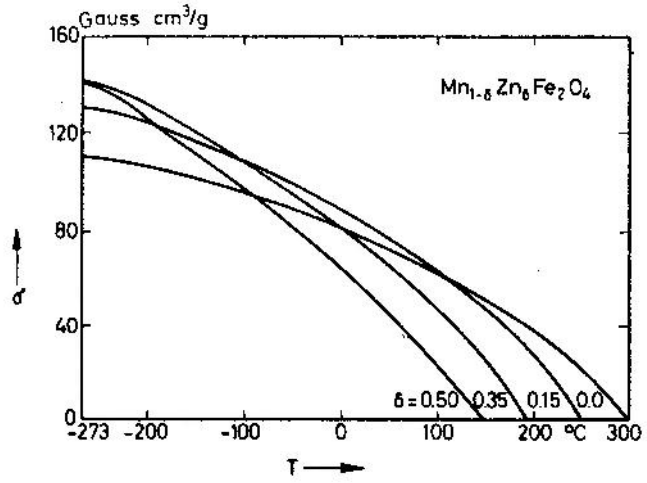

Fig.3.7. Saturation magnetization as a function of temperature for some ferrites $Mn_{1-\delta}\ Zn_{\delta}Fe_2O_4$.

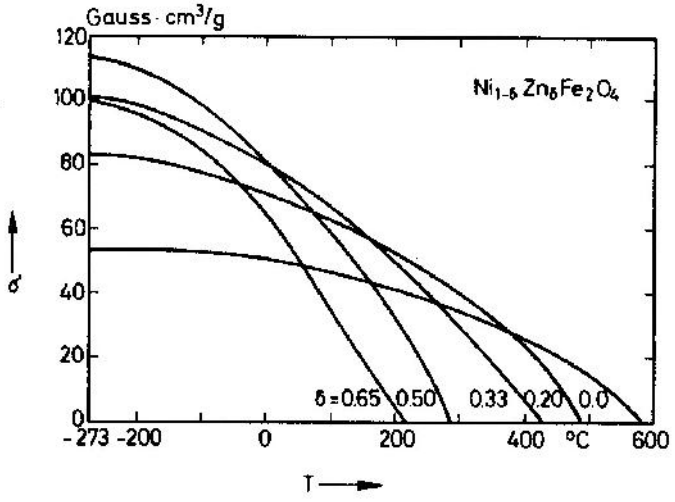

Fig.3.8. Saturation magnetization as a function of temperature for some ferrites $Ni_{1-\delta}\ Zn_{\delta}Fe_2O_4$.

It can be seen in Fig. 3.7 that at room temperature the saturation magnetization of Mn-Zn ferrites does not increase significantly with the Zn content. This is because of the decrease in the Curie temperatures. In Ni-Zn ferrites, however as shown in Fig. 3.8, and increase of more than 50% in comparison with $NiFe_2O_4$ is obtained with δ between 0.33 and 0.50.

The saturation magnetization at absolute zero and at room temperature and the Curie temperature of some simple ferrites are summarized in Table 3.4.

Table 3.4 Saturation magnetization values σ, M_s, and $4\pi M_s$, and Curie points T_c of some simple spinel ferrites.

0°K				20°C			
Ferrite	σ (gauss-cm^3/g)	M_s (gauss)	$4\pi M_s$ (gauss)	σ (gauss-cm3/g)	M_s (gauss)	$4\pi M_s$ (gauss)	T_C (°C)
$MnFe_2O_4$	112	560	7000	80	400	5000	300
$FeFe_2O_4$	98	510	6400	92	480	6000	585
$CoFe_2O_4$	90	475	6000	80	425	5300	520
$NiFe_2O_4$	56	300	3800	50	270	3400	585
$CuFe_2O_4$	30	160	2000	25	135	1700	455
$MgFe_2O_4$	31	140	1800	27	120	1500	440
$Li_{0.5}Fe_{2.5}O_4$	69	330	4200	65	310	3900	600

3.3 2 Initial permeability

For high frequency applications, the desirable property of a ferrite is the high initial permeability with low loss. The present goal of the most of the recent ferrite researches is to fulfill this requirement. The initial permeability μ_i is defined as the derivative of induction B with respect to the initial field H in the demagnetization state.

$$\mu_i = \frac{dB}{dH} \qquad H \rightarrow 0,\ B \rightarrow 0 \qquad (3.1)$$

At microwave frequency, and also in low anisotropic amorphous materials, dB and dH may be in different directions, the permeability thus a tensor character. In the case of amorphous materials containing a large number of randomly oriented magnetic atoms the permeability will be scalar. As we have

$$B = \mu_0(H+M) \qquad (3.2)$$

and susceptibility,

$$\chi = \frac{dH}{dH} = \frac{d}{dH}\left[\frac{B}{\mu_0} - H\right] = \frac{1}{\mu_0}(\mu - 1) \qquad (3.3)$$

The magnetic energy density

$$E = \frac{1}{\mu_0}\int H.dB \qquad (3.4)$$

For time dependent harmonic fields H= H_0 sin ωt, the dissipation can be described by a phase difference δ between H and B. In the case of permeability, defined as the proportional constant between the magnetic field induction B and applied intensity H;

$$B= \mu H \qquad (3.5)$$

If a magnetic material is subjected to an ac magnetic field, we get

$$B = B_0 e^{i\omega t} \qquad (3.6)$$

Then it is observed that the magnetic flux density B experiences a delay. The delay is caused due to presence of various losses and is thus expressed as

$$B = B_0 e^{i(\omega t - \delta)} \qquad (3.7)$$

where δ is the phase angle and marks the delay of B with respect to H. The permeability is then given by

$$\mu = \frac{B}{H}$$

$$= \frac{B_0 e^{i(\omega t-\delta)}}{H_0 e^{i\omega t}}$$

$$= \frac{B_0 e^{-i\delta}}{H_0}$$

$$= \frac{B_0}{H_0}\cos\delta - i\frac{B_0}{H_0}\sin\delta$$

$$\text{i.e., } \mu=\mu'-i\mu'' \qquad (3.8)$$

$$\text{where} \qquad \mu' = \frac{B_0}{H_0}\cos\delta \qquad (3.9)$$

$$\text{and } \mu''= \frac{B_0}{H_0}\sin\delta \qquad (3.10)$$

The real part μ′ of complex permeability μ' as expressed in equation 3.9 represent the component of B which is in phase with H, so it corresponds to the normal permeability. If there is no losses, we should have μ = μ'. The imaginary part μ" corresponds to the part of B which is delayed by phase angle arranging up to 90° from H. The presence of such a component requires a supply of energy to maintain the alternating magnetization, regardless of the origin of delay. It is useful to introduce the loss factor or loss tangent (tanδ). The ratio of μ" to μ', as is evident from equation gives

$$\frac{\mu'}{\mu''} = \frac{\frac{B_0}{H_0}\sin\delta}{\frac{B_0}{H_0}\cos\delta} = \tan\delta \qquad (3.11)$$

This tan δ is called the loss Factor or loss tangent. The Q-Factor or quality factor is defined as the reciprocal of this loss factor, i.e.

$$Q = \frac{1}{\tan\delta} \qquad (3.12)$$

The behavior of μ′ and μ′′ versus frequency is called the complex permeability spectrum. The initial permeability of a ferromagnetic substance is the combined effect of the permeability and rotational permeability mechanism. The complex permeability μ′ of the toroid shaped samples at room temperature can be calculated by the equation:

$$\mu_i = \frac{L}{L_0} \qquad (3.13)$$

Where L is the measured sample inductance and L_0 is the inductance of the coil of same geometric shape of vacuum. L_0 is determined by using the relation,

$$L_0 = \mu_0 N^2 A/l \qquad (3.14)$$

Here, μ_0 is the permeability of the vacuum, A is the cross sectional area of the core, N is the number of turns of wire and l is the average path length around the toroid usually taken to be $l = 2\pi(r_1+r_2)/2$, where, r_1 and r_2 are inner and outer radius of the toroid.

3.4 Electrical properties

Electrically, ferrites can be classified as somewhere between semiconductors and insulators. The technical importance of ferrites lies primarily in their high resistivity. Whereas in the metallic ferromagnetic materials the resistivity can not be made higher than about 10^{-4} ohm-cm, technical ferrites have, depending on their applications, resistivities of 1 to 10^{12} ohm-cm. In magnetic materials a low resistivity gives rise to eddy currents, and hence to joule losses. All other properties being equal, these losses are proportional to D^2f/ρ, where D is the thickness of the massive core material, f is the frequency of the ac field, and ρ is the resistivity of the core materials [3.19]. Even at 50 Hz, iron cores must be divided into isolate sheets of about 1 mm thickness to avoid large losses. In a massive ferrite core 1 cm thick of 10 ohm-cm resistivity similar eddy current losses would not occur below 600 kHz; a ferrite core of 10^{10} ohm-cm resistivity would not

show such losses below 6×10^{11} kHz, the frequency of visible light. It is clear, then that the use of massive ferrite cores effects considerable savings in magnetic components.

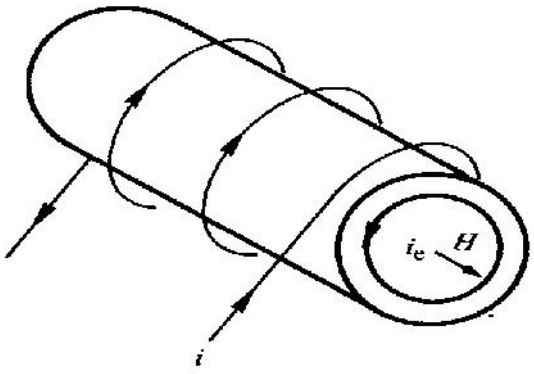

Fig. 3.9. Eddy currents. The variations in current i produced a varying field, H; an emf is generated, resulting in eddy currents, i_e. The intensity of the emf depends on the specimen magnetic permeability.

Eddy currents appear as a consequence of Faraday's law of electro-magnetic induction. Consider a cylindrical sample of material, Fig. 3.9. As the current flows in the coil, an ac magnetic field is applied to the material, depending on its permeability, an ac magnetization follows the field. As a result of the magnetic flux variations within the sample, a voltage is generated, given by: emf= $-d\phi/dt = -A\ dB/dt$ where emf is the voltage, ϕ is the magnetic flux, A is the area normal to the flux and B is the induction. This law is varied for any kind of materials, regardless of whether it is magnetic or not. In a non–magnetic material (diamagnetic, paramagnetic, antiferromagnetic), flux variations correspond practically to the magnetic field produced by the coil ($B= \mu_0 H$). In a ferro- or ferrimagnetic material, induction is dramatically greater because in these materials permeability can be 10^4 times that of vacuum. The voltage generated is therefore 10^4 times greater. In metals, there are many conduction electrons which can be excited by these voltage variations; in oxides, electron localization severely limits this process.

The main conductivity mechanism in ferrites is attributed to electron hopping between Fe^{3+} and Fe^{2+} in octahedral sites. Resistivity in spinel ferrites is very sensitive to stoichiometry; a small variation of Fe content in $Ni_{0.3}Zn_{0.7}Fe_{2+\delta}O_{4-\varepsilon}$ [3.20] results in resistivity variations of $\sim 10^7$, as shown in Fig. 3.10. Excess Fe can easily be dissolved in

the spinel phase by a partial reduction of Fe from $3Fe_2^{3+}O_3$ to $2Fe_2^{3+}O_4$. A negative δ value maintains all Fe as Fe^{3+} and tends to produce some oxygen (O) vacancies. However, since this last process requires considerable energy, it is very likely that the O vacancy concentration remains quite low and the divalent cation excess appears as a second phase. During sintering of stoichiometric mixtures at high temperatures (T > 1200°C), there is always the tendency to lose some O_2 with the corresponding reduction in Fe, even in an oxidizing atmosphere. In Mn-Zn ferrites, an O_2 atmosphere cannot be used because Mn is oxidized to Mn^{3+} producing cation vacancies and a decrease in resistivity.

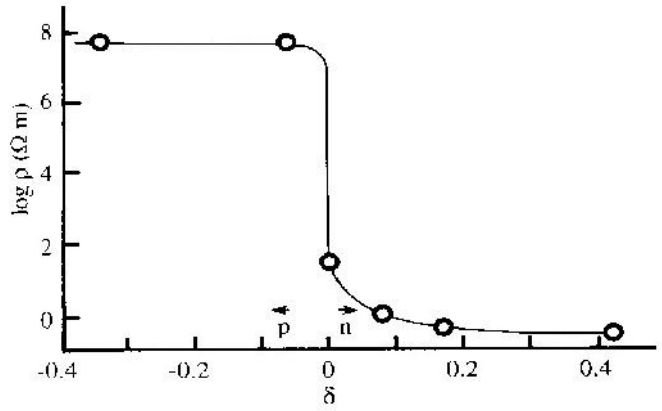

Fig.3.10. Effect of Fe content, δ , on the electrical conductivity of Ni-Zn ferrites.

In polycrystalline ferrites, grain boundaries can also have an influence on eddy current losses. In high permeability Mn-Zn ferrites, for instance, CaO and SiO_2 are used as additives to decrease Fe^{2+} content and increase the grain boundary resistivity [3.21], both processes limit eddy-current losses.

References:

[3.1] B. D. Culity, "Introduction to Magnetic Materials", Addison Wesley Pub.Comp. InC., 186 (1972).

[3.2] J. D. Dunity and L. E. Orgel, J. Phys. Chem. Solids, **3**, 318 (1957).

[3.3] L. Neel, Annales de Physique, **3** , 137 (1948).

[3.4] C. Wagner, Z. Phys. Chem., **B 34**, 309 (1936).

[3.5] R. E. Carter, J. Am. Ceram. SOC. , **44**, 116 (1961).

[3.6] S. Ogawa and Y. Nakagawa, J. Phys. Soc. Japan, **23**, 179 (1967).

[3.7] P. Reijnen, "Science of Ceramics", vol. 3, Academic Press, N. Y. 245 (1967).

[3.8] P. Reijnen, Fifth Intern. Symp. Reactivity Solids, Manich, Elsevier, Amsterdam, 562 (1965).

[3.9] L.C.F. Blackman, J. Am. Ceram. SOC. **42**, 143 (1959).

[3.10] D. Elwell, R. Parker, and C. J. Tinsley, Solid State Comm.,**4**, 69 (1966).

[3.11] J. Beretka, A. J. Marriage, Nature, **203**, 515 (1965).

[3.12] F. Solymosi, Z. G. Szabo, J. Chem. SOC. (London), 2745 (1961).

[3.13] S. L. Blum, P. C. Li, J. Am. Ceram. SOC; **44**, 611 (1961).

[3.14] J. F. Duncan, D. J. Stewart, Trans. Faraday SOC., **63**, 1031 (1967).

[3.15] U. Eng, J. Liebertz, Naturwiss, (German), **51**, 1 (1964).

[3.16] G. A. Sawatzky, F. Vander Woude, A. H. Morrish, J. Appl. Phys, **39**, 1204 (1968).

[3.17] A. Globus, P. Duplex, IEEE Trans. **MAG. 2 (3)**, 441 (1966).

[3.18] J. L. Snoek, Physica, **14**, 207 (1948).

[3.19] J. Smit, Magnetic Properties of Materials, McGraw Hill, 64, (1971)

[3.20] L. G. Van Uitert, proc. of IRE, **44**, 1294 (1956).

[3.21] M. H. Berger, J. Y. Laval, J. Y. Kools, and J. Roelofsma, "In Advances in Ferrites: Proc. 5th con. on Ferrites", **vol. 1**, 619 [1989].

Chapter Four

Preparation of Low Frequency Ferrite Core Materials

Polycrystalline ferrites are prepared normally by powder metallurgy or ceramic technology. This means that ferrites attain their homogeneous composition by reaction in the solid state and shape of the ferrite products are produced by the pressing and subsequent sintering. In particular the properties of ferrites depend on the sintered density. During sintering the oxides react to form crystallites of the required composition, these crystallites nucleating at discrete centres and growing outwards until the boundaries meet those of neighboring crystallites. During this process the density of the mass rises; if this process were to yield perfect crystals meeting at perfect boundaries the density would rise to the theoretical maximum i.e. the x-ray density, which is the mass of material in a perfect unit crystal cell divided by the cell volume. In practice imperfections occur and the sintered mass has microscopic voids both within the crystallites and at the crystallite boundaries.

The preparation procedure of polycrystalline ferrites is shown in a flow diagram of Fig. 4.1. This diagram shows alternative processes wet and dry milling, and forming of final shapes by pressing or extrusion. The raw materials are normally oxides or carbonates of the constituent metals. Purity and particle size of starting materials are important characteristics for ferrite preparation. Because minor constituents or impurities may have a great influence on the properties of the finished product. Particle size of the starting material has a profound effect on the behavior of the product. The ease of mixing, the shrinkage and the reactivity all depend on the particle size so it is normal to keep a check on the parameter to ensure quality of the ferrite. In mixed ferrites there are three or more different metal ions and this gives a wide range of possible relations. The various steps of the preparation procedure of polycrystalline ferrites are summarized in this chapter.

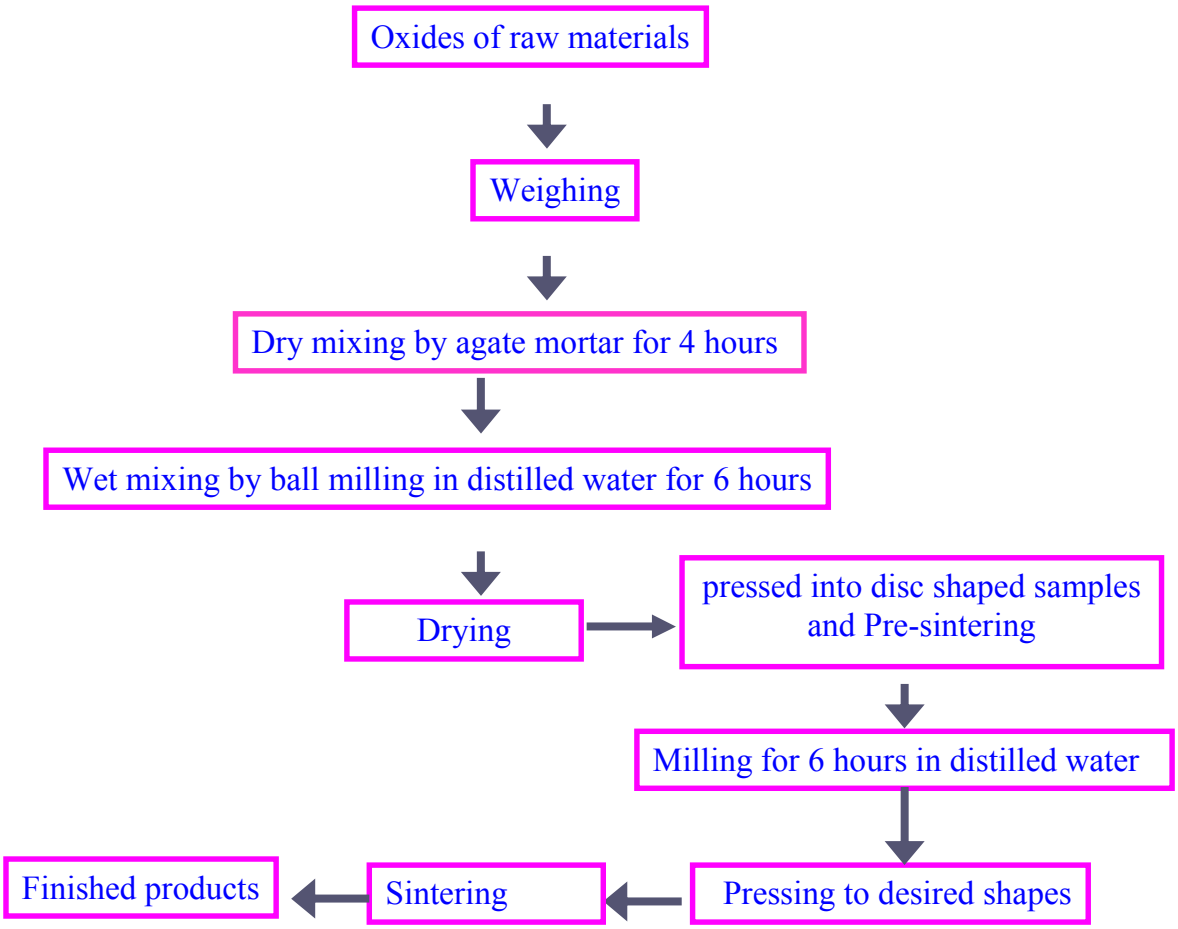

Fig. 4.1. Flow chart of ferrite sample preparation.

4.1 Mixing

The main purpose of this process is to convert all the starting materials into a thoroughly homogeneous mixture. If crystallites of uniform composition and properties are subsequently to be formed then the constituents must be present in the correct proportions in any microscopic volume of the bulk material. It is difficult to avoid unmixing i.e. one or more constituents becoming slightly more concentrated in certain regions of the mass, by virtue of the particle size or density. This may be due to agitation during mixing or in the wet process, due to sedimentation or selective filtration.

The mixing may be carried out dry or the constituents may have water added to form a slurry which may be stirred with a turbine blade. Another method is wet ball

milling. The constituents are placed in a rotating steel lined drum with steel balls and a medium such as distilled water. Steel is used because any iron picked up by the mixture due to wear of the lining and balls may be allowed for in the initial composition of the powder. Particle size reduction is not a primary aim of this process and is not usually very great. After wet mixing the product is poured off as a slurry into a filter pass where the water is squeezed out. The resulting blocks are then dried in an oven. In the dry process the powder has to be loosely pressed into blocks ready for presintering. The pressing into blocks makes the product easier to manage in the furnace and improves the thermal reactivity.

4.2 Presintering

The pressed blocks are transferred to a ceramic plate (temperature tolerance 1300°C) for prefiring at temperatures 1000°C. During this process the constituents partially react to form ferrite i.e. spinel ferrite begin to form. Swallow and Jordan [4.1] state that presintering is carried out also for the following reasons:

(i) It decomposes the carbonates or higher oxides, thereby reducing the evolution of gases in the final sintering.
(ii) It assists in homogenizing the material.
(iii) It reduces the effects of variations in the raw materials.
(iv) It reduces or controls the shrinkage occurring during the final sintering stage.

The solid-state reactions leading to the formation of a ferrite actually are achieved by counter diffusion. This means that the diffusion involves two or more species of ions which move in opposite directions, initially across the interface of two contacting particles of different component oxides. Several workers [4.1-4.2] made careful studies of the position of inert markers in diffusion couples and concluded that the counter diffusion essentially involves the movement of cations through a more or less rigid lattice of oxygen anions. Another important observation in the prefring step deals with the critical temperature below which the formation of ferrites would not be completed regardless of the length of prefiring time.

4.3 Processing the raw ferrite and forming

The raw ferrite produced in the previous step is usually in lump form, are crushed for milling. The crushed powder is milled to reduce it to small, uniformly sized crystallite.

The process is carried out in a wet ball mill or vibrating ball mill. In either case steel balls are normally used to avoid contamination. Since the extent of the milling depends on milling efficiency as well as the milling time it is preferable to mill to a certain particle size rather than a certain time. After wet milling, the slurry is drawn off and the bulk of the liquid is removed by a pressure filter. The filtered material is then oven-dried and powdered, the dry-milled powder does not, of course, required this treatment. At this stage it is usual to add the binder and lubricants. The choice of these additives depends on the subsequent granulation process, the method of forming (pressing or extrusion), the required strength of the formed piece part before firing and the avoidance of undesirable residues after burning out during sintering. Commonly used binders are gum arabic, ammonium alginate, acrylates, polyvinyl alcohol, or polyethylene glycol. These also may serve as lubricants to ease powder flow during forming.

Forming method is dry-pressing or extrusion. Normally the main purpose of this operation is to form the powder into a shape which is as near as possible to the final shape required. Another, equally important purpose of forming is to force the crystallites into close proximity so that, during sintering, they may grow to form a dense material, i.e. one having a low porosity. This is done either by die-punch assembly or by hydrostatic or isostatic compaction. Dry pressing is the simplest form. This process consists of pouring the correct quantity of granulated powder into the die and then closing the die with a prescribed pressure which is usually in the range of 400 to 4000 Kgm per square cm. In practice the flow properties of the powder must be taken into account and there-in lies the art of dry pressing. As the powder is compressed it builds up a friction between its outer surface and the adjacent die walls. Due to this friction and the viscosity of the powder, the pressure (and therefore the density) in the pressed powder is not uniform. Inhomogeneous pressed density leads to inhomogeneous magnetic properties and so degrades the product. It also leads to nonuniform shrinkage during the sintering and this causes shape distortion. The extrusion process is used mainly for rods and tubes. Such shapes cannot easily be dry pressed, because if the pressing were axial the length/diameter ratio would be too great whereas if they were pressed transversely the die punches would have feather edges. The extrusion process is very simple. The de-aerated charge of plasticized powder is placed in the cylinder of an extrusion machine. A ram then forces the charge through a suitable orifice to form a length of rod or tube.

4.4 Sintering

This is a heat treatment by which a mass of compacted powder is transformed into a dense object. As the final major step in the preparation of ferrite products, sintering must fulfill three requirements: (i) to bond the particles together so as to impart sufficient strength of the products; (ii) to densify the primary compacts by eliminating the pores and (iii) to homogenize the materials by completing the reactions left unfinished in the presintering step. The first two requirements are closely related as far as their mechanisms are concerned. For instance, as shown in Fig. 4.2, a simple way to bond two spherical particles is to form a neck at the contact by volume diffusion. The formation of necks is also a key process leading to the shrinkage of pores. Precisely how pores disappear during sintering has long been a subject of intensive investigation. The theory of Kuczynski [4.3] emphasizes the formation of necks as a key step in bonding the particles and in eliminating the pores and considers volume diffusion under surface tension as the main mechanisms of neck formation. Other processes such as plastic flow, surface or grain boundary diffusion and evaporation- condensation, could play important supporting roles. On the basis of volume diffusion induced under surface tension, an important equation for the initial stage of the sintering process is given by :

$$\Delta L/L=[\ (AD^*\gamma\ \Omega\ /\mathbf{r}^{-3}kT)\ t\ ]^{½} \qquad (4.1\ )$$

Where $\Delta L/L$ is the shrinkage of the compact, Ω the volume of a single vacancy, D* the coefficient of self-diffusion for the lowest moving species, γ the surface energy, **r** the average radius of the particles, t the sintering time and A a constant, of the approximate value of unity. Equation (4.1) indicates the sintering fulfills requirements (i) and (ii) more efficiently when the compact features high surface energy and self diffusivity and the particles are fine.

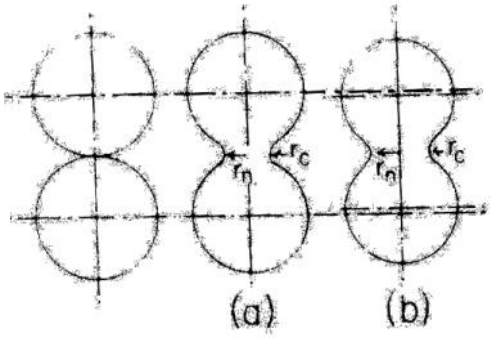

Fig. 4.2 Neck formation during sintering of spherical particles (a) when there is no overall shrinkage and (b) when shrinkage occurs.

For densification, Burke [4.4] made two important observations one is that the formation of necks only marks the initial stage of sintering; an alternative stage begins when grain growth occurs with the compact density at around 60% of the theoretical value and ends when the pore phase becomes discontinuous and the density reaches a value of ~ 95%. The other observation deals with the final stage of sintering. If discontinuous grain growth occurs after the intermediate stage, migration of grain boundaries will leave the remaining isolated pores trapped inside the grains, thus preventing further shrinkage of these interparticle pores and practically stopping the sintering process. On the other hand, if discontinuous grain growth is prohibited the last few percentages of porosity are eliminated by emitting vacancies at grain boundaries. Although only limited chemical reactions are expected during sintering in connection with requirement (iii) proper atmosphere should be provided to keep the correct stoichiometry of the ferrite produced in the presintering step intact.

4.5 Preparation of samples

4.5.1 Composition of ferrites

In the present research work a series of compositions of iron–defecient Ni-Zn and iron-excess Mn-Zn soft ferrites prepared from Fe_3O_4, a beach sand mineral with the addition of CuO,V_2O_5, Eu_2O_3, and In_2O_3 were studied.

Compositions of Ni-Zn ferrites are:

(i) $Ni_{0.65}Zn_{0.35}Fe_{1.96}O_4$+ x CuO [x=0,0.005,0.01,0.015,0.02, 0.025]

(ii) $Ni_{0.65}Zn_{0.35}Fe_{1.96}O_4$+ x V_2O_5 [x=0,0.002,0.004,0.006,0.008,0.01]

(iii) $Ni_{0.65}Zn_{0.35}Fe_{1.96}O_4$+ x Eu_2O_3 [x=0,0.005,0.01,0.015,0.020,0.025,0.030,0.035]

(iv) $Ni_{0.65}Zn_{0.35}Fe_{1.96}O_4$+ x In_2O_3 [x=0,0.005,0.01,0.015,0.020,0.025,0.030,0.035]

Compositions of Mn-Zn ferrites are:

(i) $Mn_{0.451}Zn_{0.484}Fe_{2.065}O_4$+ x CuO [x=0,0.01,0.02,0.03,0.04,0.05,0.06]

(ii) $Mn_{0.451}Zn_{0.484}Fe_{2.005}O_4$+ x V_2O_5 [x=0, 0.005,0.01,0.015,0.02,0.025,0.03]

(iii) $Mn_{0.451}Zn_{0.484}Fe_{2.065}O_4$+x Eu_2O_3 [x=0, .005,0.01,0.015,0.02,0.025,0.03,0.035,0.04]

(iv) $Mn_{0.451}Zn_{0.484}Fe_{2.065}O_4$ + x In_2O_3 [x=0, 0.005,0.01,0.015,0.02,0.025,0.03, 0.035]

4.5.2 Sample preparation technique

The preparation of polycrystalline ferrites with optimized properties has always demanded delicate handling and cautious approach in materials synthesis and appropriate knowledge of thermodynamics control of the chemical composition and homogeneity It is well known that almost all ferrites decompose at the elevated temperature if one wants to sinter them under normal conditions. This happens because the oxygen splits off at higher temperature reducing Fe^{3+} to Fe^{2+}. There are many processing methods such as solid state reaction method [4.5]; high energy ball milling [4.6]; Sol gel method [4.7]; chemical co-precipitation method [4.8]; microwave sintering method [4.9]; auto combustion method [4.10] etc for the preparation of polycrystalline ferrite materials.

The normal methods of preparation of ferrites comprise of the conventional ceramic method or solid state reaction method, chemical co-precipitation method and sol-gel method. In the present investigation solid state reaction method has been employed for the preparation of Ni-Zn and Mn-Zn ferrite samples for its relative simplicity and availability.

4.5.3 Method of preparation

A series of polycrystalline samples of mixed ferrites were prepared by the standard ceramic method at the Materials Science Division of Atomic Energy Centre, Dhaka. In this method commercial grade oxides (99.95%) of NiO, ZnO, $MnCO_3$, Eu_2O_3, CuO, V_2O_5, In_2O_3, and Fe_3O_4 (99.5% purity), a beach sand mineral collected from Cox's Bazar Pilot Plant were used for the preparation of samples.

Different ingredient oxides were weighed precisely according to their molecular weight. The weight percentage of the oxide to be mixed for various samples was calculated by using formula:

$$\text{Weight \% of oxide} = \frac{\text{M.wt. of oxide} \times \text{required weight of the sample}}{\text{Sum of Mol. wt. of each oxide in a sample}}$$

Intimate mixing of the materials was carried out using agate mortar for 4 hrs and then ball milled in a centrifugal ball mill in distilled water media for 6 hrs with stainless steel balls of different sizes and diameters. The wet milling for 6 hrs was done from two point of view, first the grain size of the starting components decreased and second the homogenization increased. After wet mixing the slurry was filtered, oven dried and

powdered. Then the powder materials was put in a die and pressed with little pressure to form big pellets from each composition for presintering. The pellets were transferred to a ceramic plate and presintered in air at temperature 1000°C in a muffle furnace for 3 hours for ferritization. In the presintering process for Mn-Zn ferrites the pellets were quenched in air soon after the presintering work. The quenching was done to avoid oxidation of Mn^{2+} to Mn^{3+} and formation of Mn_2O_3 other than ferrite compound.

The presintered pellets were crushed and put into wet milling for 6 hours to get a fine reactive powder for final densification. Before wet milling the additives such as CuO,V_2O_5, Eu_2O_3 and In_2O_3 were mixed thoroughly with nickel zinc and manganese zinc presintered and crushed materials using agate mortar for 4 hours. After 6 hours wet milling the fine powder materials were dried and then granulated by sieving with the help of polyvinyl alcohol solution as binder. Uniformity in granule size played a very important role for a good flow of materials to ensure dense compactness during the forming stage. The uniformly granules of powder was compacted into pellet and toroid shape samples by a die punch assembly under pressure of 1000 kg/cm^2 using hydraulic press. The prepared pellet and toroid samples were then sintered at 1250°C in a muffle furnace in air for three (3) hours. The rate of heating for sintering was around 200°C/hr. During the heating process the air pressure was kept relatively high, this was done to assist the burn out of the binder. As the maximum temperature was reduced gradually to a low value, the flow of air was continued during the cooling period to avoid as far as possible the loss of oxygen and the resulting formation of Fe^{2+} ions.

A series of Ni-Zn and Mn-Zn ferrite samples were prepared containing additives such as CuO, V_2O_5, Eu_2O_3 and In_2O_3 as mentioned earlier.

References:

4.1. Swallow, D. and Jordan, A. K. Proc. Br. Cream. Soc. **2,** 1 (1964).

4.2. Kooy, C. Fifth Int. Symp. Reactivity in Solids, **21**, Elsevier (1965).

4.3. Kuczynski, G. C., Powder Metallurgy, **vol. 11**, Interscience, N. Y. (1961).

4.4. Burke, J. E. Kinetics of High Temperature process, Wiley, N. Y. (1959).

4.5. L. B. Kong, Z. W. Li, G. Q. Lin and Y. B. Gan, J. Am. Ceramic Soc. **90(7)** , 2104, (2007).

4.6. S. K. Sharma, Ravi Kumar, Shalendra Kumar, M. Knobel, C. T. Meneses, V. V. Siva Kumar, V. R. Reddy, M. Sungh and C. G. Lee, J. Phys.: Condens Mater **20,** 235 (2008).

4.7. Soilah Zahi, Mansor Hashim and A. R. Daud, J. Magn. Magn. Mater. **308,** 177, (2007).

4.8. M. A. Hakim, D. K. Saha and A. K. M. Fazle Kibria, Bang. J. Magn. Mater. **283,** 57 (2007).

4.9. Bhaskar, B. Rajini Kanth and S.R. Murthy, J. Magn. Magn. Mater. **283,** 109 (2004).

4.10. Zhenxing Yue, Ji Zhou, Longtu Li, and Zhilun Gui, J. Magn. Magn. Mater. **233,** 224 (2001).

Chapter Five

Experimentals

The structural, magnetic and electrical properties of spinel ferrite samples were measured to ascertain their qualities. The surface of the sintered samples were polished with water proof silicon carbide paper disc of different grit fitted on a rotary disc of an universal polisher (Extec Corp., LABPOL 8/12). The polishing was necessary to get very accurate dimensions to calculate the volume of the samples. Sintered densities of the samples were calculated from the ratio of precision weight and the volume. Lattice constant values of the samples were calculated from X-ray diffraction pattern taken by X-ray Diffractometer (PW 3040-X'Pert PRO Philips) utilizing the respective sintered powders. Microphotograph of the samples were taken from polished and etched surface of the samples using Scanning Electron Microscope (S50 FEI Quanta Inspect).

The specific saturation magnetization of the samples were measured by using a Vibrating Sample Magnetometer (Model EV7 system). The Curie temperature were determined from the initial permeability versus temperature curve. Magnetic initial permeability spectra measurements were carried out using Hewlett Packard Impedance Analyzer (HP 4191A) in the frequency range of 1 kHz to 13 MHz. The dc electrical resistivity was carried out by a two probe method using silver paste contact on sintered pellet samples by using an Electrometer (Model No. 6514, Keithley).

All these measurement techniques are described in this chapter.

(1) XRD
(2) SEM
(3) Impedance
(4) VSM
(5) Curie Temperature
(6) Resistivity

5.1 X-ray diffraction

X-ray diffraction (XRD) provides precise knowledge of the lattice parameter as well as the substantial information on the crystal structure of the material under study.

X-ray diffraction is a versatile nondestructive analytical technique for identification and quantitative determination of various crystalline phases of powder or solid sample of any compound. XRD was done by using (PW 3040 -X'Pert PRO Philips) X-ray Diffractometer at the Materials Science Division, Atomic Energy Center, Dhaka, whose block diagram is shown in Fig. 5.1. The powder specimen were exposed to Cukα radiation wave length λ= 1.54178 Å with a primary beam of 40 Kv and 30 mA with sampling beam of 0.02°C and time for each step data collection was 1.0 sec. A 2θ scan was taken from 25° to 65° to get possible fundamental peaks of the sample. All the data of the samples were analyzed using computer software "X' PERT HIGHSCORE". X-ray diffraction pattern were carried out to confirm the crystal structure. The XRD patterns were taken and the data were analyzed to calculate d (inter planer spacing), relative intensities and Miller indices using the above mentioned soft ware.

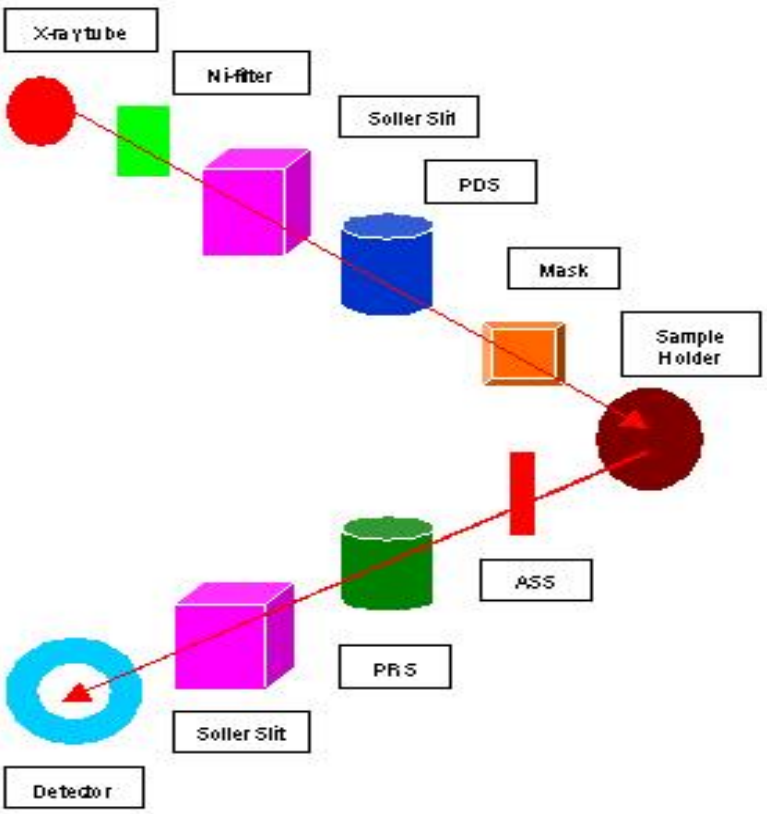

Fig. 5.1 Block diagram of the PHILIPS PW 3040 X'Pert PRO XRD system.

X-ray diffraction (XRD) can be explained in simple terms by the "reflection" of an X-ray beam from a stack of parallel equidistant atomic planes. At each atomic plane a small portion of the beam can be considered to be reflected. If those reflected beams, which are not absorbed on their way through the crystal, emerge from the crystal in such a way that they do not cancel each other by interference, a diffracted beam can be observed. The condition where the reflected beams interfere constructively to give a strong diffracted beam is given by Bragg's law: $n\lambda = 2d \sin\theta$ and can be derived by simple trigonometry from Fig. 5.2 where n is an integral number describing the order of reflection, λ is the wavelength of the X-rays, d is the spacing between the lattice planes, and θ is the Bragg angle where a maximum in the diffracted intensity occurs. At other angles there is little or no diffracted intensity, because of destructive interference. From Bragg's law: $\sin\theta = n\lambda/2d \leq 1$; $\lambda \leq 2d$ for n = 1 i.e. first order Bragg diffraction can occur only for wavelengths $\lambda \leq 2d$. Since the lattice spacing d is to the order of angstroms, visible light can not used, but X-rays are suitable for diffraction studies. In an XRD measurement, the wavelength λ is given by the radiation emitted from the X-ray tube (in laboratory experiments the most commonly used radiations are Cu-, Mo- or Cr- Kα). This means that spacing d can be easily evaluated from measurements of the first order Bragg angles θ using Bragg's law with n=1. If the regular arrangement of atoms in a crystal is considered, numerous stacks, has a different characteristic spacing d (Fig5.3). Therefore, each crystallographic phase shows a characteristic set of d spacings, which yields a characteristic diffraction pattern with intensities at the corresponding Bragg angles θ.

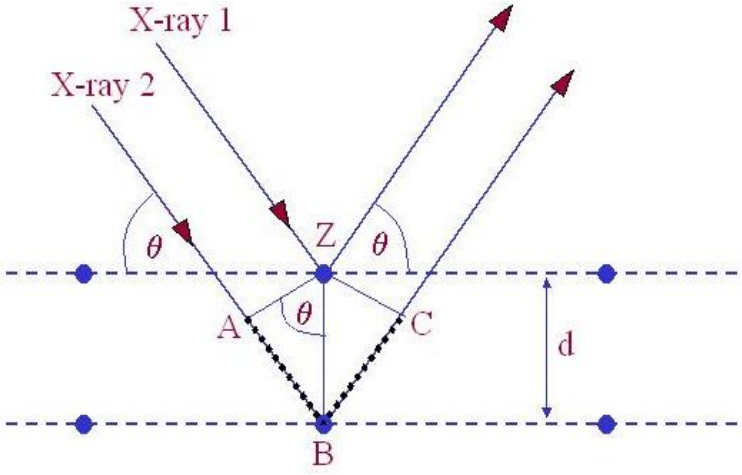

Fig. 5.2. Bragg's diffraction pattern.

A polycrystalline sample contains many small crystallites with random orientations. Therefore, a powder diffraction measurement yields the complete set of Bragg angles in the measured range, which can be regarded as a finger print of the investigated crystallographic phase. When the intensities of the diffraction line belonging to the different phases are taken into account, a quantitative analysis of the phases can be obtained. This is done conventionally with a calibration curve, which is derived from measurements of standard samples.

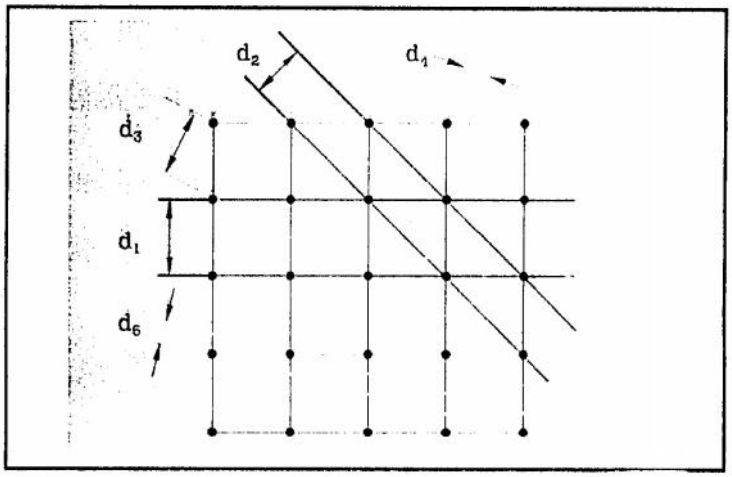

Fig. 5.3. Reflecting planes in a simple cubic lattice. A set of only two parallel planes is shown in each case.

5.1.1 Different Parts of the PHILIPS X' Pert PRO XRD System

Fig. 5.4 shows the inside view of the X' pert PRO XRD system. A complex of instruments of X- ray diffraction analysis has been established for both materials research and specimen characterization.

These include facilities for studying single crystal defects, and a variety of other materials problems.

The PHILIPS X' Pert PRO XRD system comprised of the following parts;

1. "Cu-Tube" with maximum input power of 60 kV and 55 mA,
2. "Ni- Filter" to remove Cu-K_α component,
3. "Solar slit" to pass parallel beam only,
4. "Programmable Divergent slits" (PDS) to reduce divergence of beam and control irradiated beam area,

Fig. 5.4. X-ray Powder Diffractometer (Model : PW 3040-X'Pert PRO Philips).

5. "Mask" to get desired beam area,
6. "Sample holder" for powder sample,
7. "Anti Scatter slit" (ASS) to reduce air scattering back ground,
8. "Programmable Receiving slit" (PRS) to control the diffracted beam intensity and
9. "Solar slit" to stop scattered beam and pass parallel diffracted beam only.

5.1.2 Interpretation of the XRD data

The XRD data consisting of θ_{hkl} and d_{hkl} values corresponding to the different crystallographic planes are used to determine the structural information of the samples like lattice parameter and constituent phase. Lattice parameters of Ni-Zn and Mn-Zn ferrites samples were determined from the obtained data. Normally, lattice parameter of an alloy composition is determined by the Debye-Scherrer method after extrapolation of the curve. Determination of the lattice spacing (inter planer distance), d using these reflections from the equation which is known as Bragg's Law.

$$2d_{hkl}\sin\theta = n\lambda$$

$$\text{i.e. } d_{hkl} = \frac{\lambda}{2\sin\theta} \qquad 5.1$$

Where λ is the wave length of the X-ray, θ is the diffraction angle and n is an integer representing the order of the diffraction.

The lattice parameter for each peak of each sample was calculated by using the formula:

$$a = d_{hkl} \times \sqrt{h^2 + k^2 + l^2} \qquad 5.2$$

Where h,k,l are the indices of the crystal planes.

The lattice parameter was determined through the Nelson-Riley extrapolation method. The values of the lattice parameter obtained from each reflected plane are plotted against Nelson-Riley function [5.1]. The Nelson- Riley function F(θ), can be written as:

$$F(\theta) = \frac{1}{2}\left[\frac{\cos^2\theta}{\sin\theta} + \frac{\cos^2\theta}{\theta}\right] \qquad 5.3$$

Where θ is the Bragg's angle. A straight line is generally obtained from these data fitting. The accurate values of lattice constant were estimated from the extrapolation of these line of $F(\theta) = 0$ or $\theta = 90°$

5.2 Microstructure study

Methods of study the microstructure are distinctly limited and the amount of detailed information which has been obtained does not compare with that for the magnetic metals. Ordinary metallography is far from simple for ceramic specimens. Sectioning is readily achieved using diamond saws, but grindings and polishing requires great care: there is a tendency to pluck out grains from poorly sintered specimens, giving an impression of even greater porosity. There is little quantitative data on etching, which appears to be based on trial and error practice. Porous specimen are difficult to etch since grain boundaries accessible via the pores are more reactive than the polished surfaces of the crystallites. Thermal etching, which consists of heating close to the temperature at which sintering would be appreciable, in a suitable atmosphere, is a very simple method of studying grain size, but it does not appear to indicate the porosity: pores at the surface close or migrate during the heating.

For taking the photograph of the microstructure of the spinel ferrite samples first the surfaces of the samples were polished successively with silicon carbide and fine durmax alumina suspension and then the grains were brought out by thermal etching at 1100°C. Micro photograph of the etched surface of the samples were taken by Scanning Electron Microscope (S50 FEI Quanta Inspect).

5.2.1 Scanning Electron Microscope (SEM)

The scanning electron microscope (SEM) is a type of electron microscope that is used to produce high-resolution three dimensional images of a specimen surface and to observe the surface structure of the specimen [5.2]. It creates various images by focusing a high energy beam of electrons onto the surface of a sample and detecting signals from the interaction of the incident electrons with the sample's surface. The type of signals gathered in a SEM varies and can include secondary electrons (SE), characteristic X-rays, and back scattered electrons (BSE). In a SEM, these signals come not only from the primary beam impinging upon the sample, but from other interactions within the sample near the surface. The SEM is capable of producing high-resulation images of a sample surface in its primary use mode, secondary electron imaging. Due to the manner in which this image is created, SEM images have great depth of field yielding a characteristic three-dimensional appearance useful for understanding the surface structure of a sample. This great depth of field and the wide range of magnifications are the most familiar imaging mode for specimens in the SEM. Characteristic x-rays are emitted when the primary beam causes the ejection of inner shell electrons from the sample and are used to tell the elemental composition of the sample. The back-scattered electrons emitted from the sample may be used alone to from an image or in conjunction with the characteristic x-rays as atomic number contrast clues to the elemental composition of the sample.

5.2.2 S50 FEI Quanta Inspect SEM

In our experiment, S50 FEI Quanta Inspect SEM was used for the microstructure to study the grain image and grain size of the prepared samples in the Materials Science division, Atomic Energy Centre, Dhaka. Fig. 5.5 shows the S50 FEI Quanta Inspect SEM.

Fig. 5.5 S50 FEI Quanta Inspect SEM.

The essential components of SEM include the following:

Electron Source (″Gun″)

Electron Lenses

Sample Stage

Detectors for signals of interest

Display/Data output devices

Infrastructure Requirements:

-Power Supply

-Vacuum System

-Cooling System

5.2.3 Scanning Process

In Scanning Electron Microscope (SEM), electrons are emitted from the cathode surface made of tungsten or lanthanum hexaboride and are accelerated towards the anode. Electrons can be emitted through field emission. Tungsten is used as it has the highest melting point and lowest vapor pressure of all metals, thereby favorable for electron emission at highest temperature. The energy of electron beam ranges from a few hundred eV to 100 keV, is focused by one or two condenser lenses into a beam with a spot size of 1 nm to 5 nm. The beam is passed through a pair of scanning coils in the objective lens, which deflects the horizontally and vertically so that it scans in a raster fashion over a rectangular area of the specimen surface. When the primary electron beam strikes the sample surface, the electrons lose their energy by repeated scattering and absorption with the specimen and the beam extends from less than 100 nm to around 5 μm on the specimen surface. The energy exchange between the electron beam and the sample under observation, results in the emission of electrons and electromagnetic radiations which are used to produce an image. The resolution of scanning electron microscope ranges from 1 nm to 20 nm. Fig 5.6 shows the block diagram of a SEM.

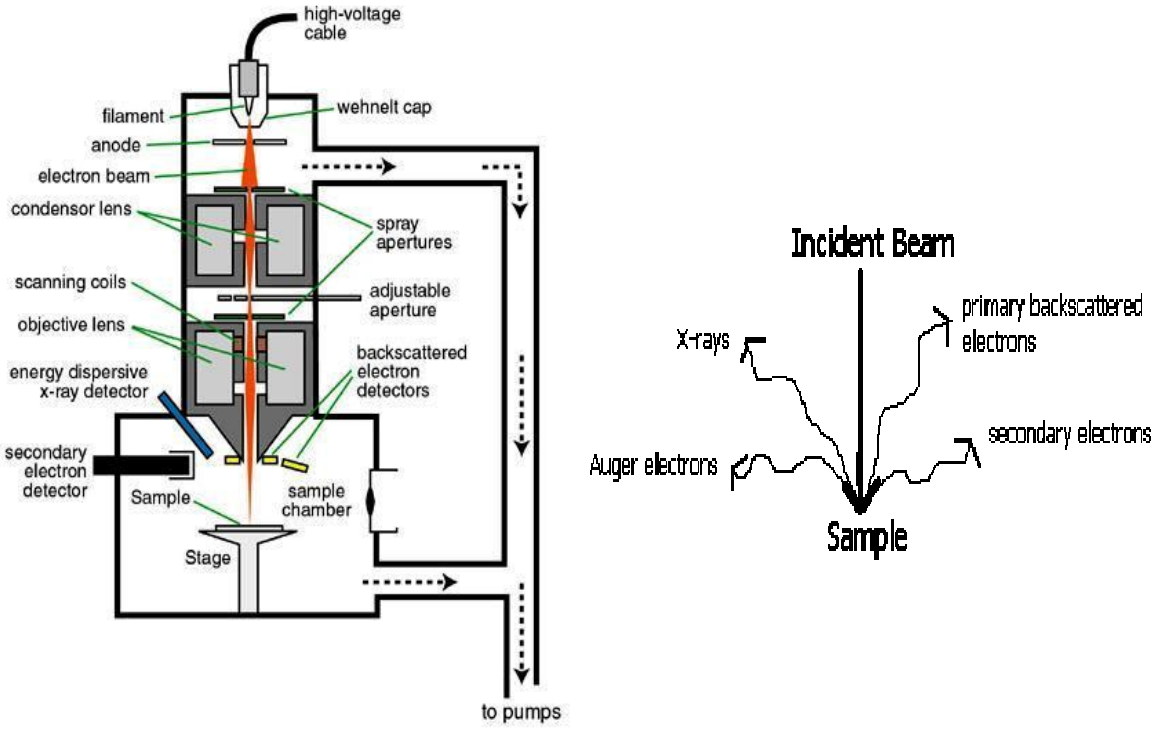

Fig.5.6. Block diagram of a SEM.

An electron microscope is a scientific instrument that uses a beam of highly energetic electrons to examine objects on a very fine scale. A focused beam of electrons is used in electron microscope to obtain much higher magnification than that of a conventional microscope. An ordinary microscope can magnify the image of an object up to 100 times whereas the electron microscope can magnify the image up to 10000 times.

This large magnification is due to the fact that the wavelength of a high –speed electron is much lower than that of visible light, and so much higher resolution is possible. A beam of electrons is emitted from the electron source and is accelerated towards the specimen using a positive electrical potential. This beam is confined and focused by metal apertures and magnetic lenses into a thin, focused and monochromatic light. Then the beam is focused on the sample with the help of magnetic lens. The interactions occur inside the irradiated sample that affect the electron beam. Ultimately, we see the magnified image.

5.3 Magnetization Measurement

In the present study magnetization has been performed using a Vibration Sample Magnetometer (VSM).

5.3.1 Vibrating Sample Magnetometer (VSM)

A vibrating samples magnetometer (VSM) operates on Faraday's Law of Induction, which tells us that a changing magnetic field will produce an electric field. This electric field can be measured and can tell us information about the changing magnetic field. A VSM is used to measure the magnetic behavior of magnetic materials. Vibrating Sample Magnetometer is a versatile and sensitive method of measuring magnetic properties developed by S. Foner [5.3] and is based on the flux change in a coil when the sample is vibrated near it. The Vibrating Sample Magnetometer (VSM) is designed to continuously measure the magnetic properties of materials as a function of temperature and field. In this type of magnetometer, the sample is vibrated up and down in a region surrounded by several pickup coils. The magnetic sample is thus acting as a time-changing magnetic flux, varying inside a particular region of fixed area. From Maxwell's law it is known that a time varying magnetic flux is accompanied by an electric field and the field induces a voltage in pickup coils. This alternating voltage signal is processed by a control

unit system, in order to increase the signal to noise ration. The result is a measure of the magnetization of the sample.

Principle of VSM

If a sample is placed in a uniform magnetic field, created between the poles of a electromagnet, a dipole moment will be induced. If the sample vibrates with sinusoidal motion a sinusoidal electrical signal can be induced in suitable placed pick-up coils. The signal has the same frequency of vibration and its amplitude will be proportional to be magnetic moment amplitude, and relative position with respect to the pick-up coils system. Fig. 5.7 shows the block diagram of vibrating samples magnetometer.

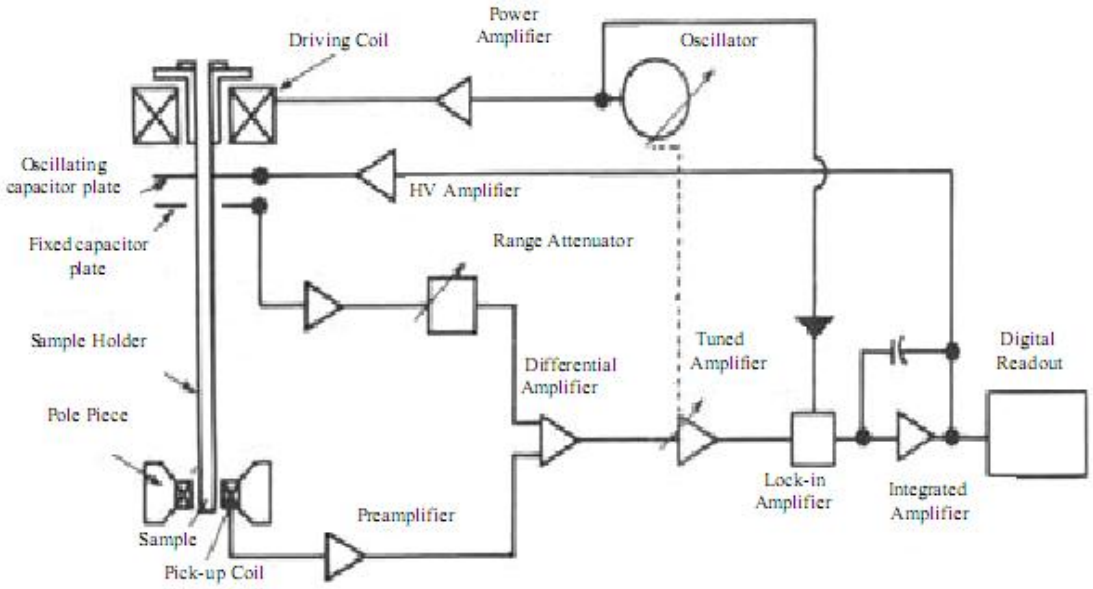

Fig. 5.7. Block diagram of Vibrating Sample Magnetometer.

The sample is fixed to a sample holder located at the end of a sample rod mounted in a electromechanical transducer. The transducer is driven by a power amplifier which itself is driven by and oscillator at a frequency of 90 Hz. So, the sample vibrates along the Z axis perpendicular to the magnetization field. The latter induced a signal in the pick-up coil system that is fed to a differential amplifier. The output of the differential amplifier is

subsequently fed into a tuned amplifier and an internal lock-in amplifier that receives a reference signal supplied by the oscillator.

The output of this lock-in amplifier, or the output of the magnetometer itself, is a DC signal proportional to the magnetic moment of the sample being studied. The electromechanical transducer can move along X, Y and Z directions in order to find the saddle point. Calibration of the vibrating sample magnetometer is done by measuring the signal of a pure Ni standard of known saturation magnetic moment placed in the saddle point. The basic instrument includes the electromechanical system and the electronic system (including a personal computer). Laboratory electromagnets or superconducting coils of various maximum field strengths may be used.

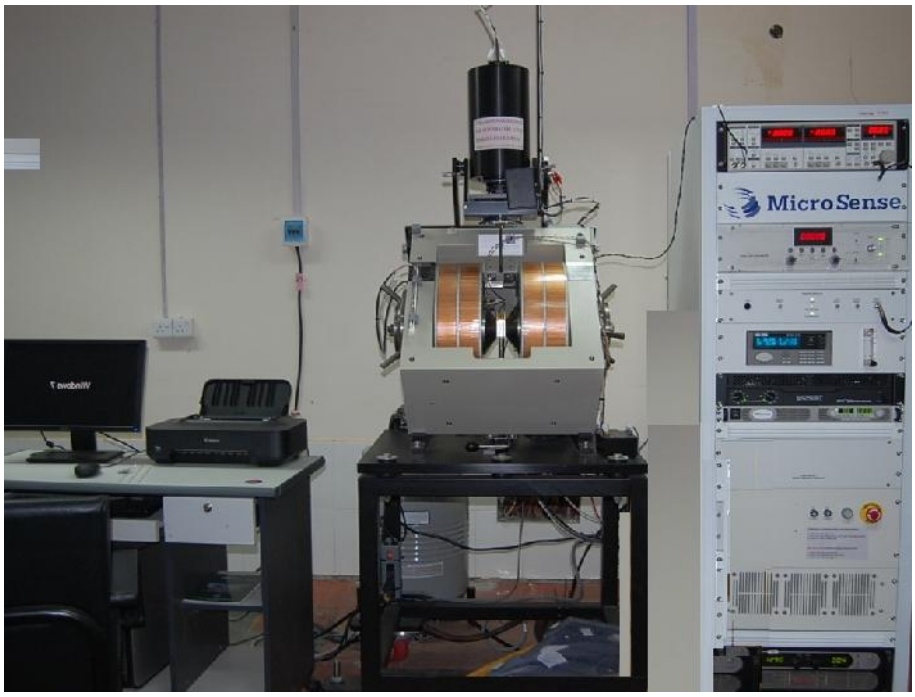

Fig. 5.8. Vibrating Sample Magnetometer (Model EV7 system).

Curie Temperature Measurement

Curie temperature measurement is one of the most important measurements because it provides substantial information on magnetic status of the substance in respect to the strengths of exchange interaction. Above Curie temperature spontaneous magnetization vanishes and ferromagnetic materials behave like paramagnetic material. The determination of Curie temperature accurately is of great importance. For ferromagnetic materials in particular, for ferrite it is customary to determine the Curie temperature by

measuring the permeability as a function of temperature. In our present research work we measured the Curie temperature of the samples by measuring the permeability against temperature. According to Hopkinson effect [5.4] which arises mainly from the intrinsic anisotropy of the material has been utilized to determine the Curie temperature of the samples. According to this phenomenon, the permeability increases gradually with temperature and reaching to a maximum value just before the Curie temperature.

The temperature dependence of initial permeability of the samples were measured by using induction method carried out by using Hewlett Packart Impedance Analyzer (shown in Fig.5.9) in conjunction with a Laboratory made oven at Material Science Division, Atomic Energy Centre, Dhaka.

When the magnetic state inside the ferrite sample changes from ferromagnetic to paramagnetic, the permeability falls sharply. From this sharp fall at specific temperature the Curie temperature was determined. For the measurement of Curie temperature, the sample was kept inside a cylindrical oven with a thermocouple placed at the middle of the sample. The thermocouple measures the temperature inside the oven and also of the sample.

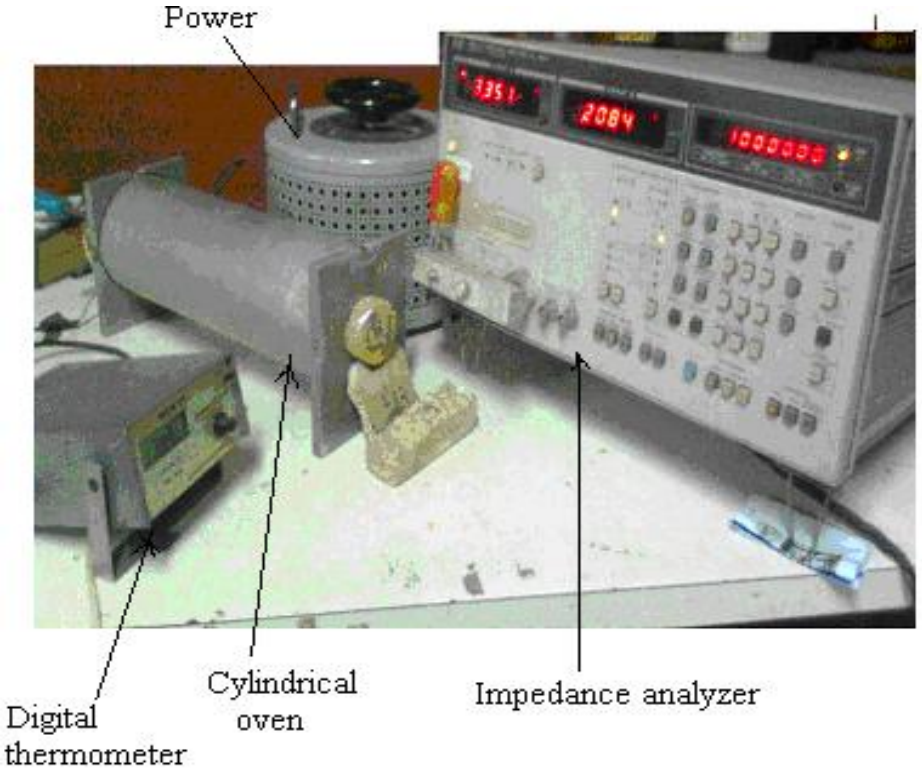

Fig. 5.9. Impedance Analyzer Model-Hewlett-Packard 4192A.

The sample was kept just in the middle part of the cylindrical oven in order to minimize the temperature gradient. The temperature of the oven was then raised slowly. If the heating rate is very fast then the temperature of the sample may not follow the temperature inside the oven and there can be misleading information on the temperature of the samples. The thermocouple showing the temperature in that case will be erroneous. Due to the closed winding of wires the sample may not receive the heat at once. So, a slow heating rate can eliminate this problem. The cooling and heating rates are maintained as approximately 0.5°C min^{-1} in order to ensure a homogeneous sample temperature. Also a slow heating ensure accuracy in the determination of Curie temperature.

The oven was kept thermally insulated from the surroundings. The temperature was measured with a digital thermometer attached close to the sample and put inside the furnace where the temperature fluctuation is almost negligible. Then the permeability versus temperature curve was plotted from which the Curie temperature was calculated.

5.4 Initial Permeability Measurement

The inductance of a circuit may be defined as the flux linkage per unit current, i.e. for an alternating current of peak amplitude **I** ; $L = N\varphi/\mathbf{I}$ Henry

For a winding of N turns on an ideal toroid if magnetic length l and cross sectional area A;

$$L = N\mathbf{B}A/\mathbf{I} = (NA/I)\ \mu_0\mu(NI/l) \qquad \therefore L=\mu_0\mu N^2A/l \quad \text{Henry}$$

$$= \mu\ L_0 \qquad 5.8$$

Where $\mu_0=N^2A/l$ is the inductance that would be measured if the core had unity permeability, the flux distribution remaining unaltered.

In general the impedance of the winding will not be a pure reactance; there will be a resistive component due to the loss of energy incurred as the magnetization alternates. The impedance may be expressed in terms of a complex permeability. Whereas a loss- free core will present a reactance $X= j\omega L= j\omega L_0\mu$ a core having magnetic loss may be represented by an impedance:

$$= j\omega L_0\mu$$

$$= j\omega L_0(\mu'-j\mu'')$$

$$= \omega L_0\mu''+j\omega L_0\ \mu' \qquad 5.9$$

Where the real or resistive part is: $R= \omega L_0 \mu''$, and the imaginary or reactive part is: $X=\omega L_0 \mu'$ and magnetic tangent is: $\tan \delta_m = \mu''/\mu'$

The resistive and reactive part of the thin ferrite toroid containing a "single turn" coaxial system to avoid stray capacitance of winding was measured by connecting directly to the impedance analyzer.

The impedance analyzer provides an auto balance bridge circuit with a combination of Null detector and Modulator, this is considered as an ideal feed back amplifier with a realized 100 MHz bandwidth (Fig.5.10) The Vector voltage Ratio Detector (VRD) detects the individual real and imaginary vector components of the two input vector signal, the test signal applied to the toroid (DUT) and the voltage across the range resistor. This provides the A-D conversion outputs which represent the magnitudes of four vector components. Detection of the vector component voltages is performed through three major processes: (i) signal selection in the process amplifier, (ii) phase detection and (iii) A-D conversion. The basic theory of the vector voltage ratio measurement is described as follows.

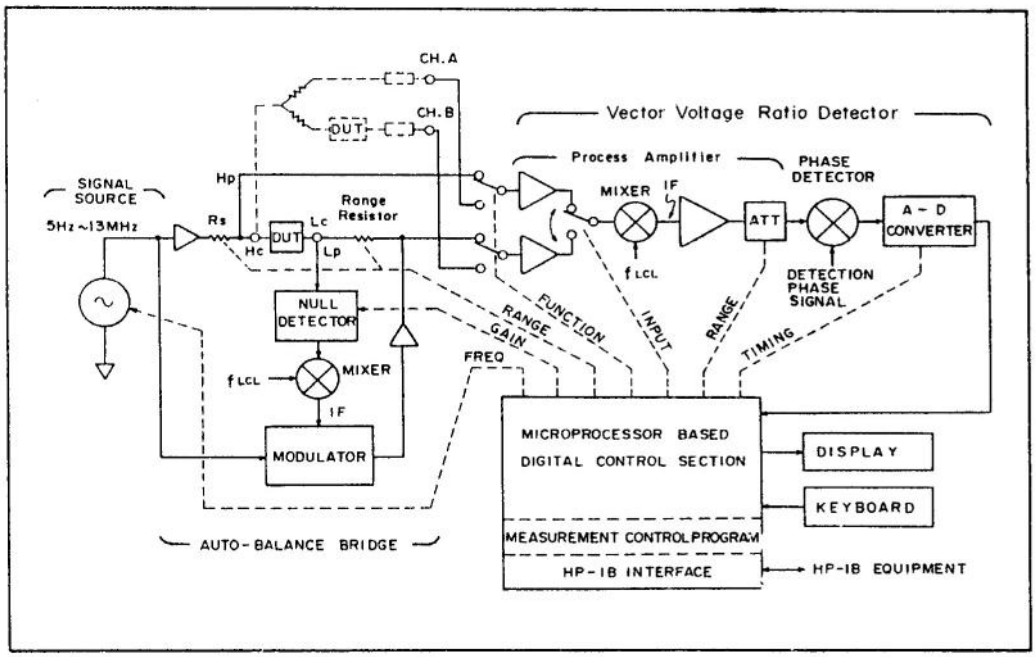

Fig. 5.10. Schematic diagram of the Impedance Analyzer.

When the bridge is balanced, the impedance, Z_x of the (DUT), the test signal applied to the DUT and the voltage across the range resistor are related to each other by the equation:

$$Z_x = R_r(e_s/e_r) \qquad 5.10$$

where, R_r is the range resistor value.

e_s is the voltage applied to the DUT.

e_r is the voltage across the range resistor.

Fig. 5.11 shows the basic circuit configuration of VRD section. For accurate measurement of the vector voltages, the process amplifier detects the e_s and e_r signals with differential input. The process amplifier alternately selects and sequentially feeds the e_s and e_r signals to the phase detector. To derive the vector ratio of the e_s and e_r signals, the phase detector separates then into their orthogonal phase components using a set of detection phase signals which are exactly 90 degrees out of phase with each other. Fig. 5.12 is a graphic representation of relationship between the measurement signals (e_s and e_r) the detection phase signals (V_{D1} and V_{D2}). With these detection phases, the e_s and e_r signals are divided into the phase components e_a, e_b, e_c and e_d. The impedance value of DUT is calculated from the four phase components is accordance with the following equations.

$$\begin{aligned} Z_x &= R_r(e_s/e_r) = Rr\ (e_c + e_d)/(e_a + je_b) \\ &= R_r\ [e_se_c + e_be_d + j(e_ae_d - e_be_c)]/(e_a^2 + e_b^2) \end{aligned} \qquad 5.11$$

The resistance and reactance values of the DUT are calculated as follows:

$$\begin{aligned} R_x &= Z_x/\text{real} = R_r(e_ae_c + e_be_d)/(e_a^2 + e_b^2) \\ X_z &= Z_x/\text{imaginary} = R_r(e_ae_d - e_be_d)/(e_a^2 + e_b^2) \end{aligned} \qquad 5.12$$

The analyzer can provide measuring frequency range from 5 Hz to 13 MHz with automatic sweep capability of the built in synthesizer. Oscillation level is variable from 5 mV to 1.1 V r.m.s with 1 mV resolution.

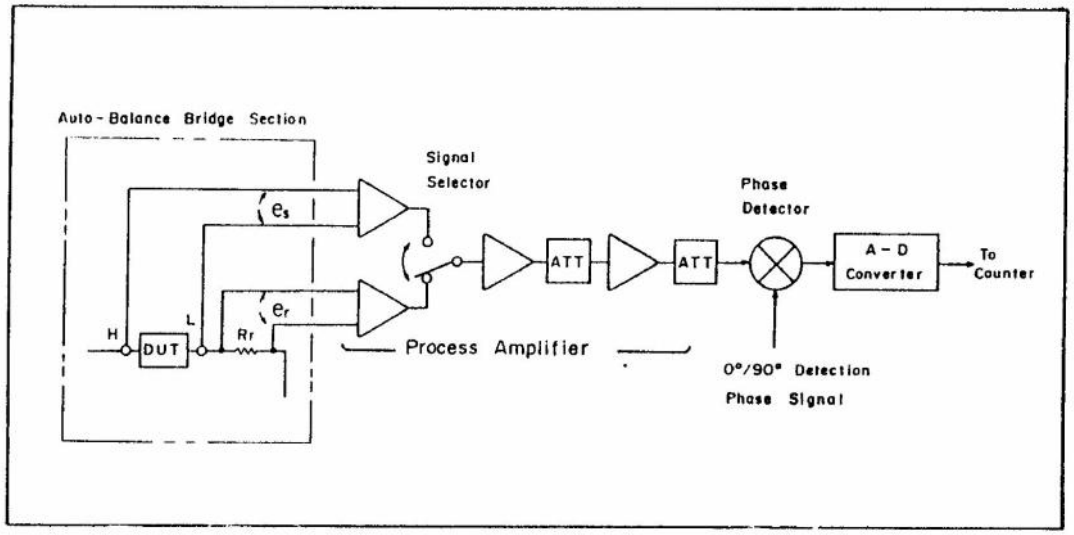

Fig. 5.11. Vector Voltage Ratio Detector basic diagram.

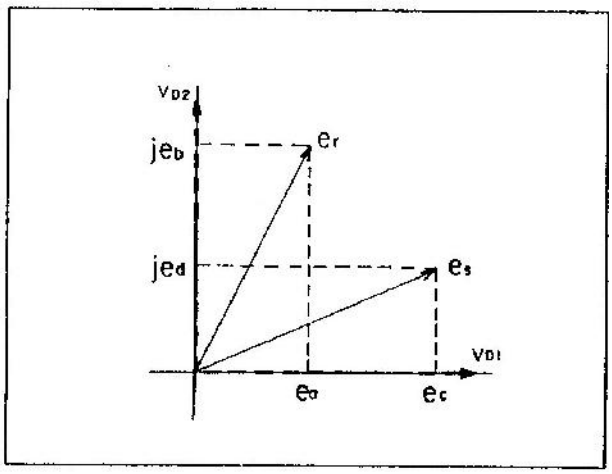

Fig.5.12. Phase detection Vector diagram.

5.5 Resistivity Measurement

Resistivity is an intrinsic property of a material. The technical importance of ferrites lies primarily in their high resistivity measurements carried out by a two probe method on silver painted samples using a Keithley Electrometer (Fig. 5.13). The electrical resistivity was calculated according to the formula:

$$\rho = \frac{RA}{l} = \frac{\pi r^2 R}{l} \quad \text{.....} \quad 5.13$$

Where R is the resistance of the pellet, r is the radius of the pellet and l is the thickness of the pellet.

Fig.5.13. Electrometer Model No. 6514, Keithley.

References:

5.1 J.B. Nelson, D.P. Riley, "An experimental investigation of extrapolation methods in the derivation of accurate unit-cell dimensions of crystals", Proc. Phys. Soc. London, **57,** 160 (1945).

5.2 R.E. Ferrell, G. G. Paulson, An Ortec Workshop, Energy Dispersive Analysis of X- ray Spectra Generated in the SEM, Braniff Place, New Orleans, Louisiana, (1973).

5.3 Simon Foner, "Versatile and sensitive Vibrating Sample Magnetometer," Rev. Sci. Instru. **30** (1959).5.4

5.4 J. Smit and H.P. J wijin, Ferrites, Wiely, New York, 250, (1959).

Study of the influence of V_2O_5, CuO, In_2O_3 and Eu_2O_3 addition on the magnetic and electrical properties of iron-deficient Ni-Zn ferrites

6.1 Introduction

Nickel-zinc (Ni-Zn) ferrites are extensively used as core materials for low frequency electronic components such as inductors, transformers, radio antenna, television line scanning transformers, picture tube deflection yokes, coils in filter circuits, power supplies and for other devices in radio, television and communication equipment due to their attractive magnetic and electrical properties. Magnetic and electrical properties of these materials are very sensitive to composition, impurity level and preparation methodology. Several workers have studied these ferrites both on the basic properties and on the influence of various substitutions or additions depending on the applications of interest [6.1-6.5]. Besides, efforts have been made to improve the magnetic and electrical properties of these ferrites by adding oxides of transition elements (divalent oxides) and elements of different valence states (trivalent oxides) depending on the applications of interest [6.6-6.10]. It has also been reported that the choice of the addition of these oxides influences favorably the characteristic properties of Ni-Zn ferrites [6.11-6.13].

A small amount of an additive which forms a liquid phase at sintering temperatures can have a great influence on the magnetic and electrical properties of ferrites. Such an additive generally lowers the sintering temperature, i.e., promotes the densification at lower temperatures. Additive oxides of transition elements such as V_2O_5 or MoO_3, melt around 700°C and form liquid phases at commonly used sintering temperatures of Ni-Zn ferrites. Densification of Ni-Zn ferrites in presence of V_2O_5 has been studied earlier [6.14-6.15]. Magnetic and electrical properties of Ni-Zn ferrites and Li-Zn ferrite [6.16-6.17] have been found to improve remarkably with the addition of V_2O_5. It has been observed that in Li-Zn ferrites, a part of the added V_2O_5 goes into the solid solution with the ferrite matrix. Incorporation of V^{5+} ions into the spinel ferrite lattice introduces many complexities including creation of Fe^{2+} ions and precipitation of Fe_2O_3 as a second phase.

It has been reported that the addition of copper oxide (CuO) in the ferrite appears to act, to some degree, as a flux. CuO decomposes to form Cu_2O at 1026°C and Cu_2O melts at 1235°C which is lower than the melting points of the other oxides in the Ni-Zn ferrite system [6.18]. The promising effect of CuO addition on the sintering behavior and electro-magnetic properties of Ni-Zn ferrites has been investigated for years [6.19-6.20]. It has been suggested that the limiting amount of copper oxide addition is favorable for the grain growth as well as enhancement of the dc resistivity of Ni-Zn ferrites.

It is known that the magnetic behavior of the ferrite compounds is largely governed by the Fe-Fe interaction (the coupling of the spins of the 3d electrons). By introducing rare-earth (R) ions in the spinel ferrite lattice, the R-Fe interactions appear too (3d-4f coupling), which can lead to changes in the magnetic properties of ferrites [6.21-6.23]. The influence of rare earth ions (Er, Yb, Dy, Tb, Eu and Gd) on Ni-Zn ferrites has been investigated earlier [6.24-6.25]. It is concluded that the permeability of Ni-Zn ferrites increases with the size of ionic radius of the rare earth ions. The results of the investigation also reveal that it is possible to increase the electrical resistivity of Ni-Zn ferrite by substituting a small quantity of Fe_2O_3 with R_2O_3. The influence of the substitutions of indium and titanium have been investigated to improve the magnetic properties of Ni-Zn ferrites [6.26].

The effect of iron deficiency in Ni-Zn ferrites have also been studied to optimize the magnetic properties, particularly those relating to quality factors, saturation magnetization, operating frequencies and microstructure of the material [6.27-6.29]. It is concluded that the iron deficient Ni-Zn ferrite provides the optimum number of vacancies for the transportation of metal ions during solid state reaction which is considered a good route to obtain high density ferrites of higher saturation magnetization, initial magnetic permeability and high resistivity. **Since Ni-Zn ferrites used as a core materials of electronic devices operating at frequencies beyond 100 kHz have an edge over the other soft ferrites, thus, an attempt has been made to investigate the influence of V_2O_5, CuO, In_2O_3 and Eu_2O_3 addition on the magnetic and electrical properties of iron-deficient Ni-Zn ferrites through this study.**

6.2 The X-ray Diffraction Analysis of the $Ni_{0.65}Zn_{0.35}Fe_{1.96}O_4$ Ferrite System:

The x-ray diffraction of the sintered ferrite powder of the system was done by using Philips X'PERT PRO X-ray Diffractometer using Cu-Kα radiation in the range of 2θ=25° to 65° in steps of 0.02°. The indexed XRD pattern is plotted in Fig 6.1 showing well defined crystalline phase cubic lattice. The x-ray diffraction pattern confirms the formation of single phase cubic spinel structure.

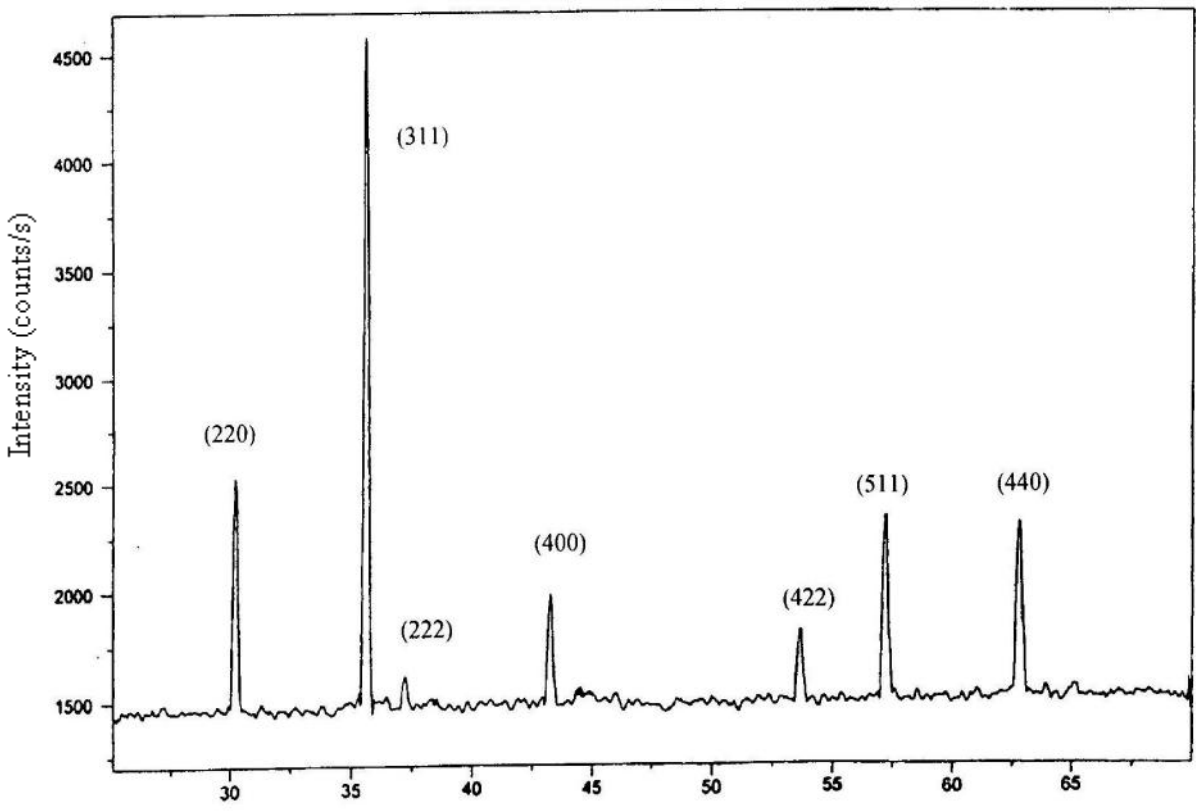

Fig. 6.1 XRD pattern of sintered $Ni_{0.65}Zn_{0.35}Fe_{1.96}O_4$ ferrite.

6.3 The ferrite system $Ni_{0.65}Zn_{0.35}Fe_{1.96}O_4+xV_2O_5$, where, x (in mol unit)= 0, 0.002, 0.004,0.006, 0.008, 0.01

6.3.1 Physical Properties:

The x-ray diffraction studies of the ferrite system with the addition of V_2O_5 are used to obtain lattice constant values. Fig. 6.2 shows the variation of sintered density (d_s) and lattice constant (**a**) for samples with increasing concentration of V_2O_5 addition. A significant increase of the density is observed up to V_2O_5 addition, x=0.004 (0.4 mol%) and then decreases with increasing amount of V_2O_5. The inclusion of low melting V_2O_5 (melting point 700°C) to the composition of iron deficient Ni-Zn ferrites increases the anion vacancy concentration, prohibit discontinuous grain growth which in turn enhances the density [6.30]. The decrease in density beyond V_2O_5, x=0.004 content is due to the segregation of second phase rich in vanadium [6.30]. The lattice constant values remain almost unaffected by the addition of V_2O_5 also shown in Fig. 6.2. V^{5+} ions have a smaller ionic radius (0.59 Å) than Fe^{3+} ions (0.64 Å), its incorporation into the ferrite lattice results in the creation of Fe^{2+} ions which have an ionic radius of 0.74 Å. This presumably results in no net change in the lattice constant values when V_2O_5 goes into solid solution in the ferrite.

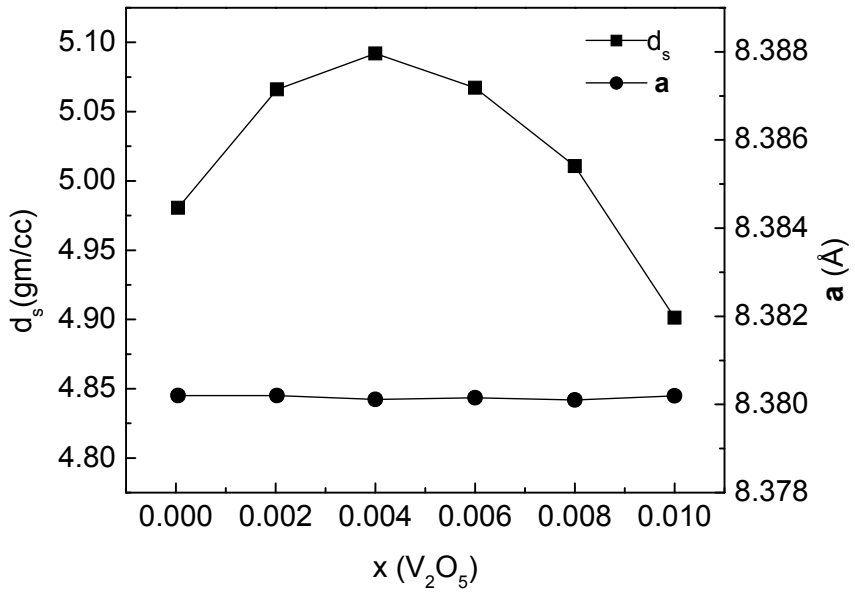

Fig. 6.2. Variation of sintered density (d_s) and lattice constant (**a)** with V_2O_5 addition.

6.3.2 Magnetic and Electrical Properties:

The variation of saturation magnetization (M_s) and Curie temperature (T_c) is shown in Fig. 6.3. An increment in the saturation magnetization as observed from the figure up to V_2O_5, x= 0.004 (0.4 mol%) is due to the increase of resultant sublattice magnetic moment as well as density. It is also observed from the figure that up to x=0.004, V_2O_5 goes into the solid solution, with ferrite matrix and increases the Curie temperature. This is probably due to some of V^{5+} ions occupy octahedral sites (B-sites) of the ferrite lattice, as a result some of Fe^{3+} ions would be pushed off from B to A-sites (tetrahedral sites) thereby increasing A-B interaction and hence the Curie temperature [6.31]. As the amount of V_2O_5 is increased the V^{5+} ions occupy the eletro-statically stable A-sites, weakening the A-B interaction and the Curie temperature decreases.

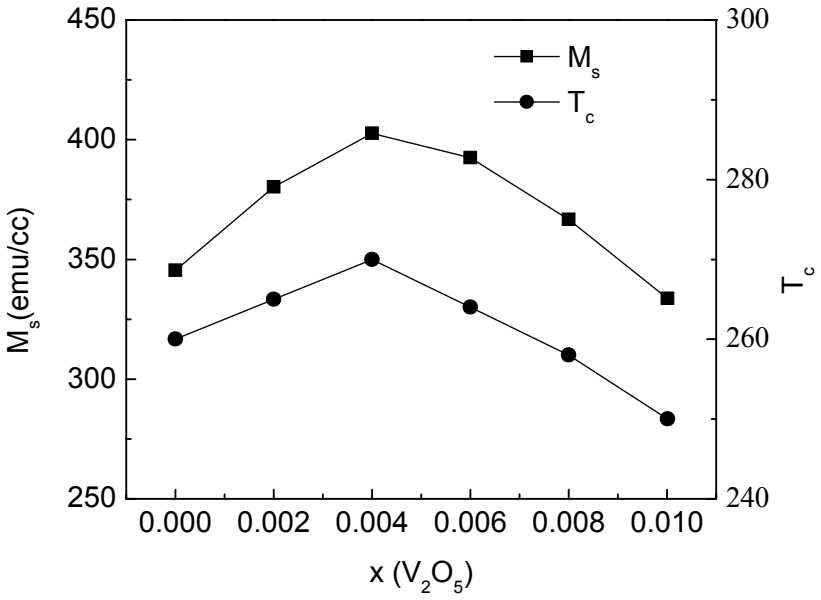

Fig. 6.3. Variation of Saturation magnetization (M_s) and Curie temperature (T_c) with V_2O_5 addition.

Frequency dependent initial magnetic permeability (μ′) i.e. permeability spectra for all the samples from 0 to 1 mol% V_2O_5 (x=0.01) content is shown in Fig. 6.4. The frequency variation is plotted in logarithmic scale and μ′ is plotted in linear scale. The initial magnetic permeability (μ') values for all the samples containing V_2O_5 are found fairly constant below the resonance frequency. Above the resonance frequency (around 10 MHz) μ' sharply decreases. The variation of initial magnetic permeability (μ′) at 100 kHz of the ferrite system with increasing concentrations of V_2O_5 is also shown in Fig. 6.5. An appreciable increase in the permeability up to V_2O_5, x= 0.004 (0.4 mol%) can be observed from the figure and then decreases with the increment of V_2O_5 addition. Maximum value

of μ' = 1480 at 100 kHz is achieved for sample containing 0.4 mol% V_2O_5 addition. Such an increase in permeability can not be attributed to densification alone. This increment is thus the reflection of the effect of V_2O_5 addition on the microstructure of the ferrite material as shown in Fig.6.6. (SEM microphotographs of the samples).

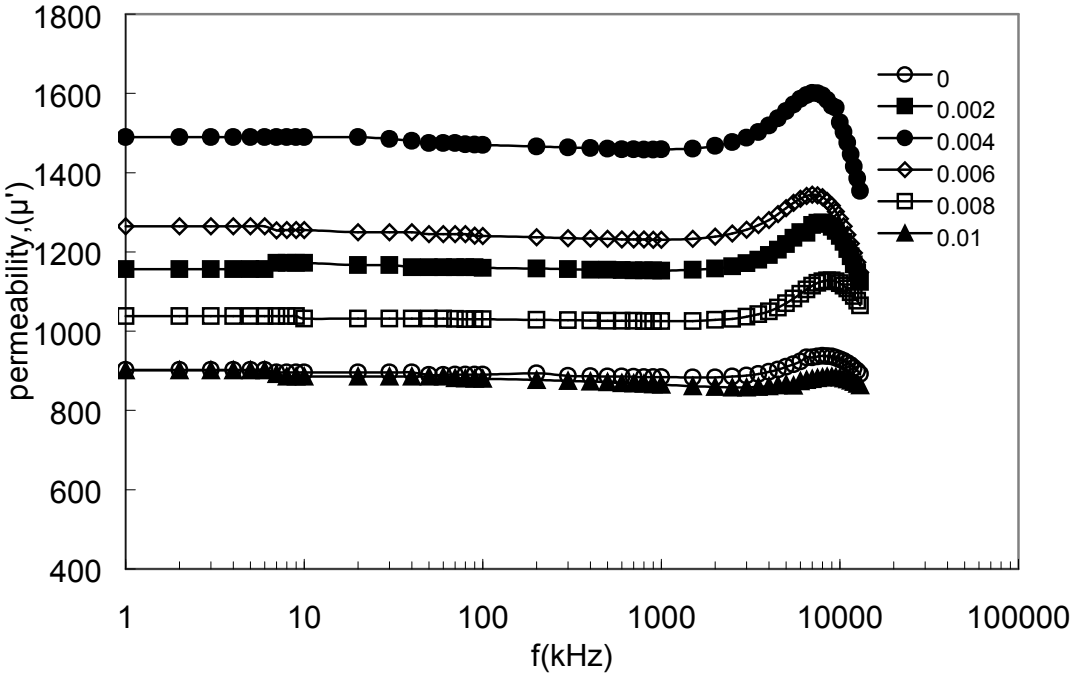

Fig. 6.4 Permeability spectra of the ferrites system with V_2O_5 addition.

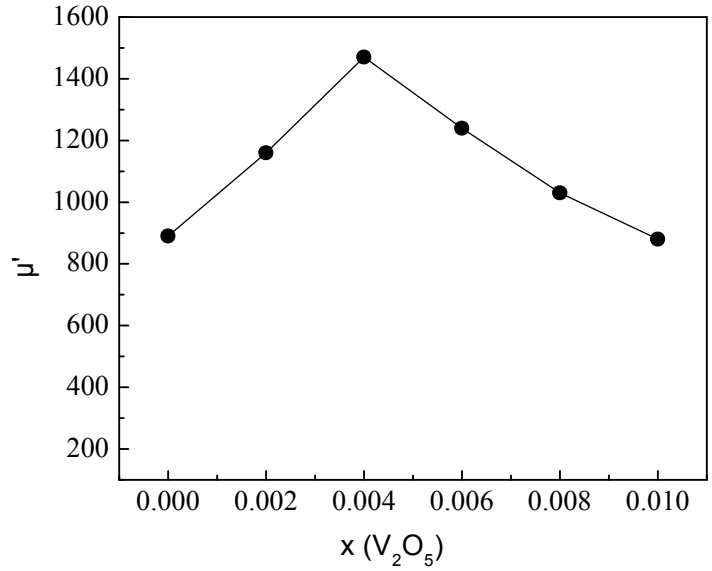

Fig. 6.5 Variation of initial magnetic permeability (μ′) at 100 kHz with V_2O_5 addition.

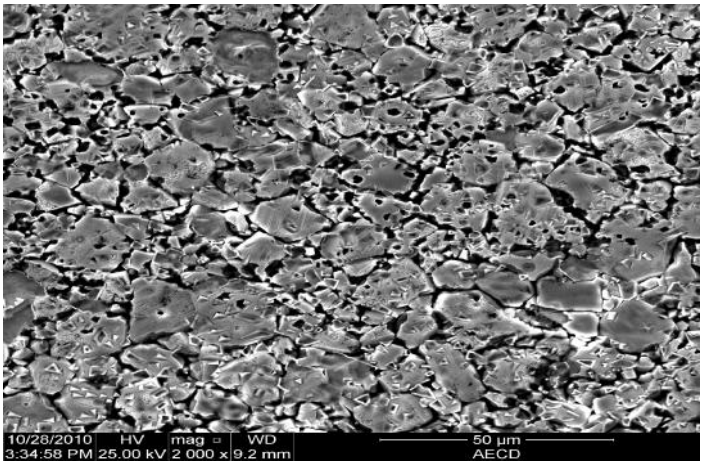

V_2O_5 (x=0.02)

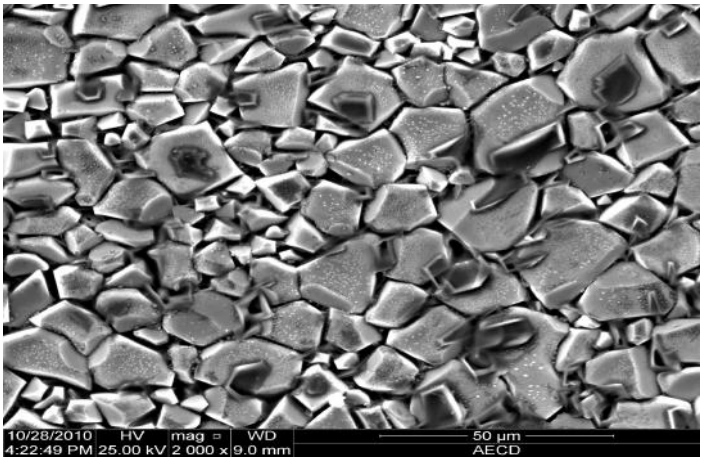

V_2O_5 (x=0.004)

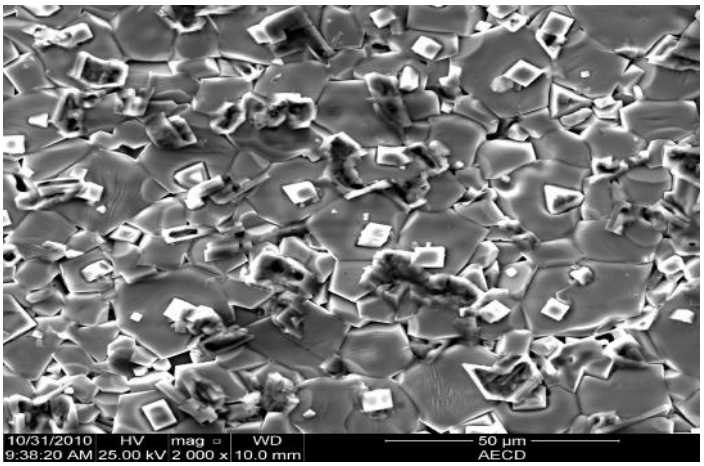

V_2O_5 (x=0.006)

Fig. 6.6. SEM Microphotographs of $Ni_{0.65}Zn_{0.35}Fe_{1.96}O_4$ ferrite samples with V_2O_5 addition.

For this composition of ferrite, as the concentration of V_2O_5 addition is increased, the grain size first increases presumably due to the creation of oxygen vacancies and the consequent increase in the rate of diffusion of oxygen ions, and then decreases as V_2O_5 forms a second phase. The second phase which appears at higher V_2O_5 addition forms a non-magnetic discontinuity around the ferrite grains and contribute towards the decrease in permeability.

The variation of normalized magnetic loss factor ($1/\mu Q$) and dc resistivity (ρ) is shown in Fig. 6.7. The loss factor ($\tan\delta$) divided by permeability (μ') is material figure of merit referred to as the normalized loss factor and written as: $\tan\delta/\mu' = 1/\mu Q$. As observed from the figure that the loss factor first decreases, reaches a minimum and then increases with increasing addition of V_2O_5. The minimum value of normalized loss factor of 0.63×10^{-5} is achieved for sample containing 0.4 mol% of V_2O_5 addition. It suggests that the increment of loss factor at higher concentration of V_2O_5 is mainly due to the drastic decrease in permeability at these concentrations of V_2O_5. It is observed from the figure that the dc resistivity of the samples with V_2O_5 addition increases almost linearly with the increasing concentration of V_2O_5. The maximum value of dc resistivity of the order of 1.25×10^{4} ohm-cm is achieved for sample containing 1 mol% of V_2O_5 addition. With the addition of V_2O_5, V^{5+} ions occupy B-sites as mentioned earlier which limit the degree of Fe^{2+} to Fe^{3+} electron hoping conduction at the equivalent lattice site (B-sites) resulting in increase in resistivity[6.32].

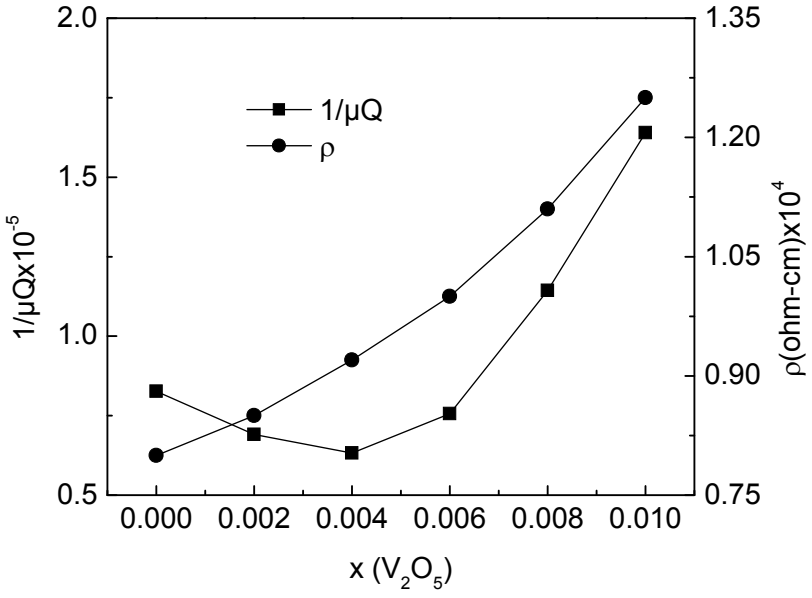

Fig. 6.7. Variation of normalized loss factor ($1/\mu Q$) and dc resistivity (ρ) with V_2O_5 addition.

High resistivity is a pre-requisite for high frequency applications of ferrites to counter eddy current losses, which degrade the ferrite performance. Eddy current loss is proportional to D^2f/ρ, where D is the thickness of the ferrite core, f is the frequency and ρ is the resistivity. Comparison of the eddy current loss at 1 kHz for increasing addition of V_2O_5 is shown in Table 6.1. The Table shows that the eddy current loss varies from 1.361×10^{-2} at 0% V_2O_5(x=0.00) to at 1 mol % V_2O_5. The minimum value of eddy current loss of the order of 8.712×10^{-3} is achieved for sample containing 1 mol% V_2O_5 addition. So, the eddy current loss of the prepared core materials decreases with the addition of V_2O_5 contents showing frequency extension for applications.

Table 6.1. Comparison of eddy current loss of $Ni_{0.65}Zn_{0.35}Fe_{1.96}O_4$ ferrite samples with V_2O_5 addition

V_2O_5 (in mol unit) x	d.c resistivity ρ (ohm-cm) $\times10^4$	Eddy current loss at 1 kHz
0.00	0.8	1.361×10^{-2}
0.002	0.85	1.281×10^{-2}
0.004	0.92	1.183×10^{-2}
0.006	1.00	1.089×10^{-2}
0.008	1.11	9.810×10^{-3}
0.01	1.25	8.712×10^{-3}

6.4 The ferrite system $Ni_{0.65}Zn_{0.35}Fe_{1.96}O_4$ + x CuO, where, x (in mol unit) = 0,0.005,0.01,0.015,0.20.

6.4.1 Physical Properties:

The x-ray diffraction studies of the ferrite system with the addition of CuO are used to obtain lattice constant values. The variations of the sintered density (d_s), lattice constant values (**a**), of all the samples are shown in Fig 6.8. The increase in density of the sintered samples up to 1 mol% CuO addition (x=0.01) can be observed from the figure. The inclusion of the low melting CuO in the composition of iron-deficient Ni-Zn ferrite enhances the chemical reactivity of the resulting mixture because it acts to some degree as a flux, CuO decomposes to form Cu_2O at 1026°C and Cu_2O melts at1235°C which is lower than the melting points of the other oxides in the Ni-Zn ferrite system. This facilitates the attainment of high degree of uniformity in the sintered body which in turn enhances the density. Highest value of density 5.024g/cc for sample containing 1 mol% CuO (x=0.01) is obtained. The decrease in sintered density as a result in the increment of porosity of sample containing 2.0 mol% CuO (x=0.02) is due to the segregations of second phase rich in copper. The lattice constant values of the ferrite system with the addition of CuO remains almost unaffected also shown in the Fig. 6.8. Though Cu^{2+} ions have larger ionic radius (0.73Å) than Fe^{3+} ions (0.64 Å), its inclusion into ferrite lattice results in the creation of Fe^{2+}ions which have an ionic radius of 0.74 Å. This results in no net change in the lattice constant values.

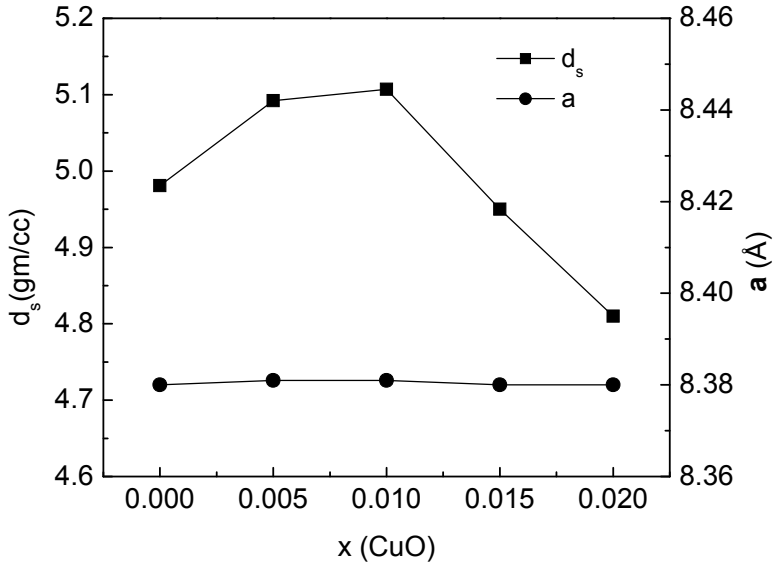

Fig. 6.8. Variation of sintered density (d_s) and lattice constant (**a**) with CuO addition.

6.4.2 Magnetic and Electrical Properties:

The variations of saturation magnetization (M_s) and Curie temperature (T_c) of all the samples are shown in Fig. 6.9. The increase in saturation magnetization up to 1 mol% CuO content (x=0.01) is due to increased density and an increase of resultant sublattice magnetic moment. The increase of Curie temperature due to presence of CuO up to 1 mol% (x=0.01) is also shown in Fig. 6.9. This increment is probably due to the fact that diamagnetic Cu^{2+} ions occupy octahedral sites (B-sites) of the ferrite lattice, as a result some of the Fe^{3+} ions may come out from octahedral to tetrahedral sites (A-sites) thereby increasing the A-B interaction [6.33]. This may cause the Curie temperature to increase. The higher value of Curie temperature for 1 mol% CuO (x=0.01) addition can be considered as showing better temperature stability in comparison with other samples.

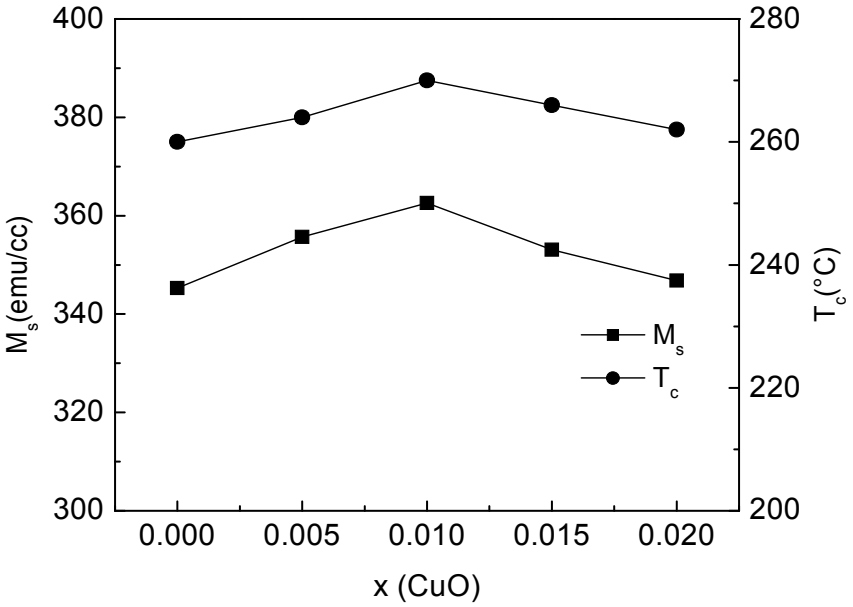

Fig. 6.9. Variation of Saturation magnetization (M_s) and Curie temperature (T_c) with CuO addition.

Frequency dependent initial magnetic permeability i.e. permeability spectra of all the samples are shown in Fig. 6.10. The frequency variation is plotted in logarithmic scale and μ′ is plotted in linear scale. The permeability spectra for all the samples show that as the frequency rises, the value of μ′ remains fairly constant upto certain higher frequencies for all the samples containing CuO.

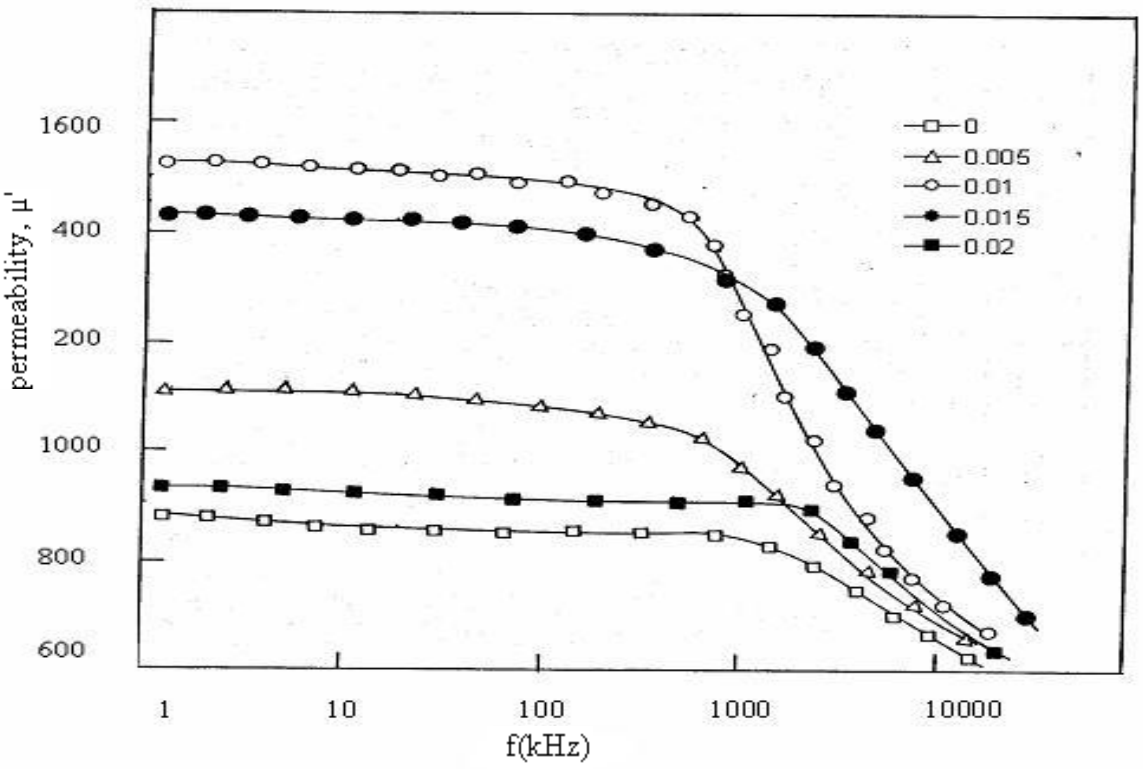

Fig. 6.10. Permeability spectra of the ferrite system with CuO addition

The variation of initial magnetic permeability (μ') at 100 kHz with increasing concentration of CuO is also shown in Fig. 6.11. The figure shows that there is a sharp increase in the permeability for the sample containing 1 mol% CuO addition (x=0.01). Highest value of μ'=1530 at 100 kHz is achieved for sample containing 1 mol% of CuO addition.

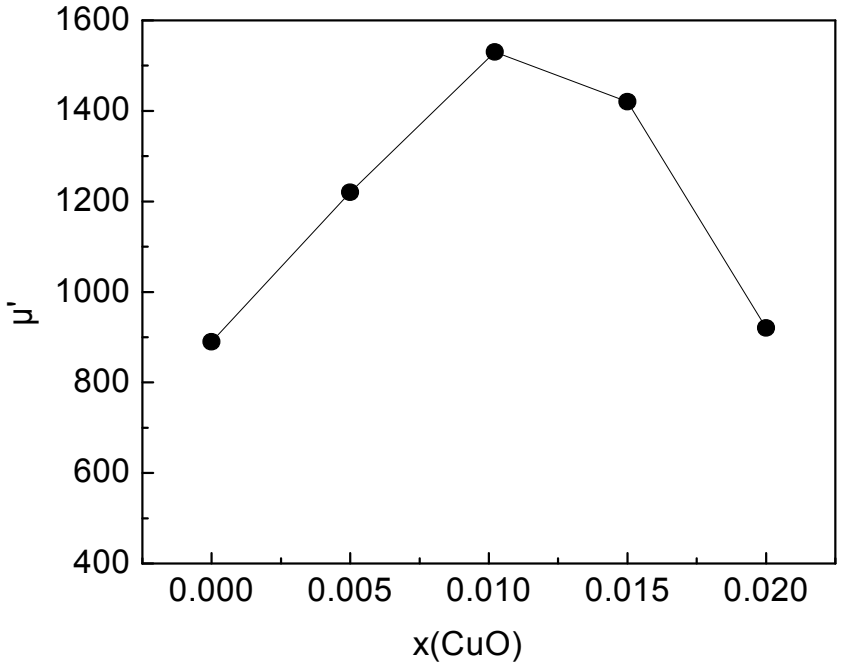

Fig. 6.11. Variation of initial magnetic permeability (μ′) at 100 kHz with CuO addition

This increase in permeability can not be due to densification alone. This is also due to the effect of CuO on the microstructure of the samples as shown in Fig. 6.12 (SEM microphotographs of the samples). For 1 mol% CuO (x=0.01) content sample, its microstructure consists of larger grains compared 0.5 mol% CuO (x=0.005) content and with little inter granular porosity, which is reflected in a sharp increase in permeability [6.34]. At 1.5 mol% CuO content (x= 0.015) permeability decreases, this is probably due to second phase which forms non-magnetic discontinuity around the ferrite grains. However, the better frequency stability up to 1.5 MHz for the sample containing 1.5 mol% CuO (x=0.015) is observed in the permeability spectra.

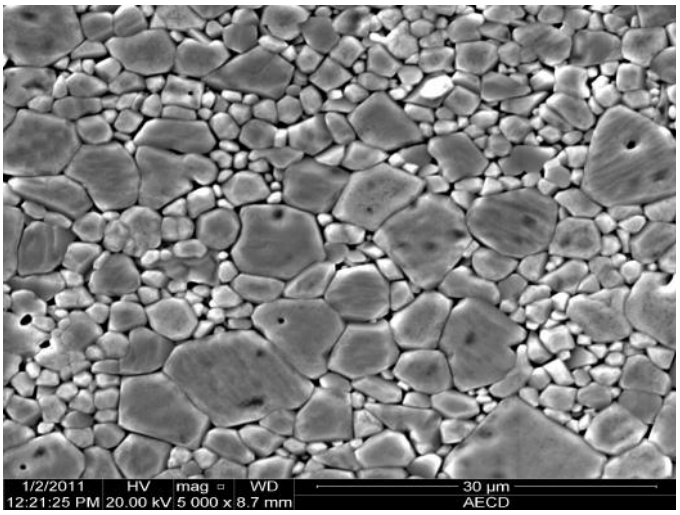

x=0.005

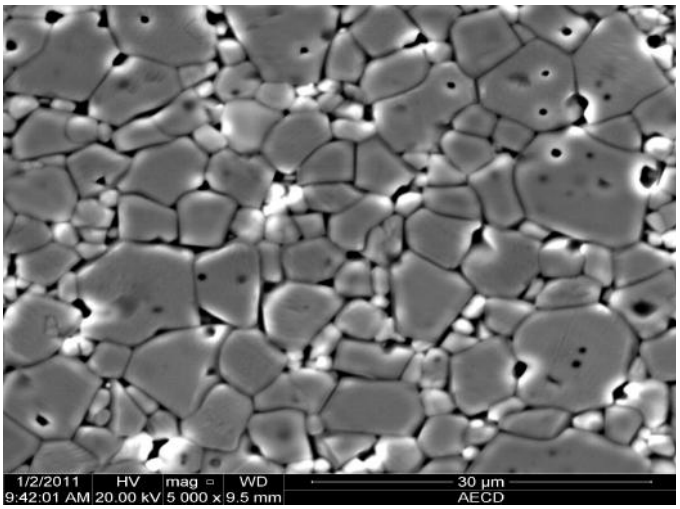

x=0.01

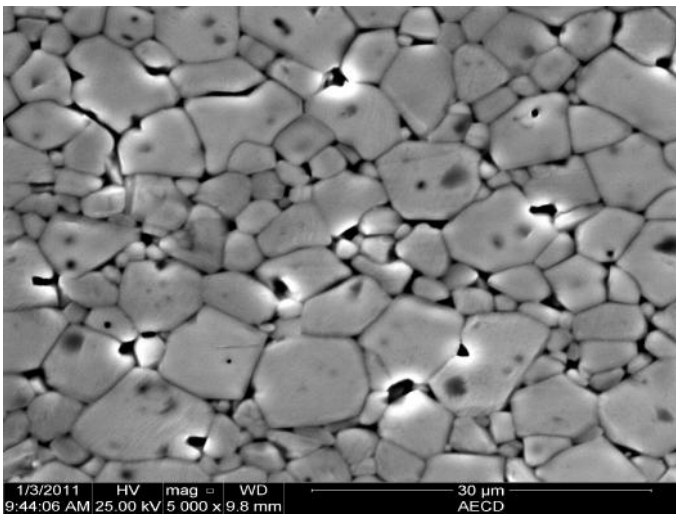

x=0.015

Fig. 6.12. SEM Microphotographs of $Ni_{0.65}Zn_{0.35}Fe_{1.96}O_4$ ferrite samples with CuO addition

The variations of normalized loss factor (1/μQ) and dc resistivity (ρ) of all the samples are shown in Fig. 6.13. As observed from the figure that the normalized loss factor first increases a little reaches a maximum value of 0.89×10^{-5} at 1 mol% CuO content and then decreases with increasing addition of CuO to 0.752×10^{-5} at 2 mol% CuO content. The minimum value of normalized loss factor of the order of 0.752×10^{-5} is achieved for sample containing 2 mol% of CuO addition.

The dc resistivity of the sample without CuO (x=0) addition is of the order of 0.8×10^{4} ohm-cm also shown in Fig. 6.13, while the resistivity of the samples with the addition of 2 mol% CuO reaches to the highest value of the order of 0.91×10^{5} ohm-cm. This ten fold increase of resistivity is due to the improved sintering due to presence of Cu which decreases the porosity and discourages over oxidation during cooling and hence limits the Ni^{2+}-Ni^{3+} conduction process [6.35].

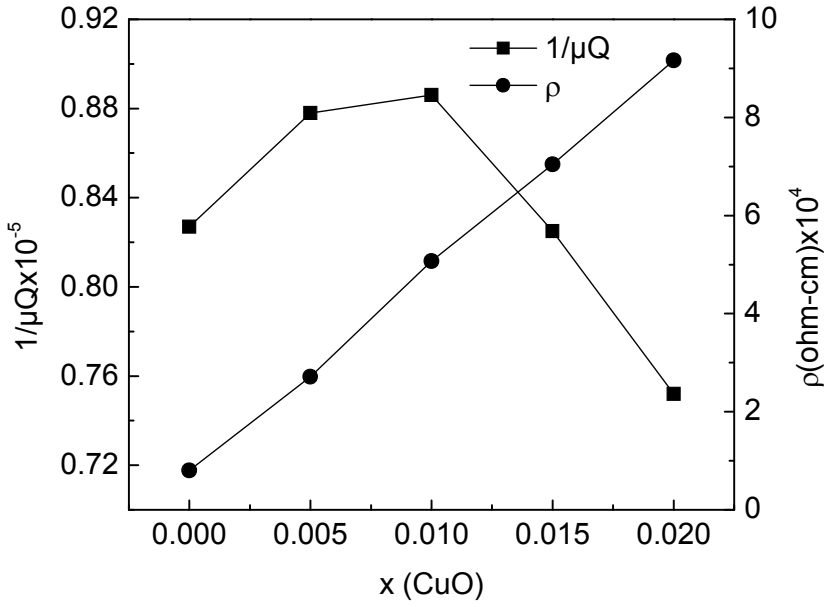

6.13. Variation of normalized loss factor (1/μQ) and dc resistivity (ρ) with CuO addition.

High resistivity is a pre-requisite for high frequency applications of ferrites to counter the eddy current losses, which degrade the ferrite performance. Eddy current loss is proportional to D^2f/ρ, where D is the thickness of the ferrite core, f is the frequency and ρ is the resistivity.

Comparison of the eddy current loss at 1 kHz for increasing CuO addition is shown in Table 6.2, it varies from 1.361×10^{-2} at 0% CuO (x=0.00) to 1.188×10^{-3} at 2 mol % CuO (x=0.02). The minimum value of eddy current loss of the order of 1.188×10^{-3} is achieved for sample containing 2 mol% CuO addition. Hence the eddy current loss decreases ten fold with the addition of CuO showing improvement of frequency range for application of the prepared core materials.

Table 6.2. Comparison of eddy current loss of $Ni_{0.65}Zn_{0.35}Fe_{1.96}O_4$ ferrite samples with CuO addition

CuO (in mol unit) x	d.c resistivity ρ(ohm-cm) $\times10^4$	Eddy current loss at 1 kHz
0.00	0.8	1.361×10^{-2}
0.005	2.71	4.018×10^{-3}
0.010	5.07	2.147×10^{-3}
0.015	7.04	1.546×10^{-3}
0.020	9.16	1.188×10^{-3}

6.5 The Ferrite system $Ni_{0.65}Zn_{0.35}Fe_{1.96}O_4$+ xIn_2O_3, where, x (in mol unit)= 0, 0.005, 0.01,0.015, 0.02, 0.025, 0.03 and 0.035.

6.5.1 Physical Properties:

The x-ray diffraction studies of the ferrite system with the addition of In_2O_3 are used to obtain lattice constant values. Figure 6.14 shows the variation of sintered density (d_s) and lattice constant (**a**) of the ferrite system with the addition of In_2O_3. Sintered density increases with the increasing addition of low melting In_2O_3 (melting point 680°C) of the ferrite system. The inclusion of In_2O_3 in this composition of Ni-Zn ferrite enhances the chemical reactivity of the resulting mixtures because it acts to some degree as a flux. So, the effect of In_2O_3 can be explained by the formation of liquid phase on the grain surface of the ferrite due to reaction of In_2O_3 with the spinel phase at 1250°C sintering temperature which eventually promotes densification. The increment in lattice constant can be defined on the basis of ionic radius of the additive ions. The ionic radius of In^{3+} ions (0.91Å) is larger than the displaced Fe^{3+} (0.64Å) ions, so the lattice bulges and the lattice constant increases with the addition of In_2O_3 [6.36].

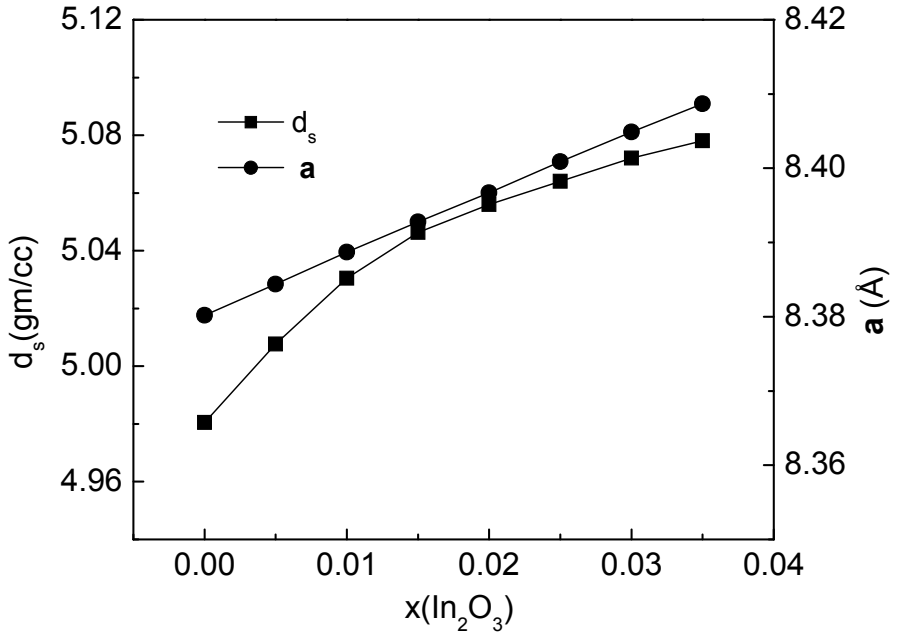

Fig.6.14. Variation of sintered density (d_s) and lattice constant (**a)** with In_2O_3 addition.

6.5.2 Magnetic and Electrical Properties:

The observed variation of saturation magnetization (M_s) and Curie temperature (T_c) with the increasing addition of In_2O_3 is shown in Fig. 6.15. Saturation magnetization of the ferrite system decreases almost linearly and Curie temperature decreases linearly with the increase of In_2O_3 addition. The decrease in magnetization with increased concentration of indium is possibly because diamagnetic In^{3+}ions occupy B-sites (octahedral sites) and replace Fe^{3+} ions from the B-sites [6.37]. When indium ions occupy B-sites and replace B-sites Fe^{3+}ions, the magnetization of B-sublattice (M_B) decreases keeping the magnetization of A-sublattice (M_A) unchanged, which in turn weakens A-B exchange interaction. Thus the resultant mangnetization according to $M= M_B-M_A$ is expected to decrease, hence the magnetization decreases. It is well-known that the replacement of Fe^{3+} ions by the paramagnetic or diamagnetic ions results in the fall of Curie temperature [6.38]. In this case, it is also true because here A-B exchange interaction becomes weak, so Curie temperature of the ferrite system decreases with the addition of In_2O_3.

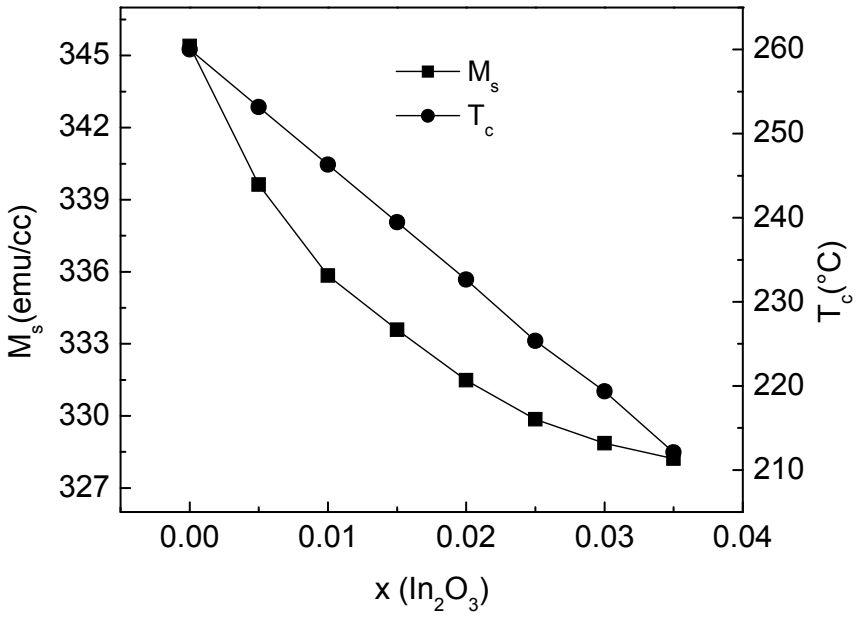

Fig. 6.15. Variation of Saturation magnetization (M_s) and Curie temperature (T_c) with In_2O_3 addition.

The frequency dependent initial magnetic permeability spectra of the ferrite system with the addition of In_2O_3 is shown in Fig. 6.16. The frequency variation is plotted in logarithmic scale and μ′ is plotted in linear scale. The permeability spectra for all the samples show that as the frequency rises permeability increases first and then remains fairly constant upto a certain frequency range.

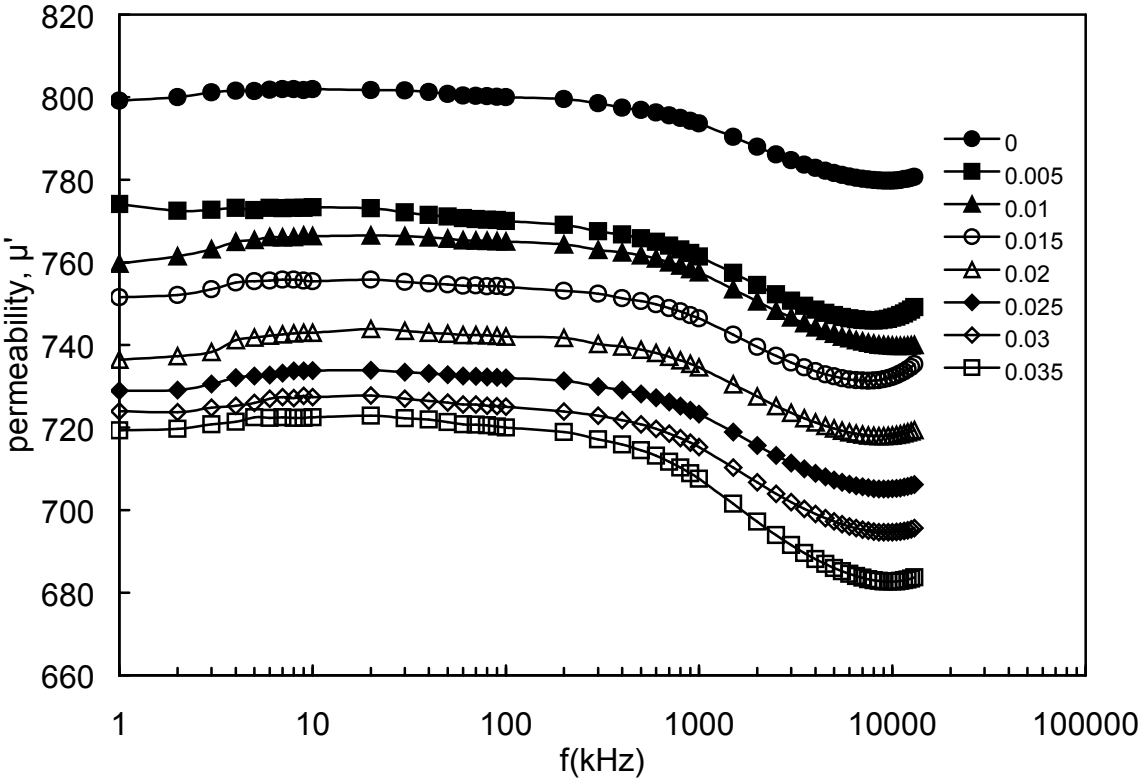

Fig. 6.16 Frequency dependent initial magnetic permeability spectra of the ferrite system with In_2O_3 addition.

The variation of initial magnetic permeability (μ′) at 100 kHz as also shown in Fig. 6.17 decreases with increased addition of indium concentration. The observed variation in initial permeability may be explained by the following considerations: the initial permeability of a ferrimagnetic material depends on many factors like reversible displacement of domain wall, bulging of domain walls, mictrostructural parameters viz., average grain size and intra-granular porosity [6.39-6.41]. The grain size variation of the material as shown in the scanning electron microphotographs (shown in Fig.6.18) is significant for considerable fall in initial permeability with increasing additions of In_2O_3.

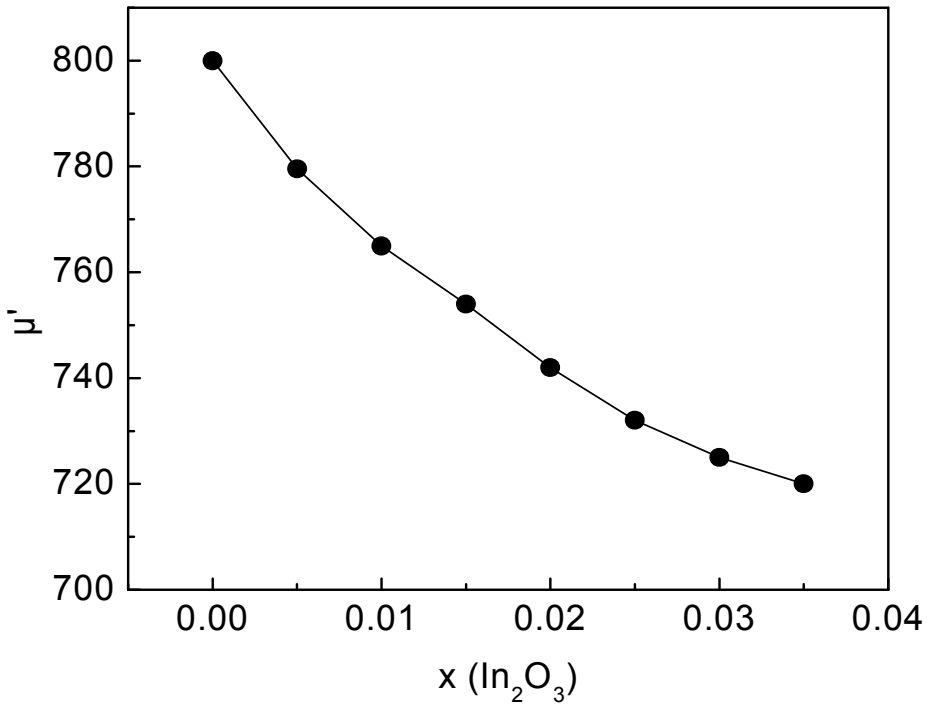

Fig 6.17. Variation of initial magnetic permeability (μ′) at 100 kHz with In_2O_3 addition.

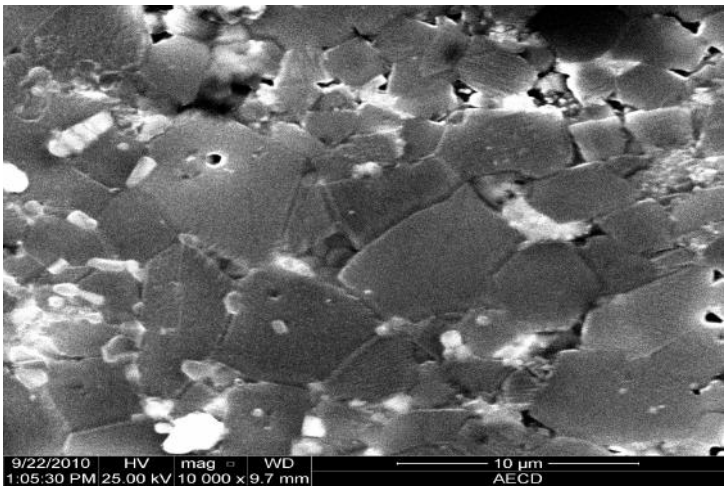

In_2O_3(x=0.01)

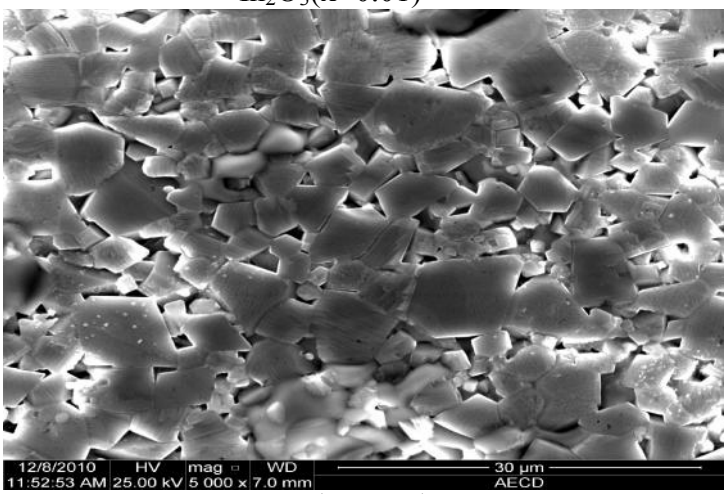

In_2O_3 (x=0.02)

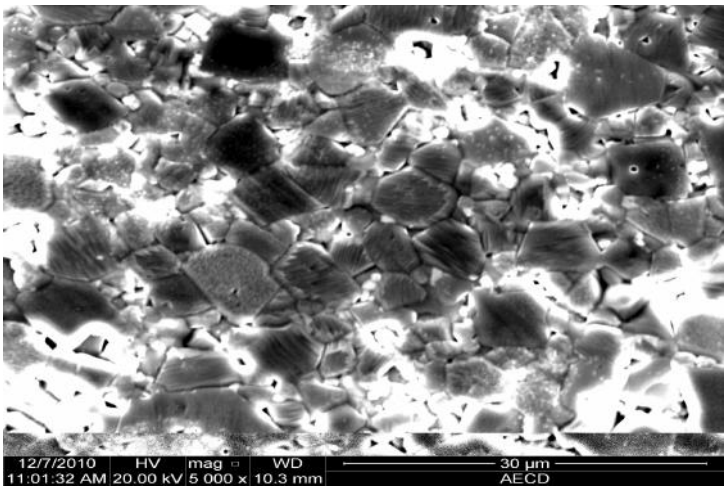

In_2O_3 (x=0.03)

Fig.6.18. SEM Microphotographs of $Ni_{0.65}Zn_{0.35}Fe_{1.96}O_4$ ferrite sample with In_2O_3 addition.

The observed variations of normalized loss factor (1/μQ) and dc resistivity (ρ) are shown in Fig.6.19. The normalized loss factor first decreases, reaches a minimum value of 0.479×10^{-5} and then increases with the addition of In_2O_3. The minimum value of normalized loss factor of the order of 0.479×10^{-5} is achieved for sample containing 1.5 mol% In_2O_3 addition. The dc resistivity of the samples increases almost linearly with the addition of In_2O_3. The minimum value of dc resistivity of the order of 2.69×10^{4} ohm-cm is achieved for sample containing 3.5 mol% of In_2O_3 addition. As mentioned earlier In^{3+} ions occupy B-sites (octahedral sites) which reduces the degree of Fe^{2+} to Fe^{3+} electron hoping conduction in this sites and contribute to increase in the resistivity. High resistivity is a pre-requisite for high frequency applications of ferrites to counter the eddy current losses, which degrade the ferrite performance.

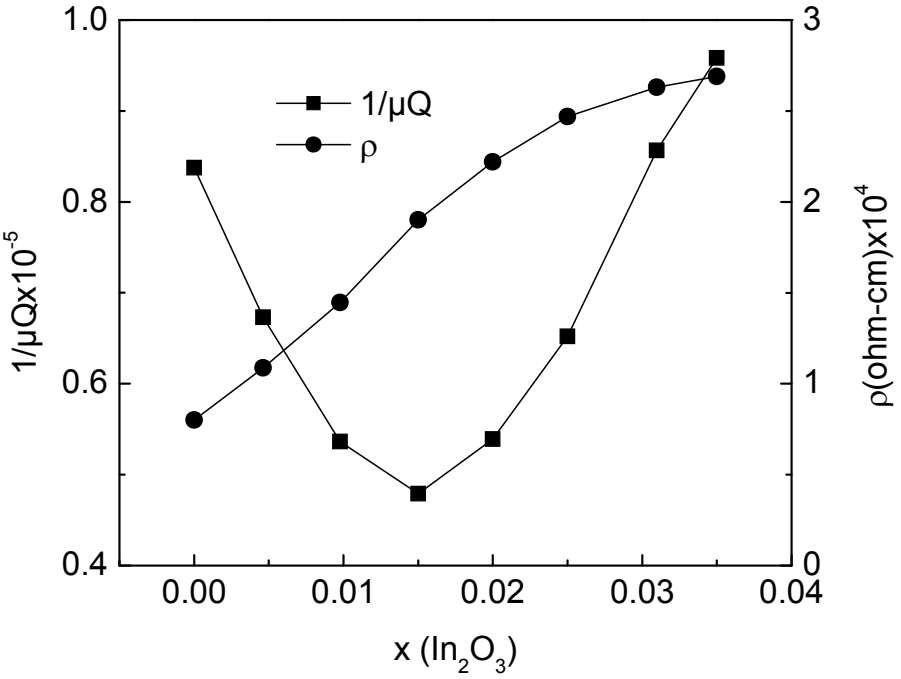

Fig. 6.19. Variation of normalized loss factor (1/μQ) and dc resistivity (ρ) with In_2O_3 addition.

Comparison of the eddy current loss at 1 kHz for increasing addition of In_2O_3 is shown in Table 6.3. The Table shows the eddy current loss varies from 1.36×10^{-2} at 0% In_2O_3 (x=0.00) to 4.048×10^{-3} at 3.5 mol% of In_2O_3. Hence the ten fold decrease of the eddy current loss with the addition of In_2O_3 shows improvement of the frequency range for applications of the prepared core materials.

Table 6.3. Comparison of eddy current loss of $Ni_{0.65}Zn_{0.35}Fe_{1.96}O_4$ ferrite samples with In_2O_3 addition

In_2O_3 (in mol unit) x	d.c resistivity ρ(ohm-cm) $\times10^4$	Eddy current loss at 1 kHz
0.00	0.8	1.361×10^{-2}
0.005	1.08	1.008×10^{-2}
0.010	1.44	7.562×10^{-3}
0.015	1.90	5.731×10^{-3}
0.020	2.22	4.905×10^{-3}
0.025	2.47	4.408×10^{-3}
0.030	2.63	4.140×10^{-3}
0.035	2.69	4.048×10^{-3}

6.6. The ferrite system $Ni_{0.65}Zn_{0.35}Fe_{1.96}O_4$+ xEu_2O_3, where, x (in mol unit)= 0, 0.005, 0.01,0.015, 0.02, 0.025, 0.030,0.035.

6.6.1 Physical Properties:

The x-ray diffraction studies of the ferrite system with the addition of Eu_2O_3 are used to obtain lattice constant values. The observed variation of the sintered density (d_s) and lattice constant values (**a**) of the ferrite system with the addition of Eu_2O_3 is shown in Fig. 6.20. The sintered density of the samples increases upto 2 mol% Eu_2O_3, (x= 0.02) and then decreases with the increasing addition of Eu_2O_3. The inclusion of the low melting Eu_2O_3 (melting point 623°C) in the composition of iron-deficient Ni-Zn ferrites increases the chemical reactivity of the resulting mixture and facilitates the attainment of high degree uniformity in the sintered body which in turn enhances the density. The increase in lattice constant as shown in the figure can be explained by considering the ionic radius of the additive ions. The ionic radius of Eu^{3+} (0.947 Å) is larger than the displaced Fe^{3+} (0.64 Å) ions, so the lattice bulges and the lattice constant increases.

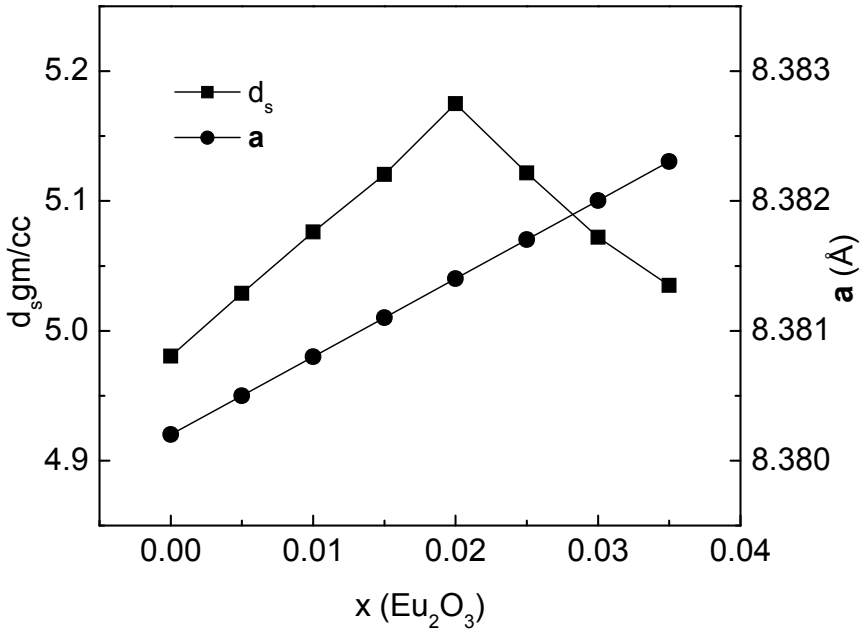

Fig. 6.20. Variation of sintered density (d_s) and lattice constant (**a**) with Eu_2O_3 addition

6.6.2 Magnetic and Electrical Properties:

Figure 6.21 shows the variation in saturation magnetization (M_s) and Curie temperature (T_c) of the samples with increasing addition of Eu_2O_3. The figure shows that magnetization increases up to 1.5 mol% Eu_2O_3, (x=0.015) and then decreases with further addition of Eu_2O_3. To explain the observed variation in saturation magnetization the following possibilities may be considered: (i) For Eu_2O_3 concentration upto x= 0.015, Eu^{3+} ions (antiferromagnetic) occupy A-sites and replace ferromagnetic Fe^{3+} ions. As a result, A-sublattice magnetization (M_A) decreases keeping the magnetization of B-sublattice (M_B) constant. Thus the resultant magnetization according to $M=M_B-M_A$ is expected to increase, hence the magnetization increases. (ii) For Eu_2O_3 concentration beyond x=0.015, Eu^{3+} ions occupy B-sites and replace B-site's Fe^{3+} ions. So, the magnetization of B-sublattice decreases keeping the magnetization of A-sublattice constant, which in turn weakens A-B exchange interaction. Thus the resultant magnetization according to $M= M_B-M_A$ is expected to decrease, hence the magnetization decreases. As shown in the figure, Curie temperature increases up to 2 mol% Eu_2O_3 (x= 0.02) due to the enhancement of A-B exchange interaction, because of the occupation of Eu^{3+} ions on A-sites. Beyond 2 mol% Eu_2O_3 the Curie temperature decreases due to the weakening of A-B exchange interaction, because of the occupation of Eu^{3+} ions on B-sites.

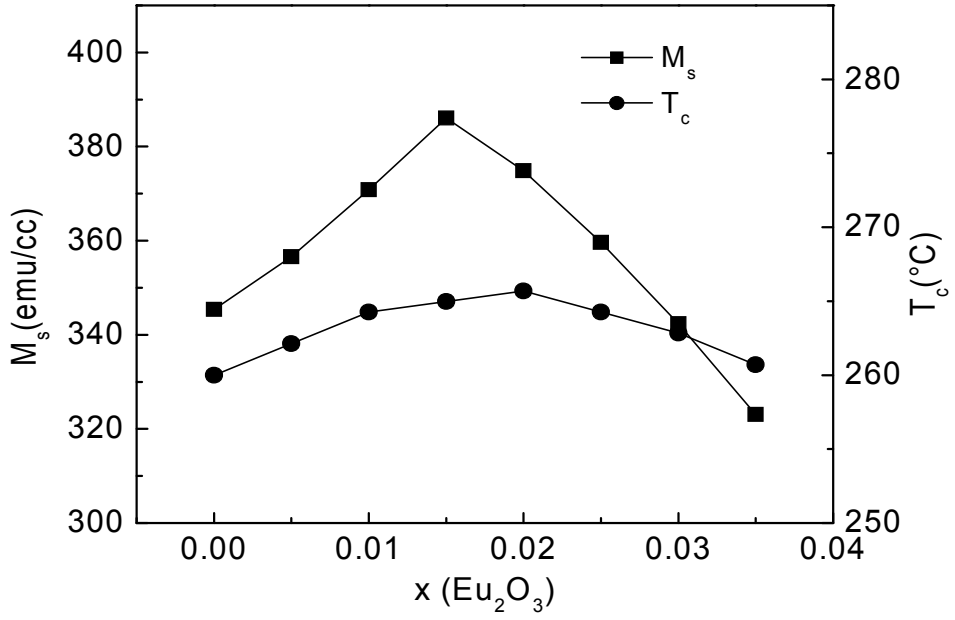

Fig. 6.21. Variation of Saturation magnetization (M_s) and Curie temperature (T_c) with Eu_2O_3 addition.

Frequency dependent initial magnetic permeability spectra of the ferrite system with Eu_2O_3 addition is shown in Fig 6.22. The frequency variation is plotted in logarithmic scale and μ′ is plotted in linear scale. The permeability spectra for all the samples show that as the frequency rises the value of μ′ remains fairly constant upto certain higher frequency ranges for all the samples containing Eu_2O_3 addition.

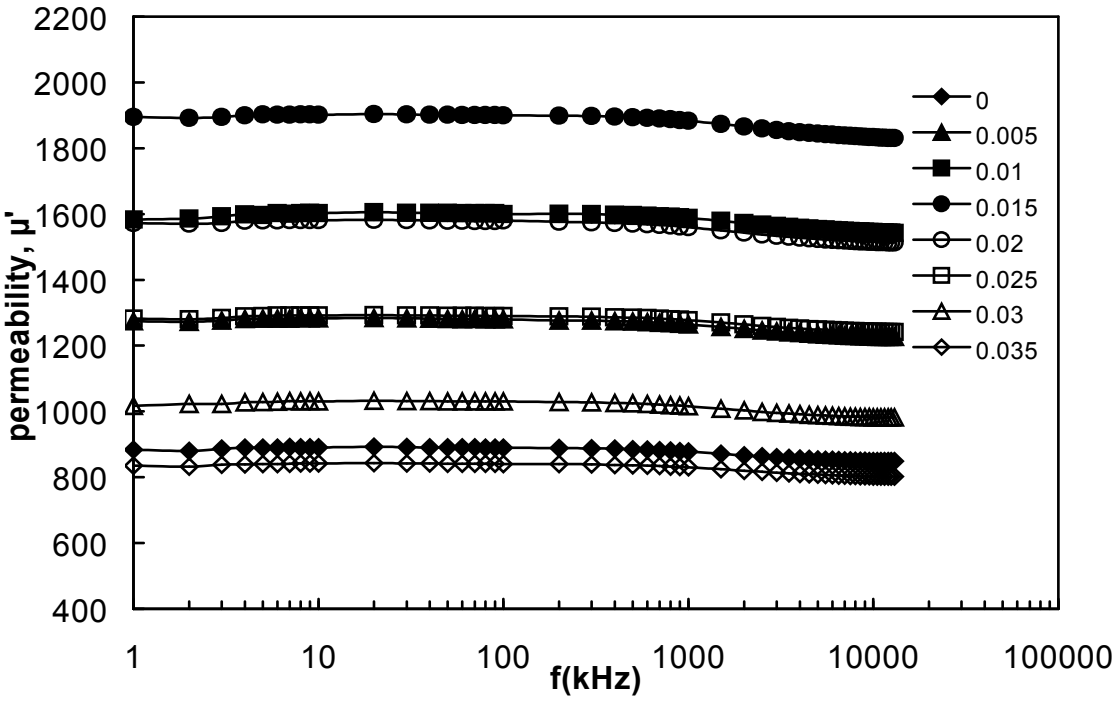

Fig. 6.22. Frequency dependent initial magnetic permeability (μ′) with Eu_2O_3 addition

The variation of initial magnetic permeability (μ′) at 100 kHz of the ferrite system with increasing concentration of Eu_2O_3 is also shown in Fig. 6.23. It is observed that an appreciable increase in permeability up to 1.5 mol% Eu_2O_3, (x=0.015) occurs. Maximum value of μ′ = 1900 at 100 kHz is achieved for sample containing 1.5 mol% of Eu_2O_3 addition. It is known that the permeability is related to two different magnetizing mechanisms; the spin rotational magnetization and the domain wall motion. Domain wall motion is affected by the grain size and enhanced with the increase of the grain size. The grain growth is a result of interparticle mass transport, possible explanation may be sought in terms of the influence of Eu ions on the diffusion process [6.42]. The grain size variation of the material as shown in the scanning electron microphotographs of Fig. 6.24 is significant for considerable variation in initial permeability with increasing additions of Eu_2O_3.

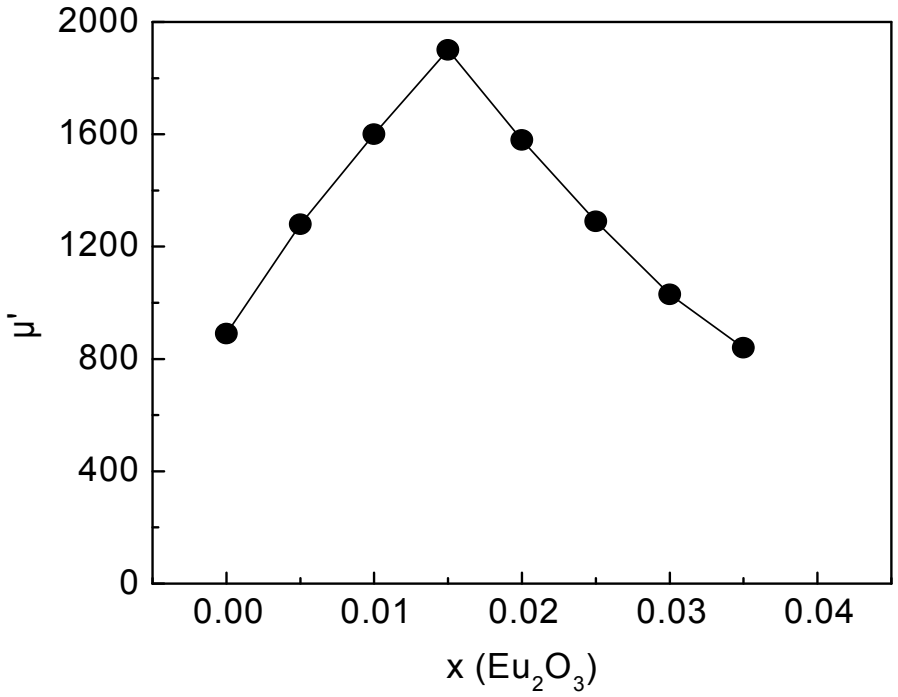

Fig. 6.23. Variation of initial magnetic permeability (μ′) at 100 kHz with Eu_2O_3 addition.

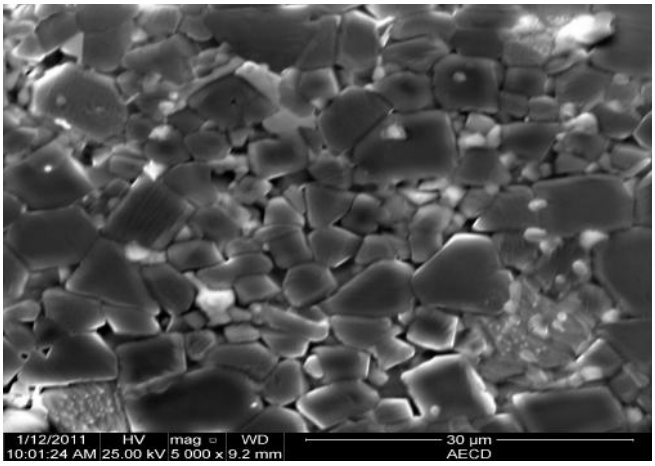

x=0.01

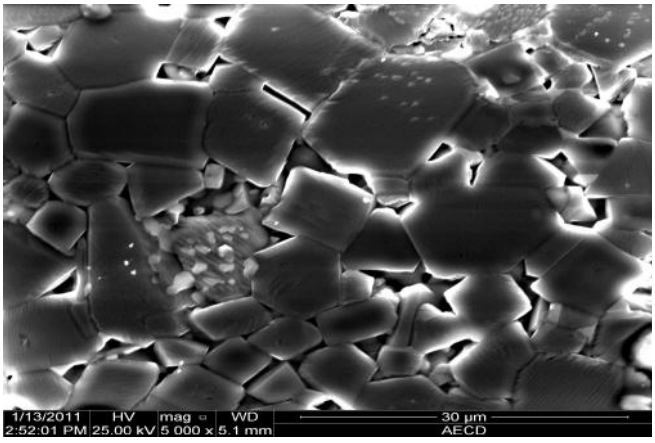

x=0.015

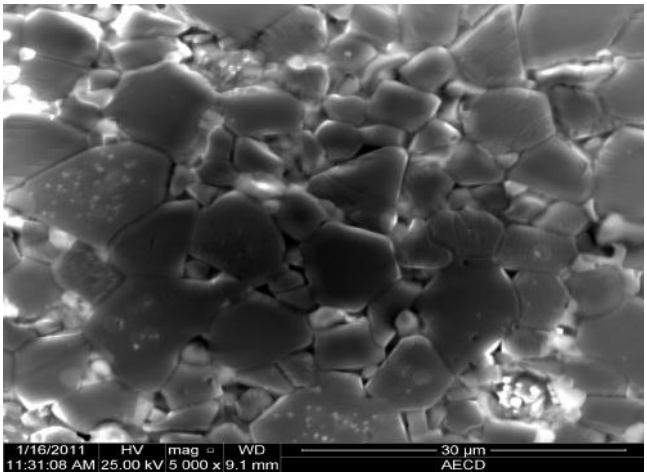

x=0.02

Fig. 6.24. SEM Microphotographs of $Ni_{0.65}Zn_{0.35}Fe_{1.96}O_4$ ferrite sample with Eu_2O_3 addition

The variation of normalized loss factor (1/μQ) at 100 kHz and the dc resistivity (ρ) of the ferrite system with increasing concentration of Eu_2O_3 is shown in Fig. 6.25. The normalized loss factor first decreases, reaches a minimum value of 0.54×10^{-5} at 1.5 mol% of Eu_2O_3 content and then increases with further addition of Eu_2O_3. The minimum value of normalized loss factor of the order of 0.54×10^{-5} is achieved for sample containing 1.5 mol% of Eu_2O_3 addition. The dc resistivity of the ferrite samples increases with increasing addition of Eu_2O_3, up to 2 mol% (x=0.02) and then decreases with further addition of Eu_2O_3. The maximum value of dc resistivity of the order of 2.42×10^4 ohm-cm is achieved for sample containing 2 mol% of Eu_2O_3 addition. Resistivity is influenced by the microstructural factors such as grain size, porosity and grain boundary area. Larger the grain size lesser would be the number of grain boundaries [6.43]. Increase in grain growth resulting in a corresponding decrease in the number of grain boundaries leading thereby to a increase in resistivity. High resistivity is a pre-requisite for high frequency applications of ferrites to counter the eddy current losses, which degrade the ferrite performance.

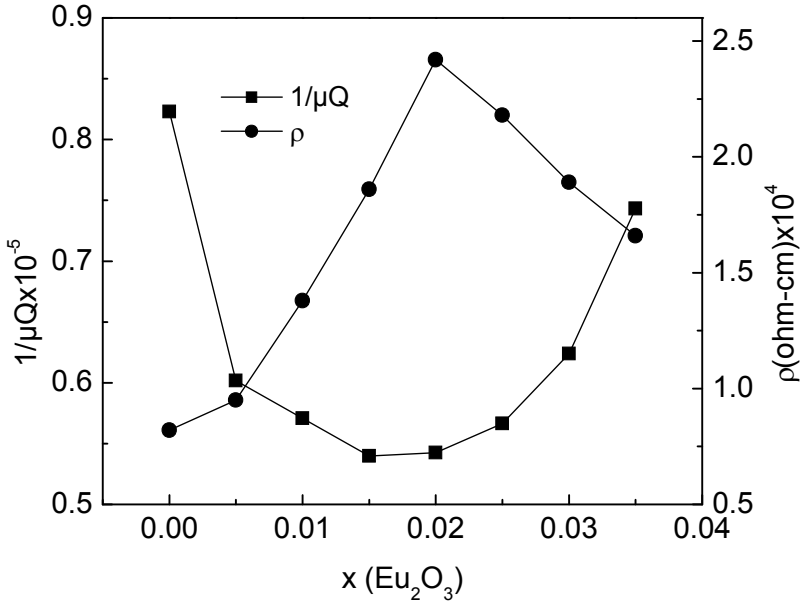

Fig. 6.25. Variation of normalized loss factor (1/μQ) and dc resistivity (ρ) with Eu_2O_3 addition

Comparison of eddy current loss at 1 kHz for increasing addition of Eu_2O_3 is shown in Table 6.4. The Table shows that the eddy current loss varies from 1.361×10^{-2} at 0% Eu_2O_3 (x=0.00) to 4.995×10^{-3} at 2.5 mol% (x=0.025) Eu_2O_3. The minimum value of eddy current loss of the order of 4.50×10^{-3} is achieved for sample containing 2 mol% Eu_2O_3 addition. Hence the ten fold decrement of the eddy current loss with the addition of Eu_2O_3 shows improvement of the frequency range for applications of the prepared core materials.

Table 6.4. Comparison of eddy current loss of $Ni_{0.65}Zn_{0.35}Fe_{1.96}O_4$ ferrite samples with Eu_2O_3 addition

Eu_2O_3 (in mol unit) x	d.c resistivity $\rho\times10^4$	Eddy current loss at 1 kHz
0.00	0.8	1.361×10^{-2}
0.005	0.95	1.146×10^{-2}
0.010	1.38	7.891×10^{-3}
0.015	1.86	5.854×10^{-3}
0.020	2.42	4.50×10^{-3}
0.025	2.18	4.995×10^{-3}
0.030	1.89	5.761×10^{-3}
0.035	1.66	6.560×10^{-3}

.

Study of the influence of CuO, V_2O_5, Eu_2O_3 and In_2O_3 addition on the magnetic and electrical properties of iron-excess Mn-Zn ferrites

6.7 Introduction

Manganese-zinc ferrites (Mn-Zn ferrite) are important as core materials over a wide range of frequencies starting from few hundred Hz to several MH_Z. The high permeability and high electrical resistivity in this frequency range make them particularly useful for the telecommunication industry. Because of their applications in telecommunication industry Mn-Zn ferrites have been investigated widely for past several years [6.44-6.55]. Ferrite properties are very sensitive to the presence of impurities [6.56-6.59]. The addition of an impurity produces change in electromagnetic properties, the knowledge of these changes provides information on the kind and the amount of impurity required for obtaining a high quality ferrite for any particular application. Different amounts of additives for obtaining a specific property have been reported by different investigators [6.60-6.63].

It is known that the iron excess Mn-Zn ferrites have a high permeability because they have an extremely low value of a magnetocrystalline anisotropy and magnetostriction constants combined with its high saturation magnetization [6.64-6.65]. Since such ferrites contain a large amount of Fe^{2+} ions, they have a low electrical resistivity which result in large eddy current loss in high frequency use. However, the electrical resistivity of these ferrites is known to be increased by adding small amount of impurities (additives) [6.66-6.67].

Mn-Zn ferrites are extensively used as core materials for low frequency radio and television components, such as; inductors for frequencies up to about 200 kHz, antenna rods for medium and long wave broadcast bands, television line scanning transformers, deflection yokes and power transformers for the frequency range of 700 Hz to 100 kHz. The primary requirements for Mn-Zn ferrites in these core components are high permeability and low losses. High permeability is required to decrease the stray inductance and to keep the dimensions as small as possible. The transformer is usually terminated by a matched load, so large losses may cause overheating which must be avoided anyway if there are stringent restriction on the amplitude and phase characteristics and amount of distortion in the transformer. For applications where large signals have to be transformed

(as in television line scanning transformers) a high magnetization is desired. The resistivity for Mn-Zn ferrites of these core materials also should be high to avoid eddy current and other associated losses.

It is well known that the addition of small quantities of several oxides some what improves the characteristic properties of Mn-Zn ferrites [6.68-6.72]. Their major benefits, however in magnetic properties namely high permeability, reduced losses, improved temperature stability and frequency extension of the properties. **In this study the influence of CuO, V_2O_5, Eu_2O_3 and In_2O_3 addition on the magnetic and electrical properties of iron-excess Mn-Zn ferrites have been investigated thoroughly.**

6.8. X-ray Diffraction Analysis of $Mn_{0.451}Zn_{0.484}Fe_{2.065}O_4$ Ferrite

The X-ray diffraction of the sintered ferrite powder of the system was performed using Philips X'PERT PRO X-ray Diffractometer by using Cu-Kα radiation in the range of 2θ=25° to 65°in steps of 0.02°. X-ray diffraction pattern of the ferrite system is shown in Fig. 6.26. The XRD pattern was indexed and crystalline cubic lattice was observed. The XRD result indicates that the ferrite material shows single phase cubic spinel structure.

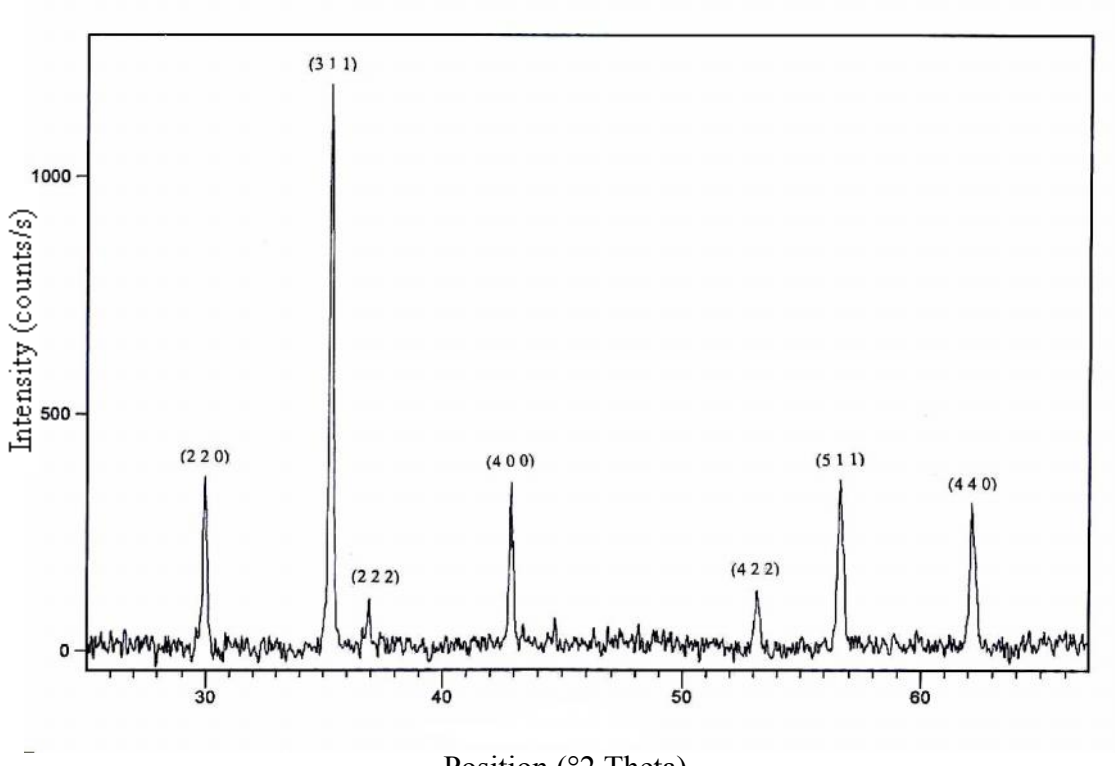

Fig. 6.26. XRD pattern of sintered $Mn_{0.451}Zn_{0.484}Fe_{2.065}O_4$ ferrite.

6.9 Ferrite system $Mn_{0.451}Zn_{0.484}Fe_{2.065}O_4$ +x CuO; where x(in mol unit)= 0, 0.01,0.02,0.03,0.04, 0.05, 0.06

6.9.1 Physical Properties:

The x-ray diffraction studies of the ferrite system with the addition of CuO are used to obtain lattice constant values. The variations of the sintered density (d_s) and lattice constant (**a**) of the samples containing CuO addition are shown in Fig. 6.27. It can be observed from the figure that sintered density of the samples increases from 4.879g/cc at zero mol % CuO (x= 0.00) to 5.13 g/cc at 4 mol % CuO (x=0.04) and then decreases beyond x=0.04. The inclusion of CuO in this composition of Mn-Zn ferrite enhances the chemical reactivity because it acts to some degree as a flux, CuO decomposes to form Cu_2O at 1026°C and Cu_2O melts at 1235°C. So, the effect of CuO can be explained by the development of liquid phase on the grain surface due to the reaction of CuO with spinel phase of the ferrite system at 1250°C sintering temperature which promotes densification [6.73]. The decrease in density beyond 4 mol % CuO content (x=0.04) is due to increased intergranular porosity resulting from discontinuous grain growth. The lattice constant values of the ferrite system by the addition of CuO remains almost unaffected (also shown in Fig.6.27). Though Cu^{2+} ions have larger ionic radius (0.73 Å) than Fe^{3+} ions (0.64 Å), its inclusion into the ferrite lattice results in the creation of Fe^{2+} ions which have an ionic radius of 0.74 Å. So, there is no appreciable change in the lattice constant of ferrite system with CuO addition.

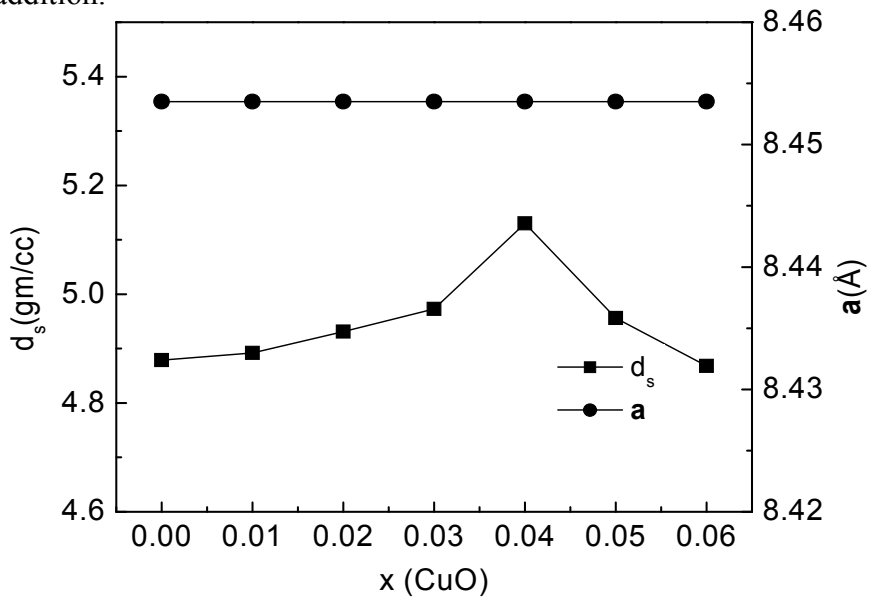

Fig. 6.27. Variation of sintered density (d_s) and lattice constant (**a**) with CuO addition.

6.9.2. Magnetic and Electrical Properties:

Variations of the saturation magnetizations (M_s) and Curie temperature (T_c) of all the samples with the addition of CuO are shown in Fig. 6.28. It can observed from the graph of the figure that the saturation magnetization of the samples increase almost linearly up to 3 mol% CuO (x=0.03), and increase abruptly up to 4 mol% CuO (x=0.04) and then decrease a little. The increment of saturation magnetization ($M_s=\sigma_s d_s$) is due to the enhancement of density with the increasing concentration of CuO. The little decrement of saturation magnetization is due to the decrease of sintered density. The little decrement of Curie temperature (T_c) from 120°C to 106°C (also shown in Fig. 6.28) is due to the decrease of A-B interaction for diamagnetic Cu^{2+} presence in the octahedral sites (B-sites) of the ferrite lattice [6.74].

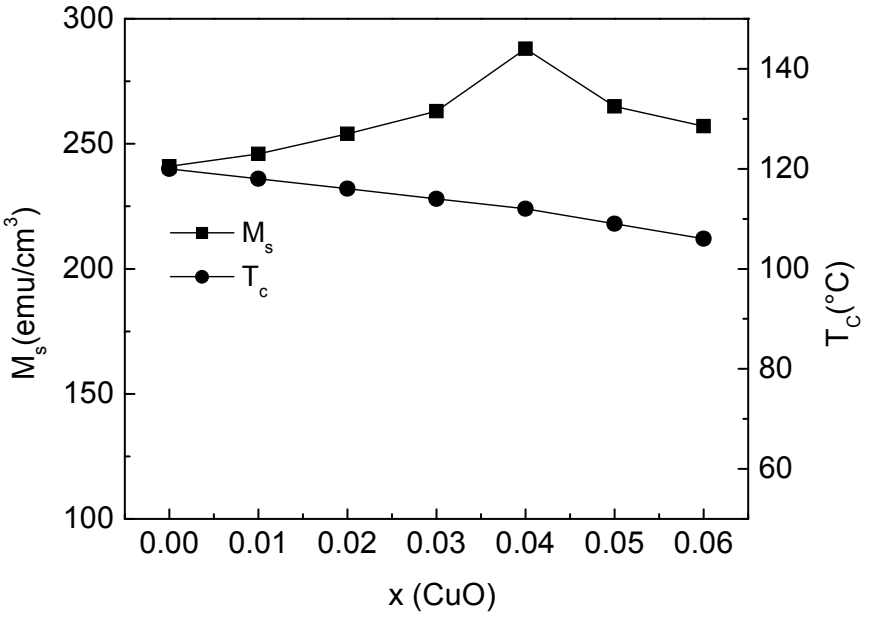

Fig. 6.28. Variation of saturation magnetization (M_s) and Curie temperature (T_c) with CuO addition.

Frequency dependent initial permeability (μ') for all the samples from 0 to 6 mol% CuO (x=0.06) content is shown in Fig. 6.29. The frequency variation is plotted in logarithmic scale and μ′is plotted in linear scale. The permeability spectra for all the samples show that as the frequency rises, the value of μ' rises up to a particular frequency, then falls a little and remain fairly constant up to higher frequencies for all the samples containing CuO.

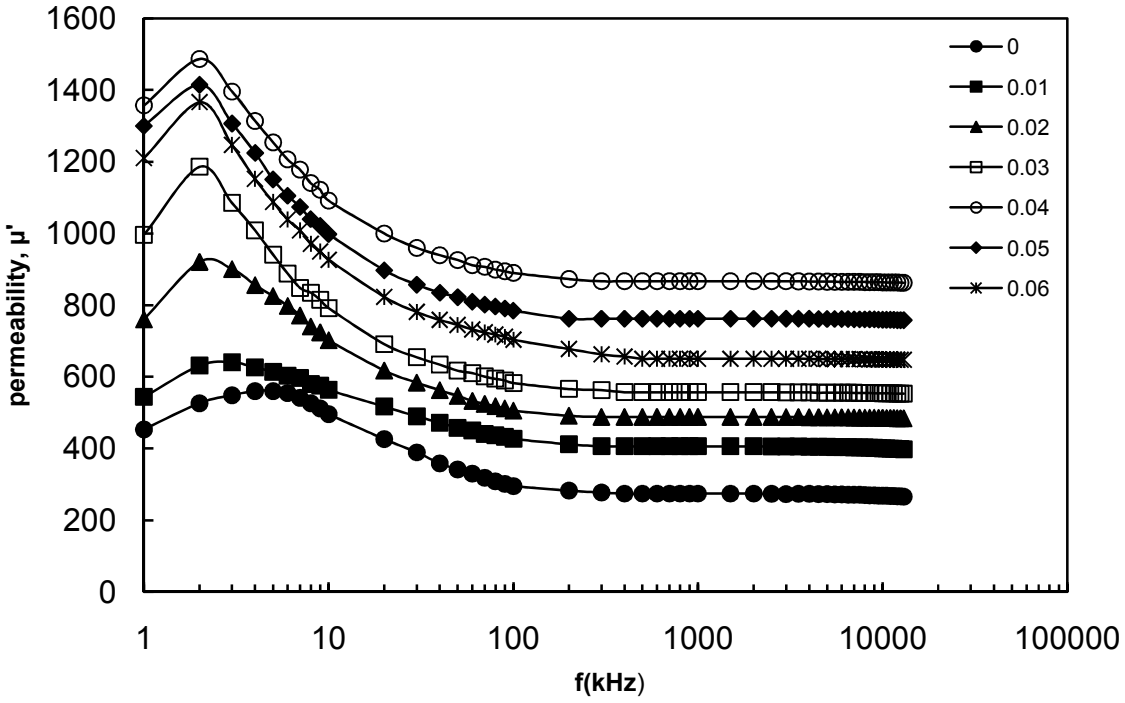

Fig.6.29. Frequency dependent initial magnetic permeability with CuO addition.

The variation of μ' at 100 kHz of the investigated ferrite system with increasing addition of CuO is also shown in Fig. 6.30. It is observed from the figure that maximum initial permeability is obtained for sample containing 4 mol% of CuO (x=0.04). Maximum value of μ′= 900 at 100 kHz is achieved for sample containing 4 mol% CuO addition. This increase in permeability is due to the effect of CuO on the microstructure of the samples as shown in Fig. 6.31 (SEM microphotographs). For 4 mol% CuO content, the microstructure of the ferrite sample consists of larger grains compared to samples of other CuO contents and with little intragranular porosity [6.75].

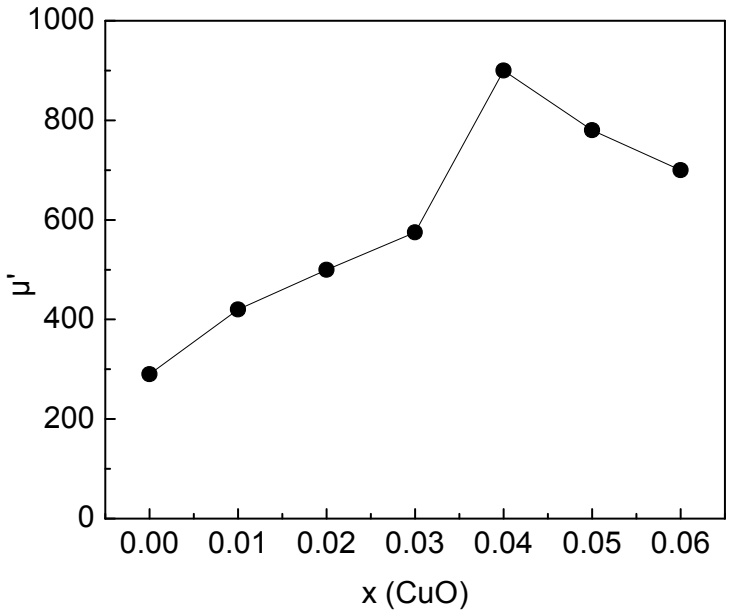

Fig. 6.30. Dependence of initial magnetic permeability (μ′) at 100 kHz with CuO addition.

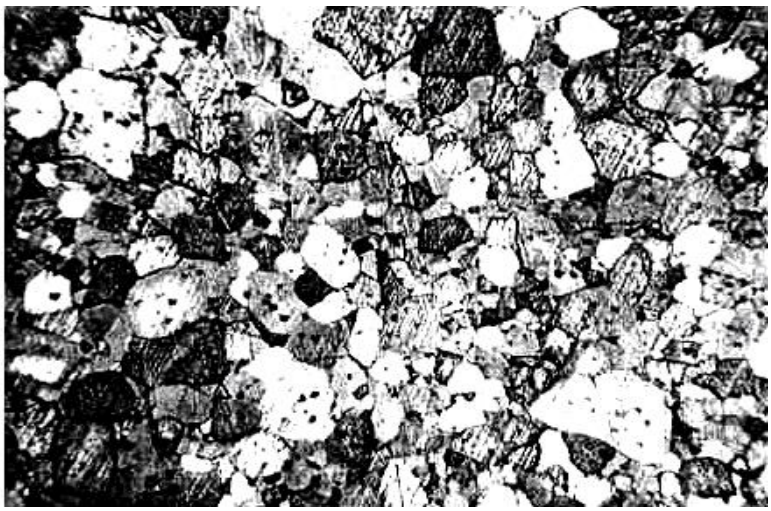

x=0.02

x=0.04

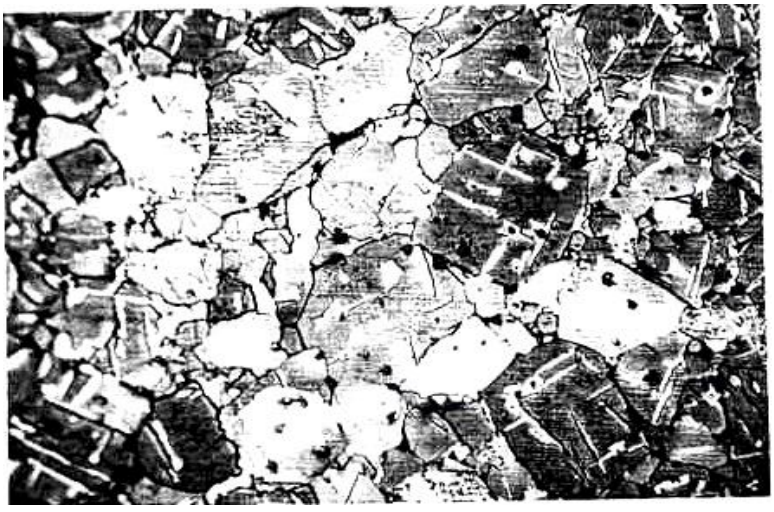

x=0.06

Fig. 6.31. SEM Microphotographs of $Mn_{0.451}Zn_{0.484}Fe_{2.065}O_4$ ferrite samples with CuO addition

The variation of normalized loss factor (1/μQ) at 100 kHz and the dc resistivity (ρ) of the investigated ferrite system for increasing addition of CuO content is shown in Fig. 6.32. The loss factor (tanδ) divided by permeability (μ′) is material figure of merit referred to as the normalized loss factor and written as: tanδ/μ′= 1/μQ. The normalized loss factor of the samples decreases up to 4 mol% CuO (x=0.04) content and then increases a little with further addition of CuO. The minimum value of normalized loss factor 6×10^{-5} is achieved for sample containing 4 mol% CuO content. The graph of the figure also shows that the dc resistivity of the samples increase almost linearly up to 3 mol% of CuO (x=0.03) and then increase abruptly to higher values up to 4 mol% CuO content. The maximum value of dc resistivity of the order of 6×10^{4} ohm-cm is achieved for sample containing 4 mol% CuO addition. In Mn-Zn ferrites, Zn ions occupy tetrahedral sites (A-sites), whereas Mn and Fe ions exist at both tetrahedral and octahedral sites (B-sites). With the addition of CuO, Cu^{2+} ions are known to occupy octahedral sites which limit the degree of Fe^{2+} to Fe^{3+} electron hoping conduction resulting in increase of resistivity [6.76]. High resistivity is a prerequisite for high frequency applications of ferrites to counter the eddy current losses, which degrade the ferrite performance.

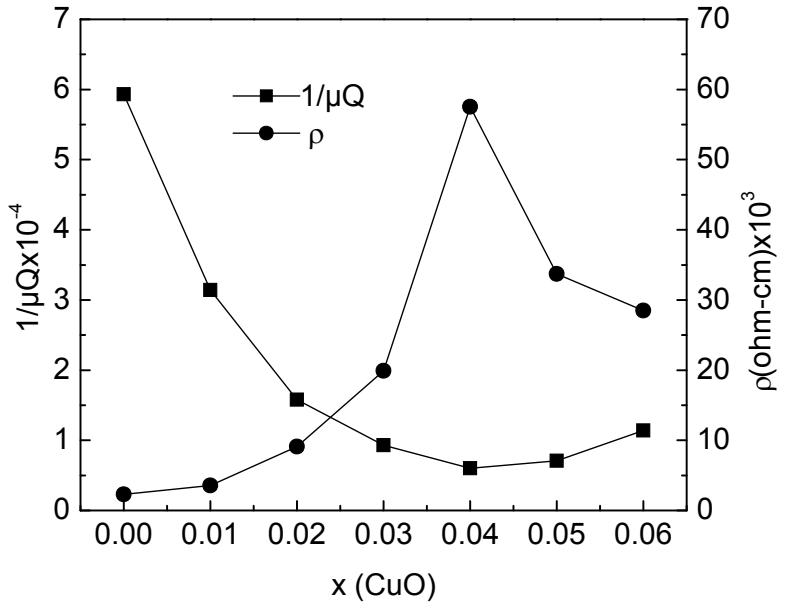

Fig. 6.32. Dependence of normalized loss factor (1/μQ) and dc resistivity (ρ) with CuO addition.

Eddy current loss of ferrite core materials is proportional to D^2f/ρ, where D is the thickness of core, f is the frequency and ρ is the resistivity of the ferrite core materials. Comparison of the eddy current loss (D^2f/ρ) at 1 kHz of the ferrite system with increasing CuO addition is shown in Table 6.5. It is observed from the Table that eddy current loss varies from 4.734×10^{-2} at 0 mol % CuO to 3.821×10^{-3} at 6 mol% of CuO (x=0.06) showing minimum value of 1.892×10^{-3} at 4 mol% CuO content. So, this ten fold decrease of the eddy current loss with the addition of CuO up to 4 mol% will ensure the achievement of frequency extension for application of the prepared core materials.

Table 6.5. Comparison of eddy current loss of $Mn_{0.451}Zn_{0.484}Fe_{2.065}O_4$ ferrite samples with CuO addition

CuO (in mol unit) x	d.c resistivity ρ(ohm-cm) $\times10^3$	Eddy current loss at 1 kHz
0.00	2.30	4.734×10^{-2}
0.01	3.56	3.067×10^{-2}
0.02	9.10	1.196×10^{-2}
0.03	19.90	5.472×10^{-3}
0.04	57.54	1.892×10^{-3}
0.05	33.71	3.230×10^{-3}
0.06	28.5	3.821×10^{-3}

6.10 Ferrite system $Mn_{0.451}Zn_{0.484}Fe_{2.065}O_4$+x V_2O_5; where, x (in mol unit)=0, 0.002, 0.004,0.006,0.008,0.01

6.10.1 Physical Properties:

The x-ray diffraction studies of the ferrite composition with the addition of V_2O_5 are used to obtain lattice constant values. Fig. 6.33 shows the variation of sintered density (d_s) and lattice constant (**a**) values for samples containing various concentration of V_2O_5 addition. It can be observed from the figure that an appreciable increment of sintered density is obtained up to 0.6 mol% V_2O_5 addition (x=0.006). Beyond 0.6 mol% V_2O_5 addition (x=0.006) density decreases a little. The effect of low melting point V_2O_5 (melts around 670°C) can be explained by the formation of liquid phase on the grain boundaries which promotes sintered density. The presence of sufficient amount of liquid phase due to V_2O_5 up to 0.6 mol% (x=0.006) helps to promote grain growth in the ferrite system which reduces the impurity and pore drag on the grain boundary motion [6.77]. The presence of V_2O_5 beyond 0.6 mol% increases the diffusion layer and the average grain size gradually decreases with the amount of added V_2O_5 which eventually decreases the sintered density [6.77]. The lattice constant values (**a**) of the samples containing V_2O_5 remains almost unaffected because of the following causes, V^{5+} ions have smaller ionic radius (0.59 Å) than Fe^{3+} ions (0.64 Å), its incorporation into the ferrite lattice results in the creation of some Fe^{2+} ions which have an ionic radius of 0.74Å. This presumably results in no change in the lattice constant value when V_2O_5 goes into solid solution in the ferrite.

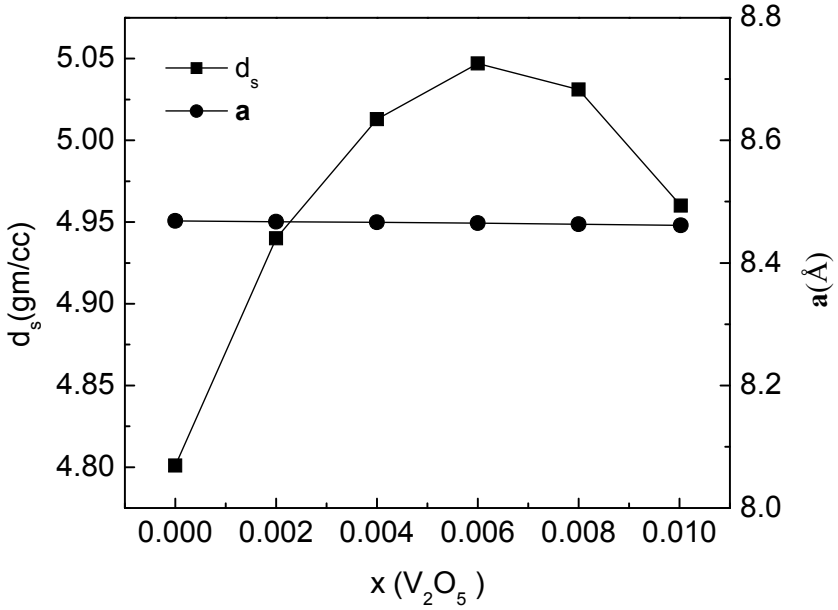

Fig. 6.33. Variation of sintered density (d_s) and lattice constant (**a**) with V_2O_5 addition.

6.10.2 Magnetic and Electrical Properties:

The variation of saturation magnetization (M_s) and Curie temperature (T_c) is shown in Fig 6.34. Saturation magnetization values of the sample increase with the addition of V_2O_5 up to 0.6 mol% (x=0.006) content and then decrease with further addition of V_2O_5. The increment in the saturation magnetization up to 0.6 mol% V_2O_5 (x=0.006) is due to the enhancement of resultant sublattice magnetic moment as well as sintered density ($M_s=\sigma_s d_s$). It can also be observed from the Fig.6.34 that the Curie temperature (T_c) of the samples increase with the addition of V_2O_5 up to 0.6 mol% (x=0.006) and decrease with further addition of V_2O_5. The increment of Curie temperature is probably due to some of V^{5+} ions occupy octahedral (B-sites) sites of the ferrite lattice, as a result some of Fe^{3+} ions would be pushed off from B to A sites (tetrahedral site) thereby increasing A-B interaction and hence the Curie temperature. As the amount of V_2O_5 is increased beyond 0.6 mol%, the V^{5+} ions occupy the electrostatically stable A sites, weakening the A-B interaction and the Curie temperature decreases [6.78].

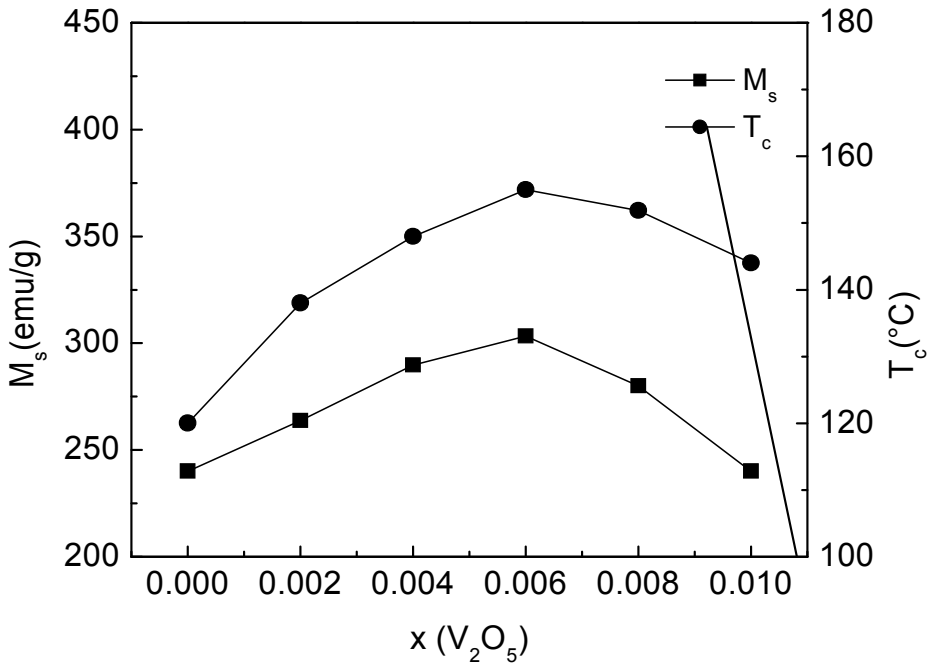

Fig. 6.34. Variation of saturation magnetization (M_s) and Curie temperature (T_c) with V_2O_5 addition.

Frequency dependent initial magnetic permeability (μ') spectra for all the samples from 0 to 1 mol% V_2O_5 content is shown in Fig. 6.35. The frequency variation is plotted in logarithmic scale and μ' is plotted in linear scale. The permeability spectra for all the samples show that as the frequency rises, the value of μ' rises a little up to around 10 kHz and then remain fairly constant up to 1MHz for all the samples containing V_2O_5.

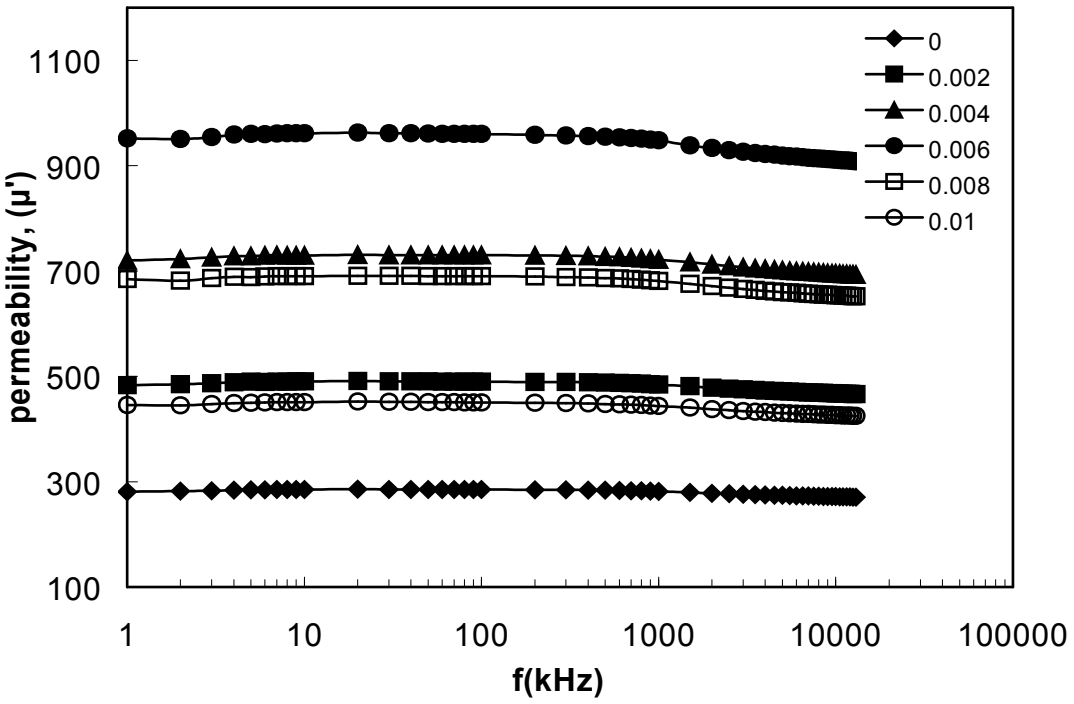

Fig.6.35. Frequency dependent initial magnetic permeability, μ' with V_2O_5 addition.

The variation of μ' at 100 kHz of the ferrite system with increasing concentration of V_2O_5 is also shown in Fig.6.36. It can be observed from the figure that maximum initial permeability value is obtained for sample containing 0.6 mol% (x=0.006) of V_2O_5. The maximum value of μ′=960 at 100 kHz is achieved for sample containing 0.6 mol% V_2O_5 addition. Formation of liquid phase due to small quantity of V_2O_5, the crystalline grain of ferrite tend to be refined and the amount of grain boundary is increased as a result the porosity in crystalline grain and grain boundary decreases homologically (SEM microphotographs of the samples as shown in Fig. 6.37), so the initial permeability increases up to 0.6 mol% of V_2O_5 [6.79]. Beyond 0.6 mol% V_2O_5 caused crystalline grain to grow more rapidly and made a great deal of pores enter the crystalline grain thus the initial permeability decreases.

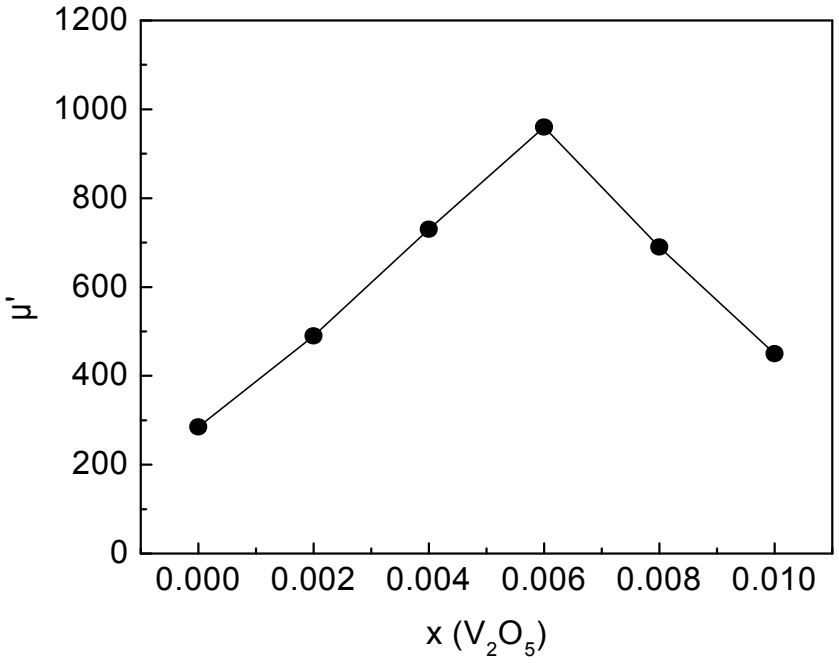

Fig. 6.36. Variation of initial magnetic permeability (μ′) at 100 kHz with V_2O_5 addition.

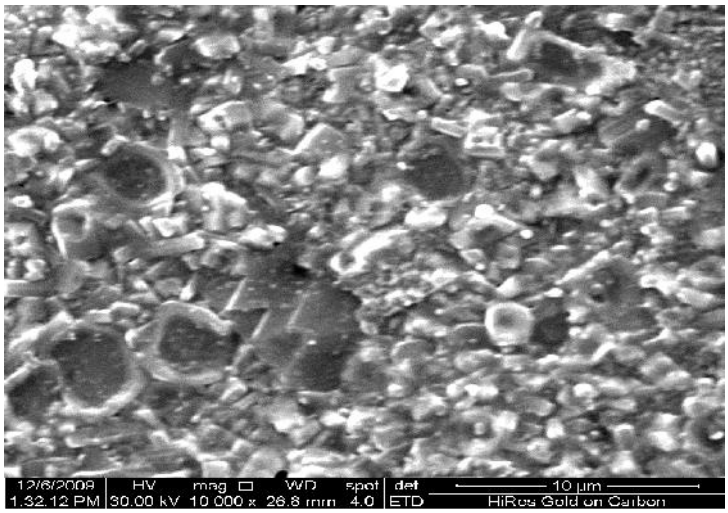

x=0.002

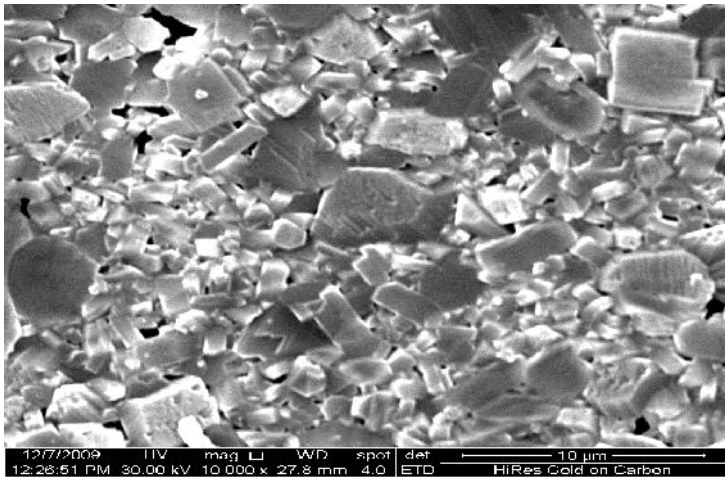

x=0.004

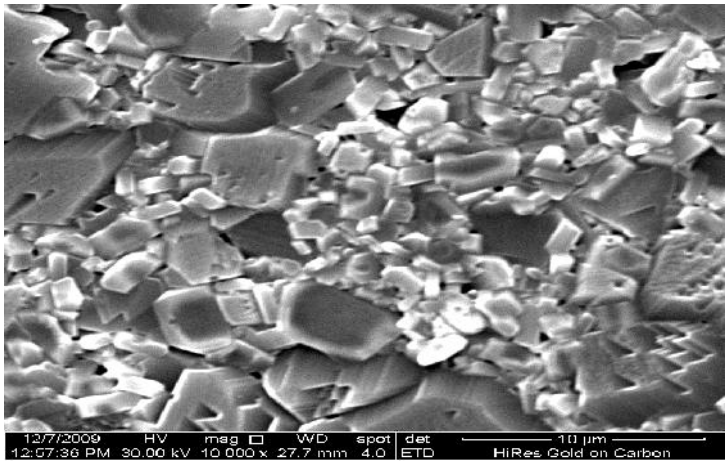

x=0.006

Fig. 6.37. SEM microphotographs of $Mn_{0.451}Zn_{0.484}Fe_{2.065}O_4$ ferrite samples with V_2O_5 addition

The variation of normalized loss factor (1/μQ) at 100 kHz and dc resistivity (ρ) of the ferrite system for increasing concentration of V_2O_5 is shown in Fig. 6.38. The normalized loss factor of the samples decreases up to 0.6 mol% V_2O_5 (x=0.006) content and then increases a little with further addition of V_2O_5. The minimum value of normalized loss factor 3×10^{-5} is achieved for sample containing 0.6 mol% V_2O_5 content. The resistivity graph of the figure (Fig. 6.38) also shows that the dc resistivity of the samples increases almost linearly. The maximum value of dc resistivity 9.2×10^{3} ohm-cm is achieved for sample containing 1 mol% of V_2O_5 addition. With the addition of V_2O_5, the amount of grain boundary increases and the V_2O_5 is separated from crystalline grain and enriched at the grain boundary, so the grain boundary resistivity increases thereby increase the dc resistivity of the ferrite system [6.80].

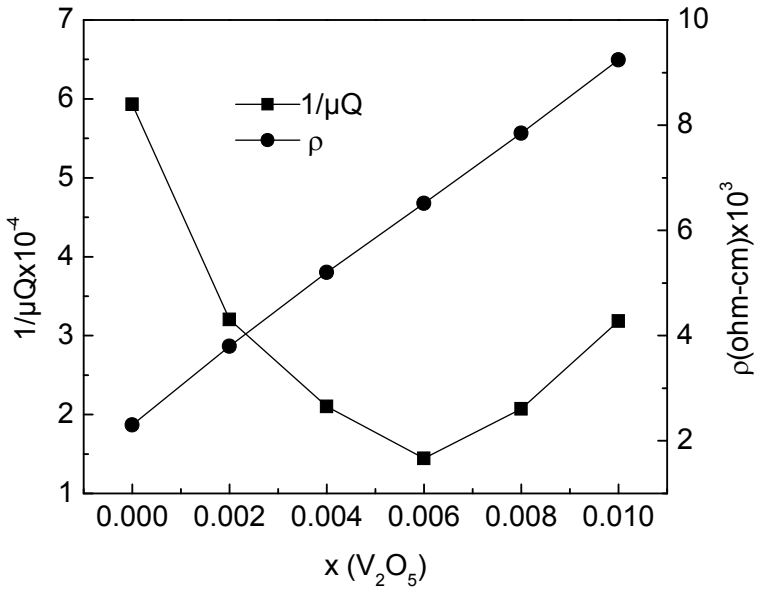

Fig. 6.38. Variation of normalized loss factor (1/μQ) and dc resistivity (ρ) with V_2O_5 addition.

Comparison of the eddy current loss (D^2f/ρ) at 1 kHz of the ferrite system with increasing addition of V_2O_5 is shown in Table 6.6. It is observed from the Table that eddy current loss varies from 4.734×10^{-2} at 0 mol% V_2O_5 to 1.178×10^{-2} at 1 mol% V_2O_5 addition. So, the eddy current loss of the prepared core materials decreases with the addition of V_2O_5 contents showing frequency extension for applications.

Table 6.6. Comparison of eddy current loss of $Mn_{0.451}Zn_{0.484}Fe_{2.065}O_4$ ferrite samples with V_2O_5 addition

V_2O_5 (in mol unit) x	d.c resistivity ρ(ohm-cm) $\times10^3$	Eddy current loss at 1 kHz
0.00	2.30	4.734×10^{-2}
0.002	3.80	2.865×10^{-2}
0.004	5.20	2.094×10^{-2}
0.006	6.51	1.672×10^{-2}
0.008	7.85	1.387×10^{-2}
0.01	9.2	1.178×10^{-2}

6.11 Ferrite system $Mn_{0.451}Zn_{0.484}Fe_{2.065}O_4$+x Eu_2O_3; where, x (in mol unit)=0, 0.005,0.01,0.015,0.02,0.025,0.03,0.035,0.04

6.11.1 Physical properties:

The x-ray diffraction studies of the ferrite composition with the addition of Eu_2O_3 are used to obtain lattice constant values. Fig. 6.39 shows the variation of sintered density (d_s) and lattice constant (**a**) for samples with increasing concentration of Eu_2O_3 addition. A significant increase of the sintered density is observed upto 2 mol% Eu_2O_3 addition (x= 0.02). The inclusion of this low melting oxide (melting point 623°C) in the composition of iron-excess Mn-Zn ferrite increases the chemical reactivity of the resulting mixture and facilitates the attainment of high degree of uniformity in the sintered body which in turn enhances the sintered density. The lattice constant values of the ferrite system increase with the addition of Eu_2O_3. A possible explanation may be the formation of solid solution. It is supposed that all Eu ions dissolve in the spinel lattice during sintering. This assumption of the solid solution formation is supported by the lattice constant values as shown in the same figure (Fig.6.39). An increase is evidenced in the lattice constant values with increasing Eu^{3+} ion (larger ionic radius of 0.947Å) content from 8.4535 Å for the ferrite without Eu_2O_3 to 8.4572 Å for 4 mol% Eu_2O_3 (x= 0.04). The increase of lattice volume usually increases the diffusion path, leading to an increase of the rate of cation interdiffusion in the solid solution. The grain boundary diffusion may also play an important role in the grain growth during sintering. For a larger Eu_2O_3 content beyond 2 mol% (x=0.02) the sintered density decreases. This decrement in density is attributed to increased intergranular porosity resulting from discontinuous grain growth [6.81].

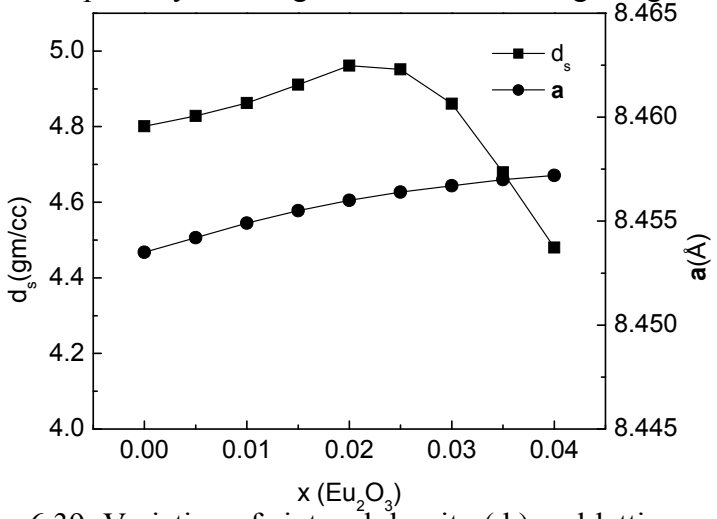

Fig. 6.39. Variation of sintered density (d_s) and lattice constant (**a**) with Eu_2O_3 addition

6.11.2 Magnetic and Electrical properties:

Fig.6.40. shows the variation of saturation magnetization (M_s) and Curie temperature (T_c) of the samples with increasing concentration of Eu_2O_3 addition. The saturation magnetization of the samples increases a little up to 2 mol% Eu_2O_3 content (x= 0.02) and then decreases beyond Eu, x=0.02 content. Neel's [6.83] two sub-lattice model of co-linear spin arrangement is applicable for samples up to Eu content x=0.02 and beyond that non-colinear spin arrangements (Y-K angles) are predominant [6.84]. Up to 2 mol % of Eu_2O_3 addition the A-B exchange interaction donates that's why magnetization increases. However, beyond 2 mol% of Eu_2O_3 addition the A-sublattice becomes so diluted that A-B exchange interaction no longer remains stronger and thereby B-B exchange interaction becomes stronger which in turn introduces canting of spins (antiparallel alignment). Spin canting effects in B-sublattice is known as Yafet-Kittle type spin arrangement. With the increase of Y-K angles due to Eu_2O_3 beyond 2 mol% B-B exchange interaction dominates and subsequent decrease in magnetization occurs. However, there is no noticeable influence of Eu_2O_3 addition on the Curie temperature of the samples as also shown in Fig. 6.40.

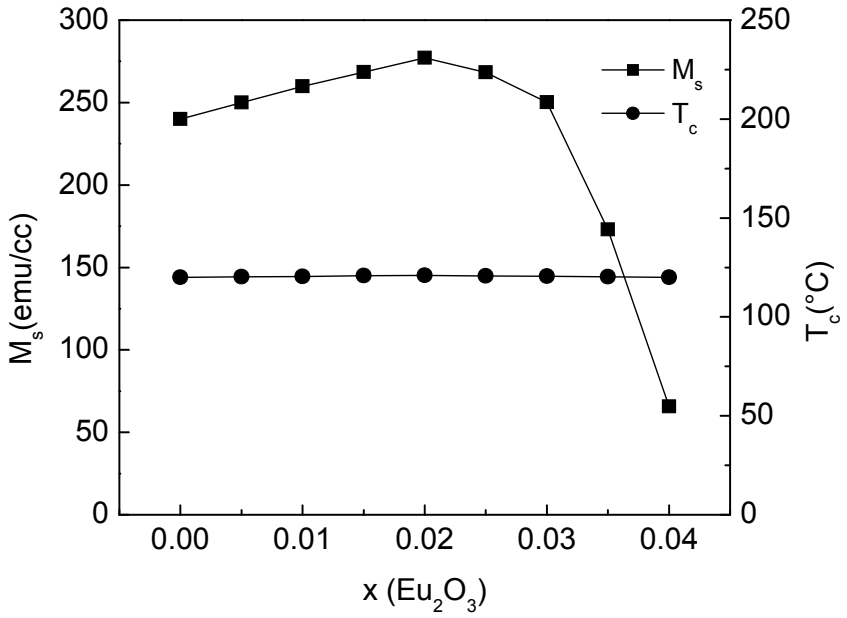

Fig. 6.40. Variation of saturation magnetization (M_s) and Curie temperature (T_c) with Eu_2O_3 addition.

Frequency dependent initial magnetic permeability (μ′) spectra for all the samples from 0 to 4 mol% (x=0.04) Eu_2O_3 content is shown in Fig.6.41. The frequency variation is plotted in logarithmic scale and μ′ is plotted in linear scale. For Mn-Zn ferrites to be used as core materials, the real part of the complex initial permeability (μ′) should remain fairly constant over certain frequency range. The permeability spectra for all the samples show that as the frequency rises the value of μ′, remains fairly constant up to 1 MHz with Eu_2O_3 addition.

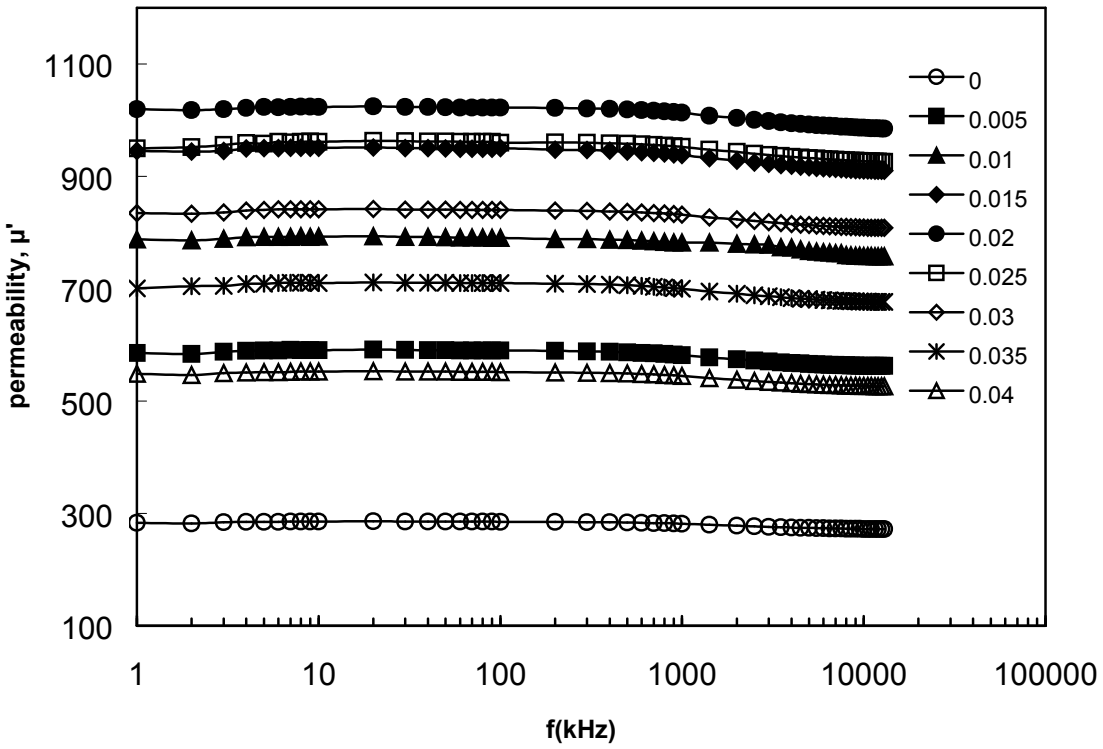

Fig.6.41. Frequency dependent initial magnetic permeability, μ' with Eu_2O_3 addition.

The variation of initial magnetic permeability (μ′) at 100 kHz of the ferrite system with increasing addition of Eu_2O_3 is also shown in Fig. 6.42. It is observed that an appreciable increase in permeability up to 2 mol% Eu_2O_3 (x=0.02) content occurs. The highest value of μ′= 1022 at 100 kHz is achieved for sample containing 2 mol% Eu_2O_3 addition. It is known that the permeability is related to two different magnetizing mechanism; the spin rotational magnetizing and the domain wall motion. Domain wall motion is affected by the grain size (SEM microphotographs of the samples shown in Fig. 6.43) and enhanced with the increase of the grain size. The grain growth is a result of interparticle mass transport, possible explanation may be sought in terms of the influence of Eu ions on the diffusion process.

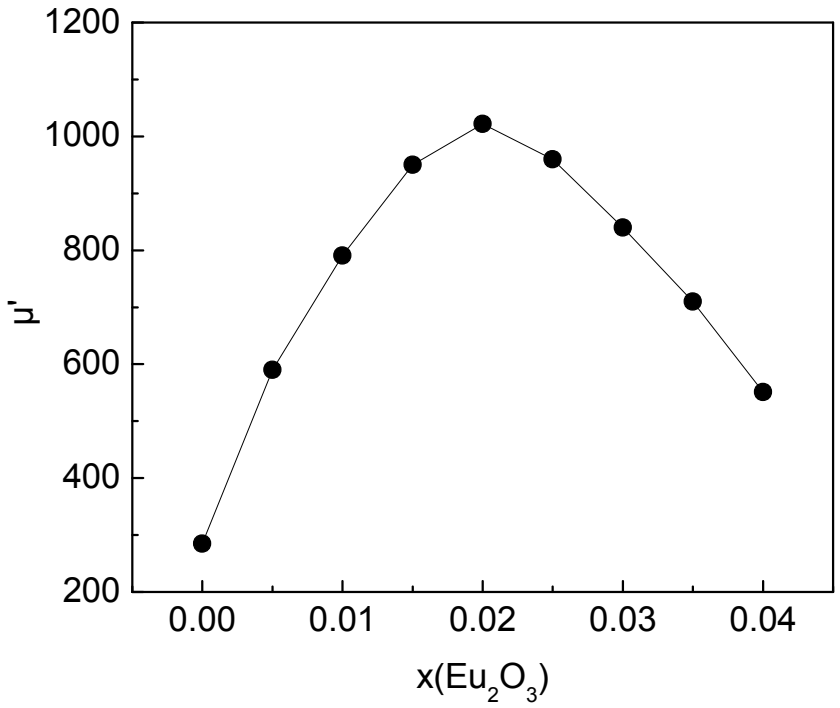

6.42. Variation of initial magnetic permeability (μ′) at 100 kHz with Eu_2O_3 addition.

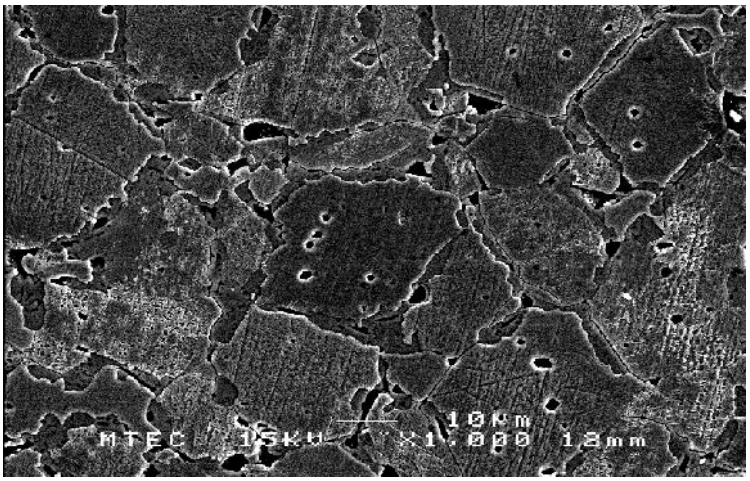

x=0.005

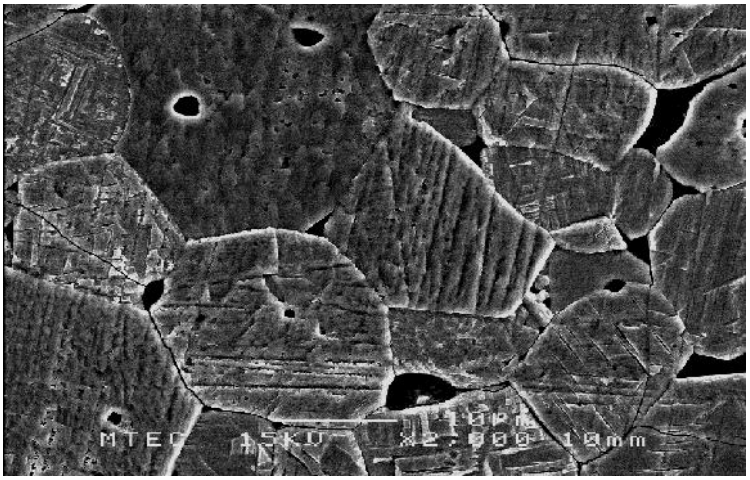

x=0.01

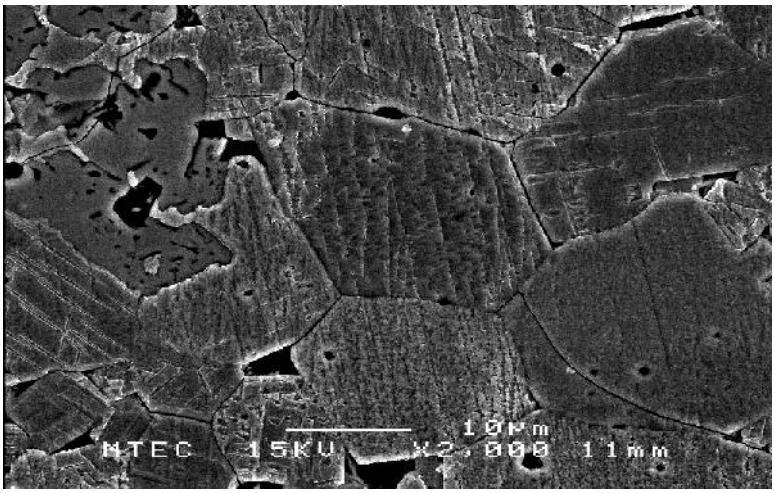

x=0.02

Fig. 6.43. SEM microphotographs of $Mn_{0.451}Zn_{0.484}Fe_{2.065}O_4$ ferrite samples with Eu_2O_3 addition.

The variation of the normalized loss factor (1/μQ) at 100 kHz and the dc resistivity (ρ) of the ferrite system with increasing Eu_2O_3 addition are shown in Fig.6.44. The loss factor (tanδ) divided by permeability (μ′) is material figure of merit referred to as the normalized loss factor and written as: tanδ/μ=1/μQ. The normalized loss factor of the samples decreases up to 2 mol% (x= 0.02) Eu_2O_3 and then increases with further addition of Eu_2O_3. Minimum value of normalized loss factor 4.12×10^{-4} is achieved for sample containing 2 mol% (x=0.02) Eu_2O_3 addition. The figure also shows that the dc resistivity of the samples increases almost linearly up to 2 mol% Eu_2O_3 (x=0.02) and then increase abruptly to higher values beyond 2 mol% Eu_2O_3 addition. The maximum value of dc resistivity of the order of 5×10^4 ohm-cm is achieved for sample containing 4 mol% Eu_2O_3 addition. In Mn-Zn ferrites Zn ions occupy tetrahedral sites, whereas Mn and Fe ions exist at both tetrahedral and octahedral sites. With the addition of Eu_2O_3, Eu^{3+} ions occupy octahedral sites which limit the degree of Fe^{2+} to Fe^{3+} electron hoping conduction resulting in increase of resistivity.

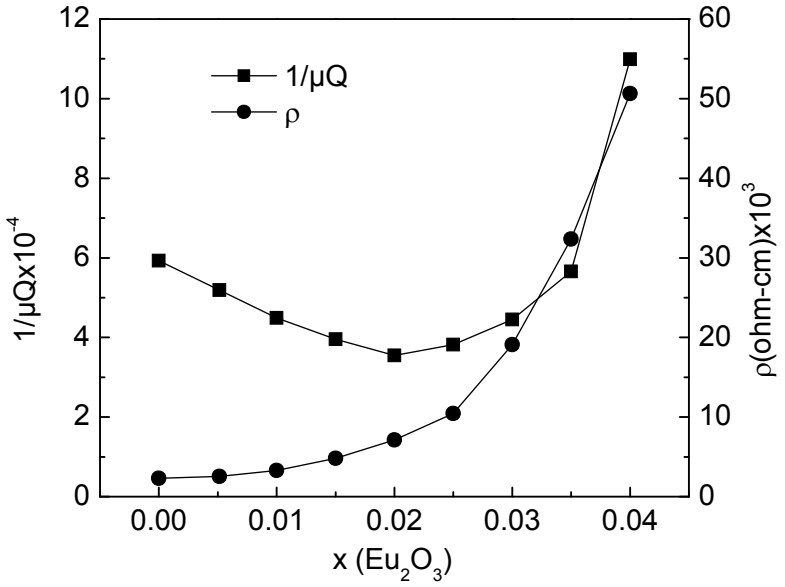

Fig. 6.44. Variation of normalized loss factor (1/μQ) and dc resistivity (ρ) with Eu_2O_3 addition.

Eddy current loss in the ferrite core materials is proportional D^2f/ρ, where D is the thickness of the core, f is the frequency of application and ρ is the resistivity of the ferrite core material. Comparison of the eddy current loss at 1 kHz for increasing addition of Eu_2O_3 is shown in Table 6.7. Eddy current loss of the core varies from 4.734×10^{-2} without Eu_2O_3 (x= 0.00) to 2.15×10^{-3} at 4 mol% Eu_2O_3, (x=0.04). This ten fold decrease of the eddy current loss with the addition of Eu_2O_3 ensures the achievement of frequency extension for application of the prepared core materials.

Table 6.7. Comparison of eddy current loss of $Mn_{0.451}Zn_{0.484}Fe_{2.065}O_4$ ferrite samples with Eu_2O_3 addition

Eu_2O_3 (in mol unit) x	d.c resistivity ρ(ohm-cm) $\times10^3$	Eddy current loss at 1 kHz
0.00	2.30	4.734×10^{-2}
0.005	2.56	4.253×10^{-2}
0.010	3.29	3.310×10^{-2}
0.015	4.82	2.259×10^{-2}
0.020	7.12	1.529×10^{-2}
0.025	10.45	1.042×10^{-2}
0.030	19.10	5.701×10^{-3}
0.035	32.34	3.367×10^{-3}
0.040	50.63	2.150×10^{-3}

6.12 Ferrite system $Mn_{0.451}Zn_{0.484}Fe_{2.065}O_4$+x In_2O_3; where, x(in mol unit)=0, 0.005,0.01,0.015,0.02,0.025,0.03,0.035:

6.12.1 Physical properties:

The X-ray diffraction studies of the ferrite system with the addition of In_2O_3 are used to obtain lattice constant values. Fig. 6.45 shows the variation of sintered density (d_s) and lattice constant (**a**) for samples containing various concentration of In_2O_3. It can be observed from the figure that a significant increment of sintered density is obtained due to the addition of trivalent In^{3+} ions in the ferrite system. The effect of low melting In_2O_3 (melting point 680°C) can be explained by the formation of liquid phase on the grain surface due to reaction of In_2O_3 with the spinel phase of the ferrite at 1250°C sintering temperature which promotes densification . The appreciable increment of lattice constant values (as observed from the figure) due to the addition of In^{3+} ions can be explained on the basis of ionic radius of this additive ions. The ionic radius of In^{3+} (0.91Å) is larger than the displaced Fe^{3+} (0.64 Å), so with increasing amount of In^{3+} ions, ferrite lattice bulges and the lattice constant increases appreciably.

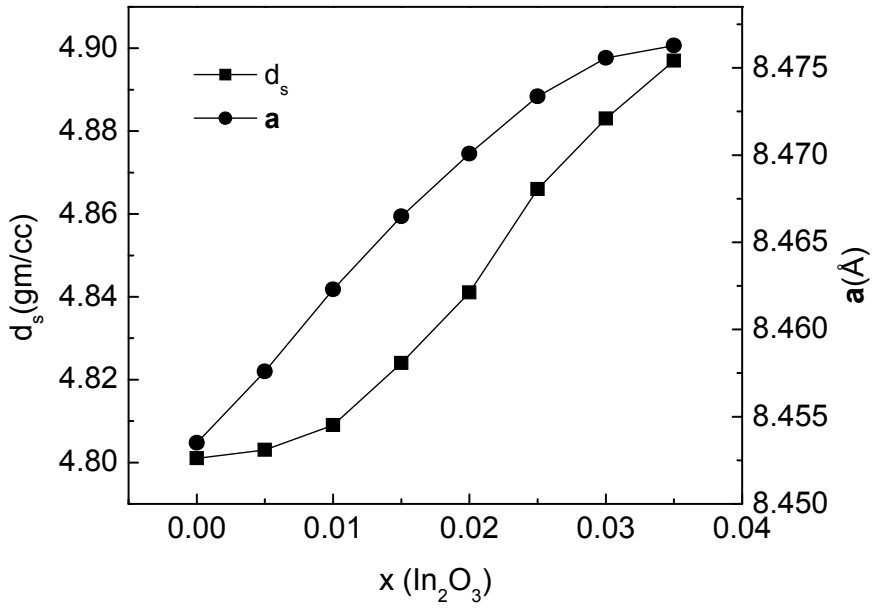

Fig. 6.45. Variation of sintered density (d_s) and lattice constant (**a**) with In_2O_3 addition.

6.12.2. Magnetic and Electrical Properties:

The variation of the saturation magnetization (M_s) with increasing addition of In_2O_3 concentration is shown in Fig. 6.46. Saturation magnetization value increases up to 2 mol% In_2O_3 (x=0.02) content and then decreases with further increment of In_2O_3 addition. To explain the observed variation in saturation magnetization the following possibilities may be considered: (i) For In_2O_3 concentration up to 2 mol% (x=0.02), the diamagnetic In^{3+} ions occupy A sites leads to a decrease in the A-sublattice magnetization (M_A), keeping the B-sublattice magnetization (M_B) constant. As a result the resultant magnetization according to $M=M_B-M_A$ is expected to increase, hence the magnetization increases. (ii) For In_2O_3 concentration beyond 2 mol% (x= 0.02), In^{3+} ions occupy B-sites leads to a decrease in the B-sublattice magnetization (M_B)), keeping the A-sublattice magnetization (M_A) constant which in turn weakens A-B exchange interaction. Thus the resultant magnetization according to $M=M_B-M_A$ is expected to decrease, hence the magnetization decreases.

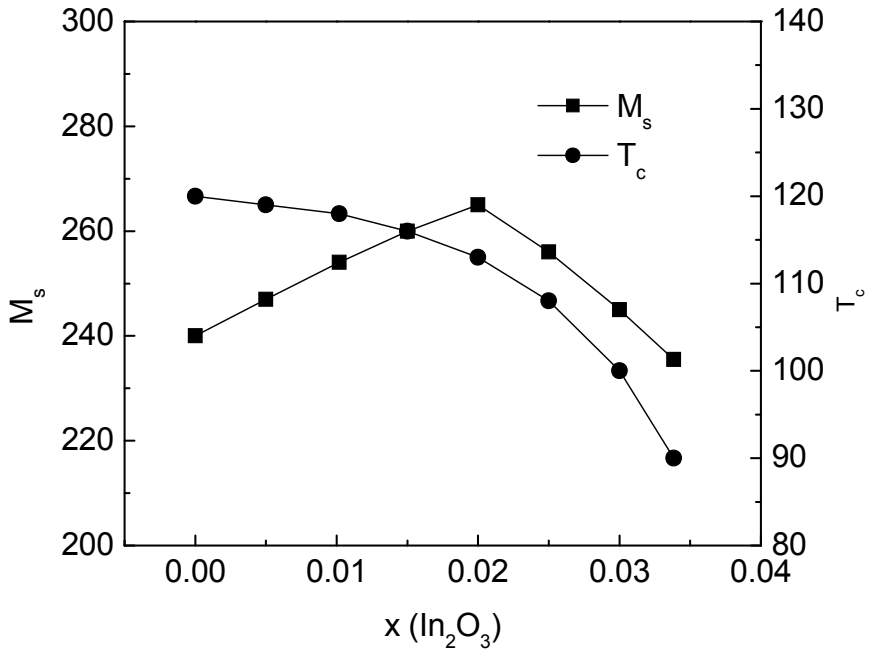

Fig. 6.46. Variation of saturation magnetization (M_s) and Curie temperature (T_c) with In_2O_3 addition.

The variation of Curie temperature (T_c) with In_2O_3 addition is also shown in Fig. 6.46. Curie temperature value decreases with the increasing addition of In_2O_3 content.

This decrease can be explained on the basis of the number of magnetic ions present in the two sublattices and their mutual interactions. As the concentration of In^{3+} ions increases at the A-site (tetrahedral site), the replaced Fe^{3+} ions go to the B-site (octahedral site). This leads to a decrease in the A-B interaction of the type Fe^{3+}(A)-O_2-Fe^{3+}(B). Since Curie temperature is determined by an overall strength of the A-B exchange interaction, the weakening of the Fe^{3+}(A)-O_2-Fe^{3+}(B) interaction results in a decrease of the Curie temperature [6.85], when the concentration of the In^{3+} increases successively in the ferrite system.

Frequency dependent initial magnetic permeability (μ') spectra for all the samples from 0 to 3.5 mol% (x=0.035) In_2O_3 content is shown in Fig. 6.47. The frequency variation is plotted on logarithmic scale and μ' is plotted on linear scale. The permeability spectra for all the samples show that as the frequency increases, the μ' rises a little up to 10 kHz frequency range and then remains fairly constant upto 1 MHz range (1000 kHz).

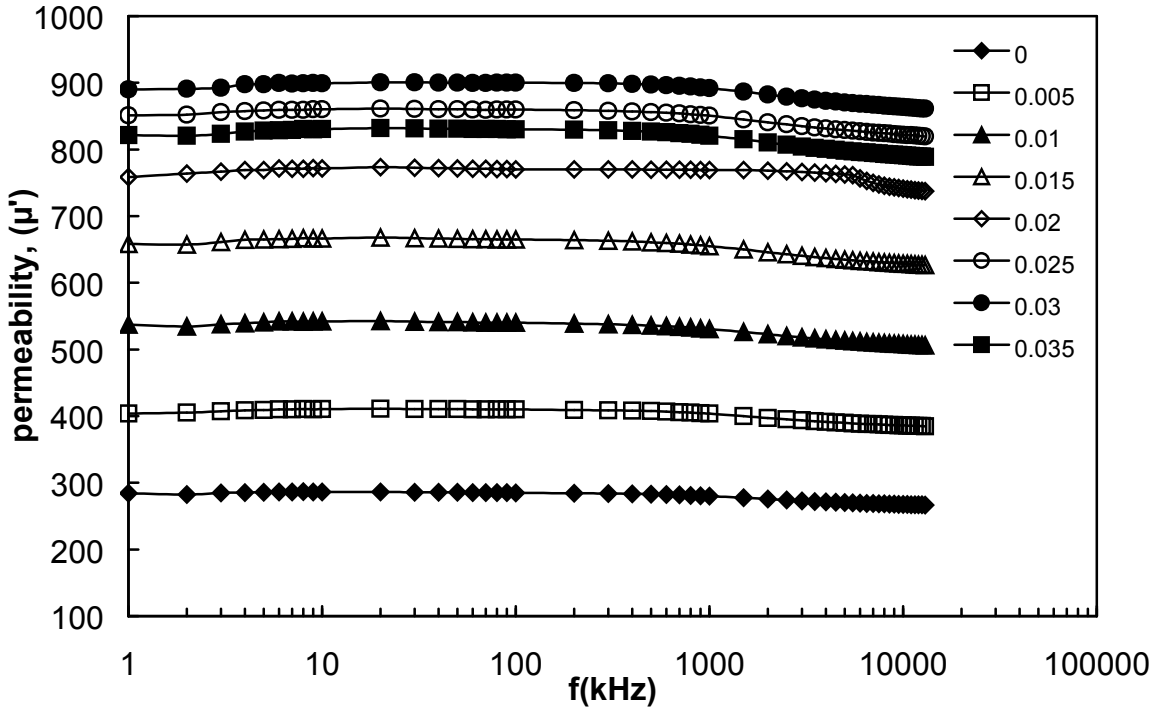

Fig.6.47. Frequency dependent initial magnetic permeability with In_2O_3 addition.

The variation of initial magnetic permeability (μ') at 100 kHz of the ferrite system with the increasing addition of In_2O_3 is also shown in Fig. 6.48. It is observed that an appreciable increment in permeability up to 3 mol% In_2O_3 (x=0.03) occurs and decreases beyond 3 mol% In_2O_3 addition. The highest value of μ′= 900 at 100 kHz is achieved for sample containing 3 mol% In_2O_3 addition. The variation of initial magnetic permeability can be explained from the following dependence of μ': $\mu' \propto M_s^2 D_m/K_1$; where D_m is the average grain diameter, K_1 is the magneto-crystalline anisotropy constant and M_s is the saturation magnetization. It can be observed from the Fig.6.49 (SEM microphotograph of the samples) that the average grain diameter changes significantly due to the addition of In_2O_3 in the Mn-Zn ferrite system. The variations of M_s and the magneto-crystalline anisotropy constant K_1 does play an important role in changing the value of initial permeability, μ', with increase in the concentration of In^{3+} ions. The net anisotropy constant K_1 is reduced to its minimum value when the concentration of In_2O_3 is 3 mol%. This in turn yields a marked increase in the maximum value of permeability at 3 mol% In_2O_3 addition.

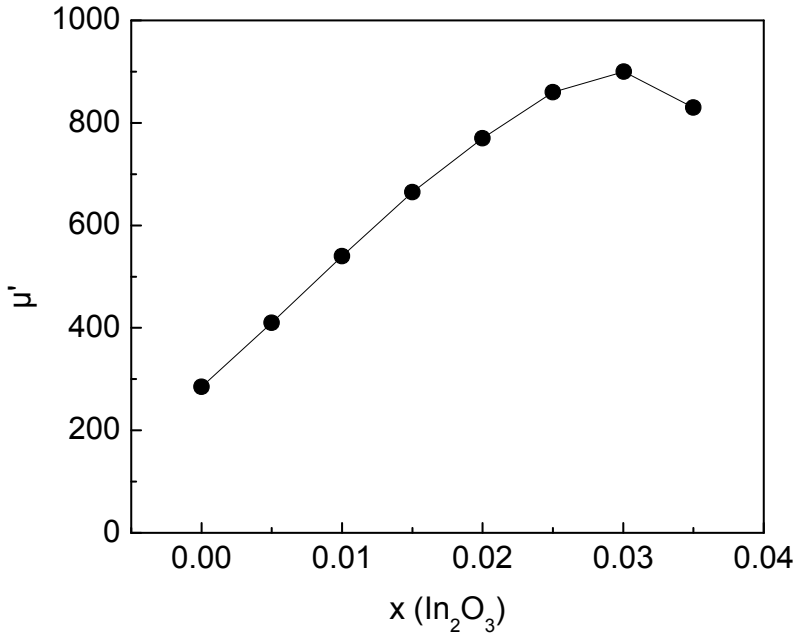

Fig. 6.48. Variation of initial magnetic permeability (μ') at 100 kHz with In_2O_3 addition

.

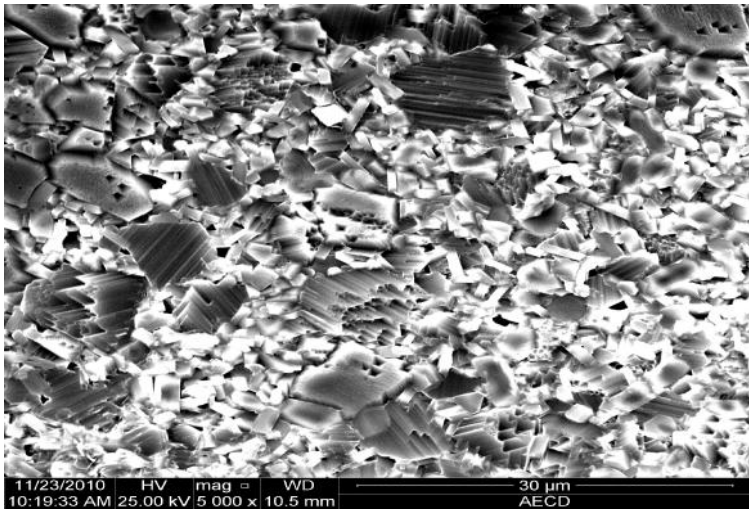

x=0.01

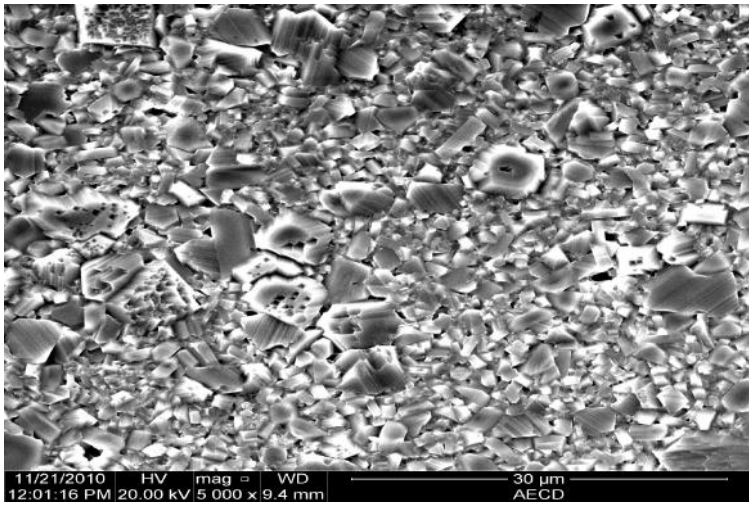

x=0.02

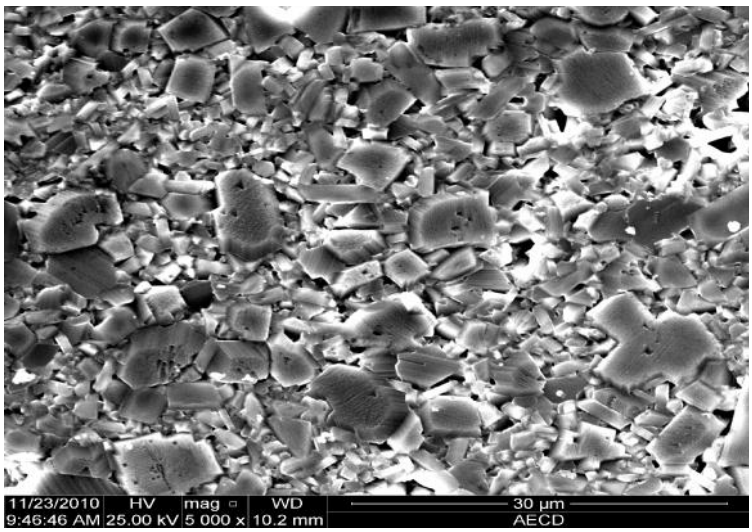

x=0.03

Fig.6.49. SEM microphotographs of $Mn_{0.451}Zn_{0.484}Fe_{2.065}O_4$ ferrite samples with In_2O_3 content.

The variation of the normalized loss factor (1/μQ) at 100 kHz and dc resistivity for all the samples of the ferrite system with increasing addition of In_2O_3 are shown in Fig. 6.50. The normalized loss factor of the samples decreases upto 1.5 mol% (x=0.015) In_2O_3 and then increases with further addition of In_2O_3. Minimum value of normalized loss factor 1.35×10^{-4} is achieved for sample containing 1.5 mol% In_2O_3 addition.

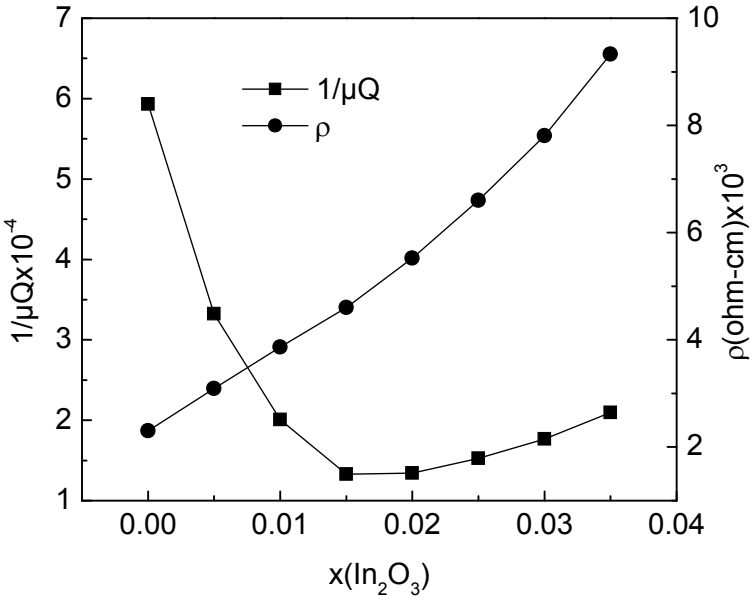

Fig. 6.50. Variation of normalized loss factor (1/μQ) and dc resistivity (ρ) with In_2O_3 addition.

The figure also shows that the dc resistivity of the samples increases almost linearly with the addition of In_2O_3 content. The maximum value of dc resistivity of the order of 0.932×10^4 ohm-cm is achieved for sample containing 3.5 mol% In_2O_3 addition. Besides this, the presence of Mn^{3+} ions , if any, at the B-site may also initiate hopping between the Mn^{2+} and Mn^{3+} ions and may thus make a small contribution to the conductivity. Since both Fe^{2+} and Mn^{3+} ions have a strong preference for occupying the B-sites they readily participate in the conduction process. However, with increasing addition of In_2O_3, In^{3+} ions besides occupying the B-sites, also have a tendency to occupy the A-sites, thus displacing and equal number of Fe^{3+} ions to the B-sites, which increases the resistivity [6.86].

Comparison of eddy current loss (D^2f/ρ) at 1 kHz of the ferrite system with the increasing addition of In_2O_3 is shown in Table 6.8. It is observed from the Table that eddy current loss varies from 4.734×10^{-2} at 0 mol% In_2O_3 to 1.168×10^{-2} at 3.5 mol% In_2O_3 addition. So, the eddy current of the prepared core materials decreases with the addition of In_2O_3 contents showing frequency extension for applications.

Table 6.8. Comparison of eddy current loss of $Mn_{0.451}Zn_{0.484}Fe_{2.065}O_4$ ferrite samples with In_2O_3 addition

In_2O_3 (in mol unit)	d.c resistivity ρ(ohm-cm) $\times10^3$	Eddy current loss at 1 kHz
0.00	2.30	4.734×10^{-2}
0.005	3.08	3.535×10^{-2}
0.010	3.86	2.821×10^{-2}
0.015	4.60	2.367×10^{-2}
0.020	5.52	1.972×10^{-2}
0.025	6.60	1.650×10^{-2}
0.030	7.80	1.396×10^{-2}
0.035	9.32	1.168×10^{-2}

References:

[6.1] G. F. Dionne, R. G. West, Appl. Phys. Letts., **48**, 1488 (1986).

[6.2] U. Varsney, R. K. Puri, IEEE Trans. Magn., **25**, 3109 (1989).

[6.3] A. Paduraru, M. Feder, O. Caltun, J. Optoelectron-Adv. Mater. **5(4),** 945(2003).

[6.4] M. F. Morariu, A. Paduraru, O. Caltun, J. Optoetectron, Adv. Mater. **5(4),** 985(2003).

[6.5] B. P. Rao, P. S. V. Subba Rao, G. V. S. Murthy, K. H. Rao, J. Magn. Magn. Maters. **268**, 315(2004).

[6.6] G. C. Jain, B.K. Das, R. B. Tripati, R. Narayan, J. Magn.Magn.Mater., **14**, 80(1979).

[6.7] R. Rezlescu, N. Rezlescu, C. Paanicu, M. L. Crauss, d. P. Poga, J. Magn. Magn. Mater., **177**, 448(1992).

[6.8] O. F. Caltun, L. Spinu, A. Stancu, J. Magn. Magn. Mater., **37**, 2353 (2001).

[6.9] B. P. Rao, P. S. V. Subba Rao, G. V. S. Murthy, K. H. Rao, J. Magn, Magn, Mater., **268**, 315 (2004).

[6.10] S. Akhter, M. A. Choudhury, J. Rahman, Proc. Int. Conf. on Magn, Magn, Mater., ICMM-2007, 252 (2007)

[6.11] K. H. Rao, S. B. Raju, K. Aggerwal, R. G. Menidratta, J. Appl. Phys., **52**, 1376 (1981).

[6.12] M. Pol, P. Brahma, D. Chakravorty, J. Magn, Magn, Mater., **152**, 370 (1996).

[6.13] D. N. Bhosalr, N. D. Chaudhuri, S. R. Swant, P.P. Bakare, J. Magn. Magn. Mater., **173**, 51(1997).

[6.14] J. Kulikowski, Sov. Powder Metal and Met. Ceram. (USA), **12**, 597 (1973).

[6.15] G. C. Jain, B. K. Das, N. C. Goel, J. Am. Ceram. Soc., **62**, 79 (1979).

[6.16] T. Limura, J. Am. Ceram. Soc., **59**, 539 (1976).

[6.17] T Limura, Y. K. Shi, J. Am. Ceram. Soc., **84**, 431 (1976).

[6.18] L. G. Van Uitert, J. Appl. Phys. **27**, 723(1956).

[6.19] N. Rezlescu, E. Rezlescu, P. D. Popa, M. L. Crauss, L. Rezlescu, J. Magn. Magn. Mater., **182**, 199(1998).

[6.20] J. H. Nam, H.H. Jung, J. Y. Shin, J. H. Oh, IEEE Trans. Magn, , **31**, 3985(1995).

[6.21] Y. C. Yang, Lin. S. Kong, Y. B. Zha, H. Sun, and X. D. Pie, J. de Phys, 49, Colloque C8, 543 (1988).

[6.22] H. S. Li, B. P. Hu, J. M. D. Coey, Solid State Commun, **66**,133(1988).

[6.23] Y. C. Yang, L. S. Kong, S. H. Sun, D. M. Gu, J. Appl. Phys., **63**, 3702 (1988).

[6.24] N. Rezlescu, E. Rezlescu, Solid State Commun., **88(2),** 139 (1993).

[6.25] J. Sun, J. Li, G. Sun, J. Magn.Magn. Mater., **250**, 20 (2002).

[6.26] B. P. Rao, O. F. Caltun, I. Dumitra, L. Spinu, J. Magn.Mater., **304**, 752 (2006).

[6.27] A. Okomoto, Ceramic Bulletin, **64**, 888 (1984).

[6.28] S. I. Pyun, J. T. Baek, Ceramic Bulletin, **64(4),** 602 (1985).

[6.29] N. Yahya, M. Mushim, R. S. Azis, N. M. Saiden, Pak. J. Of Applied Sciences, **2(10),** 965 (2002).

[6.30] G. C. Jain, B.K. Das, R. B. Tripati, R. Narayan, J. Magn.Magn.Mater., **14**, 80(1979).

[6.31] A. Globus, H. Pascard, V. Cagan, J. De. Phys. Colloq. Suppl. **38,** CI-163(1977)

[6.32] E. J. W. Verway, J. H. De Boer, Trav. Chim., Pays-Bas **55,** 531 (1936).

[6.33] A. B. Naik, S. A. Patil, J. J. Power, J. Mater. Sci. Lett. **7,** 1034 (1988).

[6.34] A. Globus, J. Phys. (Paris), Suppl.CI, Proc. ICF-3, **1** (1977).

[6.35] N. Rezluscu, E. Rezluscu, P. D. Poda, M. L. Craus, L. Rezlescu, J. Magn. Magn. Mater. **182**, 199(1998).

[6.36] B. P. Rao, K. H. Rao, J. Magn. Magn. Mater., **292**, 44(2005).

[6.37] A. Thakur, P. Mathur, M. Singh, Indian J. Pure & Appl. Phys., **46**, 42 (2008).

[6.38] A. Laksman, K. H. Rao, R. G. Mendirata, J. Magn. Magn. Mater. **250**, 92 (1971).

[6.39] J. Smit, H. P. J. Wijn, Ferrites, Johm Wiley& sons, 216 (1959).

[6.40] J. Smit, H. P. J. Wijn, Ferrites, Philips Tech. Library, Netherlands, 285 (1959).

[6.41] D. J. Peeduijn, H. P. peloschek, Proc. Brit. Ceram. Soc. **10**, 263 (1968).

[6.42] V. B. Fetisov, G. A. Kozhina, A. Y. Fishman, T. E. Kurennykh, V. B. Vykhodets, J. Appl. Phys., **83**, 6876 (1998).

[6.43] V. T. Zaspalis, E. Antoniadis, E. Papazoglou, V. Tsakaloudi, L. Nalbandian, C. A. Sikalidis, J. Magn. Magn. Mater., **250**, 98(2002).

[6.44] T. Akashi, Trans. JPn.Inst. Met., **2**, 171 (1961).

[6.45] T. Akashi, Nippon Elect. Co. Res. Dev., **8**, 89 (1966).

[6.46] T. G. W. Stijntyes, A. B. V. Groenou, R.F. pearson, J.E. Knowles, P. Rankia, Ferrites: proc. Int.conf., Japan, 194 (1976).

[6.47] T. G. W. Stinjntjes, A. B. V. Groenou, R. F. pearson, J. E. Knowles, P. Rankia, Ferrites: proc. Int. conf.,Japan, 137 (1970).

[6.48] F. M. A. Carpay, A. L. Stuijts, Sci. ceram., **8**, 23 (1975).

[6.49] K. H. Rao, S. B. Raju, K. Aggarwal, R. G. Mediratta, J. Appl. Phys. **52(3),** 1376 (1980).

[6.50] K. H. Rao, N. K. Gaur, K. Aggarwal, R. G. Mendiratta, J. Appl. Phys. **52(3),** 1122 (1982).

[6.51] De. Le Roux, F. onno, P. perriat, proc. ICF-S, India, 95 (1989).

[6.52] J. Pankert, J. Magn. Magn. Mater., **138**, 45 (1994).

[6.53] Z. Zaspalis, V.Tsakaloudi, E. papazoglou, M. Kolenbrander, R. Guenther, P.vander Valk. J. Electro-ceramics, **13**, 585 (2004).

[6.54] V. T. Zaspalis, S. Skdari, M. Kolenbrander, J. Magn. Magn. Mater., **310,** 28 (2007).

[6.55] J. Kalarus, G. Kogias, D. Holz, V. T. Zaspalis, J. Magn. Magn. Mater. **324,** 2788 (2012).

[6.56] C. Guillaud, proc. IEEE suppl. **1048**, 165 (1957).

[6.57] L. A. Vladimirtseva, G. V. Samsonov, V. A. Gorbatyuk, Sov. Powder Metall. Met Ceram. **12**, 669 (1973).

[6.58] K. H. Rao, S. B Raju, K. Aggarwal, R. G. Mendiratta, J. Appl. Phys. **52**, 1376 (1981).

[6.59] K. H. Rao, S. B. Raju, R. G. Gupta, R. G. Mendiratta, Solid state Commun., **36**, 777 (1980).

[6.60] J. Shishiga, N. Tsuga, K. Suzuki, j. Appl. Phys. Suppl. **32**, 386 (1961).

[6.61] M. Sugimoto, S. Okamota, T. Takei, Repts. Scient. Res. Inst. **32**, 61 (1956).

[6.62] T. Akashi, M. Tobita, U. S. patent **No. 3, 169**, 115 (1965).

[6.63] F. Bradley, ceram. Age, **72**, 31 (1958).

[6.64] E. Ross et.al, Zeit. F. angew. Physic, **17**, 504 (1964).

[6.65] K. ohta et.al. Japan J. Appl. Phys. **3,** 576 (1957).

[6.66] C. Guillaud, proc. IEEE., B. Suppl. **104,** 165 (1957).

[6.67] M. Paulus et.al. J. phys. Soc. Japan, **17,** 632 (1962).

[6.68] K. H.Rao, el. al. Solid State Commun. **36,** 777(1980).

[6.69] K. H. Rao et. al. J. Appl. Phys. **52,** 1376 (1981).

[6.70] R. Rezelescu el. al. J. Magn. Magn. Mat. **177**, 448 (1992).

[6.71] M. Pol et.al. J. Magn. Magn. Mat. **152**, 370 (1996).

[6.72] D. N. Bhosale et.al. J. Magn. Magn. Mat. **173**, 51(1997).

[6.73] M. Drofenik, A. Zindarsic, D. Markovec, J. Am. Ceram. Soc., **81(11),** 2841(1998).

[6.74] M. M. Haque, M. Huq, M. A. Hakim, Indian J. Phys., **78 (A),** 398 (2004).

[6.75] H. Rikukawa, IEEE Trans. On Magn. **18(6),** 1535 (1982).

[6.76] A. Verma, Op. Thakur, C. prakash, T. C. Goel, R. G. Mendiratta, Mater. Sci. Eng. **B 116,** 1 (2005).

[6.77] K. Janghorban, H. Shokrollahi, J. Magn. Magn. Mater., **308**, 238 (2007).

[6.78] G. C. Jain, B. K. Das, R. B. Tripatri, R. Narayan, J. Magn. Magn. Mat., **14**, 80 (1979).

[6.79] J. E. Burke, W. D. Kingery, Ceramic Fabrication process, Wiley, N. Y. 12 (1958).

[6.80] S. Otobe, Y. Yachi, T. Hashimoto, IEEE Trans. On Magn; **35 (5),** 3409 (1999).

[6.81] L. Neel, Annales de physique, **3,** 137 (1948).

[6.82] Y. Yaft, C. Kittel, Physical Review, **80,** 1090 (1952).

[6.83] A. Globus, J. phys. (paris) (Suppl. C1) (proc. ICF-3) , 12 (1977).

[6.84] S. Murthy, N. S. Natera, M. G. Youssef, S. I. Begum, **181**, 969 (1969)

[6.85] M. sing, S. P. Sud, Mater. Sci. Eng.B, **83**, 180 (2001).

[6.86] A. Thakur, P. Mathur, M.singh, Z phys. Chem, **221**, 1 (2007).

Chapter Seven

Conclusion

Iron deficient Ni-Zn and iron excess Mn-Zn ferrite core materials have been developed by using cheap beach sand mineral, magnetite with the addition of CuO, V_2O_5, Eu_2O_3 and In_2O_3. From the systematic investigation of iron deficient Ni-Zn ferrites and iron excess Mn-Zn ferrites with the addition of CuO, V_2O_5, Eu_2O_3 and In_2O_3 the following conclusions have been drawn:

(i). The incorporation of V_2O_5 in the composition of iron deficient Ni-Zn ferrite enhances appreciably the sintered density, saturation magnetization and Curie temperature at 0.4 mol% of V_2O_5 content. The increment of saturation magnetization and Curie temperature are due to the increase of resultant sublattice magnetic moment and A-B exchange interaction. The permeability spectra of the ferrite system shows that the initial magnetic permeability of all the samples with V_2O_5 content remains fairly constant around 10 MHz. The maximum value of initial magnetic permeability 1470 at 100 kHz can be achieved for sample containing 0.4 mol% of V_2O_5 addition. This increment of permeability is due to the effect of V_2O_5 on the grain size of the core material. The minimum value of normalized loss factor 0.63×10^{-5} and maximum value of dc resistivity 1.25×10^{4} ohm-cm are achieved for sample containing 0.4 mol% and 1 mol% of V_2O_5 addition respectively. With the addition of V_2O_5, V^{5+} ions occupy B-sites (equivalent lattice site) which limit the degree of Fe^{2+} to Fe^{3+} electron hoping conduction resulting in increase in resistivity. The minimum value of eddy current loss 8.712×10^{-3} can also be achieved for sample containing 1 mol% of V_2O_5 addition showing improvement of frequency range for applications of the prepared core materials.

(ii). The inclusion of the CuO in the iron deficient Ni-Zn ferrite system enhances markably the sintered density, saturation magnetization and Curie temperature at 1 mol% CuO content. The increase of the saturation magnetization and Curie temperature are due to the decreased porosity and increased resultant sublattice magnetic moment as well as the increase of the A-B exchange interaction. The permeability spectra of the ferrite system shows that the initial magnetic permeability

of all the samples with CuO content remains fairly constant around 1 MHz. The maximum value of initial magnetic permeability 1530 at 100 kHz can be achieved for sample containing 1 mol% CuO content. The increment of the permeability is due to the larger grains and with little intergranular porosity of the core materials in presence of CuO. The minimum value of the normalized loss factor 0.752×10^{-5} and maximum value of dc resistivity 0.91×10^{5} ohm-cm are achieved for sample containing 2 mol% CuO content. The increase of the resistivity is due to improved sintering in presence of Cu which decreases the porosity and discourages over oxidation during cooling and hence limits the Ni^{2+}-Ni^{3+} conduction process. The minimum value of eddy current loss 1.188×10^{-3} can also be achieved for sample containing 2 mol% CuO addition showing extension of frequency range for application of the prepared core materials.

(iii). The incorporation of In_2O_3 in the iron deficient Ni-Zn ferrite system enhances sintered density as well as the lattice constant values with increasing addition of In_2O_3. The increase of the lattice constant values is due to the larger ionic radius of In^{3+} ions as compared to the displaced Fe^{3+} ions. However, the saturation magnetization and Curie temperature value of the ferrite system decreases with the increasing addition of In_2O_3. The decrease in saturation magnetization of is possibly because of the presence of diamagnetic In^{3+} ions in the B-sites of the ferrite lattice replacing Fe^{3+} ions as well as the weakening of the A-B exchange interaction due to In^{3+} ions. The permeability spectra of the ferrite system with the addition of In_2O_3 shows that as the frequency rises permeability increases a little and then remains fairly constant around 1 MHz. The initial magnetic permeability at 100 kHz decreases with the addition of In_2O_3. The decrement of the initial permeability is due to the decrease of average grain size of the core materials with increasing concentration of In_2O_3. However the minimum value of normalized loss factor 0.35×10^{-5} and maximum value of dc resistivity 2.69×10^{4} ohm-cm are achieved for sample containing 1.5 mol% and 3.5 mol% of In_2O_3 addition respectively. The increment of the dc resistivity is due to the presence of In^{3+} ions at the B-sites which reduces the degree of Fe^{2+} to Fe^{3+} electron hoping conduction. The minimum value of eddy current loss 4.048×10^{-3} can be achieved for sample containing 3.5 mol% of In_2O_3 addition.

(iv). The inclusion of Eu_2O_3 in the iron deficient Ni-Zn ferrite system enhances the sintered density as well as the lattice constant values. The increase in lattice constant is due to larger ionic radius of Eu^{3+} ions in comparison with the displaced Fe^{3+} ion. Saturation magnetization of all the core samples increases markably with the addition of Eu_2O_3 up to 1.5 mol % Eu_2O_3. This increment is due to the A-sites occupation of antiferromagnetic Eu^{3+} ions and replacement of Fe^{3+} ions from A-sites to B-sites, thereby increase the resultant sublattice magnetic moment. The enhancement of the Curie temperature of the samples are due to the increase of A-B exchange interaction because of the occupation of Eu^{3+} ions on A-sites. The permeability spectra of the ferrite system shows that the initial magnetic permeability remains almost constant around 10 MHz. maximum value of initial magnetic permeability 1900 at 100 kHz is achieved for sample containing 1.5 mol% of Eu_2O_3 addition. Possible explanation of this increment is due to the effect of Eu_2O_3 on the grain size of the core materials. The minimum value of normalized loss factor 0.54×10^{-5} is achieved for sample containing 1.5 mol% of Eu_2O_3 addition. maximum value of dc resistivity 2.42×10^{4} ohm-cm is achieved for sample containing 2 mol% Eu_2O_3 addition. This increment of resistivity is due to increase in grain growth resulting in a corresponding decrease in the number of boundaries leading thereby to a increase in resistivity. The minimum value of eddy current loss 4.50×10^{-3} is achieved for sample containing 2 mol% of Eu_2O_3 addition which shows improvement of the frequency range for application of the prepared core materials.

(v). The incorporation of CuO in the composition of iron excess Mn-Zn ferrite enhances appreciably the sintered density and the saturation magnetization at 4 mol% of CuO content. The increment of saturation magnetization is due to the enhancement of density. The Curie temperature decreases a little due to the decrement of A-B exchange interaction for the occupation of Cu^{2+} ions in the B-sites of the ferrite lattice. Permeability spectra of the ferrite system shows that initial permeability of all the samples rises up to a particular frequency, then falls a little around 100 kHz and remains fairly constant around 10 MHz. The maximum value of initial magnetic permeability 900 at 100 kHz is achieved for sample containing 4 mol% of CuO addition. The increase in permeability is due to the larger grains of the prepared core materials with little intergranular porosity. The minimum value of normalized loss

factor 6×10^{-5} is achieved for sample containing 4 mol% CuO addition. The maximum value of dc resistivity 5.754×10^{4} ohm-cm is also achieved for sample containing 4 mol% CuO addition. The increment of the resistivity is due to the occupation of Cu^{2+} ions in the equivalent octahedral sites, which limit the degree of Fe^{2+} to Fe^{3+} electron hoping conduction resulting in increase of resistivity. The minimum value of eddy current loss 1.892×10^{-3} can be achieved for sample containing 4 mol% CuO addition ensuring extension of frequency for application of the prepared core materials.

(vi). The inclusion of V_2O_5 in the iron excess Mn-Zn ferrite system enhances markably the sintered density, saturation magnetization and Curie temperature at 0.6 mol% of V_2O_5 addition. The increment in the saturation magnetization is due to the enhancement of resultant sublattice magnetic moment as well as the sintered density. The increment of Curie temperature is due to the occupation of V^{5+} ions in the octahedral lattice site, as a result some of Fe^{3+} ions would be pushed off from octahedral to tetrahedral sites thereby increasing A-B exchange interaction and hence the Curie temperature. The initial magnetic permeability spectra of the ferrite system show that as the frequency rises, the initial permeability value increases a little up to around 10 kHz and then remain fairly constant up to around 1 MHz. The maximum value of initial magnetic permeability 960 at 100 kHz is achieved for sample containing 0.6 mol% of V_2O_5 addition. The increment of permeability is due to the increased amount of grain boundary and homological decrement of porosity in the crystalline grain and grain boundary. The minimum value of normalized loss factor 1.443×10^{-4} is achieved for sample containing 0.6 mol% of V_2O_5 addition. The maximum value of dc resistivity 9.2×10^{3} ohm-cm can be achieved for sample containing 1 mol% V_2O_5 addition. The increment of the resistivity is due to the increased amount of grain boundary with V_2O_5, so the grain boundary resistivity increases thereby increasing the dc resistivity of the ferrite system. The minimum value of eddy current loss 1.178×10^{-2} can also be achieved for sample containing 1 mol% V_2O_5 addition showing frequency extension for applications of the prepared core materials.

(vii). The incorporation of Eu_2O_3 in the iron-excess Mn-Zn ferrite system enhances appreciably the sintered density and the saturation magnetization at 2 mol% Eu_2O_3 addition. An increase in the lattice constant values with increasing amount of Eu_2O_3 is due to the larger ionic radius of Eu^{3+} ions. The increment of saturation magnetization is due to the existence of canted spins; canting of spin gives rise to Y-K angles which compares the strength of A-B and B-B exchange interaction. The initial magnetic permeability spectra of the ferrite system show that as the frequency rises the initial permeability value remains fairly constant up to around 1 MHz. The maximum value of initial magnetic permeability 1022 at 100 kHz is achieved for sample containing 2 mol% Eu_2O_3 addition. The increment of permeability is due to the influence of Eu ions in the diffusion process and increase of grain size of the core materials. The minimum value of normalized loss factor 4.12×10^{-4} is achieved for sample containing 2 mol% Eu_2O_3 addition. The maximum value of dc resistivity 5.063×10^{4} ohm-cm can be achieved for sample containing 4 mol% Eu_2O_3 addition. The increment of resistivity is due to the occupation of Eu^{3+} ions at the octahedral sites which limit the degree of Fe^{2+} to Fe^{3+} electron hoping conduction resulting in increase of resistivity. The minimum value of eddy current loss 2.15×10^{-3} can also be achieved for sample containing 4 mol% Eu_2O_3 addition which ensures attainment of frequency extension for application of the prepared core materials.

(viii). The inclusion of In_2O_3 in the iron excess Mn-Zn ferrite system enhances significantly the sintered density and lattice constant values. The increment of lattice constant values is due to the larger ionics radius of In^{3+} than the displaced Fe^{3+} ionics, so ferrite lattice bulges and the lattice constant increases. Saturation magnetization increases appreciably at 2 mol% In_2O_3 addition. The increment of saturation magnetization is due to the occupation of the diamagnetic In^{3+} ions on A sites which leads to a decrease in the A-sublattice magnetization, keeping the B-lattice magnetization constant, as a result the resultant magnetization increases. However, the Curie temperature value decreases with increasing addition of In_2O_3. This decrement of Curie temperature is due to the weakening of A-B exchange interaction, results in a decrease of the Curie temperature. The initial magnetic permeability spectra of the ferrite system show that as the frequency rises, the initial magnetic permeability rises a little up to around 10 kHz and then remain fairly

constant around 1 MHz. The maximum value of initial magnetic permeability 900 at 100 kHz is achieved for sample containing 3 mol% In_2O_3 addition. The increment of the initial magnetic permeability is due to the increase of saturation magnetization and average grain size of the core sample and decrease of the magneto-crystalline anisotropy constant K_1. The minimum value of normalized loss factor 1.35×10^{-4} is achieved for sample containing 1.5 mol% In_2O_3 addition. The maximum value of dc resistivity 0.932×10^{4} ohm-cm can be achieved for sample containing 3.5 mol% of In_2O_3 addition. The increment of dc resistivity is due to the occupation of In^{3+} ions on the B-sites (octahedral sites) which limit the degree of Fe^{2+} to Fe^{3+} electron hoping conduction resulting in increase of the resistivity. Minimum value of eddy current loss 1.168×10^{-2} can also be achieved for sample containing 3.5 mol% of In_2O_3 addition showing frequency extension for applications of the prepared core materials.

Achieved characteristic properties of the developed Ni-Zn ferrites and Mn-Zn ferrite core materials in comparison with the commercial ferrite core materials used as inductors, radio antennas, TV line scanning transformers, picture tube deflection yokes, coils in filter circuits are as follows [7.1-7.3]:

Ni-Zn ferrite core materials:

	Characteristic properties	Ni-Zn ferrite core materials (Developed)	Commercial Ni-Zn ferrite core materials
(i)	Saturation Magnetization ($4\pi M_s$)	4270 □ 5030 Gauss	3000 □ 4200 Gauss
(ii)	Initial magnetic permeability	700 □ 1900	500 □ 2000
(iii)	Curie temperature	210 □ 270°C	200 □ 280°C
(iv)	Resistivity	1.25×10^{4} □ 0.91×10^{5} ohm-cm	10^{3} □ 10^{5} ohm-cm
(v)	Loss Factor	0.35×10^{-5} □ 0.752×10^{-5}	1.5×10^{-4} □ 5×10^{-5}

Mn-Zn ferrite core materials:

	Characteristic properties	Mn-Zn ferrite core materials (Developed)	Commercial Mn-Zn ferrite core materials
(i)	Saturation Magnetization ($4\pi M_s$)	3015 □ 3900 Gauss	3000 □ 4000 Gauss
(ii)	Initial magnetic permeability	285 □ 1022	300 □ 1000
(iii)	Curie temperature	90 □ 155°C	90 □ 180°C
(iv)	Resistivity	2.3×10^{3} □ 5.8×10^{4} ohm-cm	10^{2} □ 5×10^{3} ohm-cm
(v)	Loss Factor	4.12×10^{-4} □ 6×10^{-5}	0.5×10^{-5} □ 1.2×10^{-5}

Therefore, it will be reasonable to say that the developed soft ferrite core materials can be used for low frequency electronic components such as inductors, transformers, radio antenna, television line scanning transformers, picture tube deflection yokes and as other devices in radio, television and communication equipment.

References:

[7.1] A. Goldman, Hand book of Modern Ferromagnetic Materials, Kluwer Academic publishers, Boston/Dordrecht/London (2002).

[7.2] A User's Guide, Magnetic Materials producers Association, Chicago, IL 60603 (1998).

[7.3] Wm. Colonel, T. McLyman, Magnetic core selection for Transformers and Inductors, Marcel Dekkar Inc., New York, (1997).

List of Publications:

a) In Indexed Journals:

1. **Shireen Akhter** M. A. Choudhury, J. Rahman, "Influences of Eu_2O_3 addition on the magnetic and electrical properties of iron excess Mn-Zn ferrite", International Conference on Magnetic Materials (ICMM-2007) Proceedings series, American Institute of Physics (AIP), pp. 252-254, 2008 .
2. **Shireen Akhter,** M. A. Choudhury and J. Rahman, "*High permeability nickel-zinc ferrite core materials for low frequency application using magnetite*", J. Bang. Academy of Sciences, **vol. 29**, No. 2, pp 187-193, Dec. 2005.
3. **Shireen Akhter** M. A. Choudhury and J. Rahman, "*Manganese-Zinc ferrite core materials for low frequency radio and television composition components using magnetite*", J. Nuclear Science and Applications, **vol. 15**, No.1, pp 5-8, June, 2006.
4. **Shireen Akhter**, M. A. Choudhury and J. Rahman, "*Influence of V_2O_5 addition on the magnetic and electrical properties of iron-deficient Ni-Zn ferrite",* Journal of Bangladesh Academy of Sciences, **vol. 33**, No -2, pp. 145-149, December, 2009.
5. **Shireen Akhter**, M. A. Choudhury and J. Rahman, *"Influence of In_2O_3 addition on the magnetic and electrical properties of iron-deficient Ni-Zn ferrite",* Journal of Bangladesh Academy of Sciences, **vol. 36**, No. 2, pp. 153-158, 2012.

Submitted for publications:

1. **Shireen Akhter,** M. A. Choudhury, J. Rahman and Z. Hasan, "*Influences of In_2O_3 addition on the magnetic and electrical properties of iron excess Mn-Zn ferrite*", J. of Magnetism and Magnetic Materials , August, 2014.
2. **Shireen Akhter** M. A. Choudhury, J. Rahman and Z. Hasan, "*Influence of Eu_2O_3 on the Magnetic and electrical properties of iron deficient Ni-Zn ferrite*", Indian J. of Pure & Applied Physics, September, 2014.

b) Paper presented in the International and National Conferences/symposiums:

1. "**Shireen Akhter** M. A. Choudhury, J. Rahman, "Influences of Eu_2O_3 addition on the magnetic and electrical properties of iron excess Mn-Zn ferrite", International Conference on Magnetic Materials (ICMM-2007) Saha Institute of Nuclear Physics, Kolkata, India, December, 11-16, 2007.
2. "**Shireen Akhter** M. A. Choudhury, J. Rahman, "*Influence of V_2O_5 addition on the magnetic and electrical properties of iron-deficient Ni-Zn ferrite*", International Conference on Magnetic Materials (ICMM-2010) Saha Institute of Nuclear Physics, Kolkata, India, October, 25-29, 2010.
3. "**Shireen Akhter** M. A. Choudhury , "Development of Mn-Zn ferrite core materials for low frequency radio and television components using magnetite", The 2nd International Conference on Structure, Processing and properties of Materials; SPPM- 2004, Dhaka , Bangladesh, February, 25-27, 2004.
4. **Shireen Akhter**, M. A. Choudhury and J. Rahman, *"Influence of In_2O_3 addition on the magnetic and electrical properties of iron-deficient Ni-Zn ferrite",* BAS-IAP-TWAS-NASIC International Conference on Gender participation in the Development of Science, Dhaka, Bangladesh, November, 14-15, 2009.